AN ABSTRACT OF THE DISSERTATION OF

Sergio G. Arias for the degree of Doctor of Philosophy in Mechanical Engineering presented on February 6, 2009.

Title: Failure Analysis of Pre-notched Composite Laminated Plates under Four-point Bending Conditions

Abstract approved: ______________________________________

Timothy C. Kennedy

Ever since composite laminate technology was introduced into the aerospace and automotive industry, there has been a need to fully understand the damage progression experienced by composite laminated plates in the presence of a notch. While numerous research studies have been conducted on this matter when subjected to in-plane loads, not much focus has been directed to the out-of-plane loading conditions. To address this issue, a comprehensive study in partnership with the Boeing Commercial Airplane Company and the Federal Aviation Administration was carried out, using laboratory tests and computer simulations, to predict the failure mechanisms of pre-notched composite laminated plates under four-point bending.

A total of 48 pre-notched laminates, varying in size, layer orientations, and thickness were tested, and the deformation data was recorded by means of strain gages. Two notch lengths of 1-in. and 4-in. with an end radius of 0.125-in. were

considered in the analysis. The laminates were also modeled in the finite element software ABAQUS to determine the concentration factors and explore the damage progression based on the Hashin criterion. The results were compared to the test data for correlation and validity.

From the simulation results, it was determined that the classical laminated plate models under-predicted the strain concentration factors, and that Reissner's models should be employed in order to conduct failure analysis on composite laminates when subjected to pure bending. The shell model that takes into account transverse shear effects was then chosen to provide the progressive damage simulation. It was found that the results of these theoretical models from ABAQUS were very similar to the results of the test samples generated in our experiments. In general, very good agreement between the simulations and the test results was obtained for the thin laminates. Particularly, as the percentage of 0-degree plies increased, so did the correlation with the test samples. Our theoretical models were capable of reproducing accurately their failure points by taking into consideration the large deformation effects and damage progression. On the other hand, the thick laminate models were not as successful in predicting failure. In most cases, they computed a failure moment higher than the ones found in the experiment.

Failure Analysis of Pre-notched Composite Laminated Plates under Four-point

Bending Conditions

by

Sergio G. Arias

A DISSERTATION

submitted to

Oregon State University

in partial fulfillment of

the requirements for the

degree of

Doctor of Philosophy

Presented February 6, 2009

Commencement June 2009

Doctor of Philosophy dissertation of Sergio G. Arias presented on February 6, 2009.

APPROVED:

Major Professor, representing Mechanical Engineering

Head of the School of Mechanical, Industrial, and Manufacturing Engineering

---

Dean of the Graduate School

I understand that my dissertation will become part of the permanent collection of Oregon State University libraries. My signature below authorizes releases of my dissertation to any reader upon request.

Sergio G. Arias, Author

ACKNOWLEDGEMENTS

To Dr. Timothy C. Kennedy: I thank you for been a great mentor and advisor, and for having the patience to explain the complexities of my research. I also want to express my gratitude for finding the funds for this research, and allowing me to take leave of absences for my internship appointments in Germany and Salem. It has been an honor to work with you for both my Master's and Doctoral projects, and I hope that some day I turn into the great mentor and engineer that you are.

To Dr. William H. Warnes: Bill, you are one of the best professors in the entire MIME department. I also believe you are a great person and very friendly to the graduate students. You were always interested in helping me with my research and available to discuss whatever issues or problems I had during these years.

To Dr. Brian K. Bay: Thank you for helping me to try to use DIC equipment in my experiments and allowing me to use your LabView equipment. I learned quite a great deal of experimental set-up with you.

To Dr. Richard B. Peterson and Dr. Michael H. Scott: Even though you were not deeply involved in my research, you both showed interests in being part of my committee and made sure I followed the PhD guidelines. I thank you for being in my committee and having the patience and understanding of my scheduling.

To Steve Adams, Chris Patton and Trenton Carpenter: I also want to express my gratitude for helping me in the ME workshop with the diverse works regarding the manufacturing of the fixtures. You were always available and allowed me to use your laboratory equipment without problems.

To William Beattie: Thanks Will. I am very grateful for helping me with the programming in LabView. I know that without your help, I would’ve had very difficult times dealing with it.

To Chris Dandeneau, Ashly Stone and Christina Package: Chris, you have been a great friend and supporter during the last year of my work. I will miss our social conversations during our many coffee breaks at Interzone. I will also never forget Euro 2008 and our movie nights. Also, thanks for your cooking events and great sense of humor. Ashly and Christina, you were my closest friends in Corvallis for the last 3 years. The times I have spent with you two gave me a social life, which kept me sane and provided me with some great memories. Thanks for being my closest friends.

To all my friends: I refrain from writing your names for fear of forgetting one of you. You know who you are, and I thank you for just being there when I needed you the most.

To my parents: Thank you for your unconditional love. Without your passion and support, I would’ve never been able to achieve this level of accomplishment. I personally dedicate my doctorate degree to you for helping me during the tough times, for inspiring me to study and work hard, and for giving me the ambition and patience in life to become the person that I strive to be. Who I am in my life, I owe it to you.

TABLE OF CONTENTS

Page

TABLE OF CONTENTS (Continued)

Page

TABLE OF CONTENTS (Continued)

Page

LIST OF FIGURES

Figure Page

LIST OF FIGURES (Continued)

LIST OF FIGURES (Continued)

LIST OF FIGURES (Continued)

LIST OF FIGURES (Continued)

Figure Page

LIST OF FIGURES (Continued)

LIST OF FIGURES (Continued)

LIST OF FIGURES (Continued)

LIST OF FIGURES (Continued)

LIST OF TABLES

Chapter 1. Introduction and Project Objectives

1.1. Introduction to Composite Laminated Materials

The concept of composite materials, which are basically the combination of two or more materials to obtain a new material, has been known for thousands of years. Our ancestors realized that by combining some particular materials in a certain way, they could produce a new material that possessed greatly enhanced material properties than by themselves. Consequently, they developed and perfected fabrication methods and tools to manufacture these materials to be used for building construction, weapons, and clothing.

Nevertheless, with the advent of steel and other metallic alloys, the interest in composite materials declined; and, as a result, the use of composites remained low-key and became practically obsolete for the greater part of the Industrial Revolution of the late 18th and early 19th centuries. Therefore, the research and investigation of composites did not prosper as quickly and steadily as steel did, for instance. Subsequently, steel became quickly the primary choice of material for all sorts of manufacturing and construction uses. Steel and its family of metallic alloys, in particular, were widely used for the automotive and aerospace industries because of their strong material properties and low cost of production. However, over the last few decades, composite materials have become increasingly more desired and have become an important structural material for a large number of industries.

Because of their superior engineering properties (i.e. high strength, stiffness-to-density ratios,) composite materials, as seen on Figure 1. 1, are now becoming widely used in advanced structures in aerospace, automotive, marine, and many other industries. Despite these excellent material properties, composites are not perfect, even though nowadays technology allows us to tailor-make composites to fit our design requirements. That is what the core function of the laminated composite materials is based on.

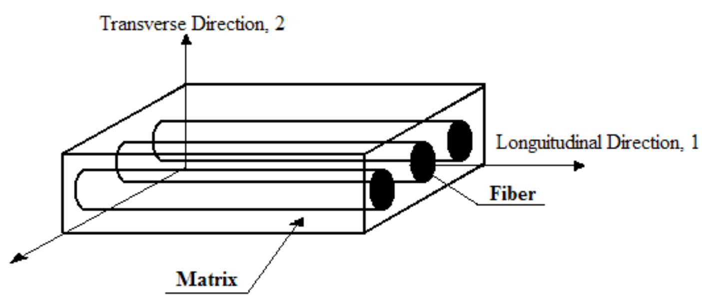

Figure 1. 1 - Schematic of a long fiber composite material

Composite materials have predominantly orthotropic properties. For example, a material like wood or a unidirectional fiber-reinforced composite exhibits much larger modulus on its principal axis (along the fibers) than on its transverse direction. Normally, these materials exhibit similar modulus in their transverse planes ($E_2 = E_3$,) and thus can be treated as transversely isotropic. As a result, these materials are very strong if loaded in the principal direction but very weak if loaded in the transverse directions. However, we can improve the material properties of the composite by combining or laying up a series of fiber-reinforced sections or “plies” in such a manner that the principal orientations are rotated. We therefore obtain an entirely new material, which no longer possesses the orthotropic properties of the single ply. Therefore, we can custom-make a material to achieve the desired properties to meet our design requirements. The thickness of the plies, their orientation, order sequence, and quantity will determine the material properties of this composite material and consequently will exhibit anisotropic, orthotropic, or quasi-isotropic behaviors.

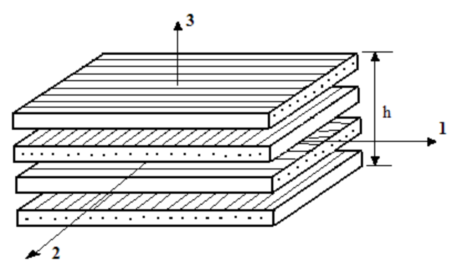

Figure 1. 2 - Example of composite laminate

Composite laminated plates, as shown in Figure 1. 2, will exhibit quasi-isotropic behavior and will display isotropic properties when they are loaded under in-plane conditions, but may not respond in the same manner when the plates are under bending. Another outcome of the fabrication of composite laminates is the formation of what is called the “coupling” of the in-plane and out-of-plane response. An example of this phenomenon is the formation of curvature when a plate is subjected to in-plane loading.

1.2. Background Information on Composite Materials Research

Because of the increasing use of composite laminates in the automotive and aerospace industries, extensive and thorough analysis and testing of them is mandatory. Most of the research conducted on composite laminated plates or shells has been addressed to in-plane loading situations. That is, testing and studies where the specimens are in tension, compression, and shear. Not much focus has been addressed to the out-of-plane loading situations, where bending and twisting of the plates are present. However, it is well known that there are many real situations where a structure would suffer from complex loading conditions, such as those found on aircraft fuselage [43], where transverse shear is a major factor in the failure of the composite laminates. Hence, it is very important to have a full understanding of the behavior of the composite laminates when they are subjected to these out-of-plane loading conditions.

There are two main theoretical models for plates and shells, and they both have been researched extensively. The first is called the Classical Plate Theory (CPT,) and, for the most part, was developed by Kirchhoff [50]. It is also referred as Kirchhoff Plate Theory (KPT). The second theory is referred as Reissner Plate Theory (RPT) [28]. The main difference between the two of them is the consideration of the transverse shear effects. Kirchhoff's theory can be applied to both in-plane and out-of-plane loading conditions. Consequently, KPT works fine for thin laminated composites materials where transverse shear effects are almost negligible. On the other hand, RPT does take into account the transverse shear effects; and, as a result, this model is more fitting for thick composite laminates.

Besides loading conditions, another important aspect of a composite structure is the ability of the material to withstand fracture. Fracture is an important aspect in the design of aircraft fuselages, for instance, because these structures are heavily influenced by damage tolerance requirements. Numerous studies have been conducted on the matter of analyzing notched composite laminated plates [43], but here again; most of the research has been directed for in-plane loading conditions. However, in the cases of aircraft fuselages, where out-of-plane loading may be induced, it is very important to have a good understanding of the failure progression that a cracked composite laminate may have in order to avoid unnecessary and costly over conservative designs due to the addition of large safety factors.

Therefore, there is a need for useful analysis techniques in the design of composite aircraft or automotive structures under out-of-plane loading. However, there are some major obstacles to be faced. In dealing with composite materials, as mentioned earlier, transverse effects might possibly influence the failure behavior under flexural loadings. Composite materials, in particular, are more likely to cause stress distribution discontinuities throughout the thickness of the laminate due to these effects (unlike homogeneous materials such as steel, for instance.) In homogenous materials, all failure modes (I, II and III) can occur simultaneously at the crack tip, during bending, shear, and twist. In the case of composite laminates, which can be highly anisotropic, these modes would act in a more complex manner. In order to simulate the behavior of these materials, an unusual degree of analytical sophistication will be necessary. Consequently, the development of these analysis techniques will require significant experimental data to support the results obtained by the theoretical models. Unfortunately, very little test data is available for the case scenarios here presented.

1.3. Project Objectives

The main purpose of this work is to obtain a good understanding of crack propagation in composite laminated plates and to develop analysis techniques that will be useful in the design of composite aircraft structures subjected to out-of-plane loading. In order to implement these analysis techniques into a practical tool to design aircraft fuselages, the produced models must be accurate, efficient, and suitable for design implementation. Also, these models will have to be sophisticated, yet simple enough that they can be thoroughly evaluated by laboratory testing.

The focus of this research will now take on a more basic approach, and the modeling efforts will be centered involving simple structures under pure bending of unstiffened laminates containing centered-notches. Also, the specimens will be large enough to avoid boundary/edge effects that may interfere with the results. Through a cooperative partnership between Oregon State University and the combined efforts of Boeing Commercial Airplane Company and the Federal Aviation Administration (FAA), we will develop these models to accomplish this objective.

Since only a small amount of experimental data for notched laminates that have been subjected to out-of-plane loading are available [14], we are faced with the prospect of performing these sorts of experiments in our own laboratory. Some experimental results were available in the Boeing test data base, but they were based on laminates with 1/4-in. holes under four-point bending. This will not give us much information, since the prediction of failure of plates containing notches 1-in. and 4-in. is necessary for our research. Due to the characteristics and irregular behaviors of composites, the information obtained from these laminates with small notches will not predict efficiently the failure of laminates with larger notches. Therefore, for a limited number of tests, we will determine the modes of failure of the laminates and evaluate the capability of a currently existing analysis technique for predicting these failures.

To accomplish our objective, then, will require both experimental and computational efforts. The project is divided into three main tasks:

1. Testing of notched laminates under four-point bending.
2. Modeling stress concentrations in notched laminates under bending.
3. Modeling progressive damage in notched laminates under bending.

1.3.1 Testing of Notched Laminates under Four-point Bending

The first task will be the testing of notched laminates under four-point bending. Two notch lengths will be considered: 1-in. long ovaloid with 1/8-in. end radius and a 4-in. long ovaloid with 1/8-in. end radius. A total of six different laminate lay-ups, consisting of 20 plies and 40 plies, will be examined. The plies will be laid up at the 0-degree, 90-degree, and ±45-degree orientations. These angles at each layer represent the angular orientation of the longitudinal direction (fiber direction) of that particular lamina with respect to the 0-degree direction at the laminate coordinate system.

Each ply of the composite laminate will have a thickness of 0.0074-in., forming 0.148-in. 20-ply laminates and 0.296-in. 40-ply laminates. For each thickness we will have three laminate types consisting of 10% 0-degree plies, 30% 0-degree plies and 50% 0-degree plies.

The laminates will be instrumented with strain gages on both sides of the laminate in several configurations in order to obtain a good quantitative and qualitative measure of the deformation rate and damage progression. The data obtained from these gages will then be compared with the results obtained from the simulation models.

1.3.2 Modeling Stress Concentrations in Notched Laminates under Bending

The second task consists of modeling stress concentrations in notched laminates under bending by computer simulation. We will use the general purpose finite element analysis software ABAQUS to construct the theoretical models for each of the laminates that we tested under four-point bending. The laminates will be modeled using 3D-Solid and Shell elements at the ply-level. Less detailed models will be constructed using conventional shell elements to determine the meshing level needed for acceptable accuracy.

Bending moment output data, as well as the strain output data, will be extracted from the simulations to determine a relationship between the concentration factors and notch length.

1.3.3 Modeling Progressive Damage in Notched Laminates under Bending

The third task will focus on progressive damage modeling of notched laminates under four-point bending. It is well known that in composite materials, a damage zone is developed ahead of the crack tip, and consequently this influences the crack propagation. For each of the laminates that we tested, we will make use of the progressive damage model for composites that is embedded in ABAQUS to simulate the growth of the notch up to ultimate failure. This ABAQUS module, which follows the Hashin model, will take into account four failure modes: Fiber tension and compression failure, and matrix tension and compression failure.

The failure modes predicted by these models will be compared to those observed in the experiments, and this will provide us with a test of validity of the model for these particular loading conditions that have not been considered previously.

Chapter 2. Literature Review: Notched Composite Laminates under Bending

2.1 Concentration Factors on Notched Plates

The analysis of stresses around notches in plates subjected to out-of-plane bending has been the subject of a number of investigations. The geometry of the typical situation is illustrated in Figure 2. 1, which shows a plate (usually of infinite extent) with a thickness of h, [39]. It contains a notch of width 2a that is either a circular hole (when a = b), an elliptical hole (when a ≠ b), or a sharp crack (when b=0).

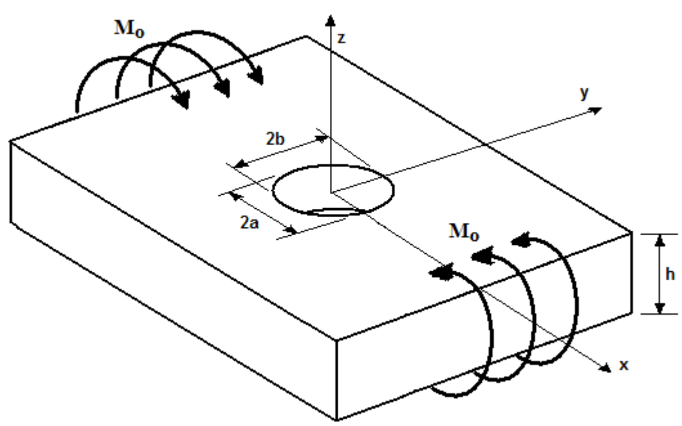

Figure 2. 1 - Typical plate with a hole/notch schematic

The typical loading situation consists of a uniform bending moment with either M_x =M_o or M_y=M_o. Analyses have been carried out using two plate theories:

Kirchhoff Plate Theory (KPT,) which ignores the effects of transverse shear deformation (this is also referred to as classical theory) and Reissner Plate Theory (RPT,) which accounts for the effect of transverse shear deformation. For uniform bending of a homogeneous, isotropic plate, the far field normal stress is linear through the thickness with a maximum value at the surface of the plate equal to:

$$\sigma_b = \frac{6\ M_0}{h^2} \tag{2.1}$$

At the notch there is a stress concentration that is normally expressed as $\sigma_{max}=k_b\ \sigma_b$ for the circular and elliptical holes. Using KPT, Goodier [12] studied the bending problem of a circular hole in an isotropic plate and found the stress concentration factor at the tip of the hole as follows:

$$k_b = \frac{5+3\nu}{3+\nu} \tag{2.2}$$

where ν is the Poisson's ratio. He found that the stress concentrations in the plate did not depend on the thickness of the plate or the size of the hole. However, Reissner, in his theory, found that the stress concentration factor was a function of the ratio of the thickness (h) and the size of the hole (diameter, a.) Reissner [31] developed his theory taking transverse shear deformation effects into account and found the following stress concentration factor:

$$k_b = \frac{3}{2} + \frac{1}{2}\left[\frac{\dfrac{3(1+\nu)K_2(\mu)}{2} - K_0(\mu)}{\dfrac{(1+\nu)K_2(\mu)}{2} + K_0(\mu)}\right] \tag{2.3}$$

where μ is a function of the thickness and hole diameter and is equal to

$\mu = a\sqrt{10}/h$, and K_0 and K_2 are modified Bessel functions. As illustrated in Figure 2. 2, we observe the influence of the ratio a/h in a plate, as k_b varies between 3 for a very thick plate (small a/h) to 1.78, with a value of ν=0.25. A three-dimensional elasticity solution was also developed by Alblas [2]. Alblas' model and Goodier's KPT results for a very thin plate are plotted here as well.

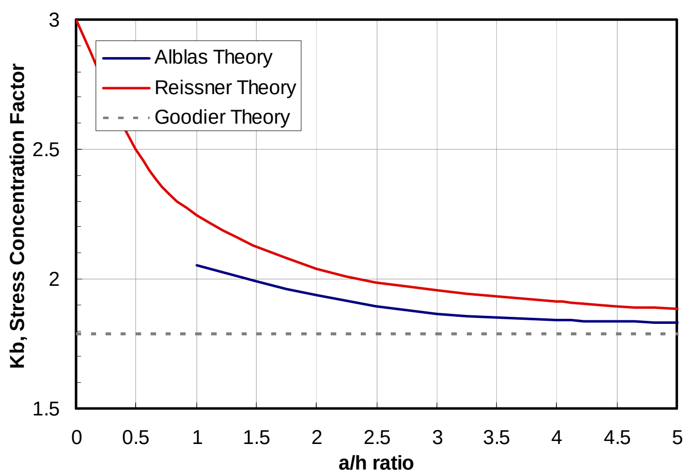

Figure 2. 2 - Stress Concentration Factors of a plate with a centered hole

Alblas found that his solution gave similar moment concentration factors to Reissner's k_b, but it differed when using stress concentration factors. Comparing Reissner's results to the elasticity solution indicates that RPT tends to over-predict the sensitivity of k_b in terms of the ratio a/h. Improvements to the theory developed in [28] were later presented by Lee [21] and Reissner [29] and are in closer agreement with the elasticity theory results.

Goodier [3] also studied stresses around an elliptical hole in an isotropic plate using KPT and found the stress concentration factor as

$$k_b = 1 + \frac{2(1+\nu)}{3+\nu}\frac{a}{b} \tag{2.4}$$

Naghdi [24] studied the same using RPT and was able to determine an approximate value for k_b for the case when the elliptical hole is not too slender. For slender ellipses, finite element analysis using RPT can be used to determine k_b. As in the case of the circular hole, k_b, depends on the ratio a/h. However, the sensitivity to thickness for an elliptical hole extends over a much larger range of a/h than it does for a circular hole.

The results described above are not directly applicable to notched laminates because of the anisotropic nature of these materials. The extension of KPT to orthotropic materials is reasonably straightforward. The case of a circular hole in an orthotropic plate under bending was studied by Lekhnitskii [22] where k_b is given as:

$$k_b = 1 + \frac{k\,n}{k + 4\,g} \tag{2.5}$$

where *k*, *n*, and *g* are functions of the flexural moduli D_{11}, D_{22}, and D_{66} (see equation 2.27). Prasad et al. [39] extended Lekhnitskii's results to the case of an elliptical hole in an orthotropic plate. Here, the solution is sufficiently complex that it is not possible to develop an explicit expression for k_b. Material anisotropy can have a significant effect on the stress concentration factor. A highly orthotropic laminate exhibits a significantly higher stress concentration factor than a quasi-isotropic laminate.

2.1 Mechanics of Composite Laminated Plates

A composite laminate is a bonded stack of laminae, or plies, at various orientations, as it was described earlier (see Figure 1. 2). The plies are normally bonded together by the same matrix material used for bonding the fiber within the layers. There are many types of composite laminates, but for this research we will focus on the fiber-reinforced composite laminate, which uses unidirectional fibers embedded in a matrix.

If we take a look at each lamina, the generalized Hooke's law gives the constitutive equation for a unidirectional ply (see Figure 1. 1) under plane-stress conditions, and can be written within the ply-axis system as:

$$\begin{Bmatrix} \sigma_1 \\ \sigma_2 \\ \tau_{12} \end{Bmatrix} = [Q] \begin{Bmatrix} \varepsilon_1 \\ \varepsilon_2 \\ \gamma_{12} \end{Bmatrix} \tag{2.6}$$

where the components of *[Q]* (the stiffness matrix) are composed of the engineering constants Q_{11}, Q_{22}, Q_{12}, Q_{16}, Q_{26}, Q_{66}, which are the following for a material that exhibits orthotropic characteristics:

$$Q_{11} = \frac{E_1}{1-\nu_{12}\nu_{21}} \qquad Q_{12} = \frac{\nu_{12}E_2}{1-\nu_{12}\nu_{21}}, \text{ or } \quad Q_{12} = \frac{\nu_{21}E_1}{1-\nu_{12}\nu_{21}}$$

$$Q_{22} = \frac{E_2}{1-\nu_{12}\nu_{21}} \qquad Q_{16} = Q_{26} = 0 \qquad Q_{66} = G_{12} \tag{2.7}$$

where the E_1 and E_2 are the elastic moduli, ν_{12}, and ν_{21} are the 1-2 plane Poisson's ratios, and G_{12} is the 1-2 plane shear modulus. Also, by using the reciprocal relation between the elastic moduli and the Poisson's ratios, we can completely define the material properties of the lamina.

$$\frac{\nu_{12}}{E_1} = \frac{\nu_{21}}{E_2} \tag{2.8}$$

Therefore, we can write the stress state of each lamina as a whole component with the following equation:

$$\begin{Bmatrix} \sigma_1 \\ \sigma_2 \\ \tau_{12} \end{Bmatrix} = \begin{bmatrix} \dfrac{E_1}{1-\nu_{12}\nu_{21}} & \dfrac{\nu_{21}E_1}{1-\nu_{12}\nu_{21}} & 0 \\ \dfrac{\nu_{21}E_1}{1-\nu_{12}\nu_{21}} & \dfrac{E_2}{1-\nu_{12}\nu_{21}} & 0 \\ 0 & 0 & G_{12} \end{bmatrix} \begin{Bmatrix} \varepsilon_1 \\ \varepsilon_2 \\ \gamma_{12} \end{Bmatrix} \tag{2.9}$$

Furthermore, we can also present the constitutive equation in terms of the strains, instead of the stress by obtaining the inverse matrix $[Q]^{-1}$

$$\begin{Bmatrix} \varepsilon_1 \\ \varepsilon_2 \\ \gamma_{12} \end{Bmatrix} = [Q]^{-1} \begin{Bmatrix} \sigma_1 \\ \sigma_2 \\ \tau_{12} \end{Bmatrix} \tag{2.10}$$

These stresses and strains are defined in the principal material coordinates (defined by the longitudinal direction of the fibers,) as shown in Figure 2. 3.

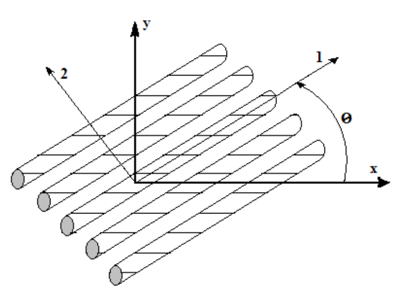

Figure 2. 3 - Rotation of principal material axes to x-y coordinates

However, because composite laminated plates present several layers with laminae at different orientations, a relation is needed between the stresses and strains in their principal material coordinates (lamina coordinates) and those in the body coordinates (laminate coordinates.) We recall the transformation method from mechanics of materials, where the transformation matrix that gives the proportional properties in the off-axis coordinate system is defined as:

$$[T]=\begin{bmatrix} Cos^2\theta & Sin^2\theta & 2\,Cos\theta\,Sin\theta \\ Sin^2\theta & Cos^2\theta & -2\,Cos\theta\,Sin\theta \\ -Cos\theta\,Sin\theta & Cos\theta\,Sin\theta & Cos^2\theta - Sin^2\theta \end{bmatrix} \tag{2.11}$$

where θ is the transformation angle from the 1-2 plane to the x-y plane (see Figure 2. 3). This transformation matrix is used to transform both stresses and strains into the x-y plane. The stresses and strains at the laminate coordinate can be expressed as:

$$\begin{Bmatrix} \sigma_x \\ \sigma_y \\ \tau_{xy} \end{Bmatrix} = [T] \begin{Bmatrix} \sigma_1 \\ \sigma_2 \\ \tau_{12} \end{Bmatrix} \tag{2.12}$$

$$\begin{Bmatrix} \varepsilon_x \\ \varepsilon_y \\ \frac{\gamma_{xy}}{2} \end{Bmatrix} = [T] \begin{Bmatrix} \varepsilon_1 \\ \varepsilon_2 \\ \frac{\gamma_{12}}{2} \end{Bmatrix} \tag{2.13}$$

The factor of ½ on the shear components of the strain is due to the classical definition of engineering shear strain, which is twice the tensor shear strain. We can further simplify these strain relations by introducing the Reuter's matrix, [R], as follows:

$$\begin{Bmatrix} \varepsilon_x \\ \varepsilon_y \\ \gamma_{xy} \end{Bmatrix} = \begin{bmatrix} 1 & 0 & 0 \\ 0 & 1 & 0 \\ 0 & 0 & 2 \end{bmatrix} \begin{Bmatrix} \varepsilon_x \\ \varepsilon_y \\ \dfrac{\gamma_{xy}}{2} \end{Bmatrix} = [R] \begin{Bmatrix} \varepsilon_x \\ \varepsilon_y \\ \dfrac{\gamma_{xy}}{2} \end{Bmatrix}, \text{ and } \begin{Bmatrix} \varepsilon_1 \\ \varepsilon_2 \\ \gamma_{12} \end{Bmatrix} = [R] \begin{Bmatrix} \varepsilon_1 \\ \varepsilon_2 \\ \dfrac{\gamma_{12}}{2} \end{Bmatrix} \tag{2.14}$$

If we apply these equations to Equations 2.6 and 2.12, we obtain the following relation:

$$\begin{Bmatrix} \sigma_x \\ \sigma_y \\ \tau_{xy} \end{Bmatrix} = [T][Q][R][T]^{-1}[R]^{-1} \begin{Bmatrix} \varepsilon_x \\ \varepsilon_y \\ \gamma_{xy} \end{Bmatrix} \tag{2.15}$$

Then, we can further simplify this expression with the following abbreviation: $[\overline{Q}] = [T][Q][T]^{-T}$. Hence, we can now define the stress-strain relations in terms of the global x-y coordinates.

$$\begin{Bmatrix} \sigma_x \\ \sigma_y \\ \tau_{xy} \end{Bmatrix} = [\overline{Q}] \begin{Bmatrix} \varepsilon_x \\ \varepsilon_y \\ \gamma_{xy} \end{Bmatrix} \tag{2.16}$$

This equation defines the relation for one lamina, and since in a composite laminated plate there are two or more laminae, we need to know the stress-strain relation for each ply in the global coordinates. Thus, this equation can be written as:

$$\{\sigma\}^k = [\overline{Q}]^k \{\varepsilon\}^k \tag{2.17}$$

where k represents the ply number, and $[\overline{Q}]^k$ represents the reduced stiffness matrix of that particular ply. So $[\overline{Q}]^k$ can be written as follows:

$$[\overline{Q}]^k = \begin{bmatrix} \overline{Q}_{11} & \overline{Q}_{12} & \overline{Q}_{16} \\ \overline{Q}_{12} & \overline{Q}_{22} & \overline{Q}_{26} \\ \overline{Q}_{16} & \overline{Q}_{26} & \overline{Q}_{66} \end{bmatrix}^k \tag{2.18}$$

where the matrix components are:

$$\begin{aligned}
\overline{Q}_{11}^k &= Q_{11}^k \cos^4\theta + 2(Q_{12}^k + 2Q_{66}^k)\sin^2\theta\cos^2\theta + Q_{22}^k \sin^4\theta \\
\overline{Q}_{12}^k &= (Q_{11}^k + Q_{22}^k - 4Q_{66}^k)\sin^2\theta\cos^2\theta + Q_{12}^k(\sin^4\theta + \cos^4\theta) \\
\overline{Q}_{22}^k &= Q_{22}^k \sin^4\theta + 2(Q_{12}^k + 2Q_{66}^k)\sin^2\theta\cos^2\theta + Q_{22}^k \cos^4\theta \\
\overline{Q}_{16}^k &= (Q_{11}^k - Q_{12}^k - 2Q_{66}^k)\sin\theta\cos^3\theta + (Q_{12}^k - Q_{22}^k + 2Q_{66}^k)\sin^3\theta\cos\theta \\
\overline{Q}_{26}^k &= (Q_{11}^k - Q_{12}^k - 2Q_{66}^k)\sin^3\theta\cos\theta + (Q_{12}^k - Q_{22}^k + 2Q_{66}^k)\sin\theta\cos^3\theta \\
\overline{Q}_{66}^k &= (Q_{11}^k + Q_{22}^k - 2Q_{12}^k - 2Q_{66}^k)\sin^2\theta\cos^2\theta + Q_{66}^k(\sin^4\theta + \cos^4\theta)
\end{aligned} \tag{2.19}$$

In order to study the stress and strain variations through the thickness of the laminate when it is subjected to in-plane loads (tension, compression, and shear) and out-of-plane loads (bending, twisting,) the resultant forces and moments of the laminate need to be obtained. For that, we turn to Laminated Plate Theory (LPT) to provide a solution of the general equilibrium equations of plates.

2.2 Classical Laminate Plate Theory - Kirchhoff Plate theory

CLPT, Classical Laminate Plate Theory, is a plane-stress analysis for describing in-plane stresses and strains in laminates. It is assumed that out-of-plane normal stress, $\sigma_{z,}$ is equal to zero, and that all the out-of-plane shear stresses and strains ($\tau_{xz} = \tau_{yz} = \gamma_{xz} = \gamma_{yz}$) are equal to zero as well. Furthermore, in laminated plates, it is also assumed that all the strains are continuous from ply to ply.

Using Kirchhoff hypothesis, we take the laminate as a single layer with unique properties instead of ply-by-ply basis because it is presumed the bonds between the layers are very strong and non-shear deformable, avoiding any delamination. Also this hypothesis takes on the Euler assumption for the deflection of beams, in which the normal line to the middle surface of the layer remains straight and perpendicular at all times under deformation (see Figure 2. 4.)

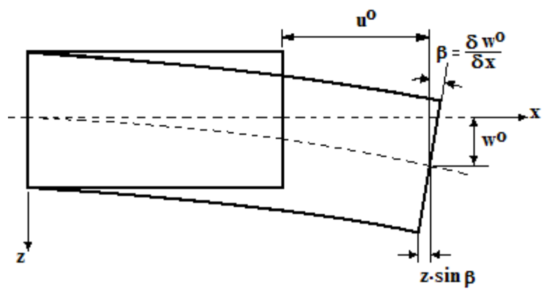

Figure 2. 4 -View of the x-z plane of the deformation of a plate

The reason for this is because we have ignored shearing strains in the planes perpendicular to the x-y plane (i.e. such is the situation found on thin plates or shells.) Because this edge is to remain straight under deformation, we find that the displacement in the x-direction for any point through the laminate thickness is equal to:

$$u_{(x,y,z)} \approx u^0_{(x,y)} - z\,\beta = u^0_{(x,y)} - z\,\frac{\partial w^0}{\partial x} \tag{2.20}$$

Similarly, the displacement in the y-direction is:

$$v_{(x,y,z)} \approx v^0_{(x,y)} - z\,\beta = v^0_{(x,y)} - z\,\frac{\partial w^0}{\partial y} \qquad (2.21)$$

Hence, now we can obtain the strains by differentiating these approximate displacements of the plate theory, giving us the strain variation through the thickness of the plate (which we assume to vary linearly across the section).

$$\begin{Bmatrix} \varepsilon_x \\ \varepsilon_y \\ \gamma_{xy} \end{Bmatrix} = \begin{bmatrix} \dfrac{\partial u}{\partial x} \\ \dfrac{\partial v}{\partial y} \\ \dfrac{\partial u}{\partial x} + \dfrac{\partial y}{\partial y} \end{bmatrix} \approx \begin{Bmatrix} \varepsilon^o_x + zk_x \\ \varepsilon^o_y + zk_y \\ \gamma^o_{xy} + zk_{xy} \end{Bmatrix} \qquad (2.22)$$

where, $\varepsilon^o{}_1$, $\varepsilon^o{}_1$, and $\gamma^o{}_{12}$ are the average plate strains at the middle plate, and κ_x and κ_y are the plate curvatures for the x and y directions, $\partial^2 w^o / \partial x^2$ and $\partial^2 w^o / \partial y^2$, respectively. The component κ_{xy} represents the twisting curvature, $2\,\partial^2 w^o / \partial x \partial y$, which defines how the slope of deformation in the x-direction changes with y. Hence, if we substitute this strain equation into the stress-strain relation of equation 2.17, the stresses per ply can be expressed in terms of the middle surface strains and curvature.

$$\begin{Bmatrix} \sigma_x \\ \sigma_y \\ \tau_{xy} \end{Bmatrix}^k = \left[\overline{Q}\right]^k \begin{Bmatrix} \varepsilon_x \\ \varepsilon_y \\ \gamma_{xy} \end{Bmatrix}^k = \left[\overline{Q}\right]^k \left[\begin{Bmatrix} \varepsilon^o_x \\ \varepsilon^o_y \\ \gamma^o_{xy} \end{Bmatrix} + z \begin{Bmatrix} k_x \\ k_y \\ k_{xy} \end{Bmatrix} \right] \qquad (2.23)$$

The determination of the reaction forces and moments acting on the laminate are obtained by integrating the stresses of each layer through the laminate thickness, t:

$$\begin{Bmatrix} N_x \\ N_y \\ N_{xy} \end{Bmatrix}^k = \int_{-t/2}^{t/2} \begin{Bmatrix} \sigma_x \\ \sigma_y \\ \tau_{xy} \end{Bmatrix}^k dz \quad \rightarrow \quad \begin{Bmatrix} N_x \\ N_y \\ N_{xy} \end{Bmatrix} = \sum_{k=1}^{N} \int_{z^k}^{z^{k+1}} \sigma^k \, d_z \tag{2.24}$$

$$\begin{Bmatrix} M_x \\ M_y \\ M_{xy} \end{Bmatrix}^k = \int_{-t/2}^{t/2} \begin{Bmatrix} \sigma_x \\ \sigma_y \\ \tau_{xy} \end{Bmatrix}^k z \, dz \quad \rightarrow \quad \begin{Bmatrix} M_x \\ M_y \\ M_{xy} \end{Bmatrix} = \sum_{k=1}^{N} \int_{z^k}^{z^{k+1}} \sigma^k \, z \, d_z \tag{2.25}$$

By substituting the stress-strain equation into these set of equations we obtain the following relation:

$$\begin{Bmatrix} N_x \\ N_y \\ N_{xy} \end{Bmatrix} = \begin{bmatrix} A_{11} & A_{12} & A_{16} \\ A_{12} & A_{22} & A_{26} \\ A_{16} & A_{26} & A_{66} \end{bmatrix} \begin{Bmatrix} \varepsilon_x^o \\ \varepsilon_y^o \\ \gamma_{xy}^o \end{Bmatrix} + \begin{bmatrix} B_{11} & B_{12} & B_{16} \\ B_{12} & B_{22} & B_{26} \\ B_{16} & B_{26} & B_{66} \end{bmatrix} \begin{Bmatrix} k_x \\ k_y \\ k_{xy} \end{Bmatrix} \tag{2.26}$$

$$\begin{Bmatrix} M_x \\ M_y \\ M_{xy} \end{Bmatrix} = \begin{bmatrix} B_{11} & B_{12} & B_{16} \\ B_{12} & B_{22} & B_{26} \\ B_{16} & B_{26} & B_{66} \end{bmatrix} \begin{Bmatrix} \varepsilon_x^o \\ \varepsilon_y^o \\ \gamma_{xy}^o \end{Bmatrix} + \begin{bmatrix} D_{11} & D_{12} & D_{16} \\ D_{12} & D_{22} & D_{26} \\ D_{16} & D_{26} & D_{66} \end{bmatrix} \begin{Bmatrix} k_x \\ k_y \\ k_{xy} \end{Bmatrix} \tag{2.27}$$

We can write these equations more conveniently in the following manner:

$$N = [A]\varepsilon^o + [B]k \tag{2.28}$$

$$M = [B]\varepsilon^o + [D]k \tag{2.29}$$

Where the *[A]*, *[B]*, and *[D]* matrices are defined by the following equations

$$A_{ij} = \sum_{k=1}^{N} \overline{Q}_{ij}^k \, (z^k - z^{k-1}) = \sum_{k=1}^{N} \overline{Q}_{ij}^k \, t^k \tag{2.30}$$

$$B_{ij} = \frac{1}{2} \sum_{k=1}^{N} \overline{Q}_{ij}^k \left[\left(z^k\right)^2 - \left(z^{k-1}\right)^2 \right] = \sum_{k=1}^{N} \overline{Q}_{ij}^k \, t^k \, z_{mid}^k \tag{2.31}$$

$$D_{ij} = \frac{1}{3}\sum_{k=1}^{N}\overline{Q}_{ij}^{k}\left[\left(z^{k}\right)^{3} - \left(z^{k-1}\right)^{3}\right] = \sum_{k=1}^{N}\overline{Q}_{ij}^{k}\, t^{k}\left[z_{mid}^{k} + \frac{\left(t^{k}\right)^{2}}{12}\right] \tag{2.32}$$

The equilibrium differential equations, derived from classical plate theory in terms of the reaction forces and resultant moments, are the following:

$$\frac{\partial N_x}{\partial x} + \frac{\partial N_{xy}}{\partial y} = 0 \tag{2.33}$$

$$\frac{\partial N_{xy}}{\partial y} + \frac{\partial N_y}{\partial y} = 0 \tag{2.34}$$

$$\frac{\partial^2 M_x}{\partial x^2} + 2\frac{\partial^2 M_{xy}}{\partial x \partial y} + \frac{\partial^2 M_y}{\partial y^2} = -p_{(x,y)} \tag{2.35}$$

where p is a transverse load. For a symmetric laminate with no in-plane loading, and assuming no bending-twisting coupling ($D_{16} = D_{26} = 0$,) the equilibrium equations can be simplified to:

$$D_{11}\frac{\partial^4 w^o}{\partial x^4} + 2(D_{12} + 2D_{66})\frac{\partial^4 w^o}{\partial x^2 \partial y^2} + D_{22}\frac{\partial^4 w^o}{\partial y^4} = p_{(x,y)} \tag{2.36}$$

The study of composite laminates under bending conditions increases in difficulty when dealing with holes or notches, but they can be analyzed using fracture mechanics.

Kirchhoff Plate Theory is inaccurate for moderately thick plates due to the effects of transverse shear and normal strain in the laminate, which are not taken into account. In a composite material, the transverse shear moduli G_{xz} and G_{yz} are usually much lower in relation to the modulus E_x, unlike for isotropic materials. Thus, the transverse shear strains can be large enough to affect the deflection of a plate.

2.3 Transverse Shear Effects - Reissner Plate Theory

Numerous researchers also studied plate theory taking into account the transverse shear effects. This is commonly known as Reissner's Plate Theory, RPT. In this theory, the asymptotic stress field calculated is derived in a similar manner as the Classical Plate Theory. Considering a plate in the x, y, and z coordinate system (see Figure 2. 4) and a loading case where there is no in-plane plate loading, equilibrium in the x and y direction can be represented as follows:

$$\frac{\partial \sigma_x}{\partial x} + \frac{\partial \tau_{xz}}{\partial z} = 0 \tag{2.37}$$

$$\frac{\partial \sigma_y}{\partial y} + \frac{\partial \tau_{yz}}{\partial z} = 0 \tag{2.38}$$

where τ_{xz} and τ_{yz}, the transverse shear stresses, are no longer assumed to be zero. We can then proceed to calculate these stresses from the bending behavior which we calculated in section 2.2, where we assumed a linear elastic response. If we recall equation 2.22, we can write the strain as follows:

$$\{\varepsilon\} = \{\varepsilon^o + z\kappa\} \tag{2.39}$$

where ε^o is the strain at the reference surface. Since we assumed a linear-elastic response, the in-plane components of the stresses at any point throughout the thickness of the plate are obtained by using equation 2.18. If we substitute equation 2.39 into that equation, we obtain the following relation:

$$\{\sigma\}^k = [\overline{Q}]^k \{\varepsilon^o\}^k + z[\overline{Q}]^k \kappa \tag{2.40}$$

where $[\overline{Q}]^k$ is the reduced elastic stiffness matrix for the k-ply, as it was described in equation 2.18, and it is defined from the elasticity and orientations of the material at the ply level, k.

Using equations 2.28 and 2.29, where we obtained a relation between the strains and curvatures of the plate with the reaction forces and moments, we can simplify those systems of equations into the following relation:

$$\begin{Bmatrix} N \\ M \end{Bmatrix} = \begin{bmatrix} A & B \\ B & D \end{bmatrix} \begin{Bmatrix} \varepsilon^o \\ \kappa \end{Bmatrix} \tag{2.41}$$

By inverting this equation, we can obtain the strains and curvatures in terms of the reaction forces and moments:

$$\begin{Bmatrix} \varepsilon^o \\ \kappa \end{Bmatrix} = [H] \begin{Bmatrix} N \\ M \end{Bmatrix} \tag{2.42}$$

where *[H]* is called the flexibility matrix. We can further reduce this relation since we assumed only out-of-plane bending as the form of loading. Thus, N = 0, and the strains and curvature can be written in terms of the moment only, [H]{M}.

Now, if we substitute this relation into equation 2.40, we can express the stress field in terms of the moment as:

$$\{\sigma\}^k = [\overline{Q}]^k [H] M + z[\overline{Q}]^k [H] M = [\overline{C}] M + z[\overline{C}] M = M([\overline{C}] + [\overline{C}] z) \tag{2.43}$$

where $[\overline{C}]$ is the matrix combination of $[\overline{Q}]^k [H]$. By substituting this stress field into the equilibrium equations 2.37 and 2.38, we can express the variation of the in-plane stresses throughout the thickness of the plate as follows:

$$\frac{\partial \sigma_x}{\partial x}^k = \frac{\partial M}{\partial x}^k ([\overline{C}] + [\overline{C}]z)^k \tag{2.44}$$

$$\frac{\partial \sigma_y}{\partial y}^k = \frac{\partial M}{\partial y}^k ([\overline{C}] + [\overline{C}]z)^k \tag{2.45}$$

Also, we know that the moment equilibrium about the y-axis is:

$$V_x + \frac{\partial M_x}{\partial x} = 0 \tag{2.46}$$

$$V_y + \frac{\partial M_y}{\partial y} = 0 \tag{2.47}$$

where V_x and V_y are the transverse shear forces. From this, we get a description of the variation of the transverse shear stresses throughout the thickness of the plate as follows:

$$\frac{\partial \tau_{xz}}{\partial z}^k = ([\overline{C}] + [\overline{C}]z)^k V_x^k \tag{2.48}$$

$$\frac{\partial \tau_{yz}}{\partial z}^k = ([\overline{C}] + [\overline{C}]z)^k V_y^k \tag{2.49}$$

By integrating these equations, we obtain the transverse shear stresses in the composite plate at the layer k.

$$\tau_{xz}{}^k = \int_{z^k}^{z^{k+1}} ([\overline{C}] + [\overline{C}]z)^k V_x^k dz \tag{2.50}$$

$$\tau_{yz}{}^k = \int_{z^k}^{z^{k+1}} ([\overline{C}] + [\overline{C}]z)^k V_y^k dz \tag{2.51}$$

2.4 Progressive Damage Model - Hashin Theory

Damage initiation in a composite laminated structure is far more complex than the damage propagation that occurs in a homogeneous material. In a composite laminate, damage progression occurs on a ply-by-ply basis. That is, when a composite laminate is under a loading condition that is greater than its allowable strength, a single ply or part of a ply in the lamina fails. Then, since this lamina cannot carry the load any further, the damage is propagated to the adjacent ply. The load is redistributed to the other laminae, leading to a reduction in the overall laminate stiffness. However, this damage progression does not necessarily mean that the structure has failed. There could be sufficient amount of residual load bearing capabilities in the composite structure before final failure occurs. This recognition gives rise to the perception of multiple failure modes that a composite laminate may experience. Furthermore, unlike a homogenous material, where failure modes occur independently, a composite structure can carry out multiple failure modes simultaneously. Failure modes in a laminated composite structure are strongly dependent on laminate geometry, ply orientation, and loading conditions.

Hence, the progressive failure model of a composite laminate is originated by a complicated damage progress. A number of studies [20], [48], [51] showed that damage evolution could be obtained using conventional damage mechanics. They obtained a damage progression model by deriving the modulus reduction as a function of the crack density and the applied stress in the laminate. This theory is similar to the stiffness reduction method, where the material properties of the loaded ply are reduced to zero as its maximum allowable strength is being reached. This theory assumes that the initiation and propagation of damage take place gradually, per ply, as the loading occurs. Thus, it is implicit that the equivalent properties of the damaged ply would degrade gradually.

So, in order to fully simulate damage propagation in a composite laminated structure, the failure analysis technique used must be able to predict the failure mode at each ply. Also, this method must successfully be able to calculate the corresponding reduction in material properties by taking into account the overall reduction in strength. Chang [33], [40] proposed a progressive failure model that described the accumulation of damage in a composite laminate by studying the internal stresses within the structure. He considered that a laminate would undergo six different failure modes, and they were fiber tension, fiber compression, fiber-matrix shearing, matrix tension, matrix compression, and delamination. Another progressive damage model was developed by Tsai-Wu in [41], where all the failure modes were combined into a single mode of failure. This is known as the Polynomial Failure criterion.

Also, Hashin [13] proposed a progressive failure mode technique that represented the notion of the reduction of strength due to the progression of damage. In it, damage evolution was based on the fracture energy that is dissipated during damage progression, and the increase of damage defines the failure modes.

Hashin's theorem, which is widely used in industry, was similar to Chang's but reduced the damage initiation mechanism to four modes: Fiber tension and compression, and matrix tension and compression.

When damage occurs (fiber buckling, matrix failure, etc), the effective load carrying area of the material is considered to be reduced, and the concept of an effective stress, $\hat{\sigma}$, is introduced to account for the area reduction.

$$\hat{\sigma} = \frac{\sigma}{1-d} \tag{2.52}$$

where σ is the nominal stress, and the quantity d is a damage variable that ranges from 0 (no damage) to 1 (development of a macrocrack.) From this, an effective stress tensor is introduced as:

$$\{\hat{\sigma}\} = [M]\{\sigma\} \tag{2.53}$$

where $\{\sigma\}$ is the usual two-dimensional stress in column-matrix form in principal material directions, and $[M]$ is a damage operator that describes the reduction of the elastic moduli by a set of deformation variables.

$$[M] = \begin{bmatrix} \frac{1}{1-d_f} & 0 & 0 \\ 0 & \frac{1}{1-d_m} & 0 \\ 0 & 0 & \frac{1}{1-d_s} \end{bmatrix} \tag{2.54}$$

where d_f, d_m, and d_s are damage variables characterizing fiber, matrix, and shear damage. These damage variables can have different values, depending on whether the damage is obtained by compression or tension. The constitutive relation for the material is affected by damage and results in a strain softening response. We obtain this by combining the effective stress tensor with equation 2.12, and it is as follows:

$$\{\hat{\sigma}\} = [M]\begin{bmatrix} \dfrac{E_1}{1-\nu_{12}\nu_{21}} & \dfrac{\nu_{21}E_1}{1-\nu_{12}\nu_{21}} & 0 \\ \dfrac{\nu_{21}E_1}{1-\nu_{12}\nu_{21}} & \dfrac{E_2}{1-\nu_{12}\nu_{21}} & 0 \\ 0 & 0 & G_{12} \end{bmatrix}\{\varepsilon\} = [C_d]\{\varepsilon\} \tag{2.55}$$

where *{ε}* is the usual two-dimensional strain in column matrix form and results in a strain softening response given by:

$$[C_d] = \frac{1}{D}\begin{bmatrix} (1-d_f)E_1 & (1-d_f)(1-d_m)\nu_{21}E_1 & 0 \\ (1-d_f)(1-d_m)\nu_{12}E_2 & (1-d_f)E_1 & 0 \\ 0 & 0 & (1-d_s)G_{12} \end{bmatrix} \tag{2.56}$$

where E_1, E_2, G_{12}, υ_{12}, and υ_{21} are the usual undamaged orthotropic elastic constant, and $D = 1-[(1-d_f)\,(1-d_m)\,\upsilon_{12}\,\upsilon_{21}]$.

The initiation of damage depends on which of the four modes of failure, described earlier, is activated. The criterion for damage initiation is governed by the following relations:

Fiber tension:

$$(\hat{\sigma}_{11} \geq 0):\;\; F_{ft} = \left(\frac{\hat{\sigma}_{11}}{X^T}\right)^2 + \alpha\left(\frac{\hat{\tau}_{11}}{S^L}\right)^2 = 1 \tag{2.57}$$

Fiber compression:

$$(\hat{\sigma}_{11} < 0):\; F_{fc} = \left(\frac{\hat{\sigma}_{11}}{X^C}\right)^2 = 1 \tag{2.58}$$

Matrix tension:

$$(\hat{\sigma}_{22} \geq 0): \ F_{mt} = \left(\frac{\hat{\sigma}_{22}}{Y^T}\right)^2 + \left(\frac{\hat{\tau}_{12}}{S^L}\right)^2 = 1 \tag{2.59}$$

Matrix compression:

$$(\hat{\sigma}_{22} < 0): \ F_{mc} = \left(\frac{\hat{\sigma}_{22}}{2S^T}\right)^2 + \left[\left(\frac{Y^C}{2S^T}\right)^2 - 1\right]\frac{\hat{\sigma}_{22}}{Y^C} + \left(\frac{\hat{\tau}_{12}}{S^L}\right)^2 = 1 \tag{2.60}$$

where X^T is the tensile strength in the fiber direction, X^C is the compressive strength in the fiber direction, Y^T is the tensile strength in the direction perpendicular to the fibers, Y^C is the compression strength in the direction perpendicular to the fibers, S^L and S^T are the longitudinal and transverse shear strength, and α is a coefficient that determines the contribution of the shear stress to the fiber tensile initiation criterion.

Chapter 3. Testing of Notched Laminates under Four-point Bending

3.1 Introduction

As it was mentioned earlier, there have been a small number of experimental tests done for notched laminates when they are subjected to a out-of-plane loading. Boeing Company has conducted several tests on composite laminates under four-point bending, but because these tests consisted of plates with a notch considerably smaller than the ones in this research, we could not use this data to validate our simulations. Therefore, we conducted four-point bending tests on laminated composites with large notches at our own laboratory facilities at Oregon State University.

The laminates chosen for these tests consisted of three different laminate types based on their widths:. They were 5-in., 10-in., and 20-in. wide laminates. All laminates had a length of 22-in. For each of these types, there were six different laminate lay-ups based on their layer orientation, which were representative of those commonly used in commercial aircraft. The material properties and lay-up sequence and orientation of the laminates were provided by the Boeing Company. Three of the six laminates were made of 20 plies, while the rest consisted of 40 plies, in which each ply or lamina had the same thickness value of 0.0074-in. Hence, the laminates can be categorized under two different laminate thicknesses: The 0.148-in. 20-ply laminates and the 0.296-in. 40-ply laminates. Two different notch sizes were analyzed: 1-in. long ovaloid centered notched with 1/8-in. end radii (see Figure 3. 1,) which were cut out of the 5-in. and 10-in. wide laminates, and a 4-in. long ovaloid centered notched with a 1/8-in. radius, which was cut out of the 20-in. laminates.

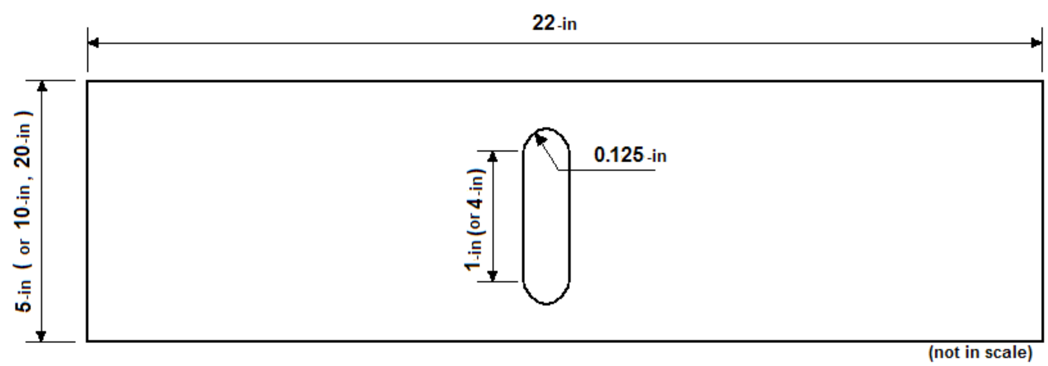

Figure 3. 1 - Laminate dimensions and notch sizes

The laminates were instrumented with strain gages on both sides of the laminate at different regions at the notch tips, in order to obtain qualitative measure of the deformation progression as the plates were bent. Strain gages were also mounted away from the notch tip to determine far-field strains in order to be able to adequately record the maximum moment obtained during failure. Visual inspection was also performed during the test and documented photographically to assess failure modes.

Boeing Company provided us with a total of 48 laminates divided among the six different laminated lay-ups labeled F, N, P, FP, AR, and AN. As described in Table 1, we had a total of eight laminates for each lay-up, distributed based on the widths of the specimens.

Table 1 - List of Laminates

Laminate	length (in.)	number of specimens 5-in. wide	10-in. wide	20-in. wide	Total #
F	22	3	2	3	8
P	22	3	2	3	8
N	22	3	2	3	8
FP	22	3	2	3	8
AR	22	3	2	3	8
AN	22	3	2	3	8
					48

Note: 1-in. notch (5-in. & 10-in. width)
4-in. notch (20-in. width)

Laminates F, P, and N have a total of 20 layers, with 10% 0-degree plies, 30% 0-degree plies, and 50% 0-degree plies, respectively. We had three replicates for the 5-in. and 20-in. wide specimens, and two replicates for the 10-in. wide specimen.

Laminates FP, AR, and AN have 40 layers, with 10% 0-degree plies, 30% 0-degree plies, and 50% 0-degree plies, respectively.

3.2 Procedure to Generate Four-point Bending

In a four-point bending test, the plate is rested freely on two supports and is loaded at two points, by means of two loading noses, with equal distance from the ends of the supports as shown in Figure 3. 2.

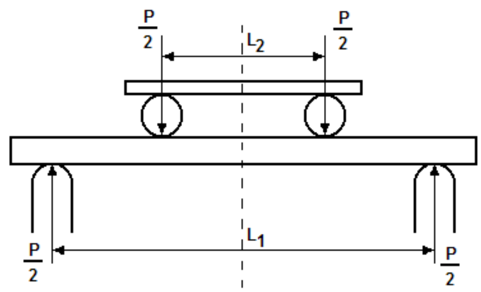

Figure 3. 2 - Test method for four-point bending

By applying a four-point bending to the plate, the maximum axial stress is uniformly distributed between the load noses. An important aspect in the fabrication of a four-point bending is that the loading noses and supports must have cylindrical surfaces in order to avoid indentation or restrict pure bending. For the design of these components, the supports and loading noses had an end radius of 0.5-in.

3.3 Laboratory Test Set-up

The testing machine that we used to generate four-point bending was the 5500R INSTRON tension loading machine. This INSTRON machine has a central moving vice, which allows the user to set up experiments for tension and compression, depending on where the loading cell is placed.

The specimens that were provided by the Boeing Company, as mentioned earlier, consisted of six different laminate types with three different widths and were properly labeled based on their laminate type and their geometric specifications. Figure 3. 3 shows clearly the differences on the specimens based on the width, of the laminates.

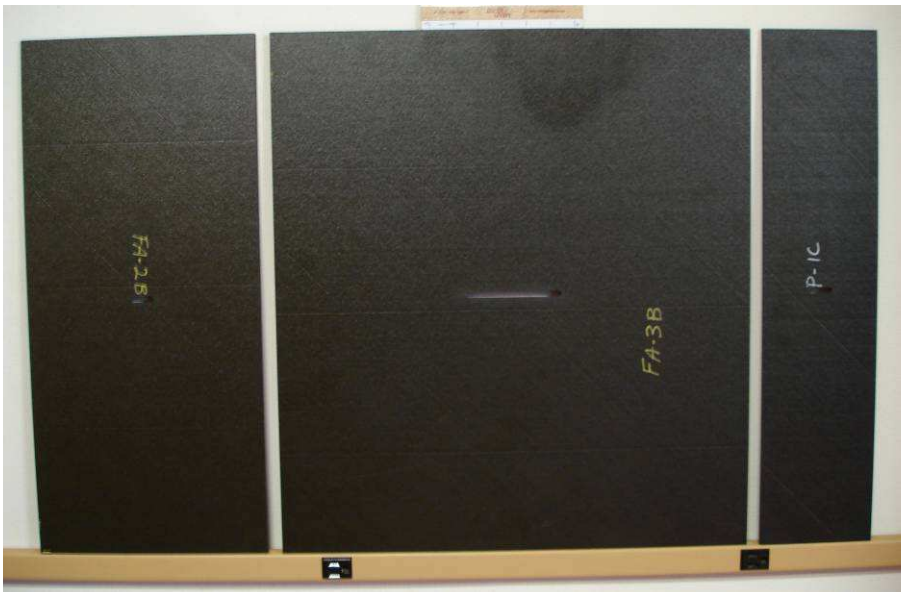

Figure 3. 3 - Test laminates with the 10-in., 20-in. and 5-in. widths

Each specimen was labeled with the laminate name, the notch size, the specimen width, and the replicate number. Thus, for instance, the third specimen of laminate F, with a localized notch of 4-in. and a width of 20-in. is labeled as “F_4_20_3”. Also, each specimen was cleaned and prepared for strain gage attachments, since this would be the method used to obtain the strain field which we will use to obtain our experimental data. Once the strain gages were attached to the specimen at pre-determined areas of the surface, they were connected to a digital acquisition (DAQ) system where the strains can be recorded as the loading is being applied to the specimen. The program used to obtain these readings from the DAQ system was National Instruments Labview.

Once the specimen was placed on the loading machine, we made sure that it was placed centered with respect to the loading cell and evenly spaced so we could perfectly produce pure bending on the specimens. INSTRON and Labview were synchronized to start recording at the same time, with a time-step of 0.1 seconds.

Once the testing was finalized, the specimen was inspected to observe if failure indeed took place. Data from the INSTRON machine, which recorded load, time, and y-displacement of the loading cell, was recorded and saved into a file. Also, data from Labview, which recorded strain and time synchronized with INSTRON, was also recorded and saved.

3.4 INSTRON Set-up

In order to properly conduct a four-point bending test in our tensile loading machine, we had to appropriately design and manufacture a set of fixtures. Design considerations were taken into account for the allowable forces and deformations that the machine would implement on the fixtures when we subject the specimens to bending. These fixtures were fabricated at the Oregon State University facilities of the mechanical engineering department. Three different fixtures were manufactured to accommodate the three widths of the laminate. Two fixture set-ups for the tension side of the loading machine were fabricated and one for the compression side. The fixtures were composed of two pieces: an upper fixture consisting of two bars separated at a predetermined distance, which was attached to the loading cell, and a lower fixture consisting also of two bars separated at a further distance, which held the specimen while bending occurred. Figure 3. 4 shows one of the lower fixtures for a tension side setup.

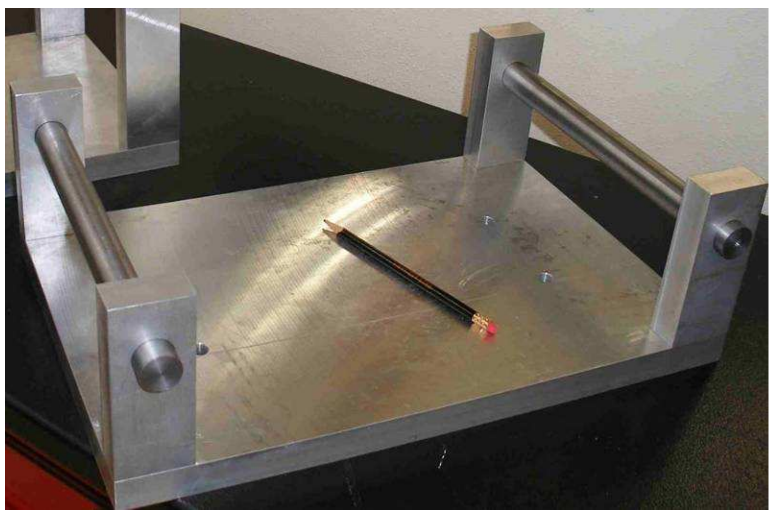

Figure 3. 4 - Lower fixture created for the testing of the 10-in. laminates

Once manufactured, these fixtures were tightly bolted to the machine. The bars on both upper and lower fixtures were free to slide and rotate through the fixture, to help specimen setup and to ensure that pure bending occurs.

The loading of the specimens was timed to create a step load every 0.1-sec.

The speed at which the loading would be implemented depended on the thickness of the specimen. For laminates consisting of 20 plies a loading speed of 2-in. per minute was employed; and, for laminates consisting of 40 plies, we used 4-in. per minute. The vertical extension and the load were recorded at that time step. Figure 3. 5 shows an example of the set-up for a four-point bending on the tension side of the INSTRON machine

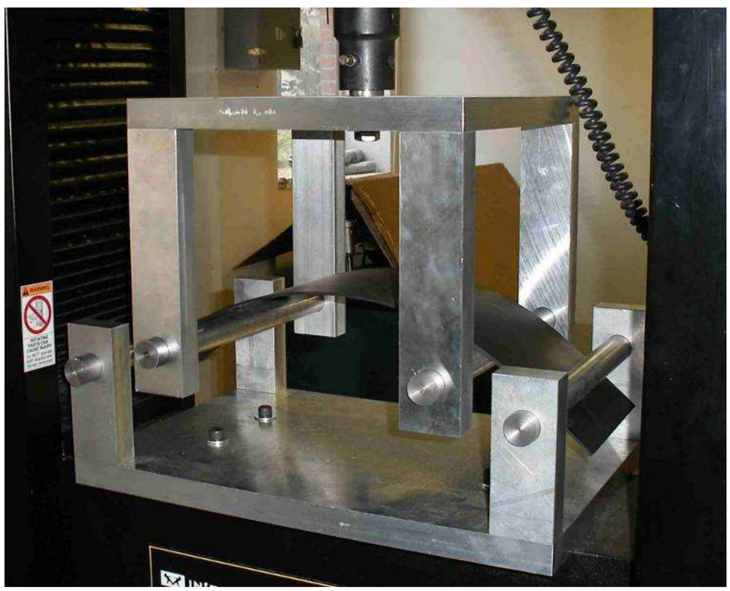

Figure 3. 5 - Four-point bending set-up for tension in INSTRON

Also, as mentioned earlier, we made use of the compression setup available in INSTRON to conduct tests. Figure 3. 6 shows the set-up for a four-point bending on the compression side of the INSTRON machine.

As shown in these pictures, the specimen was placed between the bars, and the load was applied by the two interior bars until the laminate reached a failure point. Once failure has occurred, which was observed when the specimen could not carry any more load due to total or partial breakage of the laminate, the loading procedure was stopped. The specimen was then unloaded to its original position and taken out for visual inspection.

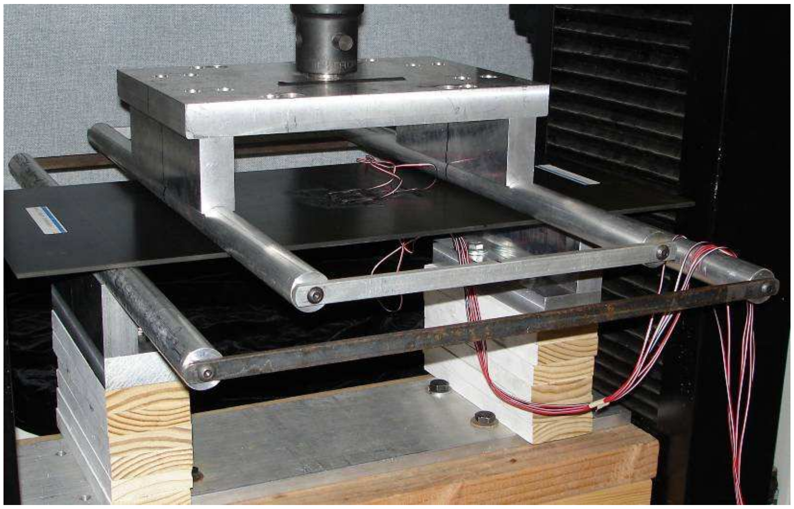

Figure 3. 6 - Four-point bending set up for compression test in INSTRON

3.5 LABVIEW Programming

Data acquisition from the testing was obtained using Labview, which is a software tool from National Instruments. The process was fairly simple: the wires from the gages were attached to a Data Acquisition (DAQ) board, whose function is to read their signals. The DAQ board at the same time was connected to a computer with the Labview software. The Labview program was created to read the signals from the strain gages and convert the voltage differential of each strain gage into strain values. The Labview program would filter as well the noise and interference signals and record the true strain signals and plot them.

The Labview program was set up to record and save the input signals at 0.1-sec. increments to match the loading step from the INSTRON machine. This way, we would be able to precisely recreate the strain field. Because of the numerous and different strain gage schematics and types that we used for the laminates, the program was written to be able to easily accommodate diverse input signals. Additionally, we made use of a linear transducer to determine the real centered deformation of the specimen.

3.6 Strain Gage Preparation and Set-up

Each specimen was cleaned and prepared for strain gage attachments on both sides of the laminate. Normally, we attached the gages on the same locations on the tension and compression sides; but, in certain cases, extra gages were placed only on one side to obtain redundancy or to acquire more information. The gage types varied depending upon the position where they were placed.

The following Figure 3. 7 indicates where we typically placed the gages on the laminates. In all cases, we set up a strain gage right next to the crack tip, gage C1 (at a distance away from the tip between 1/8-in. and 1/16-in.,) and on the far-field region, gages M1 or M2 (at a vertical distance of d = 2-in. for the 5-in. and 10-in. wide laminates and d = 4-in. for the wider 20-in. laminates.)

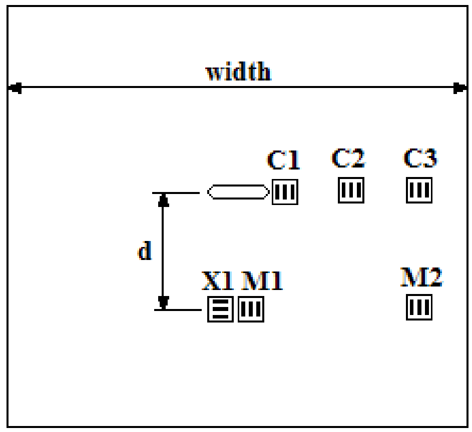

Figure 3. 7 - Mapping for the location of the strain gages

Also, in most cases, we made use of the middle and outer regions of the notch region, gages C2 and C3. In order to measure effects of transverse curvature, in some cases, we also applied a gage in the transverse direction, indicated in the figure as X1. Again, the gage installation would normally be the same for both tension and compression sides.

3.7 Testing Procedures and Photographic Documentation

Once a laminate is set up with gages, it was taken to the laboratory, and a simple pre-test examination was conducted. This pre-test consisted of loading the specimen about 0.5-in. and 0.1-in. for the 20-ply laminates and 40-ply laminates, respectively. The reason for this examination was to test if all the gages were working properly and if the system was ready for loading without producing any damage to the specimens. Once this step was done, we were ready to start loading. In most cases, the Labview program was modified to adjust for a new mapping of the strain gages, which would differ between laminates, and the different gage types used, which had distinctive gage factors. Thus, we made sure that this program was running correctly, too.

In all tests, video recordings were carried out and edited for subsequent viewing. Most of the videos were focused on the notch tip to monitor the damage initiation and its propagation as the crack spread to the sides of the laminates. Additionally, still photo recordings were performed once failure occurred on the laminates. The interest, in this case, was not on the initial centered notch, but rather on the sides of the laminates. Photos were taken to see the damage distributed throughout the thickness and to observe which plies failed and which did not fail.

Early in the experimental stage of the project, the Digital Image Correlation method (DIC) was taken into consideration to obtain the strain fields on the laminates. Strenuous and exhausting work was put into DIC to try to implement this new technology in this project. However, ultimately, due to the large out-of plane deformations that we were faced with when we loaded our laminates under bending, we were unable to put DIC into practice for our experiments.

The last step of the testing procedure was to get photographic documentation of all the laminates after failure. Numerous photographs were taken on the notch tips and the sides of the laminates.

Chapter 4. Experimental Results for the Notched Laminates

4.1 Introduction

Different fixture set ups were used in the tests in order to accommodate all 48 laminates. There are several reasons why different fixture setups were used. In some cases, we conducted the tests on the tension side of the INSTRON machine, typically the 5-in. laminates, because the loads applied during testing were within the fixture loading capabilities. For the 10-in. and 20-in. laminates, we had to make use of the compression side of the INSTRON machine because of the higher reaction loads that we projected would occur on the fixtures. Also, due to the unexpected large deformations found on some laminates, different bar spacing on the fixture were used. In most of the cases for the 20-in. wide thin laminates, deformation was so large that loading had to be stopped in order for the laminate not to slip from the bars (see Figure B. 6.) By reducing the bar spacing in the fixture, we forced the laminate to experience a larger bending, which in turn drove the laminate to fail before slippage. Failure was observed as the load carrying capabilities of the laminate decreased or dropped due to partial or total breakage of the laminate. The different setups for the bar spacing on the fixtures are as follows: [8-in./ 13-in.], [6-in./ 16-in.], [10-in./ 16-in.], [10-in./ 14.5-in.], and [10-in./ 8-in.]. The first number indicates the spacing between the bars at the top fixture, and the second number indicates the bar spacing at the lower fixture.

Without the use of these modifications, failure would not have occurred in several cases as it reached the maximum allowable deformation for a particular configuration of bar spacing. We then had to proceed to switch the lower fixture bar spacing to a more reduced bar distance to force the laminate plate to reach failure.

Table 2 gives a list of the Far-Field gages used to determine the maximum allowable strain for each laminate. Refer to Figure 3. 7 to observe the location of these gages.

Table 2 - List of the Far-Field gages used to obtain data for calculation

Specimen	F	P	N	FP	AR	AN
1_5_1	M1	M1	M1	M1	M1	M1
1_5_2	M1	M2	M2	M2	M2	M2
1_5_3	M1	M1	M1	M1	M1	M1
1_10_1	M1	M1	M1	M1	M1	M1
1_10_2	M1	M1	M1	M1	M1	M1
4_20_1	M2	M2	M2	M2	M2	M2
4_20_2	M2	M2	M2	M2	M2	M2
4_20_3	M2	M2	M2	M2	M2	M2

4.2 Testing Results for 20-ply Laminates

The results for the 20-ply laminates F, N, and P under four-point bending are listed below based on the width of the specimens. The 5-in. wide and 20-in. wide laminates have three replicates and the 10-in. wide laminates have two replicates. The results of theses tests are described in terms of their vertical load and far-field strain responses. The strain plots were obtained from the data of the far-field strain gages (M1 or M2,) located on the compression side. See Table 2 to obtain information on the mapping of these gages.

4.2.1 Results for the 5-in wide F, P, and N Laminates

The results of the four-point bending test of the F-laminate group, which is composed of replicates F_1_5_1 and F_1_5_2, are indicated in Figure 4. 1 and Figure 4. 2. Replicate F_1_5_3 had no practical data, so its results were not included in the plotting of these figures. The testing for F_1_5_3 was carried out until it reached failure, but the strain gages only recorded up to approximately 0.5% of deformation. Figure 4. 1 shows the load vs. displacement for the other two replicates. The maximum load for F_1_5_1 was 559.6-lb. At failure, we obtained a deformation of 1.83-in.

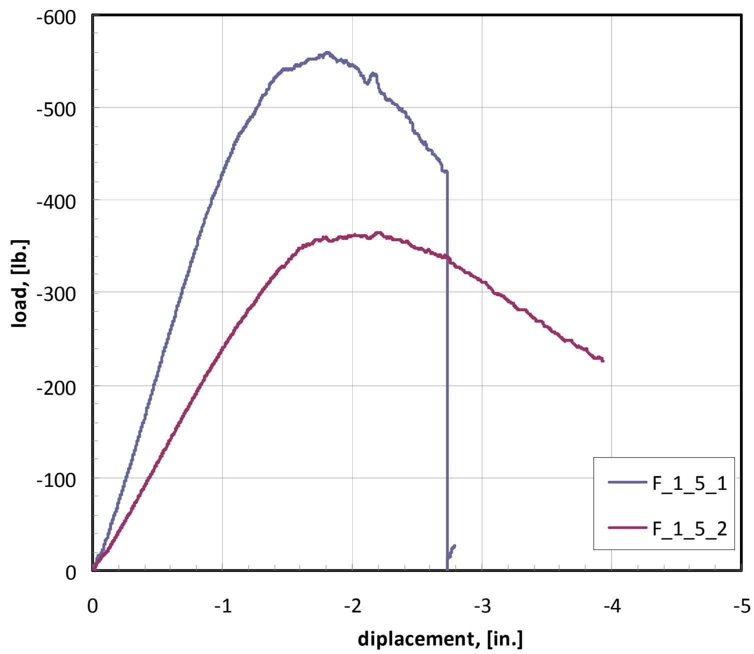

Figure 4. 1 - Laminate F, width 5-in., 1-in. notch, load vs. displacement

Laminate F_1_5_2 shows a different load-displacement curve. The reason for this is that this laminate had a different bar spacing set up [10-in. / 16-in.] than the first laminate [8-in. /13-in.] The maximum load was 362.2-lb., and the deformation at that time was 2-in.

In Figure 4. 2, we can see the strain versus displacement plot for these two laminates. The data showed that F_1_5_1 reached a maximum strain at gage M1 of 0.011 before failure, and F_1_5_2 reached a value of 0.01 at the same location.

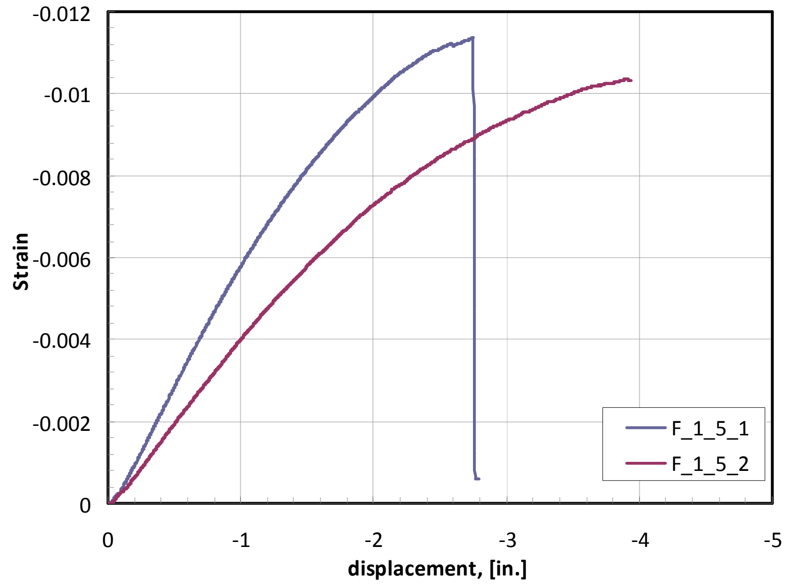

Figure 4. 2 - Laminate F, width 5-in., 1-in .notch, strain vs. displacement

The results of the four-point bending test of the P-laminate group, which is composed of replicates P_1_5_1, P_1_5_2, and P_1_5_3 are indicated in the following two figures. Figure 4. 3 shows the load vs. displacement. The maximum load for P_1_5_1 was 454.5-lb. At that load, we obtained a deformation of 2.21-in. Laminate P_1_5_2 followed a similar pattern, as can be seen in Figure 4. 3. Both laminates had a bar spacing of [10-in./ 16-in.] The maximum load for P_1_5_2 was 438.7-lb. The displacement at that point was 2.1-in. Laminate P_1_5_3, which had a different fixture with a bar spacing of [6-in./ 16-in.], had a different load-displacement curve. The maximum load was 270.6-lb. The deformation at that time was 3.13-in.

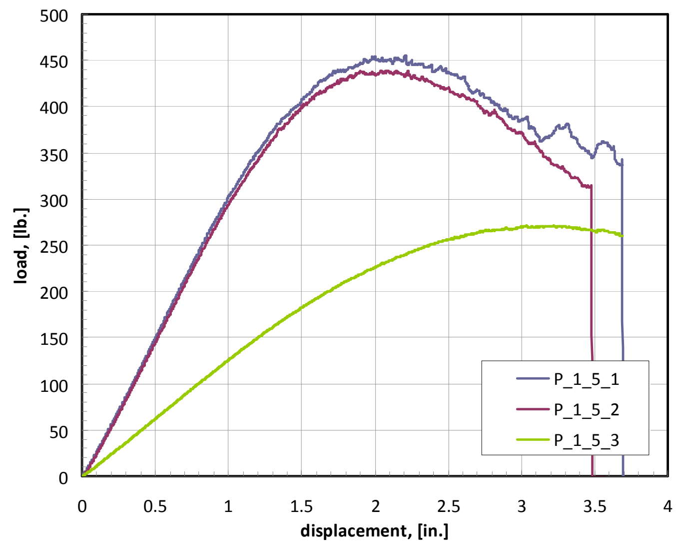

Figure 4. 3 - Laminate P, width 5-in., 1-in. notch, load vs. displacement

Figure 4. 4 shows the strain-displacement plot for these particular laminates. It was found that the maximum strains at the far fields before failure were 0.0091, 0.0098, and 0.0092 for P_1_5_1, P_1_5_2, and P_1_5_3, respectively.

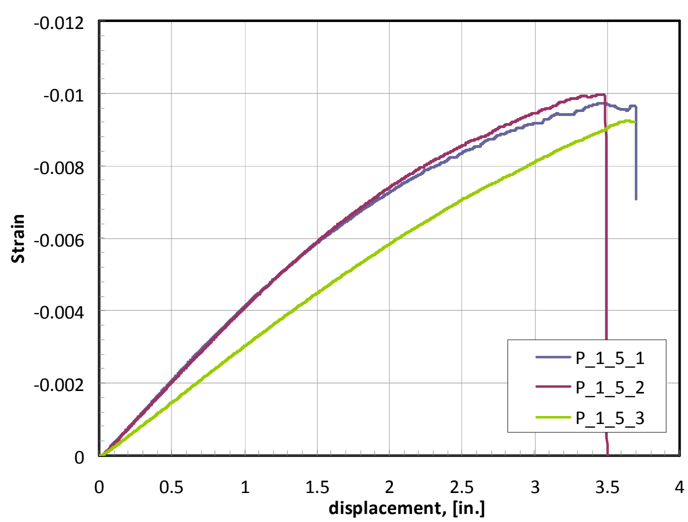

Figure 4. 4 - Laminate P, width 5-in., 1-in. notch, strain vs. displacement

The results of the four-point bending test of the N-laminate group, which is composed of replicates N_1_5_1, N_1_5_2, and N_1_5_3, are indicated in Figure 4. 5 and Figure 4. 6. Here, laminates N_1_5_1 and N_1_5_2 were tested using the same fixture set up [10-in./ 16-in.] Their maximum loads are very similar with 683.6-lb. and 678.8-lb., respectively. Laminate N_1_5_3, on the other hand, had a fixture with a bar spacing of [6-in./ _16-in.] Its maximum load was found at 404.6-lb.

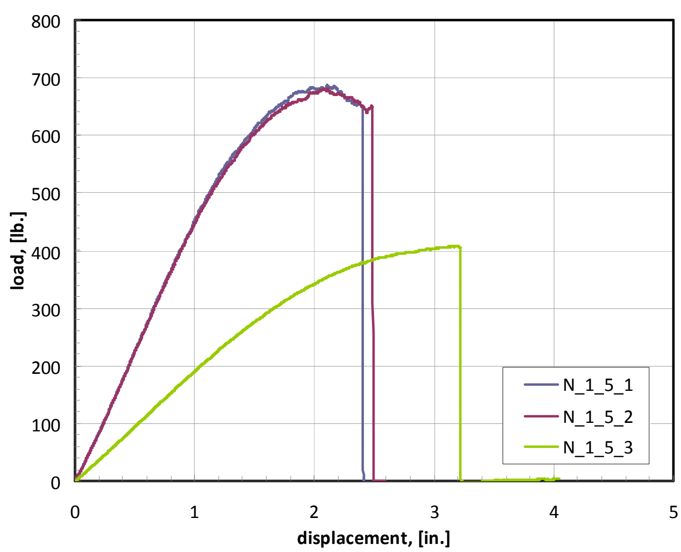

Figure 4. 5 -Laminate N, width 5-in., 1-in. notch, load vs. displacement

Figure 4. 6 shows the strain-displacement plot for this particular laminate group. It was found that the maximum strains before failure were 0.0075, 0.0082, and 0.0084 for N_1_5_1, N_1_5_2, and N_1_5_3, respectively. The position for these gages were at M1, M2, and M1, for the three replicates, respectively.

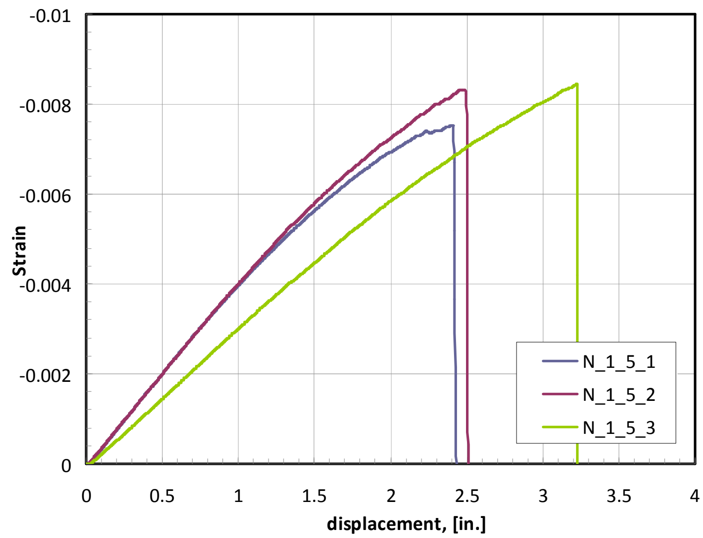

Figure 4. 6 - Laminate N, width 5-in., 1-in .notch, strain vs. displacement

4.2.2 Results for the 10-in wide F, P, and N Laminates

The results of the four-point bending test of the P-laminate group, which is composed of replicates F_1_10_1 and F_1_10_2 are indicated in Figure 4. 7 and Figure 4. 8. The maximum load for F_1_10_1 was 1235.61-lb. Laminate F_1_10_2 follows a similar pattern, as it can be seen in Figure 4. 7, with a maximum load of 1150.1-lb. Both laminates had bar spacing of [8-in./ 13-in.] The slight difference in this result is probably due to the difference in the alignment of the specimens in the fixture.

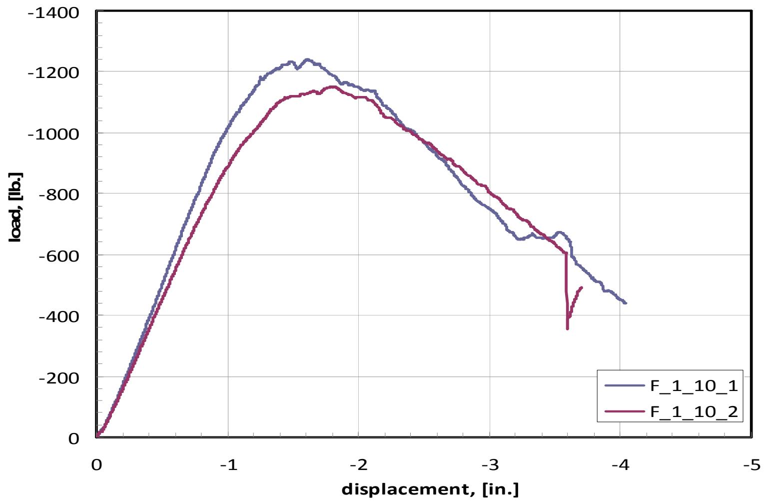

Figure 4. 7 - Laminate F, width 10-in., 1-in. notch, load vs. displacement

Figure 4. 8 shows the strain-displacement plot for this particular laminate group. It was found that the maximum strains before failure at gage location M1 were 0.011 and 0.012 for F_1_10_1 and F_1_10_2, respectively.

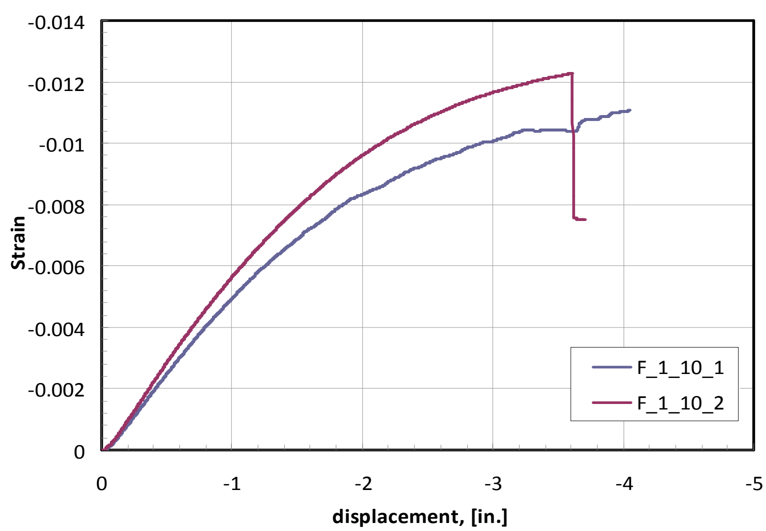

Figure 4. 8 - Laminate F, width 10-in., 1-in. notch, strain vs. displacement

The results of the four-point bending test of the P-laminate group, which is composed of replicates P_1_10_1 and P_1_10_2 are indicated in Figure 4. 9 and Figure 4. 10. The maximum load for P_1_10_1 was 843.1-lb. Laminate P_1_10_2 follows a similar pattern, as can be seen in Figure 4. 9, with a maximum load of 894.1-lb. Both laminates had bar spacing of [10-in./ 16-in.]

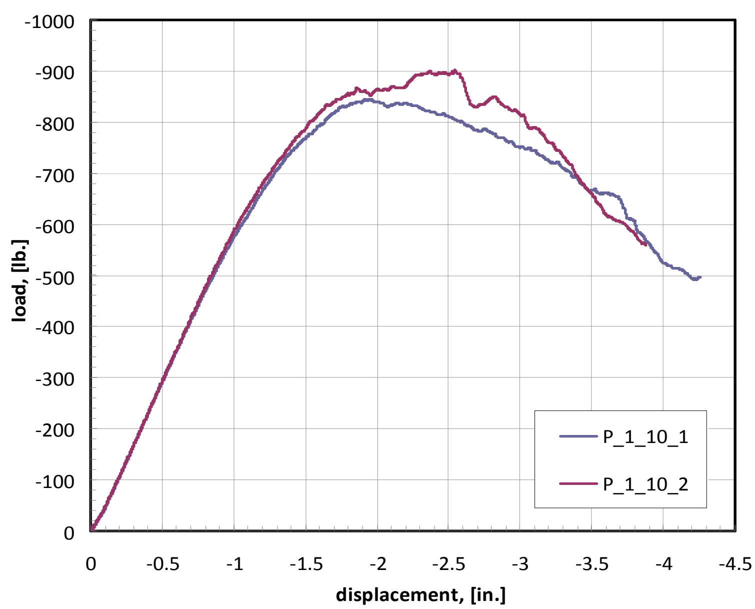

Figure 4. 9 - Laminate P, width 10-in., 1-in. notch, load vs. displacement

Figure 4. 10 shows the strain-displacement plot for this particular laminate group. It was found that the maximum strains before failure were 0.01 and 0.0095 for P_1_10_1 and P_1_10_2, respectively.

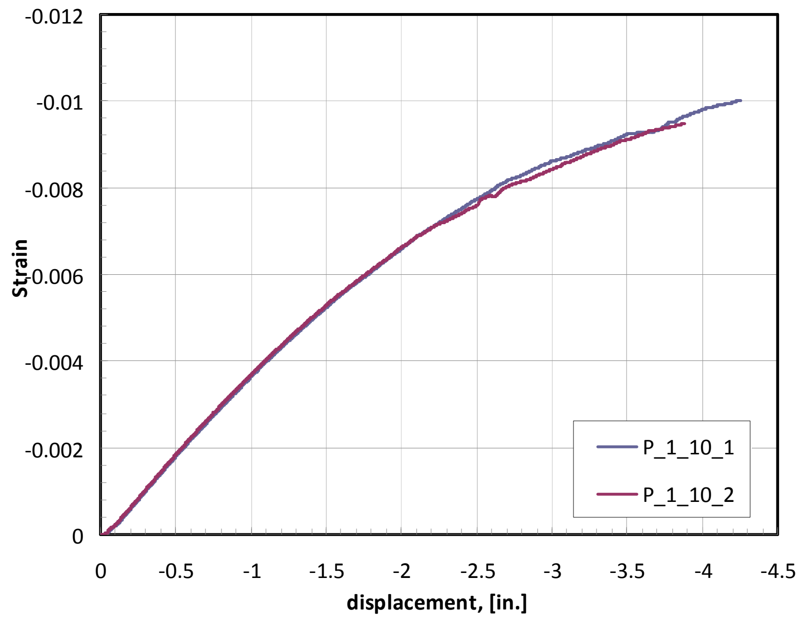

Figure 4. 10 - Laminate P, width 10-in., 1-in. notch, strain vs. displacement

The results of the four-point bending test of the N-laminate group, which is composed of replicates N_1_10_1 and N_1_10_2 are indicated in Figure 4. 11 and Figure 4. 12. The maximum load for N_1_10_1 was 1284.3-lb. Laminate N_1_10_2 follows a similar pattern, as can be seen in Figure 4. 11, with a maximum load of 1283.2-lb. Both laminates had bar spacing of [10-in./ 16-in.]

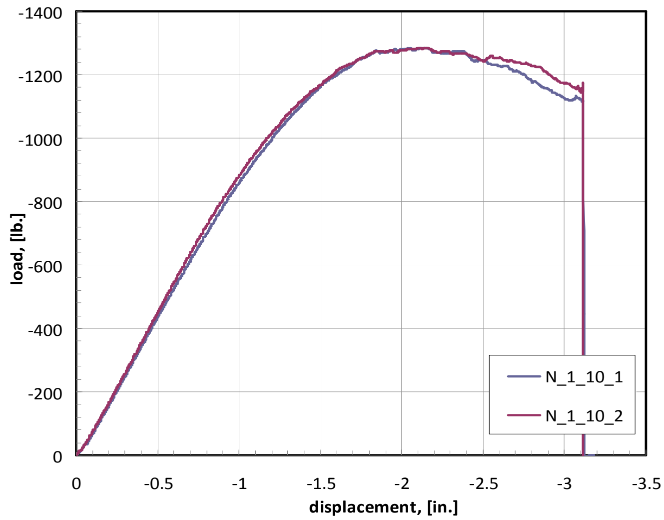

Figure 4. 11 - Laminate N, width 10-in., 1-in. notch, load vs. displacement

Figure 4. 12 shows the strain-displacement plot for this particular laminate group. It was found that the maximum strains before failure were 0.0081 and 0.0083 for N_1_10_1 and N_1_10_2, respectively.

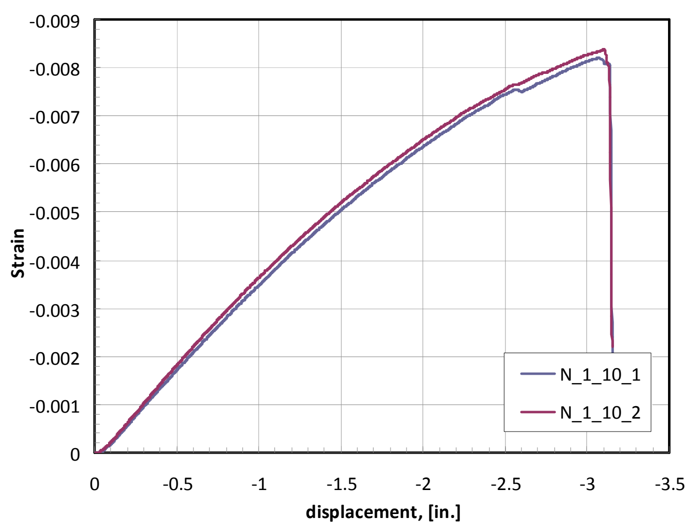

Figure 4. 12 - Laminate N, width 10-in., 1-in. notch, strain vs. displacement

4.2.3 Results for the 20-in wide F, P, and N Laminates

The results of the four-point bending test of the F-laminate group, which is composed of replicates F_4_20_1, F_4_20_2, and F_4_20_3 are indicated in Figure 4. 13 and Figure 4. 14. Laminates F_4_20_1 and F_4_20_3 used the same fixture settings [spacing of 8-in./ 13-in.] Laminate F_4_20_2 used a bar spacing of [10-in./ 14.5-in.] The maximum load for F_4_20_1 was 2260.31-lb. Laminate F_4_20_3 follows a similar pattern, as can be seen Figure 4. 13, with a maximum load 2418.9-lb. Laminate F_4_20_2 had a maximum load of 1495-lb.

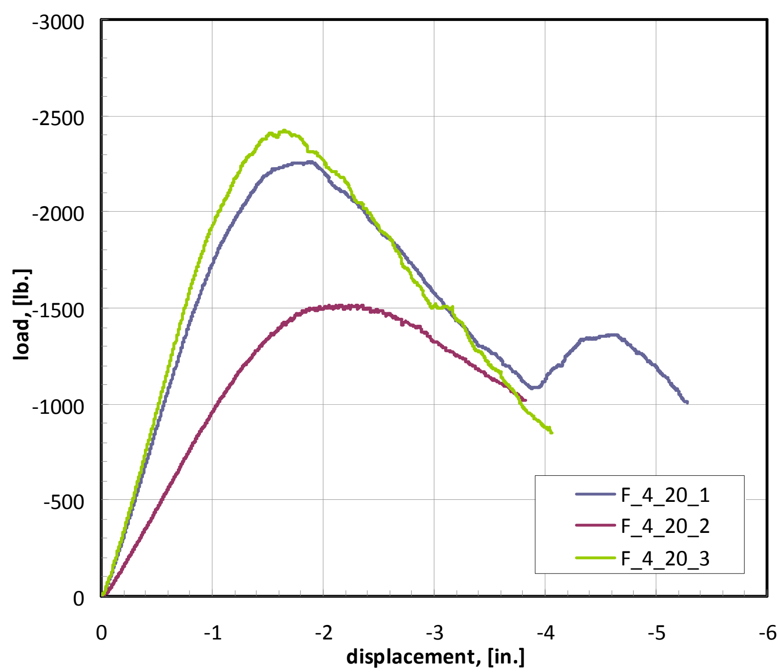

Figure 4. 13 - Laminate F, width 20-in., 4-in. notch, load vs. displacement

Figure 4. 14 shows the strain-displacement plot for this particular laminate group. It was found that the maximum strains before failure were 0.011, 0.0089, and 0.011 for F_4_20_1, F_4_20_2, and F_4_20_3, respectively.

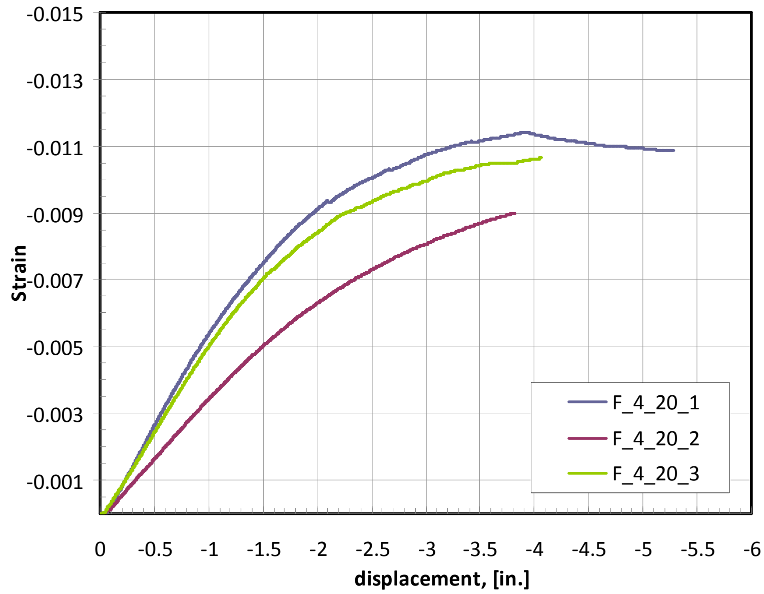

Figure 4. 14 - Laminate F, width 20-in., 4-in. notch, strain vs. displacement

The results of the four-point bending test of the P-laminate group, which is composed of replicates P_4_20_1, P_4_20_2, and P_4_20_3 are indicated in Figure 4. 15 and Figure 4. 16. Laminates P_4_20_1 and P_4_20_2 used the same fixture settings [spacing of 10-in./ 16-in.] Laminate P_4_20_3 used a bar spacing of [10-in./ 18-in.] The maximum load for P_4_20_1 was 1743.5-lb. Laminate P_4_20_2 follows a similar pattern, with a maximum load of 1625.7-lb.

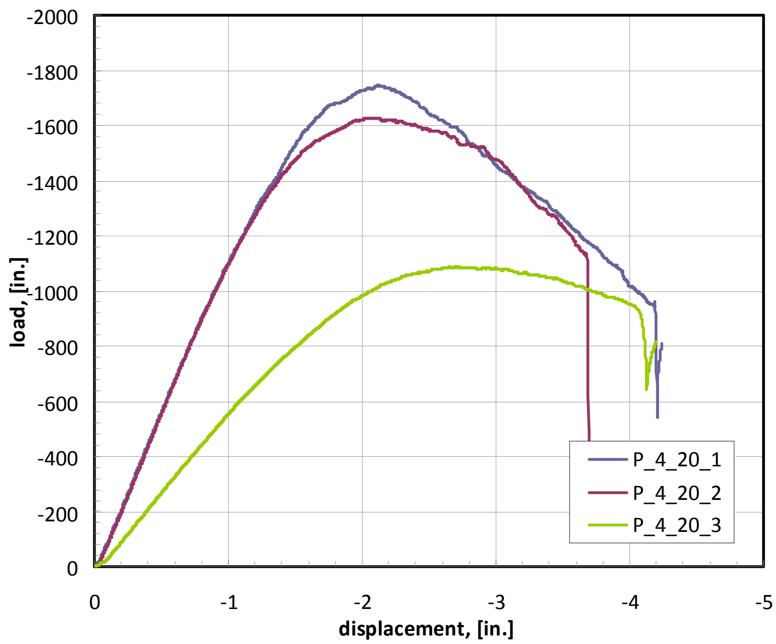

Figure 4. 15 - Laminate P, width 20-in., 4-in. notch, load vs. displacement

Laminate P_4_20_3 had a maximum load of 1087.7-lb. Figure 4. 16 shows the strain-displacement plot for this particular laminate group. It was found that the maximum strains before failure were 0.0089, 0.0089, and 0.0077 for P_4_20_1, P_4_20_2 and P_4_20_3, respectively. All the data for these specimens were obtained from the recordings at M2 gages.

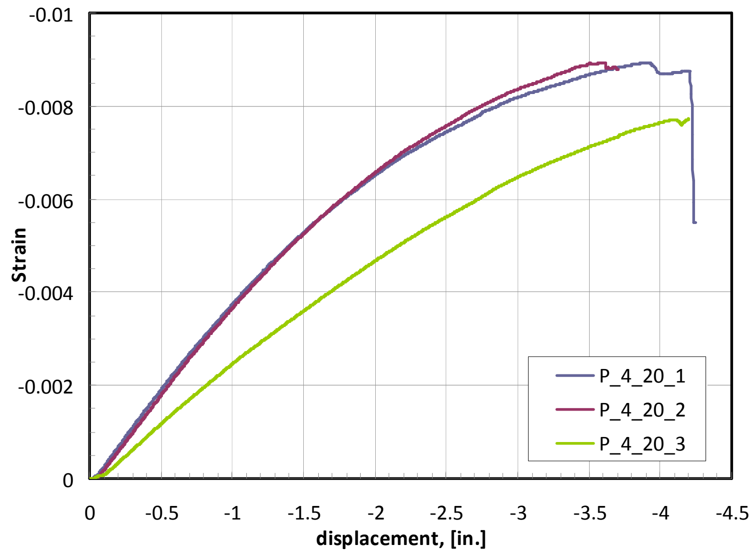

Figure 4. 16 - Laminate P, width 20-in., 4-in .notch, strain vs. displacement

The results of the four-point bending test of the N-laminate group, which is composed of replicates N_4_20_1, N_4_20_2, and N_4_20_3 are indicated in Figure 4. 17 and Figure 4. 18. Just as in the case of P-laminates, laminates N_4_20_1 and N_4_20_2 used the same fixture settings [spacing of 10-in./ 16-in.] For the laminate N_4_20_3, we initially used a bar spacing of [10-in./ 18-in.] but switched to the [10-in./ 16-in.] spacing for later tests. The maximum load for N_4_20_1 was 2609.3-lb. Laminate N_4_20_2 follows a similar pattern, as can be seen in Figure 4. 17, with a maximum load of 2463.1-lb. Laminate N_4_20_3 had a maximum of 2514-lb.

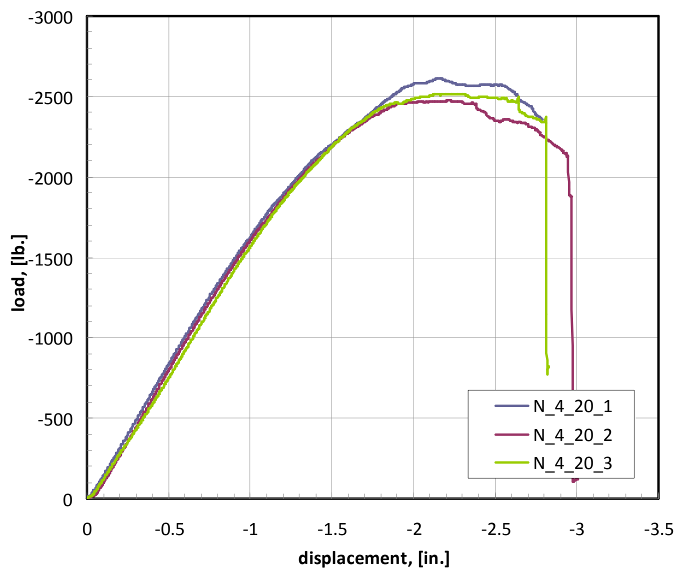

Figure 4. 17 - Laminate N, width 20-in., 4-in. notch, load vs. displacement

Figure 4. 18 shows the strain-displacement plot for this particular laminate group. It was found that the maximum strains before failure were 0.0076, 0.0071, and 0.0072 for N_4_20_1, N_4_20_2, and N_4_20_3, respectively.

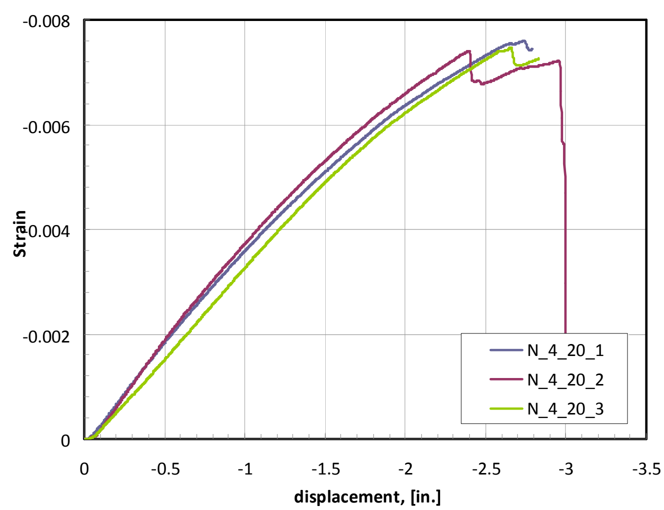

Figure 4. 18 - Laminate N, width 20-in., 4-in. notch, strain vs. displacement

4.3 Testing Results for 40-ply Laminates

The results for the 40-ply laminates FP, AR, and AN under four-point bending are listed below. Laminates with the 5-in. and 20-in. notches have three replicates, and laminates with the 10-in. notch have two replicates. The results of theses tests are described in terms of their load and strain responses. Similar to the data plots on the 20-ply laminates, the strain plots were obtained from the strain gages on the far-field (either M1 or M2), on the compression side. See Table 2 for detail in the mapping of the gages.

4.3.1 Results for the 5-in wide FP, AR, and AN Laminates

The results of the four-point bending test of the FP-laminate group, which is composed of replicates FP_1_5_1, FP_1_5_2, and FP_1_5_3 are indicated in Figure 4. 19 and Figure 4. 20. The maximum load for FP_1_5_1 was 1477.1-lb. Laminate FP_1_5_2 follows a similar pattern, as can be seen in Figure 4. 19, with a maximum load of 1500.1-lb. Both laminates had a bar spacing of [10-in./ 18-in.] Laminate FP_1_5_3 had a bar spacing of [6-in./ 16-in.] and followed a different load-displacement curve than the other two replicates. It had a maximum load of 1211.6-lb.

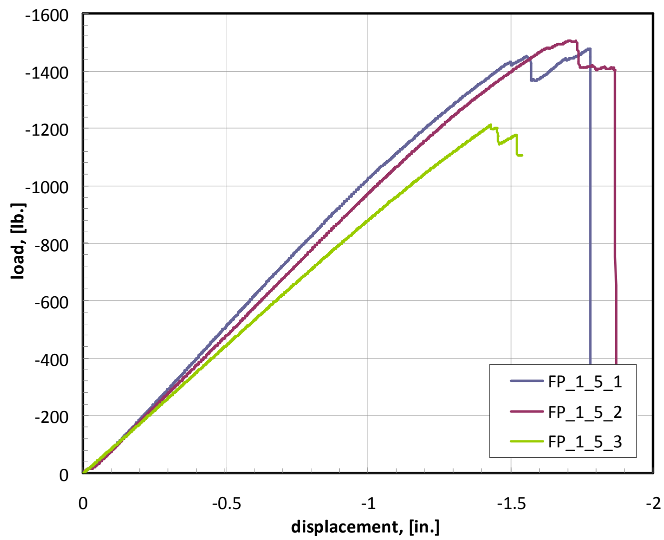

Figure 4. 19 - Laminate FP, width 5-in., 1-in. notch, load vs. displacement

Figure 4. 20 shows the strain-displacement plot for this particular laminate group. It was found that the maximum strains before failure were 0.0085, 0.0083, and 0.0086 for FP_1_5_1, FP_1_5_2, and FP_1_5_3, respectively.

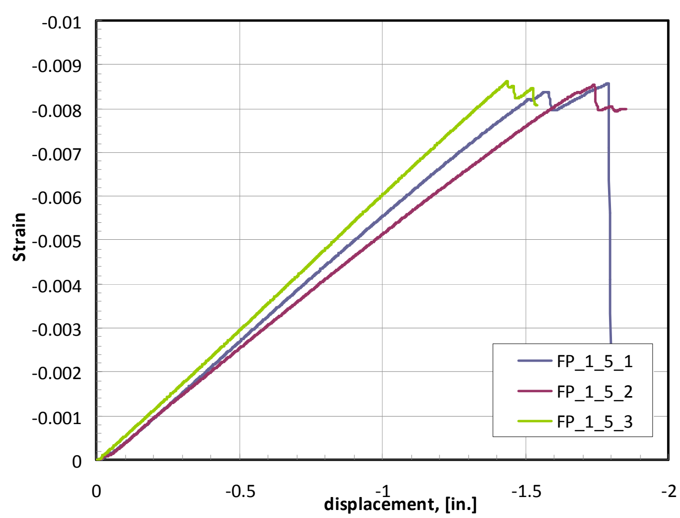

Figure 4. 20 - Laminate FP, width 5-in., 1-in. notch, strain vs. displacement

The results of the four-point bending test of the AR-laminate group, which is composed of replicates AR_1_5_1, AR_1_5_2, and AR_1_5_3 are indicated in Figure 4. 21 and Figure 4. 22. The maximum load for AR_1_5_1 was 1857.3-lb. Laminate AR_1_5_2 follows a similar pattern, as can be seen in Figure 4. 21, with a maximum load of 1942.9-lb. Both laminates had a bar spacing of [10-in./ 18-in.] Laminate AR_1_5_3 had a bar spacing of [6-in./ 16-in.] and apparently failed earlier at different load. The specimen reached a maximum load of 1424.6-lb.

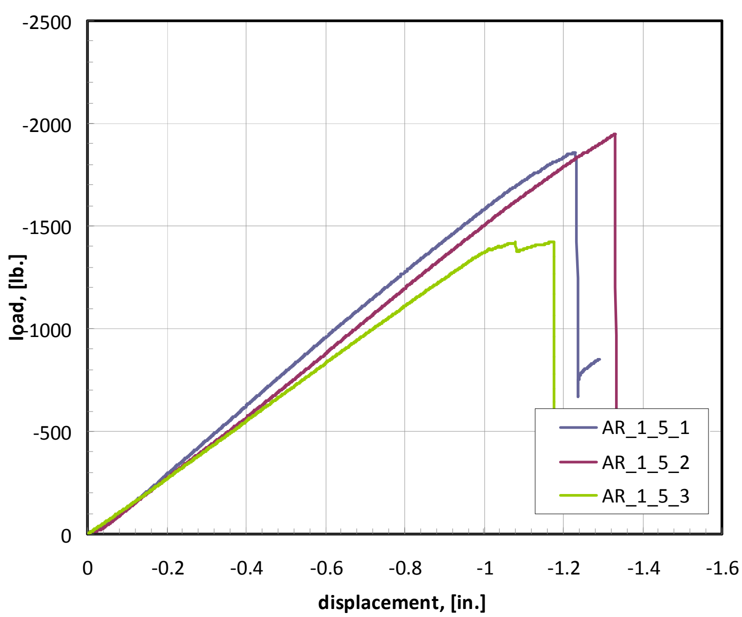

Figure 4. 21 - Laminate AR, width 5-in., 1-in. notch, load vs. displacement

Figure 4. 22 shows the strain-displacement plot for this particular laminate group. It was found that the maximum strains before failure were 0.0062, 0.0065, and 0.006 for AR_1_5_1, AR_1_5_2, and AR_1_5_3, respectively.

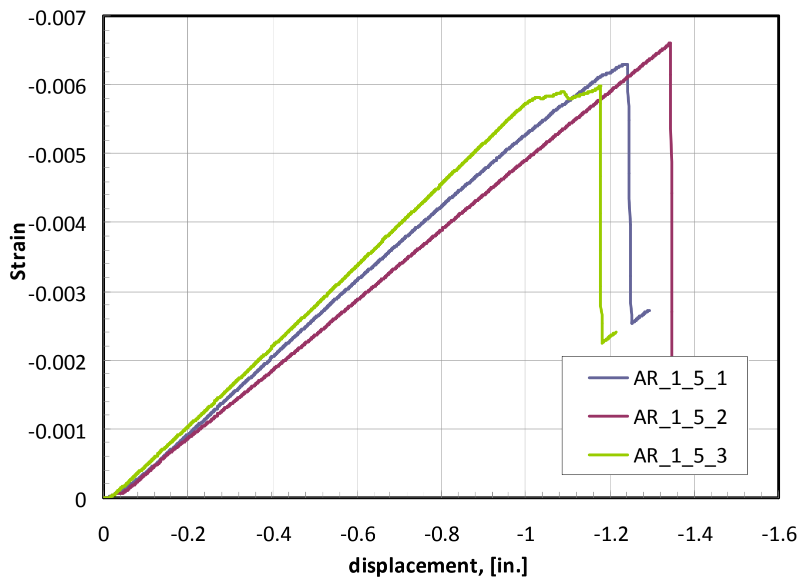

Figure 4. 22 - Laminate AR, width 5-in, 1-in notch, strain vs. displacement

The results of the four-point bending test of the AN-laminate group, which is composed of replicates AN_1_5_1, AN_1_5_2, and AN_1_5_3 are indicated in Figure 4. 23 and Figure 4. 24. The maximum load for AN_1_5_1 was 2338.4-lb. Laminate AN_1_5_2 follows a similar pattern, as can be seen in Figure 4. 23, with a maximum load of 2333.8-lb. Both laminates had a bar spacing of [10-in./ 18-in.] Laminate AN_1_5_3 had a bar spacing of [6-in./ 16-in.] and failed earlier at different load. This specimen failed at a maximum load of 1872.8-lb.

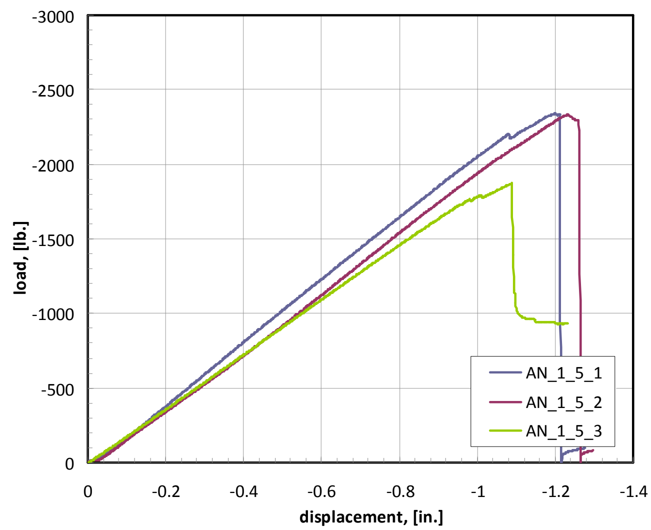

Figure 4. 23 - Laminate AN, width 5-in., 1-in. notch, load vs. displacement

Figure 4. 24 shows the strain-displacement plot for this particular laminate group. It was found that the maximum strains before failure were 0.006, 0.0058, and 0.0056 for AN_1_5_1, AN_1_5_2, and AN_1_5_3, respectively.

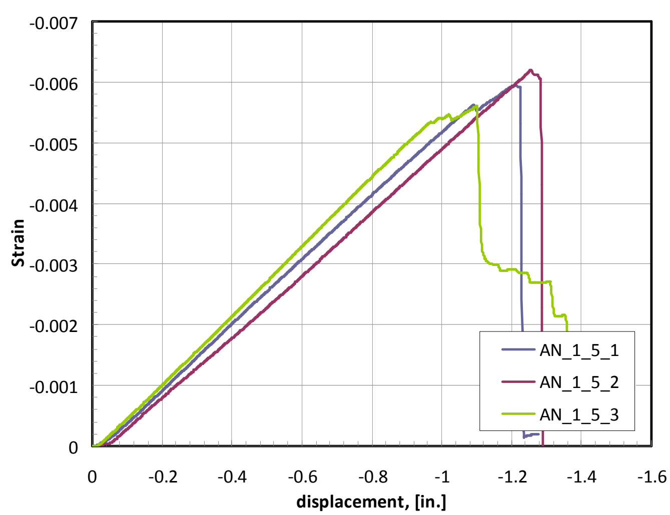

Figure 4. 24 - Laminate AN, width 5-in., 1-in. notch, strain vs. displacement

4.3.2 Results for the 10-in wide FP, AR, and AN Laminates

The results of the four-point bending test of the FP-laminate group, which is composed of replicates FP_1_10_1, FP_1_10_2 are indicated in Figure 4. 25 and Figure 4. 26. The maximum load for FP_1_10_1 was 3269.3-lb. Laminate FP_1_10_2 follows a similar pattern, as can be seen in Figure 4. 25, with a maximum load of 3296.8-lb. Both laminates had a bar spacing of [10-in./ 18-in.]

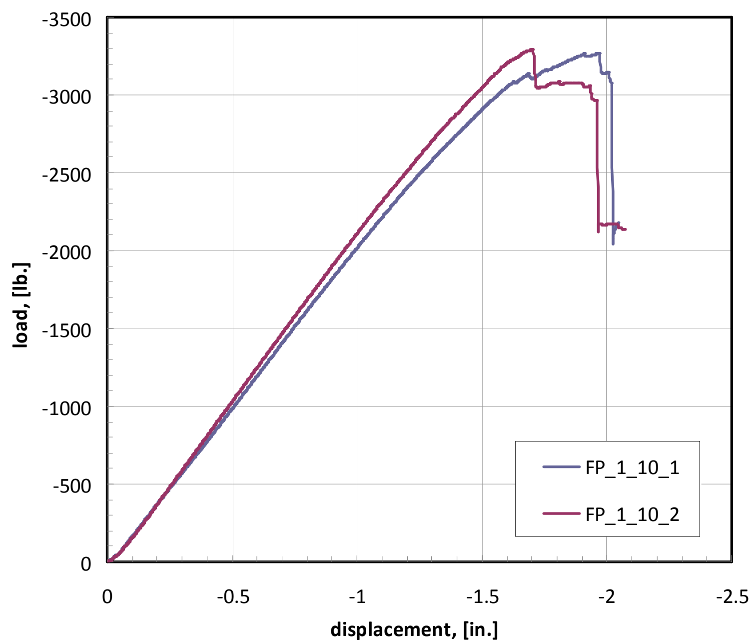

Figure 4. 25 - Laminate FP, width 10-in., 1-in. notch, load vs. displacement

Figure 4. 26 shows the strain-displacement plot for this particular laminate group. It was found that the maximum strains before failure were 0.0087 and 0.0084 for FP_1_10_1 and FP_1_10_2, respectively.

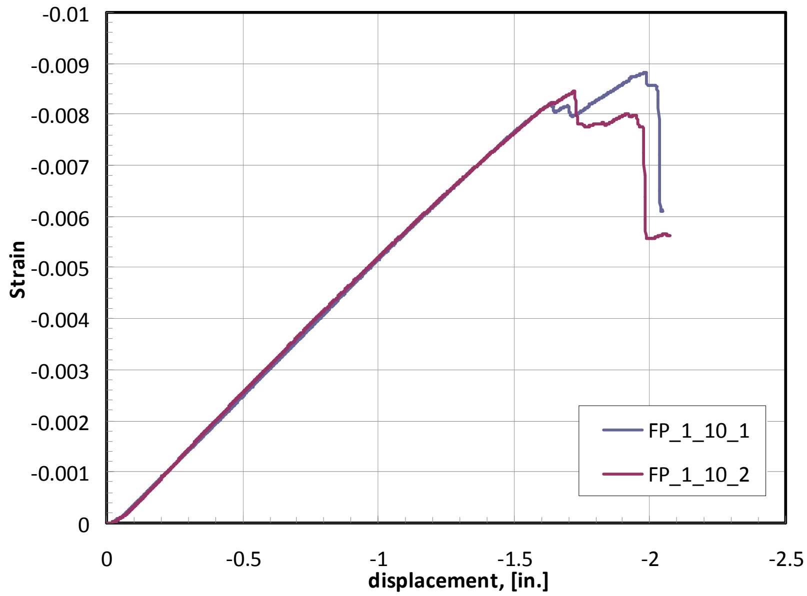

Figure 4. 26 - Laminate FP, width 10-in., 1-in. notch, strain vs. displacement

The results of the four-point bending test of the AR-laminate group, which is composed of replicates AR_1_10_1 and AR_1_10_2 are indicated in Figure 4. 27 and Figure 4. 28. The maximum load for AR_1_10_1 was 3885.2-lb. Laminate AR_1_10_2 follows a similar pattern, as can be seen in Figure 4. 27, with a maximum load of 3998.3-lb. Both laminates had a bar spacing of [10-in./ 18-in.]

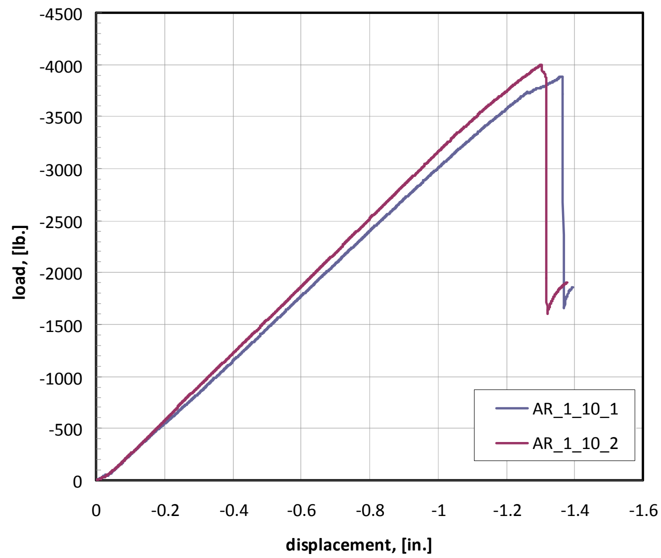

Figure 4. 27 - Laminate AR, width 10-in., 1-in. notch, load vs. displacement

Figure 4. 28 shows the strain-displacement plot for this particular laminate group. It was found that the maximum strains before failure were 0.0059 and 0.0061 for AR_1_10_1 and AR_1_10_2, respectively.

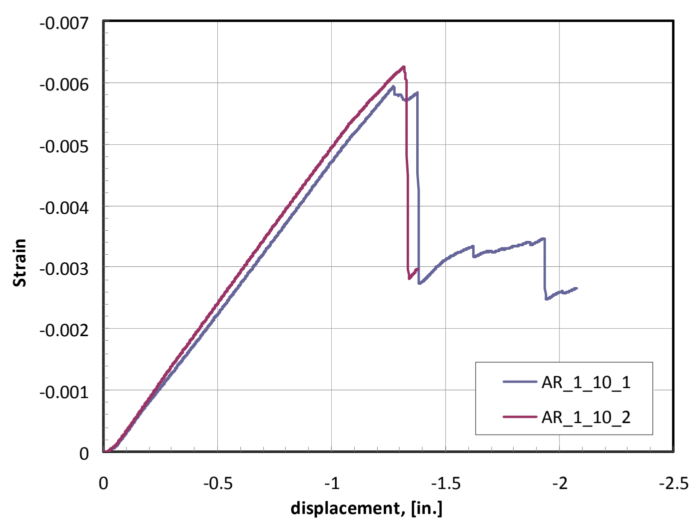

Figure 4. 28 - Laminate AR, width 10-in., 1-in. notch, strain vs. displacement

The results of the four-point bending test of the AN-laminate group, which is composed of replicates AN_1_10_1 and AN_1_10_2 are indicated in Figure 4. 29 and Figure 4. 30. The maximum load for AN_1_10_1 was 5132.8-lb. Laminate AN_1_10_2 follows a similar pattern, as can be seen in Figure 4. 29, with a maximum load of 5139.7-lb. Both laminates had a bar spacing of [10-in./ 18-in.]

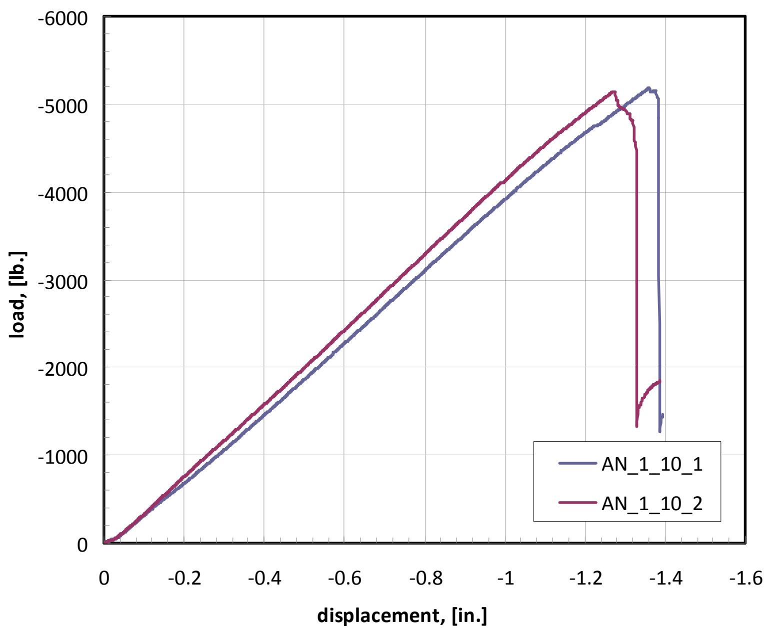

Figure 4. 29 - Laminate AN, width 10-in., 1-in. notch, load vs. displacement

Figure 4. 30 shows the strain-displacement plot for this particular laminate group. It was found that the maximum strains before failure were 0.0057 and 0.0059 for AN_1_10_1 and AN_1_10_2, respectively.

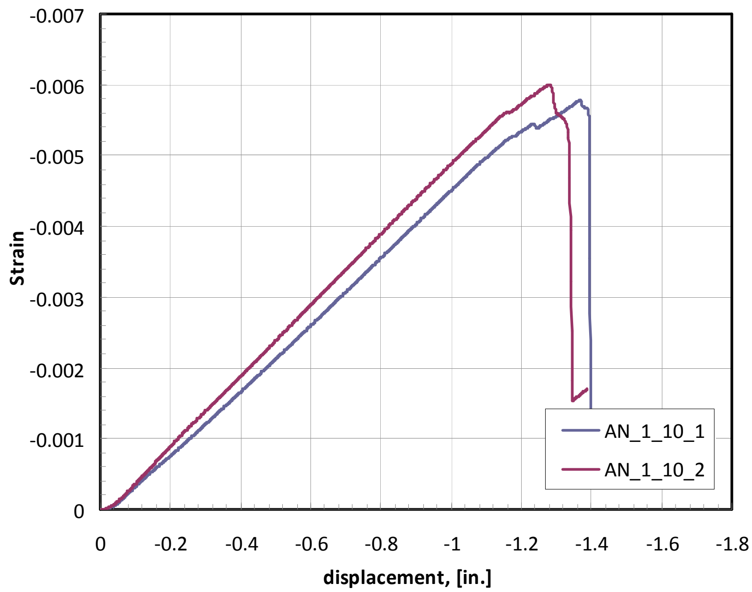

Figure 4. 30 - Laminate AN, width 10-in., 1-in. notch, strain vs. displacement

4.3.3 Results for the 20-in wide FP, AR, and AN Laminates

The results of the four-point bending test of the F-laminate group, which is composed of replicates FP_4_20_1, F_4_20_2, and FP_4_20_3, are indicated in the Figure 4. 31 and Figure 4. 32. All these laminates used the same fixture with a bar spacing of [10-in./ 18-in.] Thus, the results were very similar. The maximum load for FP_4_20_1 was 6479.9-lb. Both laminates FP_4_20_2 and FP_4_20_3 follow a similar pattern, as can be seen in Figure 4. 31, with maximum load of 5790.7-lb. and 5947.6-lb., respectively.

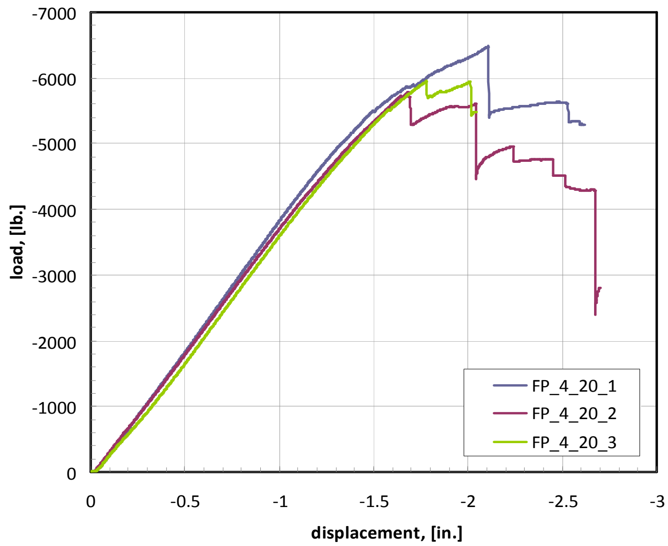

Figure 4. 31 - Laminate FP, width 20-in., 4-in. notch, load vs. displacement

Figure 4. 32 shows the strain-displacement plot for this particular laminate group. It was found that the maximum strains before failure were 0.0089, 0.0076, and 0.0087 for FP_4_20_1,FP_4_20_2, and FP_4_20_3, respectively.

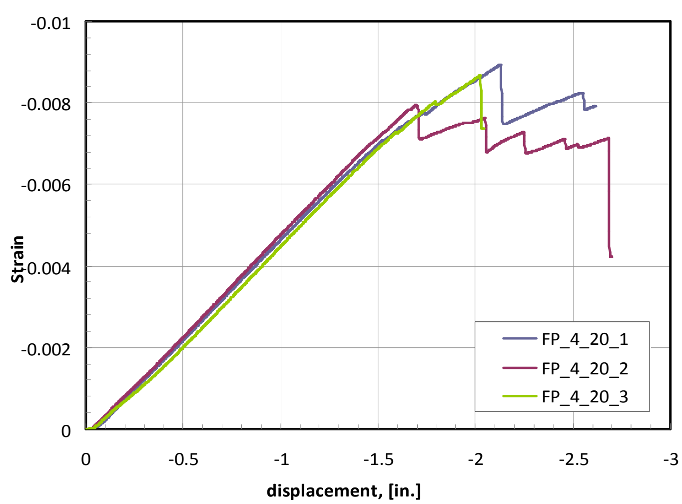

Figure 4. 32 - Laminate FP, width 20-in., 4-in. notch, strain vs. displacement

The results of the four-point bending testing of the P-laminate group, which is composed of replicates AR_4_20_1, AR_4_20_2, and AR_4_20_3 are indicated in Figure 4. 33 and Figure 4. 34. All these laminates used the same fixture with a bar spacing of [10-in./ 18-in.] The maximum load for AR_4_20_1 was 7012.1-lb. Both laminates AR_4_20_2 and AR_4_20_3 follow a similar pattern, as can be seen in Figure 4. 33, with maximum load of 6850.4-lb. and 6988.9-lb., respectively.

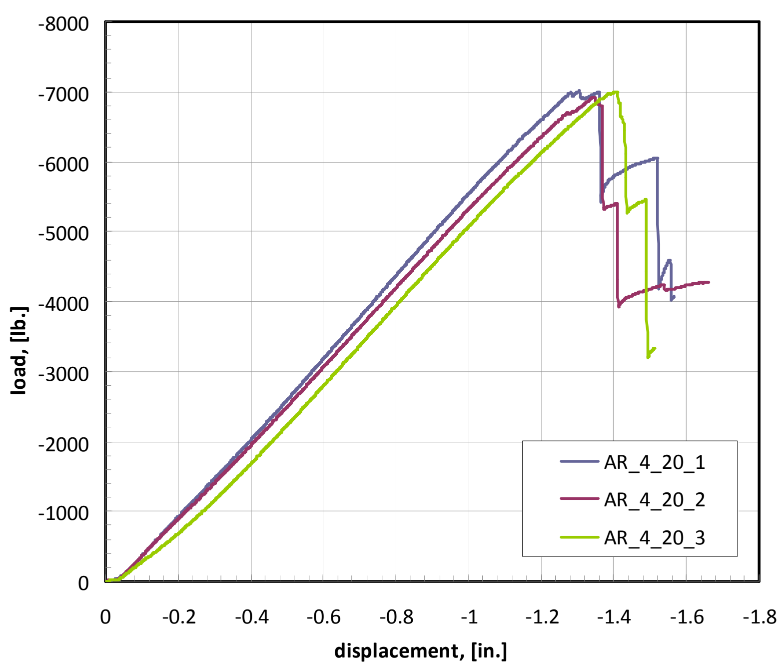

Figure 4. 33 - Laminate AR, width 20-in., 4-in. notch, load vs. displacement

Figure 4. 34 shows the strain-displacement plot for this particular laminate group. It was found that the maximum strains before failure were 0.0058, 0.0054, and 0.0061 for AR_4_20_1, AR_4_20_2, and AR_4_20_3, respectively.

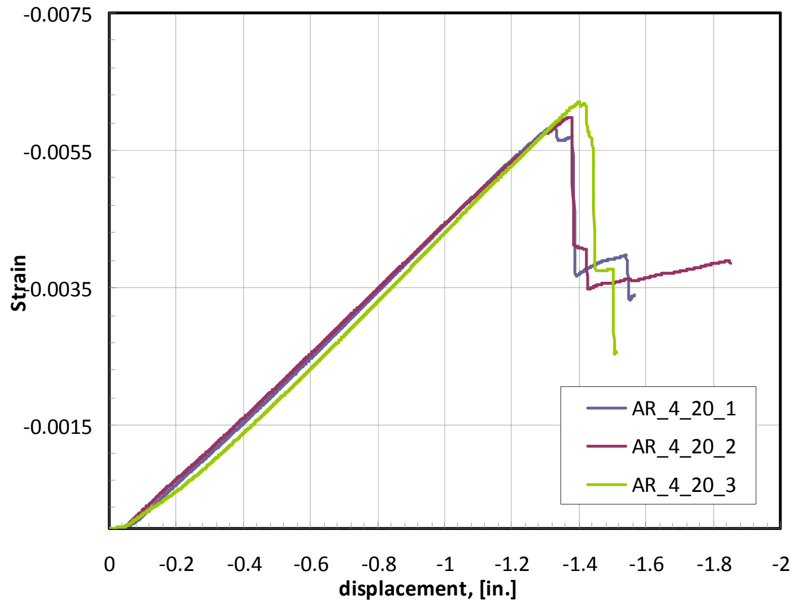

Figure 4. 34 - Laminate AR, width 20-in., 4-in. notch, strain vs. displacement

The results of the four-point bending testing of the AN-laminate group, which is composed of replicates AN_4_20_1, AN_4_20_2, and AN_4_20_3 are indicated in Figure 4. 35 and Figure 4. 36. All these laminates used the same fixture with a bar spacing of [10-in./ 18-in.] The maximum load for AN_4_20_1 was 10349.8-lb. Both laminates AN_4_20_2 and AN_4_20_3 follow a similar pattern, as can be seen in Figure 4. 35, with maximum load of 9836.7-lb. and 9458-lb., respectively.

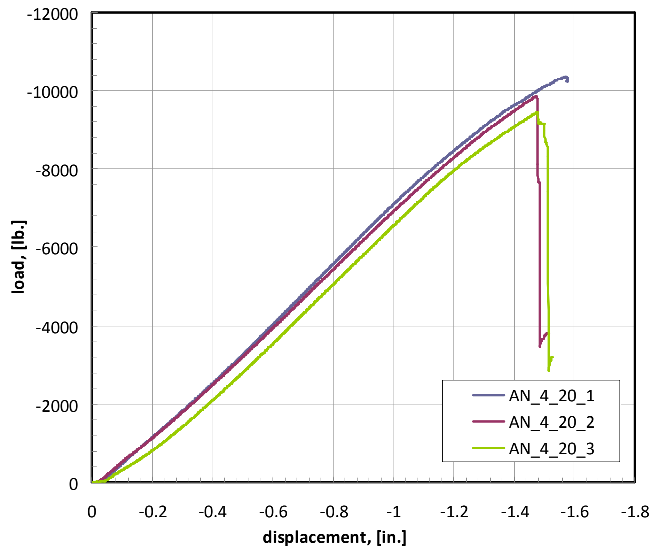

Figure 4. 35 - Laminate AN, width 20-in., 4-in. notch, load vs. displacement

Figure 4. 36 shows the strain-displacement plot for this particular laminate group. It was found that the maximum strains before failure were 0.0066, 0.0057, and 0.0063 for AN_4_20_1 and AN_4_20_2, and AN_4_20_3, respectively.

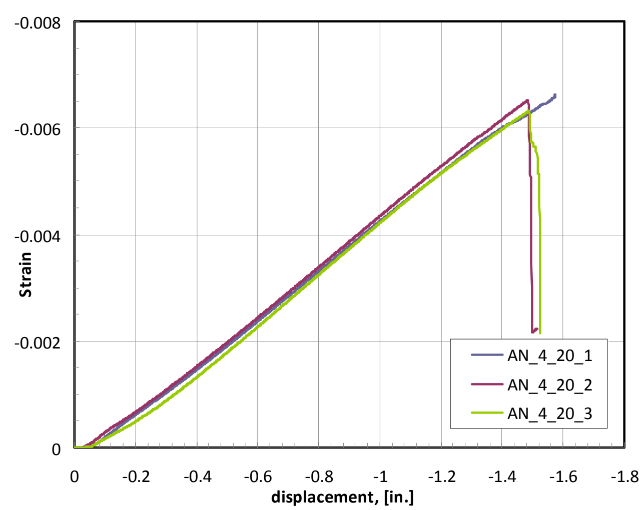

Figure 4. 36 - Laminate AN, width 20-in., 4-in. notch, strain vs. displacement

4.4 Comments on Testing Results

After testing all the laminates, we found some interesting disparities and similarities between all the laminates. We observed that in our test setup the specimens would react differently depending upon what laminate was used. Hence, lamina lay-up had an effect in the bending performance. Also, the width of the specimen and fixture settings (the bar spacing) would cause the laminates to react differently, as it is clearly shown in every figure that shows load versus displacement.

We found that normally all laminates of the same group would produce the same strain-displacement plot, regardless of the loading conditions. The following tables list important test information such as loading, time, and the far-field gage output for each specimen tested (refer to Figure 3. 7 and Table 2 for information on the location of these gages.)

Table 3 - Test results for the 5-in. wide 20-ply Laminates

Specimen Label	% of 0-degree plies	Bar Spacings	Test Time (sec.)	Loading (lb.)	Far Field Gage (Comp.)	Displacement failure (in.)
F-1-5-1	10	8-in & 13-in	84	559.6	0.0113	1.83
F-1-5-2	10	10-in & 16-in	118	362.2	0.0103	2
P-1-5-1	30	10-in & 16-in	114	454.5	0.00914	2.21
P-1-5-2	30	10-in & 16-in	107	438.7	0.00981	2.1
P-1-5-3	30	6-in & 16-in	110	270.6	0.00924	3.13
N-1-5-1	50	10-in & 16-in	74.4	683.6	0.00752	2
N-1-5-2	50	10-in & 16-in	77	678.8	0.00821	2
N-1-5-3	50	6-in & 16-in	130	404.6	0.00842	3.2

Table 3 shows the results of the 5-in. wide laminates with 20 plies. The displacement listed on the last column refers to the INSTRON crosshead displacement and not the displacement experienced at the center of the specimens. It is important to note that, in reality, the maximum displacement of the laminate would be significantly higher, since the laminate would further deform as it is bent by the separation of the top bars of the fixture with respect to the two bottom bars. By taking a look at the load data of the specimens with the same bar spacing, we noticed an increase of strength as we increase the 0-degree plies in the laminate. The P-laminates and N-laminates had an increase of 19% and 47% in strength with respect to the F-laminate, respectively. Laminate F_1_5_3 gave us very little useful data, so it was not taken into account for any of the analysis. Table 4 shows the results of the 10-in. wide laminates with 20 plies.

Table 4 - Test results for the 10-in. wide 20-ply Laminates

Specimen Label	% of 0-degree plies	Bar Spacings	Test Time (sec.)	Loading (lb.)	Far Field Gage (Comp.)	Displacement to failure (in.)
F-1-10-1	10	8-in & 13-in	121.4	1235.6	0.01108	1.61
F-1-10-2	10	8-in & 13-in	111.2	1150.1	0.01227	1.79
P-1-10-1	30	10-in & 16-in	124.7	843.1	0.01	1.95
P-1-10-2	30	10-in & 16-in	116.3	894.1	0.00951	2.54
N-1-10-1	50	10-in & 16-in	95.5	1284.3	0.00818	2.11
N-1-10-2	50	10-in & 16-in	94.7	1283.2	0.00831	2.15

We observed that the F-laminates deformed considerably less than the other two laminates, but this could be due to the difference in bar spacing. The N-laminates experienced an increase of 32% in strength with respect to the P-laminates.

Table 5 - Test results for the 20-in. wide 20-ply Laminates

Specimen Label	% of 0-degree plies	Bar Spacings	Test Time (sec.)	Loading (lb.)	Far Field Gage (Comp.)	Displacement to failure (in.)
F-4-20-1	10	8-in & 13-in	158.4	2260.3	0.01141	1.87
F-4-20-2	10	10-in & 14.5-in	114.6	1495	0.00897	2
F4-20-3	10	8-in & 13-in	121.8	2418.9	0.01063	1.65
P-4-20-1	30	10-in & 16-in	127.3	1743.5	0.00892	2.11
P-4-20-2	30	10-in & 16-in	112	1625.7	0.00891	2
P-4-20-3	30	10-in & 18-in	126.1	1087.7	0.00773	2.7
N-4-20-1	50	10-in & 16-in	88	2609.6	0.0076	2.15
N-4-20-2	50	10-in & 16-in	90	2463.1	0.00714	2
N-4-20-3	50	10-in & 18-in	85	2514	0.00725	2.2

Table 5 shows the results of the 20-in. wide laminates with 20 plies. During the first tests, we noticed that the F-laminate deformed considerably more than we had initially expected and did not reach failure. Thus, fixtures with more reduced bar spacing were used. By comparing the load data with similar bar spacing, the P-laminates only gained about 1% of strength with respect to the F-Laminate. However, the N-laminates had an increase of 41% in strength with respect to the 10% 0-degree ply laminate.

Table 6 shows the results of the 5-in. wide laminates with 40 plies. As expected, we found that this new set of laminates required less deformation for failure. We observed that, under the same loading conditions, the 10% 0-degree laminates required considerably less load to fail and deformed further than the other two 40-ply laminates. The AR-laminates and AN-laminates had an increase of 20% and 36% in strength with respect to the FP-laminates, respectively. An interesting observation is that both the AR and AN laminates behaved very similar under the same loading conditions, but we observed an increase of 20% in strength for the 50% 0-degree laminates.

Table 6 - Test results for the 5-in. wide 40-ply Laminates

Specimen Label	% of 0-degree plies	Bar Spacings	Test Time (sec.)	max. Loading (lb.)	Far Field Gage (Comp.)	Displacement failure (in.)
FP-1-5-1	10	10-in & 18-in	109.7	1477.11	0.00856	1.77
FP-1-5-2	10	10-in & 18-in	113.5	1500.1	0.00834	1.72
FP-1-5-3	10	6-in & 16-in	92.4	1211.64	0.00859	1.43
AR-1-5-1	30	10-in & 18-in	77.6	1857.3	0.00623	1.23
AR-1-5-2	30	10-in & 18-in	82.6	1942.9	0.00647	1.32
AR-1-5-3	30	6-in & 16-in	73	1424.16	0.00598	1.17
AN-1-5-1	50	10-in & 18-in	76.6	2338.4	0.00591	1.19
AN-1-5-2	50	10-in & 18-in	77.8	2333.8	0.00582	1.22
AN-1-5-3	50	6-in & 16-in	88.7	1872.8	0.00558	1.1

Table 7 shows the results of the 10-in. wide laminates with 40 plies. We obtained a similar increase of strength between the laminates as in the case of the 5-in. specimen testing. In these tests, the AR-laminates and AN-laminates had an increase of 17% and 36% in strength with respect to the FP-laminates, respectively.

Table 7 - Test results for the 10-in. wide 40-ply Laminates

Specimen Label	% of 0-degree plies	Bar Spacings	Test Time (sec.)	max. Loading (lb.)	Far Field Gage (Comp.)	Displacement failure (in.)
FP-1-10-1	10	10-in & 18-in	122.8	3269.3	0.00874	1.97
FP-1-10-2	10	10-in & 18-in	124.5	3296.8	0.00842	1.7
AR-1-10-1	30	10-in & 18-in	124.5	3885.2	0.00588	1.36
AR-1-10-2	30	10-in & 18-in	82.7	3998.3	0.00611	1.3
AN-1-10-1	50	10-in & 18-in	86.5	5132.8	0.00573	1.36
AN-1-10-2	50	10-in & 18-in	83.3	5139.7	0.00597	1.27

Again, both the AR and AN laminates behaved very similarly under the same loading conditions, but we observed an increase of 23% in strength for the 50% 0-degree laminates. Similar to the 5-in. wide specimen testing, the F-laminate required larger deformations to fail.

Table 8 shows the results of the 20-in. wide laminates with 40 plies.

Table 8 - Test results for the 20-in. wide 40-ply Laminates

Specimen Label	% of 0-degree plies	Bar Spacings	Test Time (sec.)	max. Loading (lb.)	Far Field Gage (Comp.)	Displacement to failure (in.)
FP-4-20-1	10	10-in & 18-in	157	6479.9	0.00894	2.1
FP-4-20-2	10	10-in & 18-in	162	5790.7	0.00762	1.67
FP-4-20-3	10	10-in & 18-in	122.7	5947.6	0.00868	2
AR-4-20-1	30	10-in & 18-in	93.9	7012.1	0.00586	1.3
AR-4-20-2	30	10-in & 18-in	135.6	6850.4	0.0054	1.33
AR-4-20-3	30	10-in & 18-in	91.6	6988.9	0.00617	1.4
AN-4-20-1	50	10-in & 18-in	99	10349.8	0.00661	1.57
AN-4-20-2	50	10-in & 18-in	91	9836.7	0.00577	1.47
AN-4-20-3	50	10-in & 18-in	91.6	9458	0.0063	1.47

As expected, the AR-laminates and AN-laminates had an increase of 13% and 39% in strength with respect to the FP-laminate, respectively. Also, we noticed that the 50% 0-degree AR-laminate experienced a 30% gain in strength under the same loading conditions, with respect to the 30% 0-degree AN laminate.

By looking at the test data, we can conclude that, under the same loading conditions, there is a gain of approximately 35% of strength between the 30% 0-degree and 50% 0-degree 20-ply laminates. For the tests of the 40-ply laminates, we observed this increase of strength to about 25%.

Chapter 5. Modeling Stress Concentrations in Notched Laminates under Bending

5.1 Introduction to Modeling Notched Laminates

The analysis of stress in plates subjected to out-of-plane bending has been studied and researched for many years. Typically, the design for ultimate load for plates and shells when notches or indents are present is carried out by obtaining the stress concentration factors.

For our simulation analysis, moment concentration factors of the laminates under pure bending at the edge of the several different notch types (0.25-in. diameter hole, 1-in. long ovaloid, and a 4-in. long ovaloid) were calculated. As described earlier, two laminate thicknesses were studied consisting of 20 plies and 40 plies. For each thickness, three laminate types were studied: one with 10% 0-degree plies, one with 30% 0-degree plies, and one with 50% 0-degree plies.

Three different types of finite element models were constructed using ABAQUS to model the stress concentration factors in notched laminates: one consisting of shell elements with transverse shear effects (called “Shell” model,) a second one consisting of shell elements without transverse shear effects (called “Shell_tri” model,) and a third model consisting of quadratic 3-D continuum solid elements with two elements through the thickness of each ply (called “Solid” model.) We made use of symmetry throughout all these tests, even though a symmetry assumption is not entirely valid because of the coupling between bending and twisting. However, this effect has little consequence in the calculations of the moment concentration factors. Modeling the entire laminate with solid elements gave results that were within one percent of those of the current model.

5.2 The Shell Element Model

As mentioned earlier, two types of Shell models were constructed on ABAQUS. One model, which we simply called “Shell,” would take into account the transverse shear effects, and another model called “Shell-tri” would use elements that do not take into consideration the shear effects. The “Shell” model was constructed using type S4 elements and the “Shell_tri” model was constructed using STRI3 elements. Figure 5. 1a and Figure 5. 1b show the mesh for both shell models with S4 and STRI3 elements, respectively.

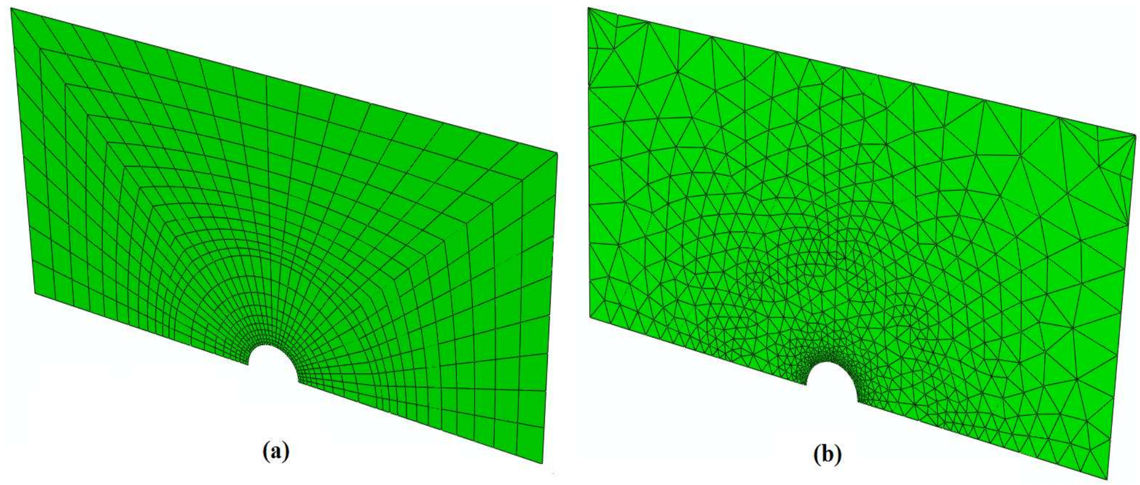

Figure 5. 1 - (a) ABAQUS shell model with S4 elements. (b) ABAQUS shell model with STRI3 elements.

5.3 The 3-D Solid-Shell Model

The creation of the 3-D solid element model in ABAQUS required a more complex approach. Because using a model composed entirely of 3-D solid elements required far more computational time, the model was designed using both solid and shell elements. The plate was modeled using Shell elements at some arbitrary distance away from the hole, and then we added 3-D solid elements on the section of the plate immediately around the hole. Symmetry was used for the analysis of these models, and the mesh had the same planar density as the shell element mesh. The model, depicted in Figure 5. 2, shows the upper portion of a Solid-Shell model.

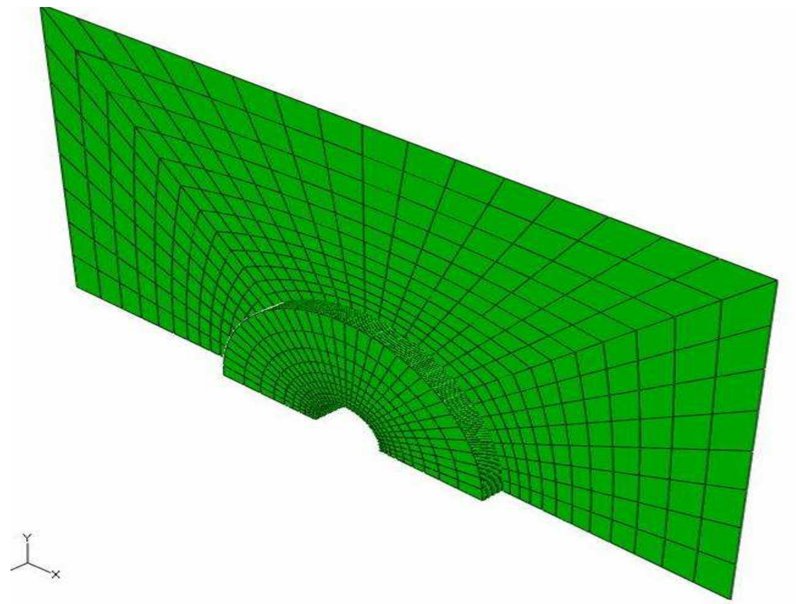

Figure 5. 2 - Solid-Shell element model in ABAQUS

The solid region was created using hexahedron type elements (type C3D8I for the circular hole analysis and C3D20 for the ovaloid notch analysis). Figure 5. 3 shows a close-up of the solid element region.

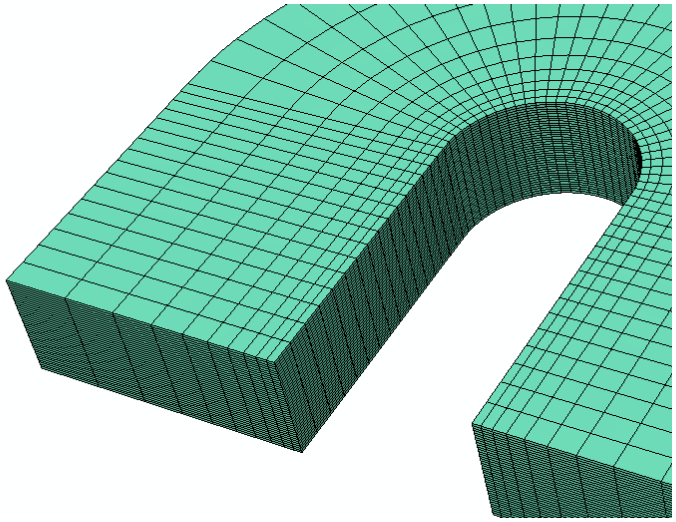

Figure 5. 3 – C3D20 Solid elements on the Solid-Shell model with a 1-in. notch

It is important to mention that since 3-D solid elements do not give moment results as part of the element output solution, we had to study the solid model using the stress solution. We made use of a FORTRAN program to convert the stress output generated by ABAQUS into a moment result.

Because two different element types were used, it was necessary to create two parts: one for the shell region (the area away from the notch) and another for the solid region (the area near the notch.) When designing a model that uses both shell and solid elements, it is important to take into consideration how these are linked together. Hence, it is vital to understand how they interact and that they do it properly in ABAQUS. In order to ensure that both parts are acting as one, we must create a shell-to-solid coupling, which allows for a smooth transition between these two different element types. The coupling is defined by two user-specified interferences. The shell interface, referred as “shell edge,” is coupled with the solid surface, which bounds the shell region.

The model will then have two different section properties: one for the Shell region and another for the Solid region. Initially, we started using steel as the material for analysis; but later on, as we verified our results, we switched to the more complex non-homogeneous composite layered materials.

5.4 Comparison of Concentration Factors between Theoretical Model with ABAQUS Model

We additionally carried out a comparison of the concentration factor results between our ABAQUS model and the theoretical models (classical plate theory and Reissner theory.) Both theories are described in section 2.1.

For our ABAQUS results, we calculated a stress concentration distribution based on a material made of steel. The plot of the stress concentration factors between our ABAQUS model and the theoretical models can be seen in Figure 5. 4. As shown in the figure, our ABAQUS model follows the same concentration factor distribution as the Reissner’s model.

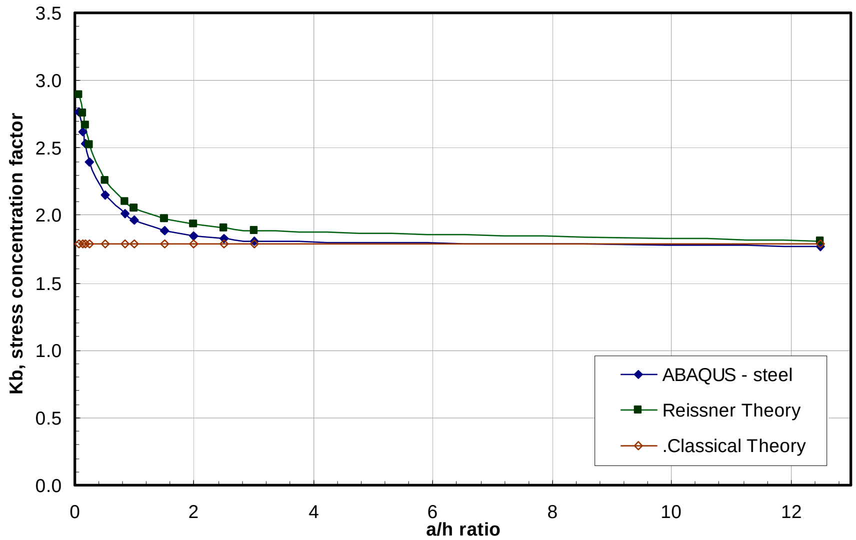

Figure 5. 4 - ABAQUS and Reissner's distribution of Stress Concentration Factor vs. a/h ratio

An important observation is that as we increase the ratio a/h, we decrease the ratio of transverse shear stress with the normal stress, τ_{max}/σ_{max}, because we are reducing the area where these shear stresses act. That is, the shearing stresses are almost negligible in contrast with effect of the loading couples (the bending of the plate) as the plate becomes thinner. Hence, as we approach the tangent of the slope, we get a more approximate depiction of the classical plate theory, KPT, which was, as mentioned earlier, described by Goodier [12].

5.5 Calculation of Moment Stress Concentration Factors of Laminates on ABAQUS

For our simulation analysis of the laminates under pure bending, moment concentration factors at the edge of the different notch types (the 0.25-in. diameter hole, 1-in. long ovaloid, and a 4-in. long ovaloid) were calculated.

As mentioned earlier, the models were simulated using symmetry to reduce computation time; hence, only half of the plates were modeled. It was found that the symmetry effect had little consequence in the calculations on the moment concentration factors.

5.5.1 Analysis of the Laminates with the ¼-in. Diameter Hole

The six different laminate lay-ups N,P,F, AN, AR, and FP were modeled. The model for the case with the 0.25-in diameter hole was a plate 2.5-in. wide and 2.5-in. long, with the hole cut out in the center. Every layer of the laminate had a thickness of 0.0074-in. The laminate types were classified in terms of two different thicknesses: the 20-ply laminates, which had a thickness of 0.148-in., and the 40-ply laminates, which had a thickness of 0.296-in.

We analyzed each laminate using three different ABAQUS models: Two shell models (with and without transverse shear effects), and one 3-D solid model (which uses 3D elasticity theory.) The shell model, which was composed of elements that took into account the transverse shear effects, was named simply

"Shell." The shell model, which was composed of elements that neglected the transverse shear effects, was labeled the "Shell_tri" model. The 3-D solid model was simply named "Solid." As mentioned earlier, this solid model was composed of both 3-D solid and shell elements to reduce computation time. In the region of the 3-D solid elements, two elements were created per layer. The process to obtain the moment results was performed using a FORTRAN code, which would use the stress output data (S11, S22, and S12) from ABAQUS to obtain the maximum moment.

The following table shows the simulation results for the 0.25-in centered hole analysis of all the laminates. Table 9 shows what the moment concentration factors are for each laminate. This was calculated using the following expression:

$$k_b = \frac{M_{t\_(a,\frac{\pi}{2})}}{M_0} \tag{5.7}$$

Table 9 - Moment Concentration Factor for the 0.25-in. hole laminated plates

	Moment Concentration Factors		
LAMINATES	**Shell**	**Shell_tri**	**Solid**
F (10% 0-degree)	2.117	1.611	1.573
P (30% 0-degree)	2.330	1.739	2.130
N (50% 0-degree)	2.508	1.819	2.523
FP (10% 0-degree)	2.378	1.650	1.913
AR (30% 0-degree)	2.906	1.897	3.017
AN (50% 0-degree)	3.064	1.959	3.197

From these results it is clear that the Shell_tri model, which follows the classical theory, in general, produces lower moment concentration factors than the other two models. This is more pronounced in the results of the thick 40-ply laminates. Also, it is important to note that as we increase the percentage of the 0-degree laminae, we obtain higher moment concentration factors.

5.5.2 Analysis of the Laminates with 1-in. and 4-in. Centered Notch.

In this next step, we used the same previous models and modified them to adjust for the size and shape of the notches instead of the circular hole. We also used the same computational procedure to calculate the moment concentration for all the laminates (N, P, F, AN, AR, and FP) for this analysis. The dimensions of the notches were 1-in. and 4-in. long, with an end radius of 1/8-in. The dimensions of the plates maintained a 1/10 ratio with respect of the notches: They consisted of 10-in. wide and 10-in. long for the 1-in. notch model, and 40-in. wide and 40-in. long for the 4-in. notch model.

The analysis of these laminates, just like in the previous simulations, was grouped into the three different simulation models: Shell, Shell_tri and Solid models.

Table 10 shows what the moment concentration factors are for each laminate for the 1-in. centered notch analysis.

Table 10 - Moment Concentration Factors for 1-in. notch models

	Moment Concentration Factors		
LAMINATES	**Shell**	**Shell_tri**	**Solid**
F (10% 0-degree)	2.961	2.377	2.142
P (30% 0-degree)	3.290	2.622	2.967
N (50% 0-degree)	3.590	2.785	3.535
FP (10% 0-degree)	3.323	2.428	2.850
AR (30% 0-degree)	4.147	2.923	4.800
AN (50% 0-degree)	4.421	3.062	4.800

We observed an overall increase in the moment concentration factors of all the ABAQUS models for all the laminate types, with respect to the case of the simulations of the circular hole.

Except for the case of the 20-ply 10% 0-degree laminate, we noticed that the Shell_tri model, which follows the classical plate theory, gave us lower concentration factors in comparison with the other two models.

Table 11 shows what the moment concentration factors are for each laminate for the 4-in. centered notch analysis.

Table 11 - Moment Concentration Factors for 4-in. notch models

LAMINATES	Moment Concentration Factors Shell	Shell_tri	Solid
F (10% 0-degree)	4.791	4.181	3.540
P (30% 0-degree)	5.449	4.545	5.200
N (50% 0-degree)	5.991	4.895	6.200
FP (10% 0-degree)	5.174	4.163	4.450
AR (30% 0-degree)	6.738	5.144	7.800
AN (50% 0-degree)	7.231	5.451	8.350

The results that we obtained were similar to those found on the analysis of the 1-in. notch laminated plates. In all the laminate types, the classical model "Shell_tri" gave us lower moment concentration factors than the other two model types.

5.5.3 Comments on the Analysis of the Moment Concentration Factors

The bending moment concentration factors as a function of notch length for the three 20-ply laminates are shown in the next three figures. Figure 5. 5 shows the moment concentration factors for the 10% 0-degree laminate for all three ABAQUS models. As expected the shell element results with transverse shear effects are higher than those without transverse shear effects. Also, we observe that the solid model gives us lower moment concentration factors than the other two models.

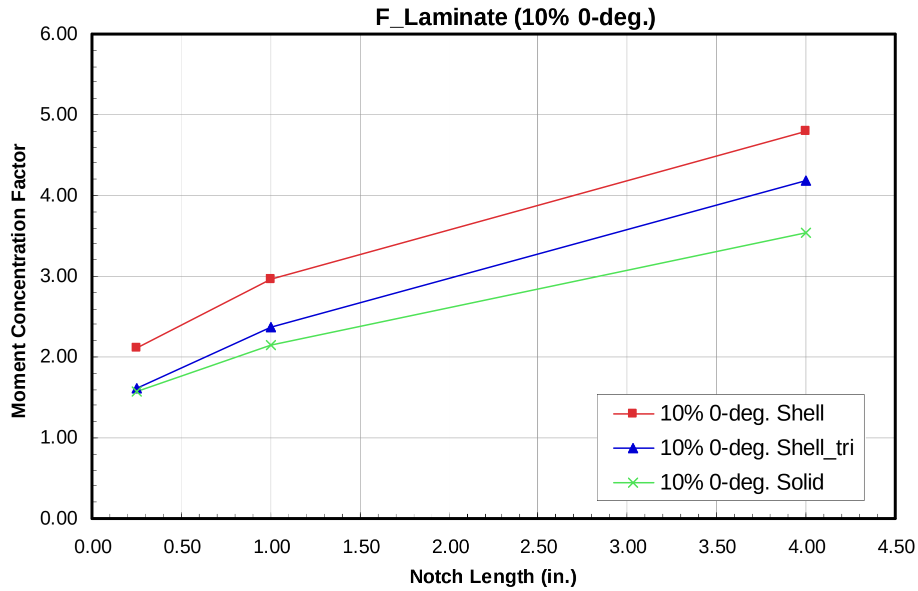

Figure 5. 5 - Moment Concentration Factors for F-laminate

Figure 5. 6 shows the moment concentration factors for the 30% 0-degree laminate for all three models. We can see a deviation of the moment concentration factors as a function of the notch length for the Solid model between the 10% 0-degree laminate and the 30% 0-degree laminate. The effects of the 0-degree plies seemed to be higher for the Solid model than for the other two ABAQUS models.

We can observe the same divergence on the laminate with higher content of 0-degree laminae on the next figure, Figure 5. 7, which shows the moment concentration factors for the 50% 0-degree laminate for all three models.

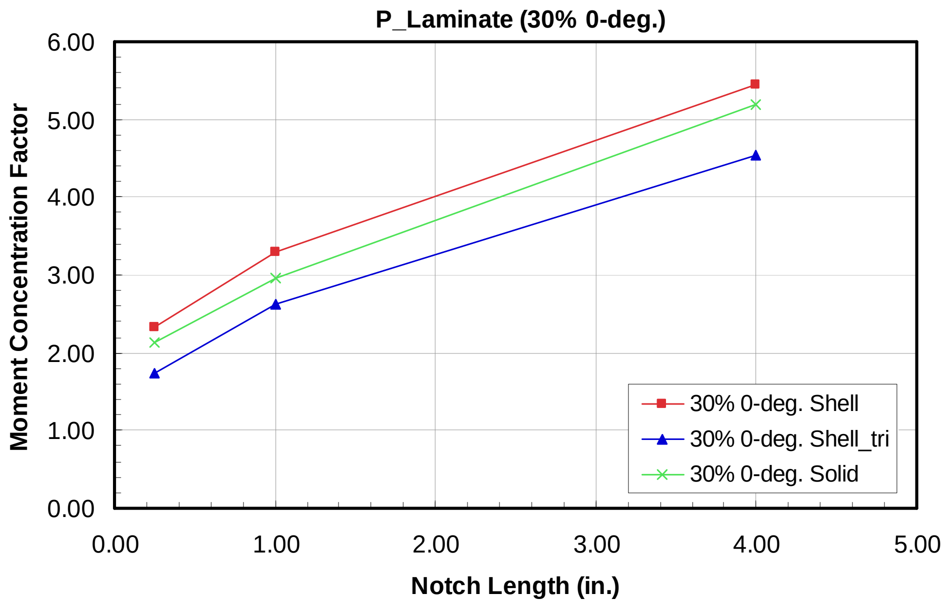

Figure 5. 6 - Moment Concentration Factors for P-laminate

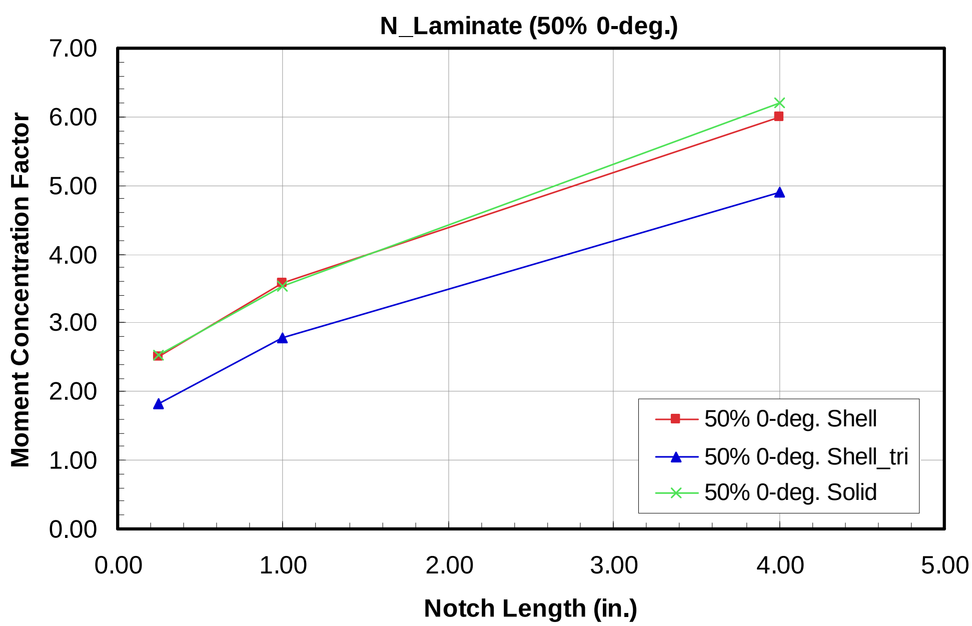

Figure 5. 7 - Moment Concentration Factors for N-laminate

Therefore, we come to the conclusion that the agreement between the results for shell elements with transverse shear effects and the results for the 3D solid elements is generally not good for the 20-ply laminate cases.

We can also observe similar circumstances for the thicker laminates. Figure 5. 8 shows the distribution of the moment concentration factors for the model with 10% 0-degree laminate.

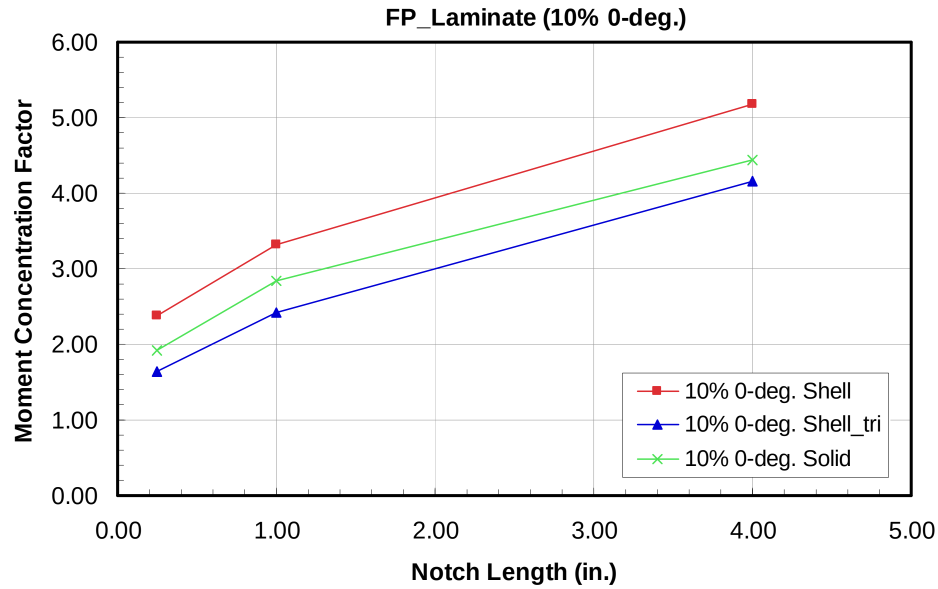

Figure 5. 8 - Moment Concentration Factors for FP-laminate

We noticed again that the results of the Shell model are higher than those of the classical model, which was also true for all 40-ply laminates. Figure 5. 9 shows the results for the 30% 0-degree laminate, for all notch lengths. The Solid model is again here affected by the increase of number of 0-degree laminae.

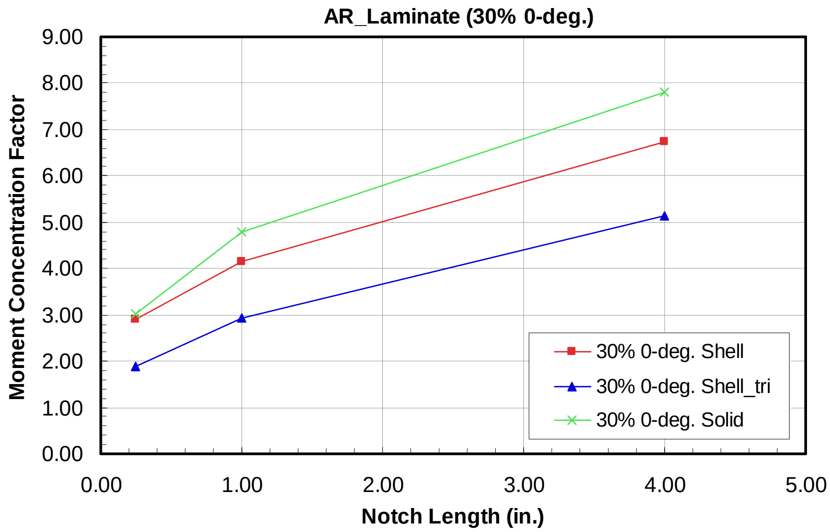

Figure 5. 9 - Moment Concentration Factors for AR-laminate

Figure 5. 10 shows the results for the case of the AN-laminate, which has 50% 0-degree laminae.

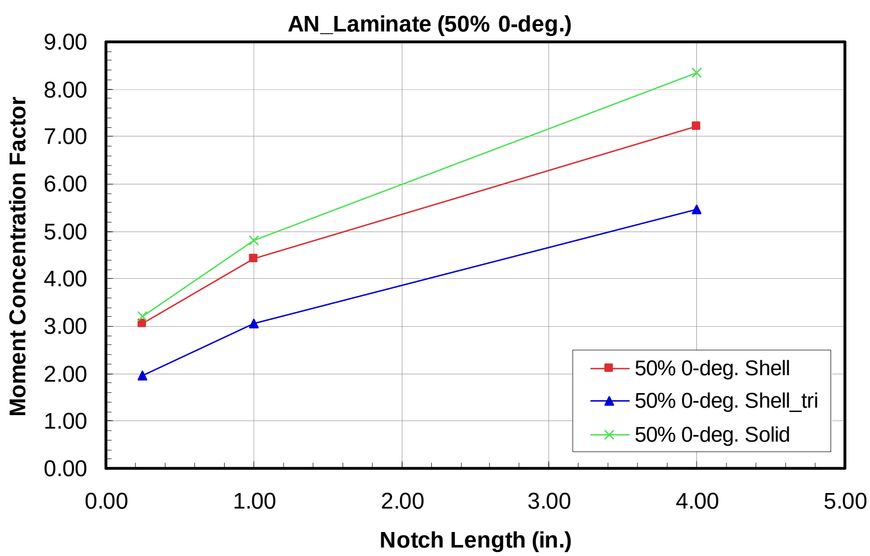

Figure 5. 10 - Moment Concentration Factors for AN-laminate

5.6 Conclusions of Modeling Stress Concentrations for Notched Laminates under Bending

To investigate the discrepancy of the 3-D solid models further, we focused on the case of the 0.25-in. diameter hole in the 20-ply laminate with 10% 0-degree plies (the F-laminate.)

First, we looked at mesh density of the 3D Solid model. In order to ascertain whether two elements through the thickness gave us enough accuracy, the calculation was repeated using four elements through the thickness of the ply. We obtained a good agreement between the two models, which gave credibility to the adequacy of the two elements per ply model.

Then, we paid attention to the strain distribution throughout the thickness of the laminate. When trying to determine the far field strain allowable for composite aircraft structures, it is probably more useful to deal with the strain output rather than the internal bending moments.

The strain distribution through the thickness of the 20-ply laminate with 10% 0-degree plies, the F-laminate, at the edge of the 0.25-in. diameter hole is shown in Figure 5. 11. Both the 3-D solid model and the shell model, with transverse shear effects, were plotted.

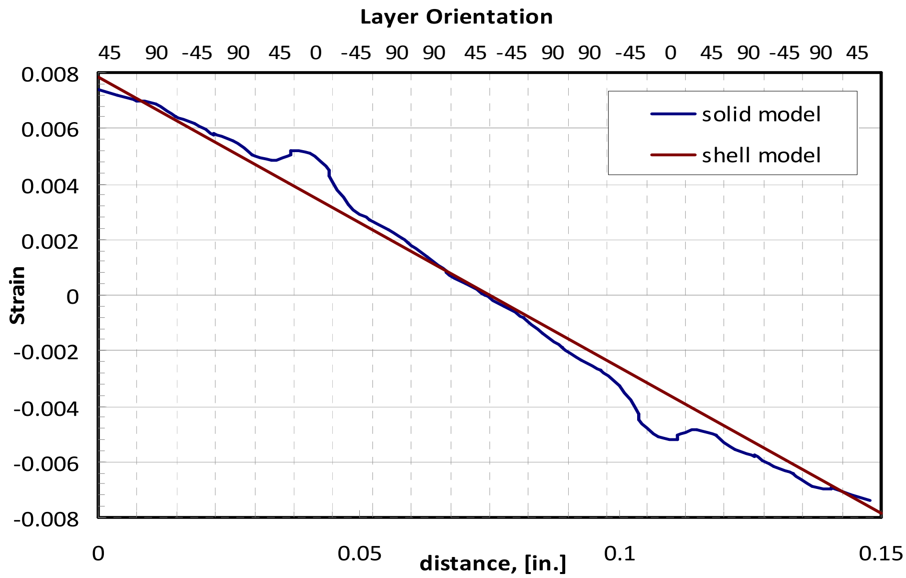

Figure 5. 11 - Strain distribution of F-laminate throughout the thickness at notch tip

As expected, the strain from the shell model is linear throughout the thickness. The strain from the 3D solid model is nearly linear except for two pronounced bulges in the layer location of the 0-degree plies, which can be easily appreciated in the plot. The difference between the two results is likely to be a free-edge effect [9]. The free-edge effect is a consequence of the singularities formed on a free edge when transverse shear and normal stresses are present.

This becomes more apparent if we look at the strain distribution through the thickness predicted by the two models at a point 0.025-in away from the edge of the hole, as shown in Figure 5. 12. Here, the strains are in relatively good agreement.

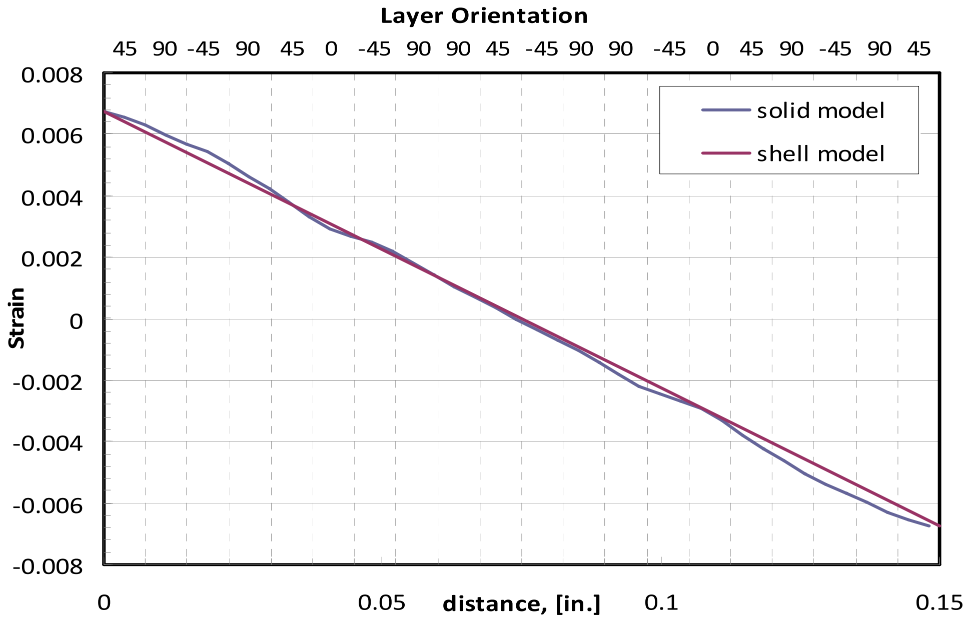

Figure 5. 12 - Strain distribution of F-laminate throughout the thickness at 0.025-in. away from the notch tip

The pronounced bulges at the 0-degree layer are no longer present. This same conclusion can be reached if we were to examine the results for the other laminates. The previous calculations that we used to obtain the moment concentration factors were repeated for each laminate, but this time a strain concentration factor was calculated based on the maximum strain found in the outermost 0-degree ply. The results for the 20-ply laminates (F, P, and N) are shown in the following three figures.

Figure 5. 13 shows the results of the strain concentration factor in terms of the notch length for the case of the F-laminate, which has 10% 0-degree plies.

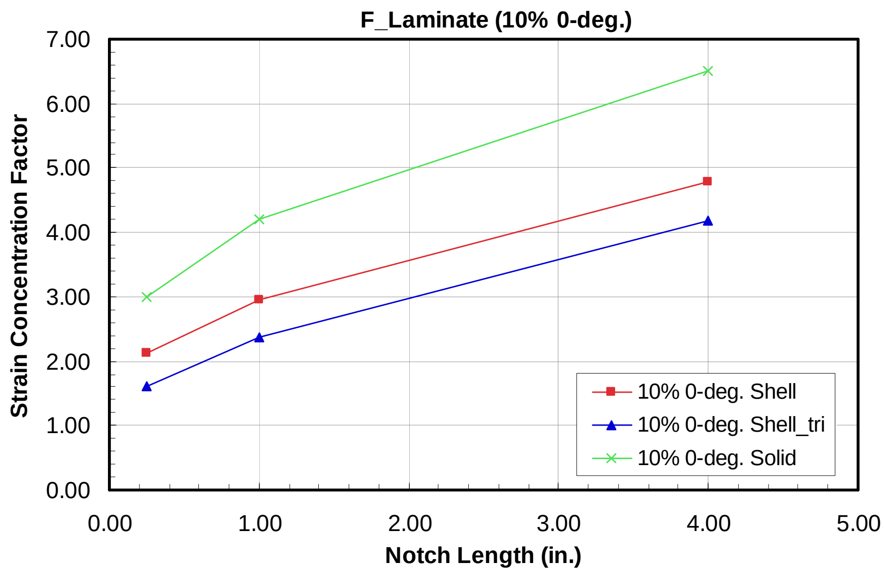

Figure 5. 13 - Strain Concentration Factors for F-laminate

Figure 5. 14 shows the results of the strain concentration factor in terms of the notch length for the case of the P-laminate, which has 30% 0-degree plies.

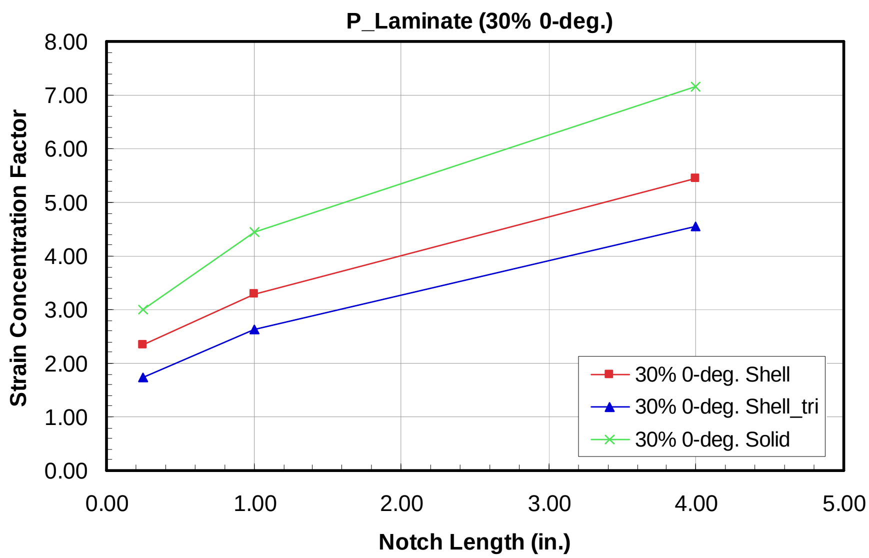

Figure 5. 14 - Strain Concentration Factors for P-laminate

Lastly, Figure 5. 15 shows the results for the case of the N-laminate, which has 50% 0-degree plies.

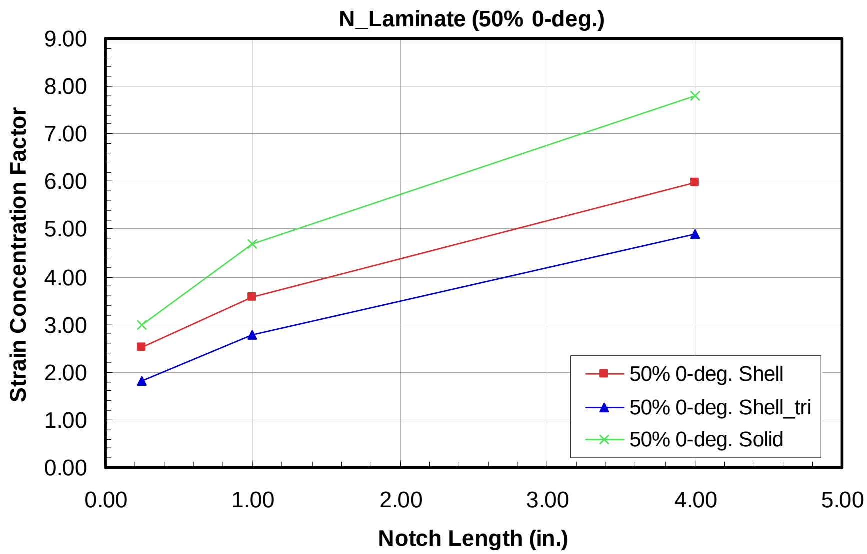

Figure 5. 15 - Strain Concentration Factors for N-laminate

The results from the two shell models follow the same pattern as the distribution obtained using the moment output because the strain is directly proportional to the moment for these two theories. However, the results from the 3D solid models are drastically different. The same can be found on the results of the 40-ply laminates.

Figure 5. 16 shows the results of the strain concentration factor in terms of the notch length for the case of the FP-laminate, which has 10% 0-degree plies.

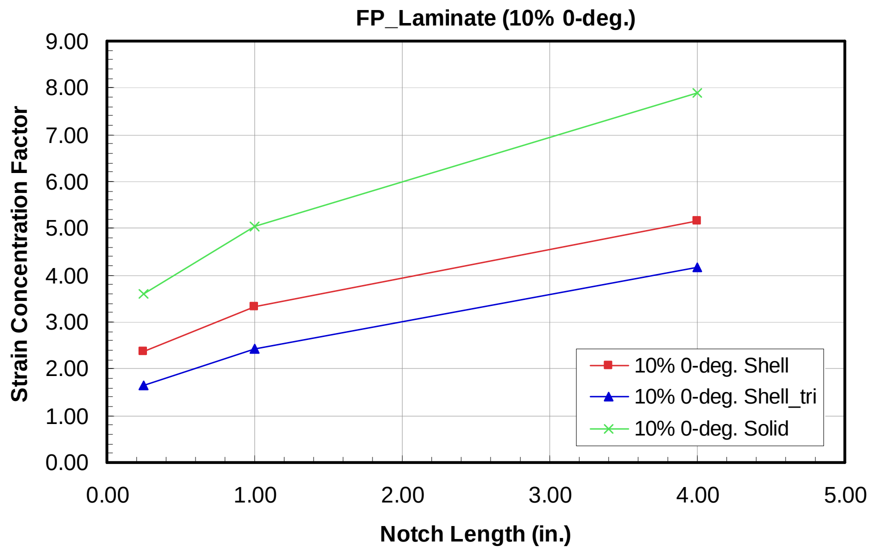

Figure 5. 16 - Strain Concentration Factors for FP-laminate

The results for the other two 40-ply laminates (AR and AN laminates) are shown in the following figures (Figure 5. 17 and 5. 18, respectively).

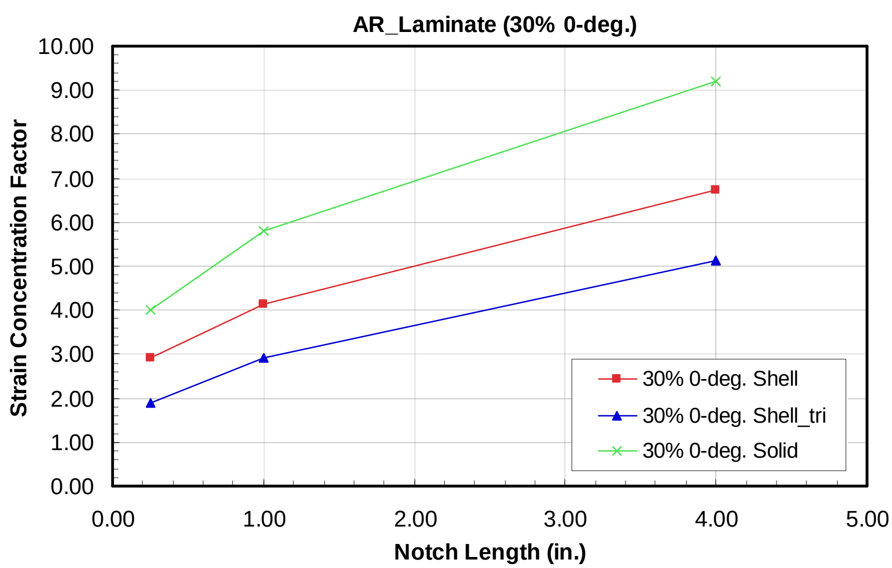

Figure 5. 17 - Strain Concentration Factors for AR-laminate

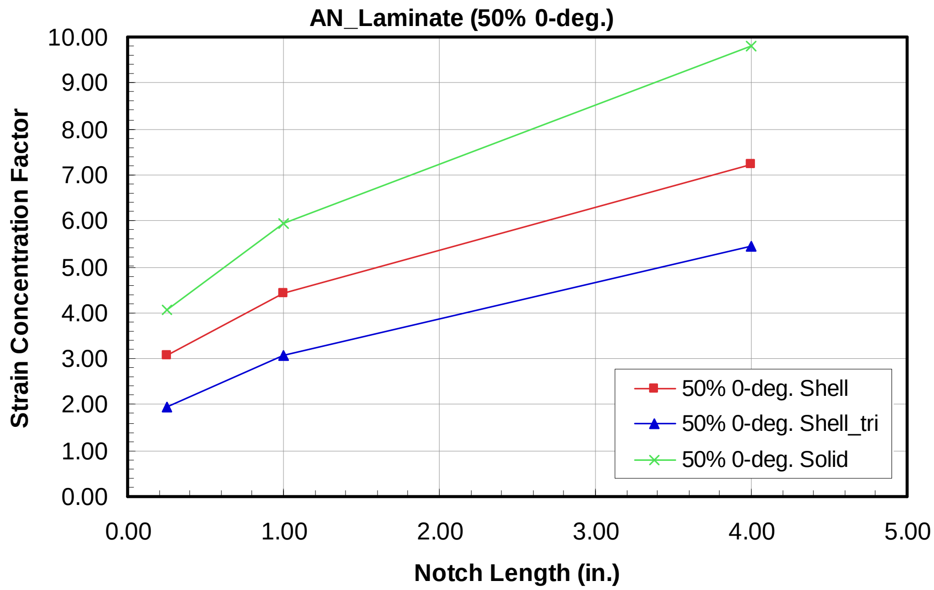

Figure 5. 18 - Strain Concentration Factors for AN-laminate

In every case, for both the 20-ply and 40-ply laminates, the 3D solid model predicts a higher strain concentration factor than the two shells models.

Table 12 shows the results, in percentage, between all the ABAQUS models in terms of the strain concentration factors. The first section of the table shows the difference between the shell models for the 0.25-in. hole, 1-in. and 4-in. cases. The other two sections show the difference between the solid model and the two shell models.

Table 12 - Difference of strain concentration factors between all ABAQUS models

	Difference Shell vs. Shell_tri			**Difference Solid vs. Shell_tri**			**Difference Solid vs. Shell**		
	hole	**1-in. notch**	**4-in. notch**	**hole**	**1-in. notch**	**4-in. notch**	**hole**	**1-in. notch**	**4-in. notch**
N	37.9%	28.9%	22.4%	64.8%	68.8%	59.3%	30.2%	30.2%	30.2%
P	33.9%	25.5%	19.9%	72.4%	69.7%	57.3%	31.2%	31.2%	31.2%
F	31.7%	24.6%	14.6%	86.3%	76.7%	55.5%	35.7%	35.7%	35.7%
AN	56.1%	44.4%	32.7%	106.6%	94.3%	79.8%	35.5%	35.5%	35.5%
AR	53.2%	41.9%	31.0%	110.5%	98.5%	78.9%	36.5%	36.5%	36.5%
FP	44.2%	36.9%	24.3%	118.2%	108.0%	89.8%	52.7%	52.7%	52.7%
average	43%	34%	24%	93%	86%	70%	37%	37%	37%

For the 0.25-in. diameter hole, the strain concentration factor predicted by the shell model with transverse shear effects is, on average, 43% higher than that predicted by the shell model without the transverse shear effects. For the 1-in. long notch, it is 34% higher and for the 4-in. long notch it is 24% higher.

The strain concentration factors predicted by the 3D solid model are, on average, 83% higher than those predicted by the shell model without transverse shear effects and 37% higher than those predicted by the shell with transverse shear effects.

Chapter 6. Modeling Progressive Damage in Notched Laminates under Bending

6.1 Introduction to Progressive Damage in Notched Laminates

In this chapter, we are going to simulate the propagation of a notch in a composite laminate under out-of-plane bending. Petit and Waddoups [38] were among the first to investigate the failure behaviors (or modes) of composite laminates by progressive failure analysis. They made used of the Classical Laminate Plate Theory (CLPT) to predict the stress generated in a plate and then used an incremental loading to account for the progressive damage for failure analysis.

Williams [46] calculated the crack tip stress and displacement fields for a crack in an infinite isotropic plate under bending using KPT. He found the usual square root singularity in stress at the crack tip, which can be expressed as

$$\sigma = \frac{k_1}{\sqrt{2r}} \frac{2z}{h} \tag{6.1}$$

Where k_1, is the stress intensity factor. A number of other studies [45-51] have been carried out to calculate stress intensity factors for orthotropic materials using Reissner Plate Theory and out-of-plane loading conditions.

In a composite material, a zone of damage of considerable influence is known to develop in advance of the notch. This is the result of a combination of different failure modes such as fiber breaking and matrix cracking. Consequently, the usual fracture mechanics procedures that have worked successfully in metal structures do not work well for composites. The simulation of damage progression in a composite is best done with theories that incorporate principles from the field of damage mechanics. Several theories [1], [6], [23] that treat damage development in the laminate as a whole rather than on a ply-by-ply basis have been successful in simulation notch growth under in-plane loading. In the case of bending, there is a non-uniform strain throughout the thickness of the laminate. A theory that treats damage progression at the ply level will be needed for this case.

6.2 Hashin Constitutive Model for Damage Progression

As mentioned earlier in Chapter 2, our constitutive model in ABAQUS follows the Hashin criterion. The constitutive model considers four different modes of failure: (1) fiber rupture in tension, (2) fiber buckling and kinking in compression, (3) matrix cracking under transverse tension and shearing, and (4) matrix crushing under transverse compression and shearing. According to Hashin theory, when damage occurs, the effective load carrying area of the material is considered to be reduced, and the concept of an effective stress is introduced to account for the area reduction. The propagation of damage depends on which of the four modes of failure, described earlier in Chapter 2, is activated.

6.3 Modeling Progressive Damage in ABAQUS

For our progressive damage analysis, we used the built-in model in ABAQUS for composite materials, which is based on the work of Matzenmiller et al. (1995,) Hashin and Rotem (1973,) Hashin (1980,) and Camanho and Davila (2002.) Then, damage simulation was modeled using the progressive damage model for composites described by Hashin theory. In this model, damage is accounted for in each individual ply, but there is assumed to be perfect bonding at the ply interfaces. That is, delamination is assumed negligible.

All Finite element models of the laminates were constructed using the conventional shell element type S4, as seen in Figure 6. 1 for the case of a 5-in. 20-ply laminate with 1-in notch.

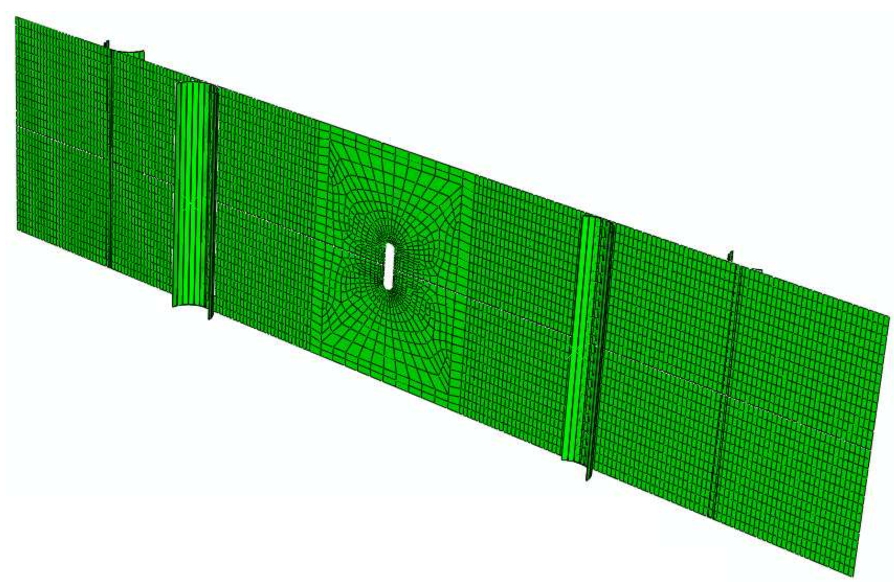

Figure 6. 1 - Damage finite element model for the 1-in. notch case (full view)

In the damage progression models, we simulated the bars of the fixture to mimic our tests on the laboratory and to provide us with a more accurate response of the loading mechanism. We employed surface elements to generate these bars on ABAQUS. Also, contact surfaces with master and slave nodes were added to these regions and to the contact zones in the shell model, to ensure seamless connectivity between them. We set up a two-step loading condition to make sure this connectivity was secured.

Since it is well known that a damage zone is developed ahead of the crack when it propagates in a composite material, we must pay attention to the strain softening effect of the material. Figure 6. 2 shows the typical stress-strain curve for a linear softening laminate; that is, a material that we assume softens linearly after it goes over the peak loading.

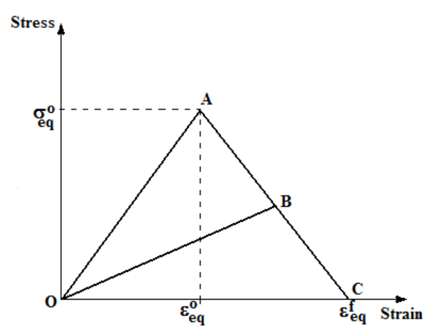

Figure 6. 2 - Strain-softening diagram for a linear softening composite

The incorporation of strain softening into a finite element analysis usually results in calculations that are mesh sensitive. This occurs because as the mesh is refined, there is a tendency for the damage zone to localize to a zero volume. The energy dissipated is then proportional to that volume, rather than to the area of the damaged zone. Consequently, this leads to zero energy dissipation, which is physically impossible. Several techniques have been proposed to address this issue. One of the simplest, which was pioneered by Hillerborg, is the use of a stress displacement law rather than a stress-strain law in the damaged material.

The ABAQUS program accomplishes this by introducing a characteristic length, L^c, based on the element size. Figure 6. 3 shows the calculation of this parameter, where A_{ip} is the total surface area of the element, and L_1 is the distance between nodes.

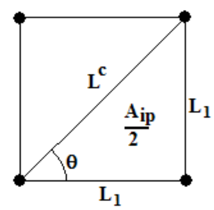

Figure 6. 3 - ABAQUS characteristic length, L_c

$$L^c = \sec(\theta)\sqrt{A_{ip}} \tag{6.2}$$

The strain can be expressed as the ratio of the deformation over the original dimension ($\varepsilon = \delta / L$). If we look at the area under the stress-displacement diagram, which is the fracture energy, called G_c, we realize that the area under the distribution can be expressed as:

$$Energy = G_c = \frac{1}{2}\ \delta \sigma_0 \tag{6.3}$$

By combining this formula with the general expression of strain, we attain that the equivalent strain is in terms of the characteristic length.

$$\varepsilon_{eq}^{f} = \frac{2\,G_c}{\sigma_0\, L^c} \tag{6.4}$$

For a given failure mode, the stress-displacement law takes on the form similar to Figure 6. 2. The part of the curve with a positive slope (OA) follows the usual linear elastic relationship, and if we use displacements instead of strains it can be expressed as:

$$\sigma_{eq} = \frac{\delta_{eq}}{\delta_{eq}^{0}}\sigma_{eq}^{0} \tag{6.5}$$

The point at (A) represents the initiation of damage. Displacement beyond this point results in a decreasing stress. This part of the curve can be represented by:

$$\sigma_{eq} = \frac{\left(\delta_{eq}^{f} - \delta_{eq}\right)}{\left(\delta_{eq}^{f} - \delta_{eq}^{0}\right)}\sigma_{eq}^{0} \tag{6.6}$$

After experiencing damage, the material unloads and reloads along line OB, which has a smaller slope than the original line OA. This reduced new slope is accounted for using the damage variable d, as follows:

$$slope_{OB} = \frac{\sigma_{eq}^{0}}{\delta_{eq}^{0}}(1-d) \tag{6.7}$$

Combining the last three equations with equation 2.52 gives the damage variable as:

$$d = \frac{\left(\delta_{eq} - \delta_{eq}^{0}\right)\delta_{eq}^{f}}{\left(\delta_{eq}^{f} - \delta_{eq}^{0}\right)\delta_{eq}} \tag{6.8}$$

From this, equivalent displacements and equivalent stresses according to

Hashin criterion are defined for the four modes of failure as follows:

Fiber tension $(\hat{\sigma}_{11} \geq 0)$:

$$\delta_{eq}^{ft} = L^c \sqrt{\varepsilon_{11}^2 + \alpha\,\varepsilon_{12}^2} \tag{6.9}$$

$$\sigma_{eq}^{ft} = L^c \frac{\langle \sigma_{11} \rangle \langle \varepsilon_{11} \rangle + \alpha\,\tau_{12}\varepsilon_{12}}{\delta_{eq}^{ft}} \tag{6.10}$$

Fiber compression $(\hat{\sigma}_{11} < 0)$:

$$\delta_{eq}^{fc} = L^c \langle -\varepsilon_{11} \rangle \tag{6.11}$$

$$\sigma_{eq}^{fc} = \langle -\sigma_{11} \rangle \tag{6.12}$$

Matrix tension $(\hat{\sigma}_{22} \geq 0)$:

$$\delta_{eq}^{mt} = L^c \sqrt{\varepsilon_{22}^2 + \varepsilon_{12}^2} \tag{6.13}$$

$$\sigma_{eq}^{mt} = L^c \frac{\langle \sigma_{22} \rangle \langle \varepsilon_{22} \rangle + \tau_{12}\varepsilon_{12}}{\delta_{eq}^{mt}} \tag{6.14}$$

Matrix compression $(\hat{\sigma}_{22} < 0)$:

$$\delta_{eq}^{mc} = L^c \sqrt{\varepsilon_{22}^2 + \varepsilon_{12}^2} \tag{6.15}$$

$$\sigma_{eq}^{mc} = L^c \frac{\langle -\sigma_{22} \rangle \langle \varepsilon_{22} \rangle + \tau_{12}\varepsilon_{12}}{\delta_{eq}^{mc}} \tag{6.16}$$

When running a progression damage analysis in ABAQUS, the following parameters must be specified at the material property section: Damage Evolution and Damage Stabilization parameters. On the damage evolution section, we are asked to put in the strength properties of the material, the dissipation and fracture energies (the area under the OAC curve of the stress-displacement diagram,) for each failure mode. These parameters are purely empirical and were produced at the Boeing testing facilities.

6.4 Test Results and Damage Analysis

As mentioned earlier, both testing and ABAQUS analysis were performed on all the notched laminates. The following figure, Figure 6. 4, shows a simulation of the deformation of one of these laminates when subjected to this loading condition. We found that during tests, the laminates experienced large deflections before failure occurs. This event is illustrated in Figure 6. 5b, which shows all the reaction forces between the laminate and the bars in a large deformation setting.

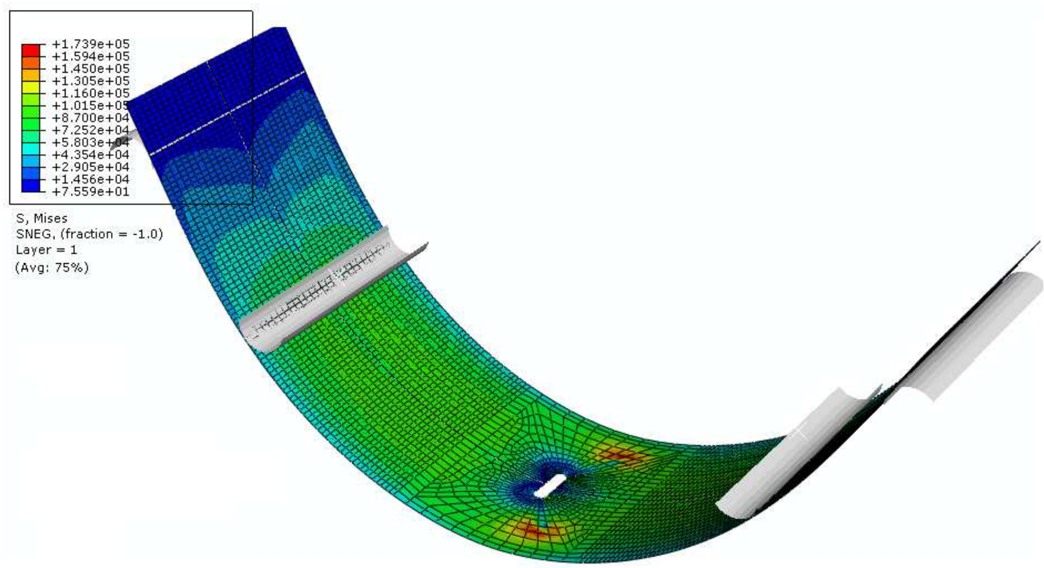

Figure 6. 4 - ABAQUS simulation of four-point bending

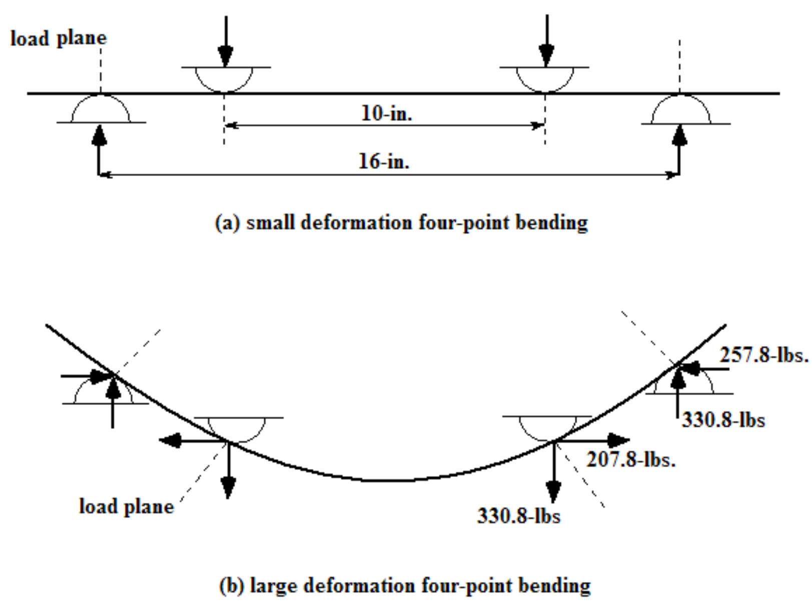

Figure 6. 5 - (a) small deformation on a four-point bending test.
(b) large deformation for a four-point bending test

The initial external loads, created by INSTRON either on the tension or compression set-up, are normal to the surface of the laminate (as depicted on Figure 6. 5a.) However, as the laminate rotates during deflection due to large deflections, a significant horizontal component of force develops in addition to the vertical. Note that the horizontal forces are, in general, not equal, which produces a small axial load effect that is superposed on the bending moment at the center. Since the load cell in the testing machine records only the vertical component of the load, the load data from INSTRON cannot be used to determine the bending moment at the center.

Therefore, it was necessary to determine the bending moment using the strain gage output coupled with the analysis results. A comparison of far field strains on the compression and tension sides of the specimen from the test and from the theoretical model for the 5-in. wide 40-ply laminates with 50% 0-degree plies containing 1-in. notch (laminate AN_1_5_2) is shown in Figure 6. 6.

A similar comparison of strains at the notch tip and at a point 1-in. away from the notch tip for this same laminate is shown in the next figure, Figure 6. 7.

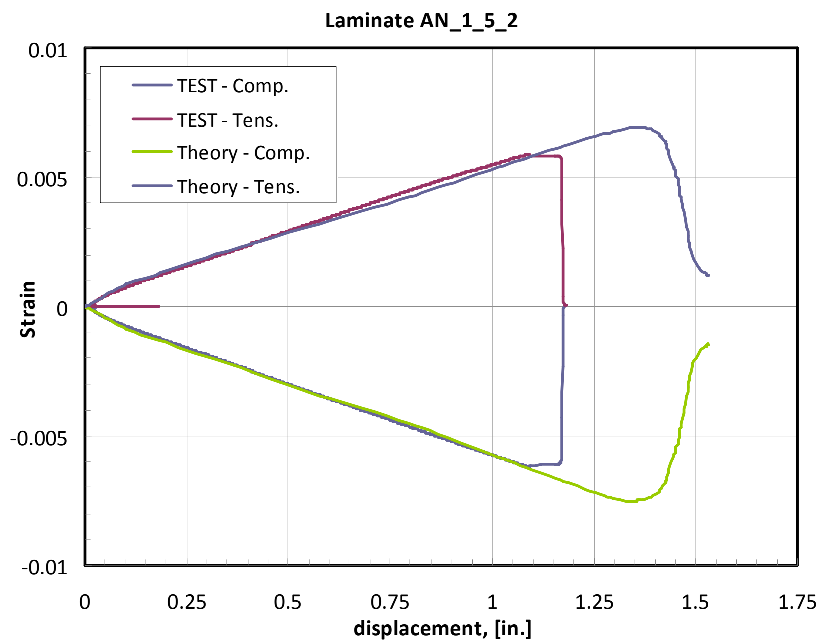

Figure 6. 6 - Comparison of far-field strains between ABAQUS and test data for Laminate AN_1_5_2

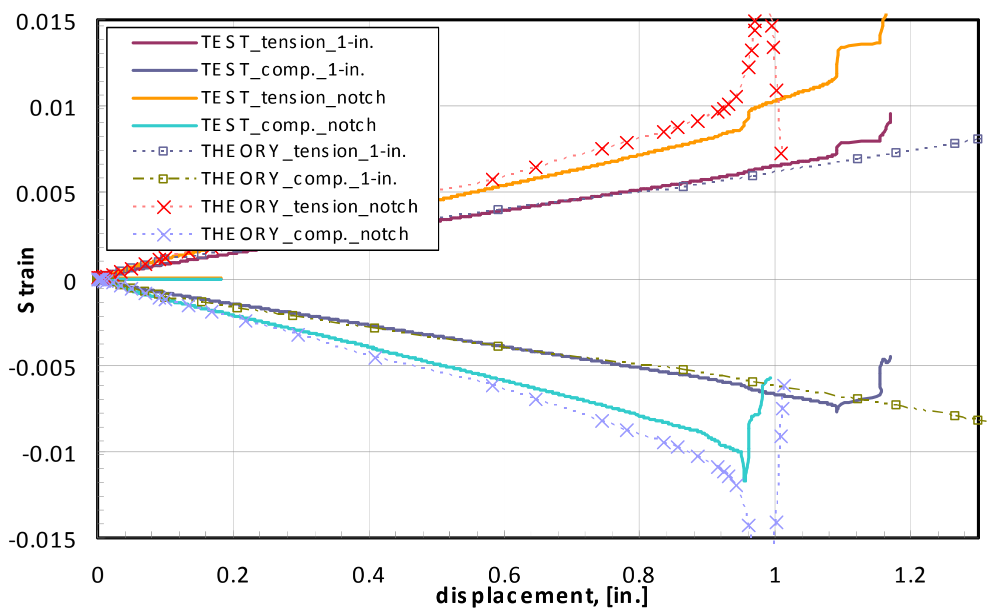

Figure 6. 7 - Comparison of strains at notch tip and 1-in. away for Laminate AN_1_5_2

The agreement between the test results and theoretical predictions is fairly good with the exception that the theory predicts a significantly higher failure strain for this case. It was found that this was true for each case, i.e. the agreement between measured strain and predicted strain was good as the load increased (the only disagreement was the load point for maximum strain.)

Thus, we can have some confidence that our ABAQUS models represent the response of the laminates for points below the ultimate load. We used these analysis results to determine the test failure moment. First, we assumed that the ultimate moment is reached when the measure of far-field strain peaked. We then checked the response state of the model at this strain. For this state, an average bending moment per unit length along a line extending out from the notch to the side was calculated, as indicated in Figure 6. 8.

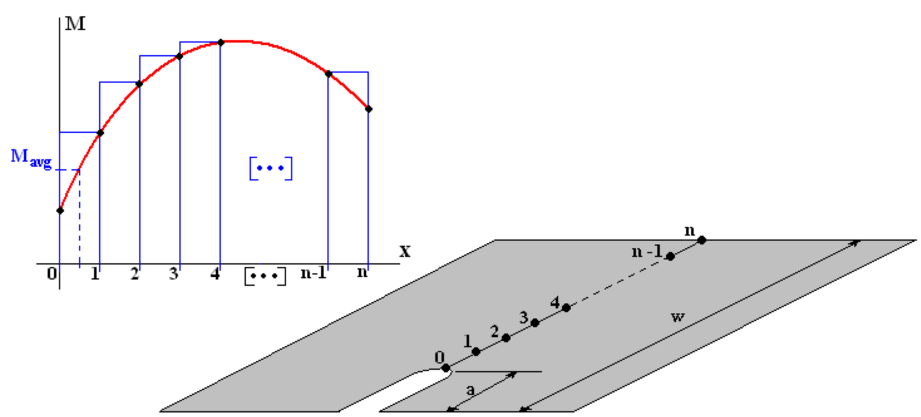

Figure 6. 8 - Calculation of the average bending moment along a line in a plate

We obtained the maximum moment achieved on the plate by computing the average moment, using the following formula:

$$M^{ABAQUS}{}_{avg} = \frac{1}{w-a}\int_a^w M_y \, d_y \tag{6.17}$$

where M_{avg} is the bending moment per unit length, a is the notch half-length, and w is the specimen half-width. This load was taken as the test failure load.

6.4.1 Effects of Large Deformations under Pure Bending

A consequence of large deflections involves anticlastic curvature effects [43]. During pure bending of a long, flat plate with a constant uniform thickness, a radius of curvature R_x is formed in the principal bending direction as shown in Figure 6. 9.

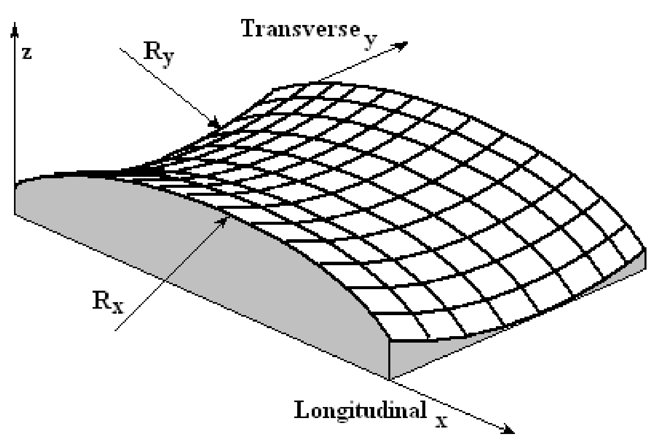

Figure 6. 9 - Poisson's effect - anticlastic curvature

But the Poisson's effect causes curvature of the plate in the transverse direction with radius R_y. This is because in pure bending the only present stress is σ_x (all the other stresses are zero,) but there are strains other than ε_x present, and they are:

$$\varepsilon_x = \frac{1}{E}\left[\sigma_x - \nu\left(\sigma_y + \sigma_z\right)\right] = \frac{\sigma_x}{E} \tag{6.18}$$

$$\varepsilon_y = \frac{1}{E}\left[\sigma_y - \nu\left(\sigma_x + \sigma_z\right)\right] = -\nu\frac{\sigma_x}{E} \tag{6.19}$$

$$\varepsilon_z = \frac{1}{E}\left[\sigma_z - \nu\left(\sigma_x + \sigma_y\right)\right] = -\nu\frac{\sigma_x}{E} \tag{6.20}$$

Plate theory tells us that the curvature of a plate is $\partial w/\partial x = -u/z$, where u, v, and w are the displacements of a point in the plate in the x, y, and z directions, respectively (see Figure 6. 9). Also, we know that the x-direction normal strain ε_x is equal to $\partial u/\partial x$, hence, we obtain the following expression:

$$\varepsilon_x = -z\frac{\partial^2 w}{\partial x^2} = -z\,\kappa_x \tag{6.21}$$

Thus, we obtain a curvature along the principal bending direction of $\kappa_x = -\varepsilon_x/z$. But this is accompanied by a lateral contraction due to the Poisson's effect, causing a curvature transverse to the main beam axis, which is calculated using the previous equations.

$$\varepsilon_y = -z\frac{\partial^2 w}{\partial y^2} = -z\,\kappa_y = -\nu\varepsilon_x \tag{6.22}$$

This transverse curvature is $\kappa_y = -\nu\kappa_x$, which is known as the anticlastic curvature, and has an opposite sign and is orthogonal to κ_x. This transverse curvature tends to move the fibers near the edge of the plate away from the principal axis of curvature causing them to go into tension. It also tends to move the fibers at the center of the plate closer to the principal axis of curvature causing them to go into compression. The combination of these two effects tends to flatten the plate in the transverse direction, causing it to bend into the shape of a cylinder. This in turn causes a transverse bending moment to develop, except at the edges where the transverse moment must be zero. The severity of this effect is a function of the Searle Parameter, described as:

$$SearleParameter = \frac{b^2}{R_x t} \tag{6.23}$$

where b is the plate width and t is the plate thickness. This effect is amplified in our tests by the loads being applied by relatively rigid bars in the test fixture. A finite element Analysis was performed on a plate without a notch. Figure 6. 10 shows a contour plot of the bending moment per unit length along the longitudinal (principal bending) direction.

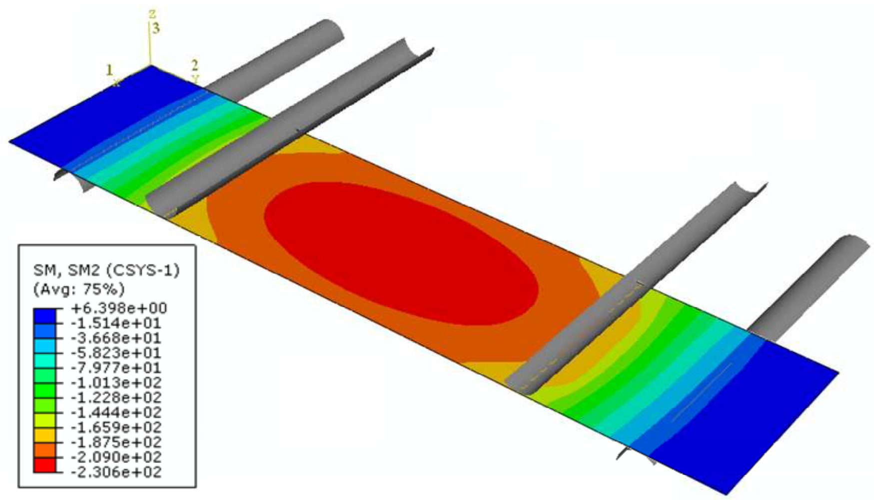

Figure 6. 10 – Contour plot of the principal bending moment of a plate

We observe in this picture that the moment is not quite uniform in the center portion of the plate, inside the two interior bars. Figure 6. 11 shows a contour plot of the bending moment per unit length along the transverse direction.

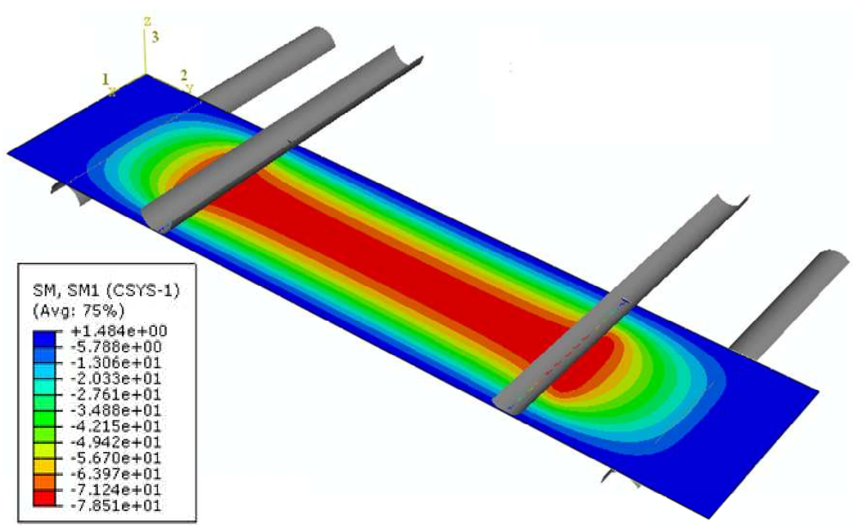

Figure 6. 11 - Contour plot of the transverse bending moment of a plate

As it is clearly shown in this picture, the transverse moment is also non-uniformly distributed in the center of the interior bars. We found that the maximum value of this transverse moment is about one third that of the longitudinal moment. Thus, we can conclude that in our tests damage will be propagated in advance of the notch tip in a non-uniform biaxial bending field. The degree of this biaxial state will be a function of plate thickness.

6.4.2 ABAQUS Results with Damage Propagation Application

In our tests, we found that the transverse strains were negligible for all of the 20-ply thick laminates (on average less than 1% of the longitudinal strains.) These strains were measured by reading the output data from the strain gages X1 (see gage mapping in Chapter 2.) The same was true for the 40-ply thick laminates with a 4-in. notch. However, for the 40-ply laminates with 1-in. notch and 5-in. specimen width, the transverse strains were on average 13% of the longitudinal strains (as seen in Figure 6. 12.)

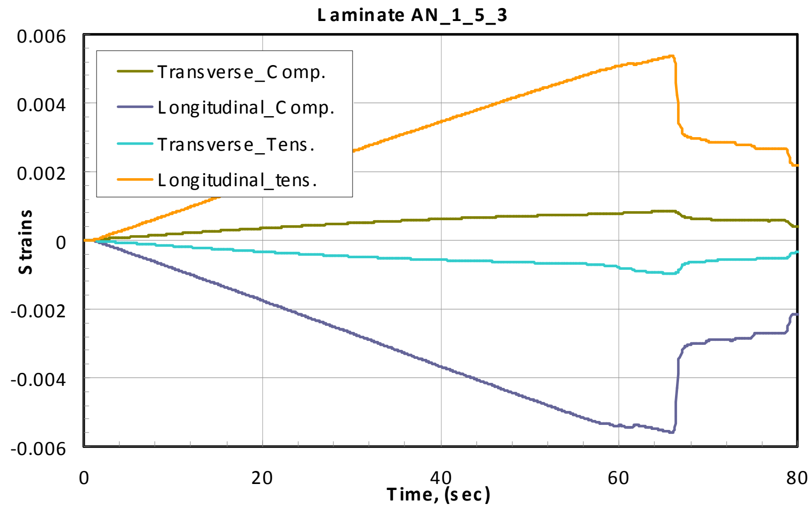

Figure 6. 12 - Far-Field gage comparison of a typical 5-in. wide 40-ply laminate

When the specimen width was increased to 10-in. for this case, the transverse strain dropped to about 2% of the longitudinal strain. Thus, except for the 40-ply thick laminates with 1-in. notches and 5-in. specimen width, the specimens experienced bending to a cylindrical surface.

Tables 13, 14, and 15 give a list of test results for the 20-ply thick laminates. Tables 16, 17, and 18 give a list of test results for the 40-ply thick laminates. The spacing between the inner and outer pairs of bars in the test fixture is indicated in column 5 of the tables. The bending moment per unit length for failure, determined by the theoretical model and test, are given in columns 6 and 7, respectively. The difference between these moments is given in column 8. Note that the predicted bending moment per unit length is influenced by the bar spacing. A probable explanation for this difference in test moments is due to the change in axial loads exerted on the plate, as it is deformed, due to the change in bar spacing (see Figure 6. 5.)

Table 13 - Failure Moments of the 5-in. wide 20-ply Laminates

Specimen Label	% of 0-degree plies	No. of Plies	Notch Length (in.)	Bar Spacings	Theory Moment (lb.)	Test Moment (lb.)	Difference
F-1-5-1	10	20	1	8-in & 13-in	256.2	273	6.2%
F-1-5-2	10	20	1	10-in & 16-in	224.7	224.9	0.1%
P-1-5-1	30	20	1	6-in & 16-in	176.9	169.7	4.2%
P-1-5-2	30	20	1	10-in & 16-in	249.3	236.7	5.3%
P-1-5-3	30	20	1	10-in & 16-in	249.3	255.6	2.5%
N-1-5-1	50	20	1	10-in & 16-in	348.5	401.9	13.3%
N-1-5-2	50	20	1	10-in & 16-in	348.5	377.6	7.7%
N-1-5-3	50	20	1	6-in & 16-in	347.9	357.6	2.7%

Comparing the test results with the ABAQUS model predictions, we observe good agreement for all of the 5-in. wide 20-ply thick laminates (except for laminate N_1_5_1.) Table 14 shows the results for the 10-in. wide 20-ply laminates.

Table 14 - Failure Moments of the 10-in. wide 20-ply Laminates

Specimen Label	% of 0-degree plies	No. of Plies	Notch Length (in.)	Bar Spacings	Theory Moment (lb.)	Test Moment (lb.)	Difference
F-1-10-1	10	20	1	8-in & 13-in	229.3	217.9	5.2%
F-1-10-2	10	20	1	8-in & 13-in	229.3	197	16.4%
P-1-10-1	30	20	1	10-in & 16-in	227.5	213.4	6.6%
P-1-10-2	30	20	1	10-in & 16-in	227.5	218.9	3.9%
N-1-10-1	50	20	1	10-in & 16-in	337	360.8	6.6%
N-1-10-2	50	20	1	10-in & 16-in	337	353.6	4.7%

We still observe a good agreement between the failure test moments and the theoretical moments (around 5%, except for the case of laminate F_1_10_2.) Table 15 shows the failure moments for the 20-in. wide laminates.

Table 15 - Failure Moments of the 20-in. wide 20-ply Laminates

Specimen Label	% of 0-degree plies	No. of Plies	Notch Length (in.)	Bar Spacings	Theory Moment (lb.)	Test Moment (lb.)	Difference
F-4-20-1	10	20	4	8-in & 13-in	233.9	212.3	10.2%
F-4-20-2	10	20	4	10-in & 14.5-in	190	198.2	4.1%
F4-20-3	10	20	4	8-in & 13-in	233.9	200	17.0%
P-4-20-1	30	20	4	10-in & 16-in	196.7	177.5	10.8%
P-4-20-2	30	20	4	10-in & 16-in	196.7	177.5	10.8%
P-4-20-3	30	20	4	10-in & 18-in	220.2	228.4	3.6%
N-4-20-1	50	20	4	10-in & 16-in	266.8	251.5	6.1%
N-4-20-2	50	20	4	10-in & 16-in	266.8	255.1	4.6%
N-4-20-3	50	20	4	10-in & 18-in	268.1	252	6.4%

We found good agreement between failure moment results, especially for the N-laminates. Laminates F and P show good to fair agreements of 4% to 10%. The next set of tables show the results for the 40-ply laminates; and, in most cases, we found either fair to poor agreements between the failure moment results. Table 16 shows the results for the 5-in. wide cases.

Table 16 - Failure Moments of the 5-in. wide 40-ply Laminates

Specimen Label	% of 0-degree plies	No. of Plies	Notch Length (in.)	Bar Spacings	Theory Moment (lb.)	Test Moment (lb.)	Difference
FP-1-5-1	10	40	1	10-in & 18-in	936.3	1151.5	18.7%
FP-1-5-2	10	40	1	10-in & 18-in	936.3	1078.9	13.2%
FP-1-5-3	10	40	1	6-in & 16-in	934	1133.1	17.6%
AR-1-5-1	30	40	1	10-in & 18-in	1125.4	1342.2	16.2%
AR-1-5-2	30	40	1	10-in & 18-in	1125.4	1313.7	14.3%
AR-1-5-3	30	40	1	6-in & 16-in	1119.2	1396.5	19.9%
AN-1-5-1	50	40	1	10-in & 18-in	1520.4	1939.3	21.6%
AN-1-5-2	50	40	1	10-in & 18-in	1520.4	1817.2	16.3%
AN-1-5-3	50	40	1	6-in & 16-in	1459.3	1850.1	21.1%

We observe poor agreement between theoretical and test moments at around 15% to 20% difference. The difference decreases with increasing width of the plates, as seen in Table 17, which shows the moment results for the 10-in. laminates.

Table 17 - Failure Moments of the 10-in. wide 40-ply Laminates

Specimen Label	% of 0-degree plies	No. of Plies	Notch Length (in.)	Bar Spacings	Theory Moment (lb.)	Test Moment (lb.)	Difference
FP-1-10-1	10	40	1	10-in & 18-in	862.5	961.2	10.3%
FP-1-10-2	10	40	1	10-in & 18-in	862.5	1007.8	14.4%
AR-1-10-1	30	40	1	10-in & 18-in	1053	1308.9	19.6%
AR-1-10-2	30	40	1	10-in & 18-in	1053	1269.9	17.1%
AN-1-10-1	50	40	1	10-in & 18-in	1313	1529.1	14.1%
AN-1-10-2	50	40	1	10-in & 18-in	1313	1501.2	12.5%

Now the moment difference is between 10% to 19%, for most laminates types. Table 18, which shows the moment results for the 20-in. wide tests, gives us better agreement with the test results.

Table 18 - Failure Moments of the 20-in. wide 40-ply Laminates

Specimen Label	% of 0-degree plies	No. of Plies	Notch Length (in.)	Bar Spacings	Theory Moment (lb.)	Test Moment (lb.)	Difference
FP-4-20-1	10	40	4	10-in & 18-in	715.1	612.5	16.8%
FP-4-20-2	10	40	4	10-in & 18-in	715.1	688.6	3.8%
FP-4-20-3	10	40	4	10-in & 18-in	715.1	634.1	12.8%
AR-4-20-1	30	40	4	10-in & 18-in	929.3	1144.5	18.8%
AR-4-20-2	30	40	4	10-in & 18-in	929.3	1111.8	16.4%
AR-4-20-3	30	40	4	10-in & 18-in	929.3	1090.3	14.8%
AN-4-20-1	50	40	4	10-in & 18-in	1120.5	1068.3	4.9%
AN-4-20-2	50	40	4	10-in & 18-in	1120.5	1119.8	0.1%
AN-4-20-3	50	40	4	10-in & 18-in	1120.5	1133.7	1.2%

The difference between the theoretical moment and test moment is, on average, 16% for the AR-laminates and 12% for the FP-laminates. AN-laminates gave us very good agreement in the results, with around 2% difference.

6.5 Comments of Video and Photo Test Results

The observations taken from the video and photo documentation for each laminate are explained in this section. In summary, during the test of the 20-ply thick laminates we observed that they exhibited negligible visible damage before failure, which, in most cases, was sudden and usually resulted in the laminate being broken into two pieces. The 40-ply thick laminates exhibited a gradual progression of damage which usually began with wrinkling of the outer ply on the compression side. This was followed by de-lamination at the outermost 0-degree ply and the surface. The tension side of the laminate exhibited considerably less visible damage for most test cases. Tables 19 and 20 provide a summary of the observations taken from the photos and videos collected at the laboratory. Appendices B and C present a collection of the photos of all the laminates tested showing the side view, revealing the visible damage throughout the layers.

6.5.1 Observations for Laminates F, P, and N

All the F-laminates did not break off completely during testing (see Figures B. 1 through B. 8.) Photographs show that there is delamination next to two 0-degree layers for the 5-in. wide tests. We also found that there is some partial delamination of the top layers on both tension and compression side near the crack edges. The video for the 5-in. wide F-laminates shows a slow crack propagating to a distance of about 0.5-in. to 1-in. before reaching collapse. The tests for the 10-in. F-laminates varied slightly from the 5-in. wide specimens. In these tests, the crack did not propagate all the way throughout the thickness of the laminate (see Figures B. 4 and B. 5.) We obtained failure when the crack propagated only through the compression side. We also found that the 0-degree layers on the tension side did not delaminate like they did for the slender specimens. Also, here the video shows collapse without total detachment. Similarly, the 20-in. wide F-laminates did no break off during testing, and showed very little indication of failure or crack propagation before collapse. And in some cases, we had difficulty reaching failure loading conditions, as shown in Figure B. 6. Delamination of the 0-degree layers were similar to those found on the 10-in. wide specimens.

Unlike the F-laminates, all the P-laminates (see Figures B. 9 through B. 16) were broken off completely during tests. Post-breakage photos for the 5-in. wide tests show that there is delamination of the top layers in both tension and compression sides. We also noticed the 0-degree layers of both tension and compression sides to have been delaminated. The videos also show no to very little (~2-in.) crack propagation, and it shows the laminate snapping off completely when reaching failure. The test for the 10-in. wide P-laminates were different. Videos show that it took several tries to reach failure, and in the case of P_1_10_1, the laminate failed during unloading. No visible crack propagation was observed before failure. Unlike the first two P-laminate types, the 20-in. wide laminate did not break off completely after reaching failure. Videos show that the laminate exhibited crack formation thoroughly to the sides before absolute collapse. Also, the crack did not propagate throughout the thickness; it only reached the outermost layers on both tension and compression sides, as can be seen in Figures B. 14, B. 15, and B. 16. Furthermore, unlike the 5-in. and 10-in. wide specimens, we only found 0-degree layer delamination on the compression side only.

All the N-laminates broke off completely during testing (see Figures B. 17 through B. 24.) Consequently, the crack reached all layers throughout the thickness. We noticed that all specimen types for the N-laminate (5-in., 10-in., and 20-in. wide specimens) behaved in a very similar manner. In all cases, we found 0-degree layer delamination in the outermost layers of both tension and compression sides, and severe delamination of the top layers on the compression side (this can be observed at Figures B. 21 and B. 22.) In some cases, videos indicate some partial damage propagation before breaking off. Table 19 provides a summary of the observations taken from the laminates F, P, and N. The fifth column from the left describes the distance the crack travels from the tip of the notch before the laminate reaches failure. In column six, we indicate whether the surface layers of the tension and compression sides were delaminated. Also, described in the last column, we point up how far the crack propagated throughout the thickness of the laminate before it failed.

Table 19 - Test observations for the 20-ply thick laminates

Laminates	**Complete Break off**	**0-degree delamination (Tens.)**	**0-degree delamination (Comp.)**	**Crack Distance before Failure**	**Top Layer Delamination**	**Crack propagation on thickness**
F_5-in. wide	No	Yes	Yes	~ 1-in.	No	Yes
F_10-in. wide	No	No	Yes	~ 1-in.	C	C
F_20-in. wide	No	No	Yes	< 0.5-in.	No	C
P_5-in. wide	Yes	Yes	Yes	~ 2-in.	T , C	Yes
P_10-in. wide	Yes	Yes	Yes	No	T , C	Yes
P_20-in. wide	No	No	Yes	Total	T , C	Outermost layers
N_5-in. wide	Yes	Yes	Outermost layers	~ 0.5-in.	T , C	Yes
N_10-in. wide	Yes	Yes	Outermost layers	> 2-in.	C	Yes
N_20-in. wide	Yes	Yes	Outermost layers	> 2-in.	C	Yes

Note: T and C denote "tension side" and "compression side", respectively.

6.5.2 Observations for Laminate FP, AR, and AN

All the 40-ply laminates did not break off completely during testing (see Figures C. 1 through C. 8.) Photographs show that there is no delamination on the 0-degree layer of the tension side for the 5-in. wide tests (see Figure C. 3.) In fact, all specimen types for the FP-laminate (5-in., 10-in., and 20-in. wide specimens) behaved in a very similar manner. The videos for the 5-in. wide F-laminates show a slow crack propagating all the way across the width of the plate before reaching collapse. In general, we observed that only the outermost layers were damaged by the crack propagation (this can be seen in Figure C. 2.) The tests for the 10-in. FP-laminates varied slightly from the 5-in. wide specimens. In these tests, the crack only propagated throughout the compression layers (see Figures C. 4 and C. 5). Also, the videos show a crack propagating through the width before failure. Similarly, the 20-in. wide F-laminates showed total crack propagation before collapse.

The AR-laminates did not break off completely during testing (see Figures C. 9 through C. 16,) and crack reached only the compression side. We noticed that the 5-in., 10-in., and 20-in. wide AR-laminates behaved in a very similar manner. In all cases, we found 0-degree layer delamination in the compression side, and none in the tension sides (this can be observed at Figure C. 9.) Videos indicate some partial damage propagation in proportion to the specimen width before breaking off. We also noticed some top layer delamination on the compression side for the 20-in. wide specimens, as seen in Figure C. 16.

Similar to the AR-laminates, the AN-laminates did not break off completely during testing (see Figures C. 17 through C. 24,) and the cracks propagated only to the compression side. In some cases, damage was limited to the outermost layers of the tension side as well (although, it is unclear whether this is due to overloading of the specimen after it has failed.) We noticed that the 5-in., 10-in., and 20-in. wide AN-laminates behaved also in a very similar manner. In all cases, we found 0-degree layer delamination in the compression side and none in the tension sides (this can be observed in Figure C. 21,) although for the 5-in. wide specimens, we observed some damage on the tension side (see Figure C. 18.)

Videos for the AN-laminates indicate some partial damage propagation in proportion to the specimen width before breaking off, but for the 20-in. wide tests we could not observe any crack propagation from their test videos. We also noticed top layer delamination on the compression side for all the AN-type specimens. Table 20 lists the observations taken from the laminates FP, AR, and AN.

Table 7 - Test observations for the 40-ply thick laminates

Laminates	**Complete Break off**	**0-degree delamination (Tens.)**	**0-degree delamination (Comp.)**	**Crack Distance before Failure**	**Top Layer Delamination**	**Crack propagation on thickness**
FP_5-in. wide	No	No	Yes	Total	C	Outermost only
FP_10-in. wide	No	No	Yes	Total	C	C
FP_20-in. wide	No	No	Yes	Total	C	C
AR_5-in. wide	No	No	Yes	~ 1-in.	No	C
AR_10-in. wide	No	No	Yes	~ 2-in.	No	C
AR_20-in. wide	No	No	Yes	> 5-in.	C	C
AN_5-in. wide	No	No	Yes	~ 2-in.	C	C
AN_10-in. wide	No	No	Yes	> 5-in.	C	C
AN_20-in. wide	No	No	Yes	-	C	C

Note: T and C denote "tension side" and "compression side", respectively.

Chapter 7. Summary and Conclusions

7.1 Testing and Simulation Summary

As expected, we obtained different test and simulation results between the 20-ply and 40-ply laminates. During testing, the thin laminates exhibited extremely large deformations and showed no signs of visible damage before failure (this was more evident with the wider specimens.) Nonetheless, internal damage was certainly being developed as it could be observed by the sound of cracking. On the other hand, the thicker 40-ply laminates produced considerably less deformation before failure and revealed visual damage as they were deformed. Of the 20-ply laminates, only the 50% 0-degree ply specimens broke in half completely after reaching failure (although the 5-in. wide P-laminates, which consist of 30% 0-degree laminae, also snapped off into two pieces.) None of the thicker laminates completely broke apart. Delamination of the outermost 0-degree plies at the compression side occurred for all specimens, and in most cases for the thin laminates, delamination of the 0-degree plies occurred at the tension side as well. No delamination of 0-degree plies at the tension side occurred for any of the 40-ply laminates. Overall, as expected, we noticed an increase of strength as we increase the 0-degree plies in the laminates.

It was found that the laminates experienced large deformations before failure occurred. This was particularly true for the thin 20-ply laminates with some deflections in excess of 5-in. Since the laminates produced these remarkable deflections, we no longer had only vertical reactions that generate a bending moment (which were the only reactions we were capable of recording.) Instead, the large deformation effects created horizontal reactions, which contributed significantly to the bending moment. Hence, we were faced with the added difficulty of finding the test failure moment. To solve this problem, we determined the maximum bending moment using the far-field gage output coupled with the ABAQUS analysis results.

Regarding the calculation of strain concentrations using ABAQUS, we found that the strain in the 0-degree plies was affected significantly by the free edge effect right at the notch with the 3D solid models. This effect was not present in the shell models. We decided to use the maximum strain output of the outermost 0-degree layer to calculate the concentration factors because this value is frequently used in aircraft design. In Table 12, we can observe the difference in results generated by the three ABAQUS models. We noticed that in all cases, the models followed a similar distribution based on notch size. Also, in every case, the 3D solid model predicts a higher strain concentration factor than the other two shell models. We came to the conclusion that the classical model, which does not take into account transverse shear effects, under-predicts the concentration factors of a composite laminate under pure bending.

For modeling the propagation of damage in our simulations, we decided to make use of the shell models. We used a damage module already included in

ABAQUS to incorporate the damage progression into our models. We compared the output data of the far-field gages from our experiments with the strain data obtained from these analytical models. As it is shown on the graphs of Appendix A, in general, we found good agreement between our experimental and analytical results for strain before failure. For the 20-ply laminates P and N, ABAQUS was able to predict the failure moment with reasonably good accuracy. For most of the 40-ply laminates, the models over-predicted the failure moment (in some cases up to 20%.)

7.2 Research Conclusions

This research work on composite laminates provided us with useful information for failure analysis modeling of notched composite laminates subjected to pure bending. We observed that the classical laminated plate models seemed to under-predict the strain concentration factors. This tells us that transverse shear stresses are an important effect in the overall behavior of composite laminates when subjected to pure bending. As expected, we also determined that the notch size plays an important role in the failure analysis of composite laminates. We found that the strain concentrations increased considerably as we increased the notch size from a 0.25-in hole to a 4-in. elongated notch.

We also found that for most of the 20-ply laminates, the failure models in ABAQUS were able to replicate the results generated in our experiments. Our theoretical models were capable of reproducing accurately their failure points by taking into consideration the large deformation effects and damage progression. We discovered that the thicker laminates raised more complications for determining failure loads, probably due to the higher delamination occurrences and larger transverse shear effects. At any rate, our ABAQUS models accurately represented the strain behavior of the laminates for points below the ultimate load.

7.3 Recommendations for Future Work

Some of the laminates exhibited extremely large deformations, and it took several test runs to obtain a maximum moment to achieve failure. Additionally, we found some deviations in the test results of replicate laminates that used the same bottom fixture setup. Laminate slippage, causing off-centered loading, could have triggered these deviations. Therefore, if more experiments were to be conducted, it would be advised to construct a fixture to adjust for these complications. In addition, digital image correlation (DIC) could be a very useful tool to determine the strain field of the laminates. In such a case, it would be recommended to adequately design fixtures for the DIC equipment and to adapt this technology for out-of-plane large deformations.

In terms of improving the modeling of progressive damage, it would be important to dedicate time in developing new damage property values. ABAQUS uses these values to generate the evaluation of damage and produce a reduction of the material properties. Therefore, an improved set of these values might increase the accuracy of the failure predictions generated by the models. In addition, we made use of the shell models to run the damage progression on the pre-notched laminates. Previously, we found that the solid models produced 30% higher strain concentration factors than our shell models. It could be interesting to study damage progression models using the 3D-solid models.

Also, other methods could be taken into consideration to improve the simulation models. The virtual crack closure technique (VCCT) by Rybicki and Kanninen [32] could be implemented in this research. Since we have obtained delamination on most of the specimens tested, VCCT could be an efficient method to predict delamination growth instead of using Hashin theory, which overlooks delamination effects.

Additionally, there are also a number of investigations that can be implemented in the research of these composite laminates. Thermal effects are an important omission in this work. If we look at the strain variation equations of a laminate, mentioned in Chapter 2, we assumed that the thermal strains are not present, since they are assumed to be very small. However, a thermally induced strains, ε_T, which is equal to $\alpha\Delta T$, where α is the coefficient of linear thermal expansion, should be taken into consideration if the working conditions of the laminates will force them to experience high or low temperatures. In the case of an airplane fuselage, where it will be functioning under considerably high temperature differences, it could be interesting to reproduce the damage progression tests by taking into account the thermal factor.

Experimental testing has already been conducted on reinforcing laminated plates by stitching strips, and they have shown to have better damage tolerance, hence reducing the probability of catastrophic failure. Qing et al. [40] showed that strips can improve the structural design of a composite laminate without the need for a major restructuring change in the model. Therefore, it could be interesting to conduct a finite element analysis on reinforced stripped composite laminates with the simulation conditions carried out on this research.

REFERENCES

[1] D.R. Ambur, N. Jaunky, M.W. Hilburger, Progressive failure studies of stiffened panels subjected to shear loading, Composite Structures, Vol. 65. 2004, pp. 129-142.

[2] J.B. Alblas, Theorie van de Dreidimensionale Spanningstoestand in een Doorboorde Plaat. Dissertation, Delft. 1957.

[3] R.S. Alwar, K.N. Ramachandran, Three dimensional finite element analysis of cracked thick plates in bending, International Journal for Numerical Methods in Engineering, Vol. 19, 1983, pp. 293-303.

[4] C.G. Aronsson, J. Backlund, Tensile fracture of laminates with cracks, Journal of Composite Materials, Vol. 20, 1986, pp. 287-307.

[5] J. Backlund, C.G. Aronsson, Tensile fracture of laminates with holes, Journal of Composite Materials, Vol. 20, 1986, pp. 259-286.

[6] R.D. Bradshaw, S.S. Pang, Failure analysis of composite laminated plates with circular holes under bending, American Society of Mechanical Engineers, Petroleum Division (PD), Vol. 37, Composite Material Technology, 1999, pp. 125-135.

[7] C.W. Bert, H. Zeng, Generalized bending of a large, shear deformable isotropic plate containing a circular hole or rigid inclusion, American Association of Mechanical Engineers, Vol. 68. 2001, pp. 230-233.

[8] L. Chattopadhyay, Analytical solution for an orthotropic plate containing cracks, International Journal of Fracture, Vol. 134, 2005, pp. 305-317.

[9] WH. Chen, TF. Huang, Three dimensional interlaminar stress analysis at free edges of composite laminate, Computers & Structures, Vol. 32. 1989.

[10] F. Delale, F. Erdogan, The effect of transverse shear under skew-symmetric loading, Journal of Applied Mechanics, Vol. 46, 1979, pp. 618-624.

[11] B. Dopker, D.P. Murphy, L.B. Ilcewiz, T.H. Walker, Damage tolerance analysis of composite transport fuselage structure, 35th AIAA/ASME/ASCE/AHS/ASC Structures, Structural Dynamics and Materials Conference, 1994, pp. 58A-1-58A-8.

[12] J.N. Goodier, The influence and elliptical holes on the transverse flexure of plates, Philosophical Magazine, Vol. 22, 1936, pp. 69-80.

[13] Z. Hashin, Failure Criteria for Unidirectional Fiber Composites, Journal of Applied Mechanics, Vol. 47, 1980, pp. 329-334.

[14] L.B. Ilcewiz, T.H. Walker, D.P. Murphy, B. Dopker, D.B. Scholz, Tension fracture of laminates for transport fuselage –part 4: damage tolerance analysis, Fourth NASA Advanced Technology Conference, NASA CP3229, 1993, pp. 264-298.

[15] D.L. Jones, Subramonian, An analytical and experimental study of the plate tearing mode of fracture, Engineering Fracture Mechanics, Vol. 17, 1983, pp. 47-62.

[16] R. Jones, H. Alesi, On the analysis of composite structures with material and geometric non-linearities, Composite Structures, Vol. 50, 2000, pp. 417-431.

[17] T.C. Kennedy, M.F. Nahan, A simple nonlocal damage model for predicting failure of notched laminates, Composite Structures, Vol. 35, 1996, pp. 229-236.

[18] T.C. Kennedy, M.F. Nahan, A simple nonlocal damage model for predicting failure in a composite shell containing a crack, Composite Structures, Vol. 39, 1997, pp. 85-91.

[19] R. Krueger, T.K. O'Brien, A shell 3D modeling technique for the analysis of delaminated composite laminates, Composites: Part A, Vol. 32, 2001, pp. 25-44.

[20] I. Lapczyk, J.A. Hurtado, Progressive damage modeling in fiber-reinforced materials, Composites: Part A, Vol. 38, 2007, pp. 2333-2341.

[21] C.W. Lee, G.D. Conlee, Bending and twisting of thick plates with a circular hole, Journal of the Frankling Institute, Vol. 285, 1968, pp. 377-385.

[22] S.G. Lekhnitskii, Anisotropic Plates, Gordong & Breach, 1968, pp. 403-410.

[23] R.A.W. Mines, A. Alias, Numerical simulation of the progressive collapse of polymer composite sandwich beams under static loading, Composites: Part A, Vol. 33, 2002, pp. 11-26.

[24] P.M. Naghdi, The effect of elliptic holes on the bending of the thick plates, Journal of Applied Mechanics, Vol. 22, 1955, pp. 89-94.

[25] T. Nishioka, S.N. Atluri, Stress analysis of holes in angle-ply laminates: an

efficient assumed stress “special-hole-element” approach and a simple estimation method, Computers & Structures, Vol. 15, 1982, pp. 135-147.

[26] VT. Nguyen, JF. Caron, K. Sab, A model for thick laminates and sandwich plates, Composites Science and Technology, Vol. 65, 2005, pp. 475-489.

[27] Y.S.N. Reddy, C.M. Dakshina, J.N. Reddy, Non-linear progressive failure analysis of laminated composite plates, International Journal of Non-Linear Mechanics, Vol. 30, 1995, pp. 629-649.

[28] E. Reissner, The effect of transverse shear deformation on the bending of elastic plates, Journal of Applied Mechanics, Vol. 67, 1945, pp. A69-A77.

[29] E. Reissner, On transverse bending of plates, including the effects of transverse shear deformation, International Journal of Solids and Structures, Vol. 11, 1975, pp. 569-573.

[30] E. Reissner, On the analysis of first and second-order shear deformation effects for isotropic elastic plates, Journal of Applied Mechanics, Vol. 47, 1980, pp. 959-961.

[31] E. Reissner, Stress couple concentrations for cylindrical bent plates with circular holes or rigid inclusions, Journal of Applied Mechanics, Vol. 50, 1983, pp. 85-87.

[32] E.F. Rybicki, M.F. Kanninen, A finite element calculation of stress intensity factors by a modified crack closure integral, Engineering Fracture Mechanics, Vol. 9, 1977, pp. 931-938.

[33] I. Shadid, F.K. Chang, An accumulative damage model for tensile and shear failures of laminated composite plates, Journal of Composite Materials, Vol. 29, 1995, pp. 926-981.

[34] R.P. Shimpi, H.G. Patel, A two variable refined plate theory for orthotropic plate analysis, International Journal of Solids and Structures, Vol. 34, 2006, pp. 6783-6799.

[35] H.T. Sun, F.K. Chang, X. Qing, The response of composite joints with bolt-clamping loads, part-1: model development, Journal of Composite Materials. Vol. 36, 2002, pp. 47-67.

[36] T.K. Paul, K.M. Rao, Stress analysis around circular holes in FRP laminates under transverse load, Computer & Structures, Vol. 33, 1989, pp. 929-937.

[37] T.K. Paul, K.M. Rao, Stress analysis around an elliptical hole in thick FRP laminates under transverse load, Computer & Structures, Vol. 35, 1990, pp. 553-561.

[38] P.H. Petit, M.E. Waddoups, A method of predicting the nonlinear behavior of laminated composites, Journal of Composite Materials, Vol. 3, 1969, pp. 2-19.

[39] C.B. Prasad, M.J. Shuart, Moment distributions around holes in symmetric composites laminates subjected to bending moments, AIAA Journal, Vol. 28, 1990, pp. 877-882.

[40] X. Qing, F.K. Chang, Damage tolerance of notched composite laminates with reinforcing strips, Journal of Composite Materials, Vol. 37, 2003.

[41] S.W. Tsai, E.M. Wu, A General Theory of Strength for Anisotropic Materials, Journal of Composite Materials, Vol. 5, 1971, pp. 58-80.

[42] T.H. Walker, W.B. Avery, L.B. Ilcewiz, C.C. Poe, Tension fracture of laminates for transport fuselage –part 1: material screening, Second NASA Advanced Technology Conference, NASA CP3154, 1991, pp. 197-238.

[43] T.H. Walker, L.B. Ilcewiz, D.R Polland, C.C. Poe, Tension fracture of laminates for transport fuselage –part 2: large notches, Third NASA Advanced Technology Conference, NASA CP3178, 1992, pp. 727-758.

[44] J.F. Wang, R.H. Wagoner, D.K. Matlock, F. Barlat, Anticlastic curvature in draw-bend springack, International Journal of Solids and Structures, Vol. 42, 2005, pp. 1287-1307.

[45] N. Wang, Effects of plate thickness on the bending of an elastic plate containing a crack, Journal of Mathematics and Physics, Vol. 47, 1968, pp. 371-390.

[46] M. Williams, The bending stress distribution at the base of a stationary crack, Journal of Applied Mechanics, Vol. 28, 1961, pp. 78-82.

[47] B.H. Wu, F. Erdogan, The surface and through crack problems in orthotropic plates, International Journal of Solids and Structures, Vol. 25, 1989, pp. 167-188.

[48 M.J. Young, C.T. Sun, On the strain energy release rate for a cracked plate subjected to out-of-plane bending moment, International Journal of Fracture, Vol. 60, 1993, pp. 227-247.

[49] A.T. Zehnder, C.Y. Hui, Stress intensity factors for plate bending and

shearing problems, ASME Journal of Applied Mechanics, Vol. 61, 1994, pp. 719-722.

[50] A.T. Zehnder, M.J. Viz, Fracture mechanics of thin plates and shells under combined membrane, bending and twisting loads, Applied Mechanics Reviews, Vol. 58, 2005, pp. 37-48.

[51] A. Zucchini, C.Y. Hui, A.T. Zehnder, Crack tip stress fields for thin, cracked plates in bending, shear, and twisting: a comparison of plate theory and three-dimensional elasticity solutions, International Journal of Fracture, Vol. 104, 2000, pp. 387-407.

APPENDIX A – List of Figures for Progressive Damage Modeling

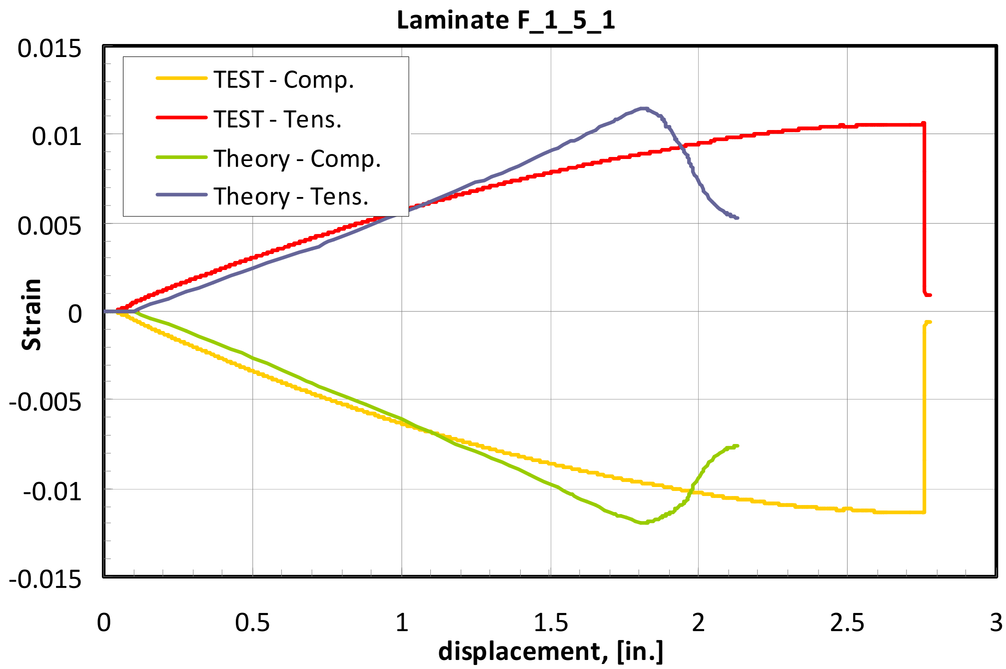

Figure A. 1 - Progressive Damage of Laminate F_1_5_1

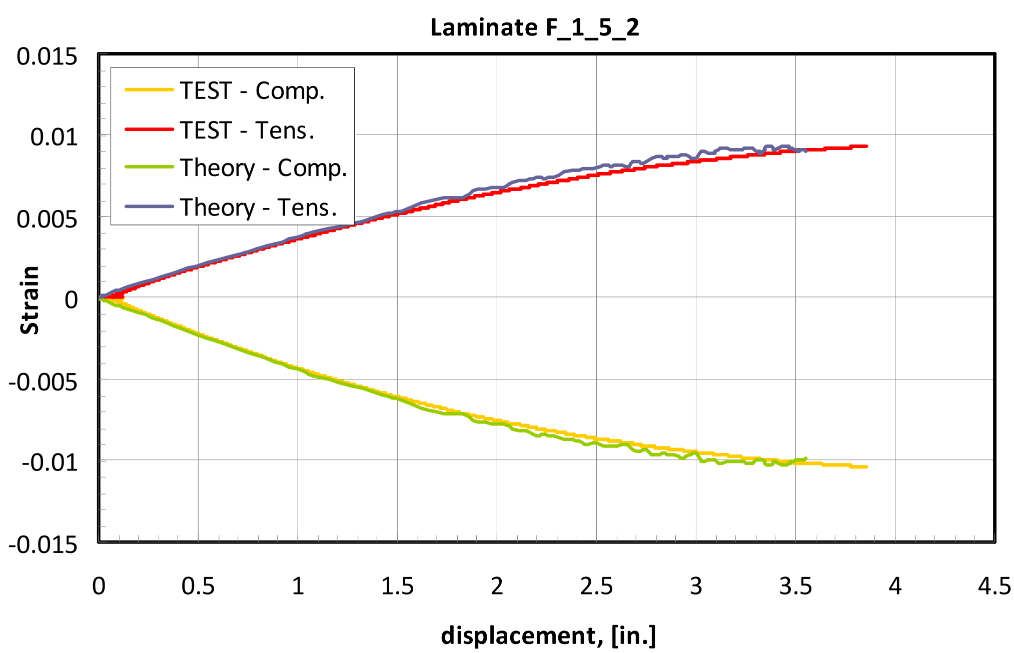

Figure A. 2 - Progressive Damage of Laminate F_1_5_2

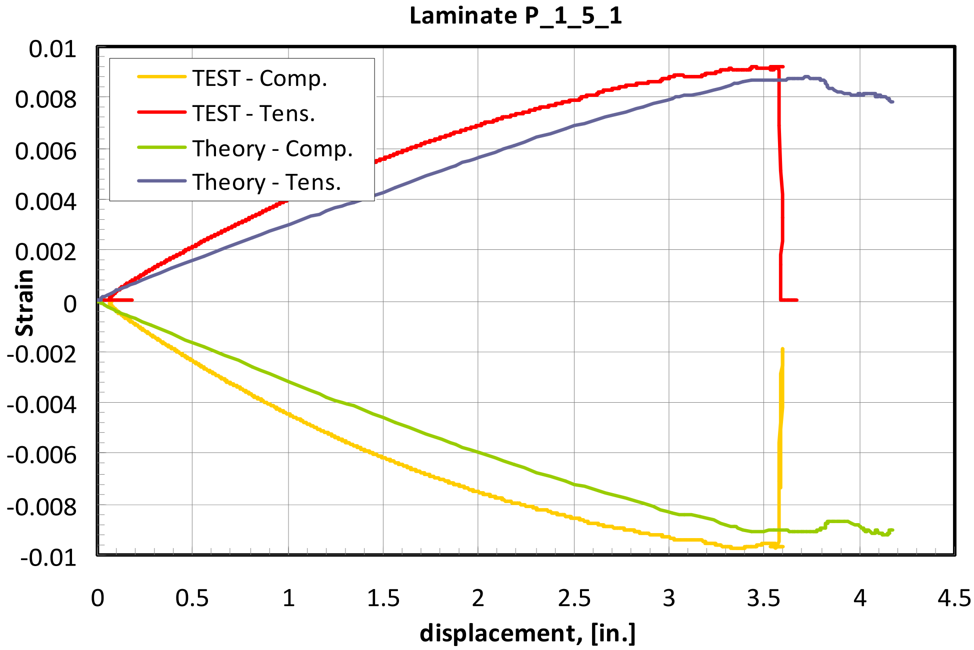

Figure A. 3 - Progressive Damage of Laminate P_1_5_1

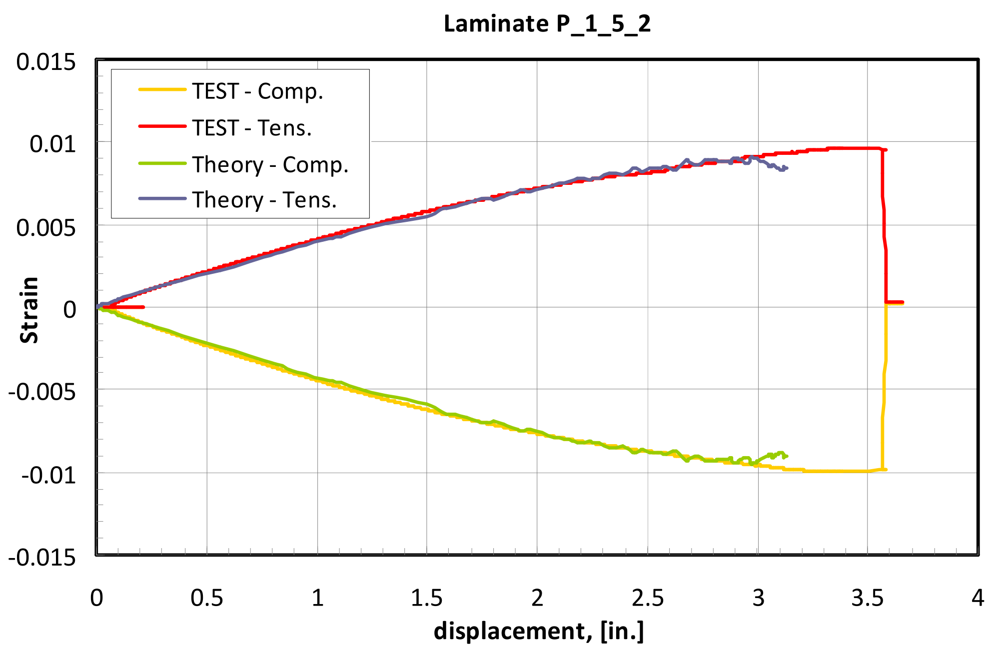

Figure A. 4 - Progressive Damage of Laminate P_1_5_2

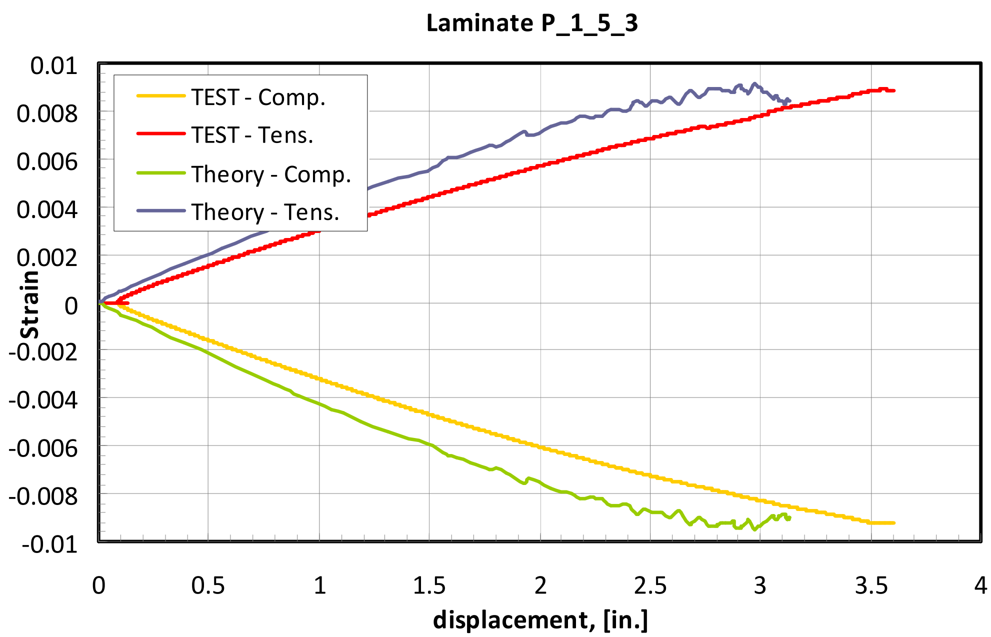

Figure A. 5 - Progressive Damage of Laminate P_1_5_3

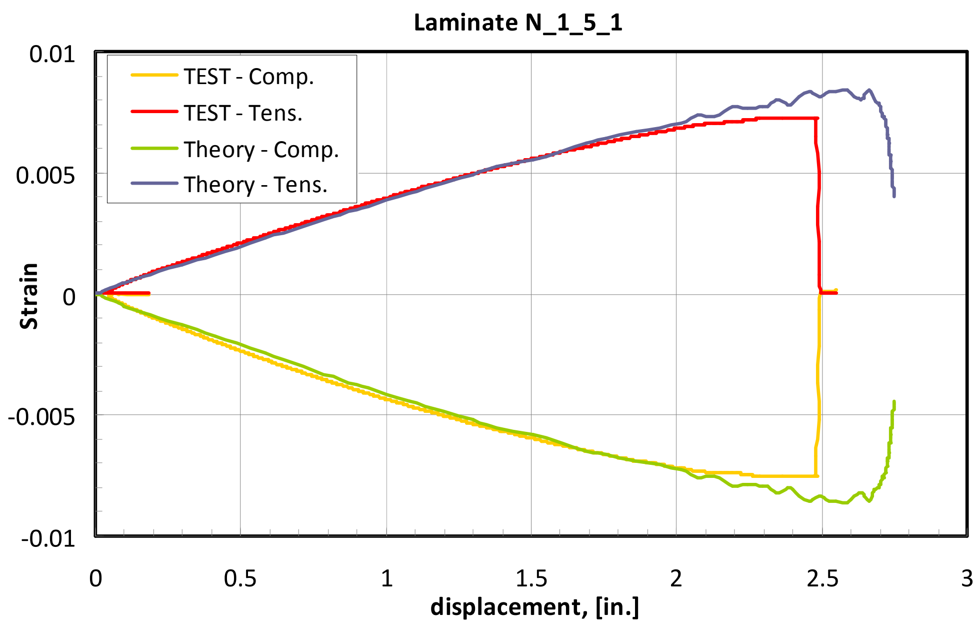

Figure A. 6 - Progressive Damage of Laminate N_1_5_1

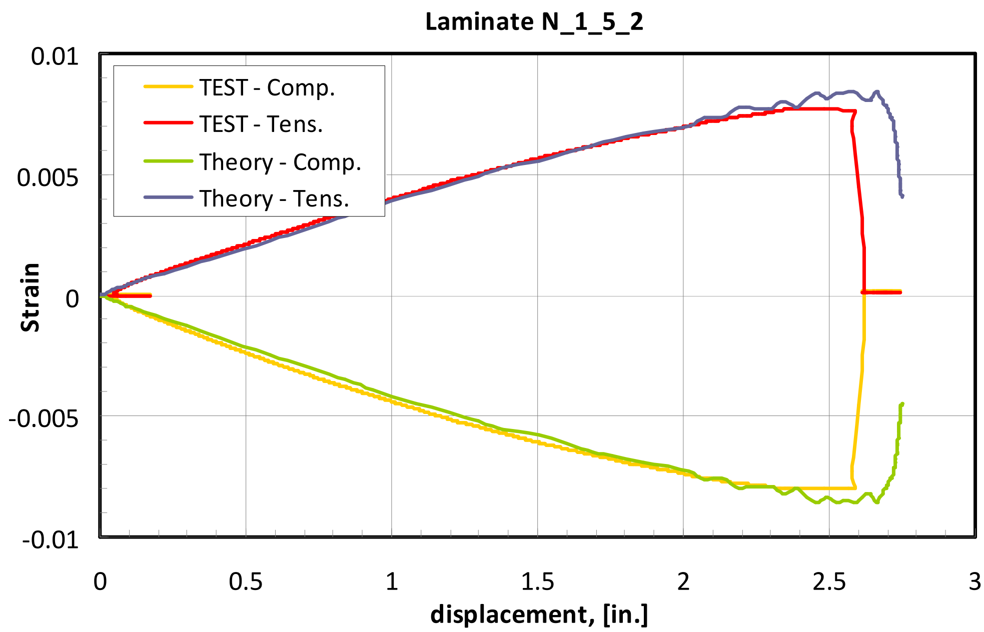

Figure A. 7 - Progressive Damage of Laminate N_1_5_2

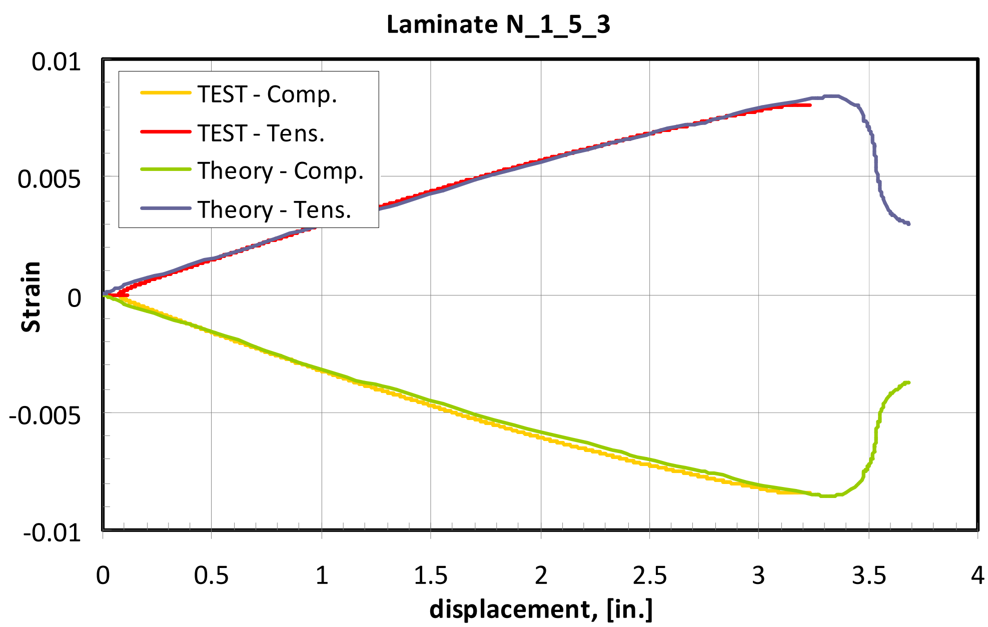

Figure A. 8 - Progressive Damage of Laminate N_1_5_3

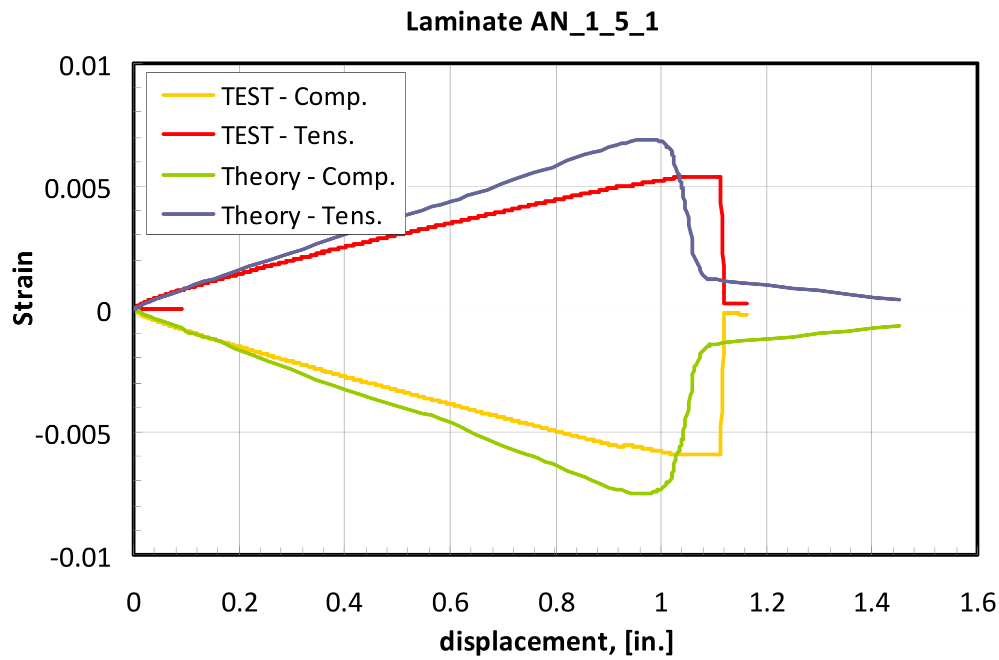

Figure A. 9 - Progressive Damage of Laminate AN_1_5_1

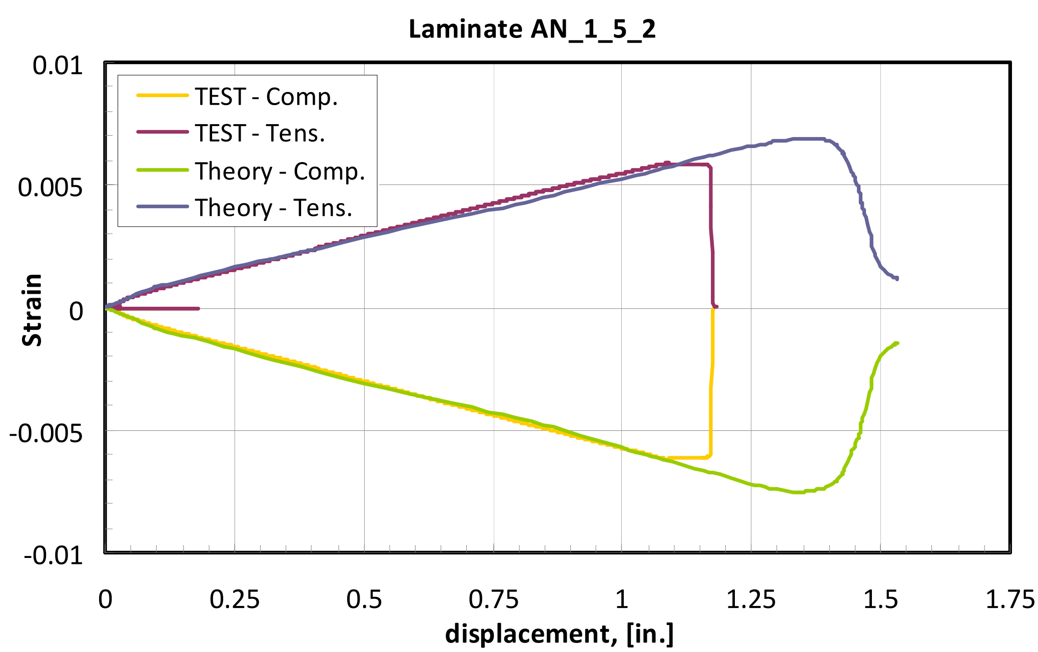

Figure A. 10 - Progressive Damage of LaminateAN_1_5_2

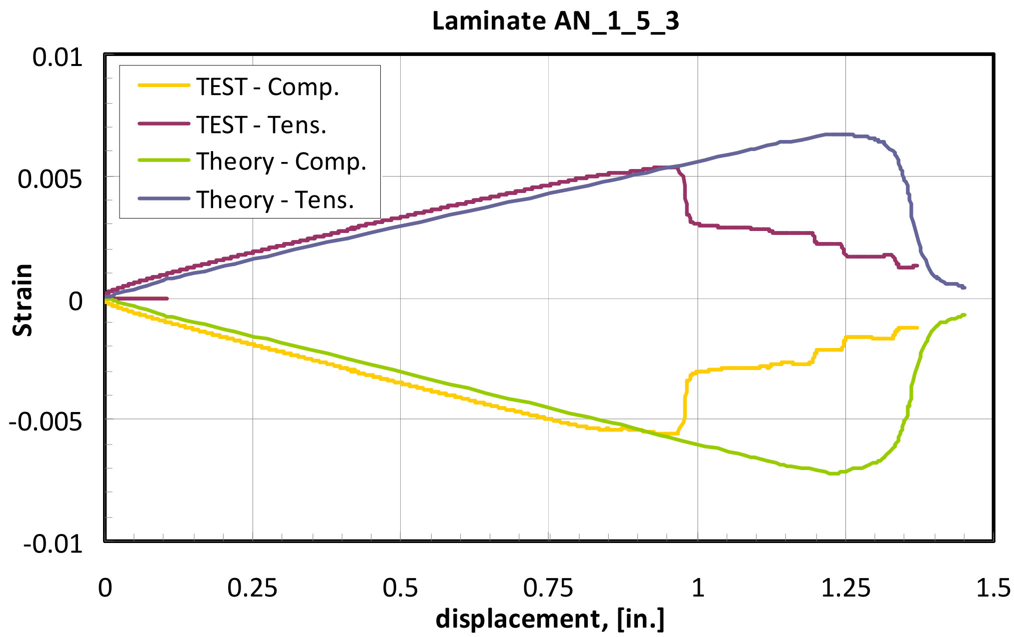

Figure A. 11 - Progressive Damage of Laminate AN_1_5_3

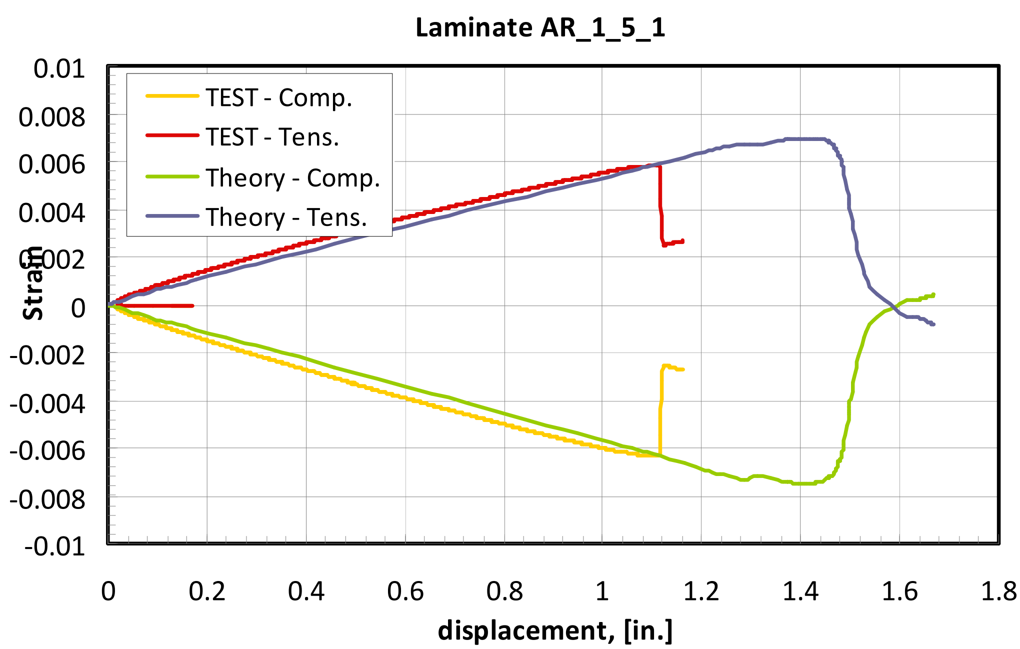

Figure A. 12 - Progressive Damage of Laminate AR_1_5_1

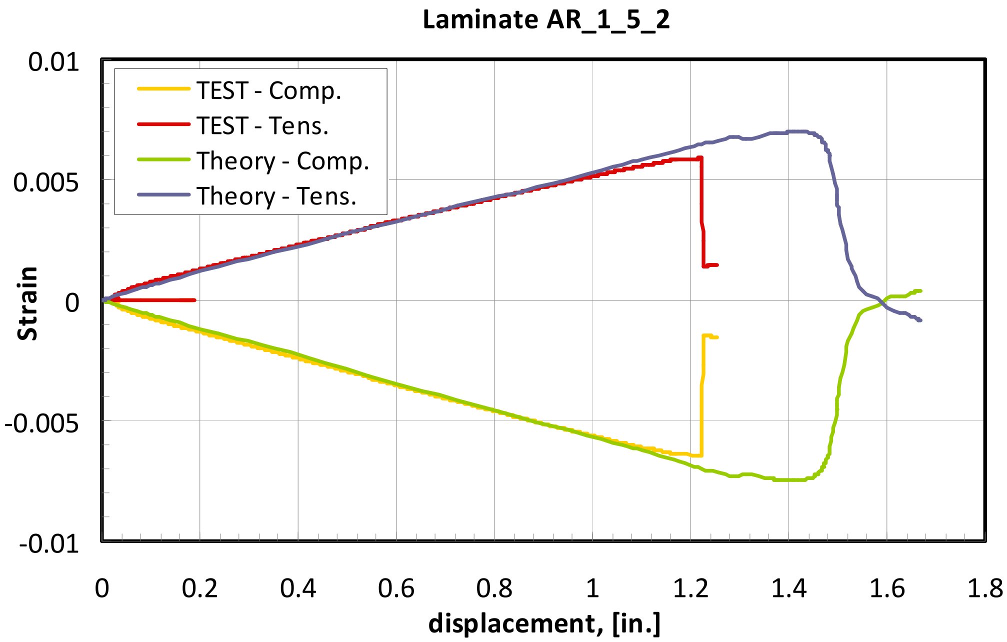

Figure A. 13 - Progressive Damage of Laminate AR_1_5_2

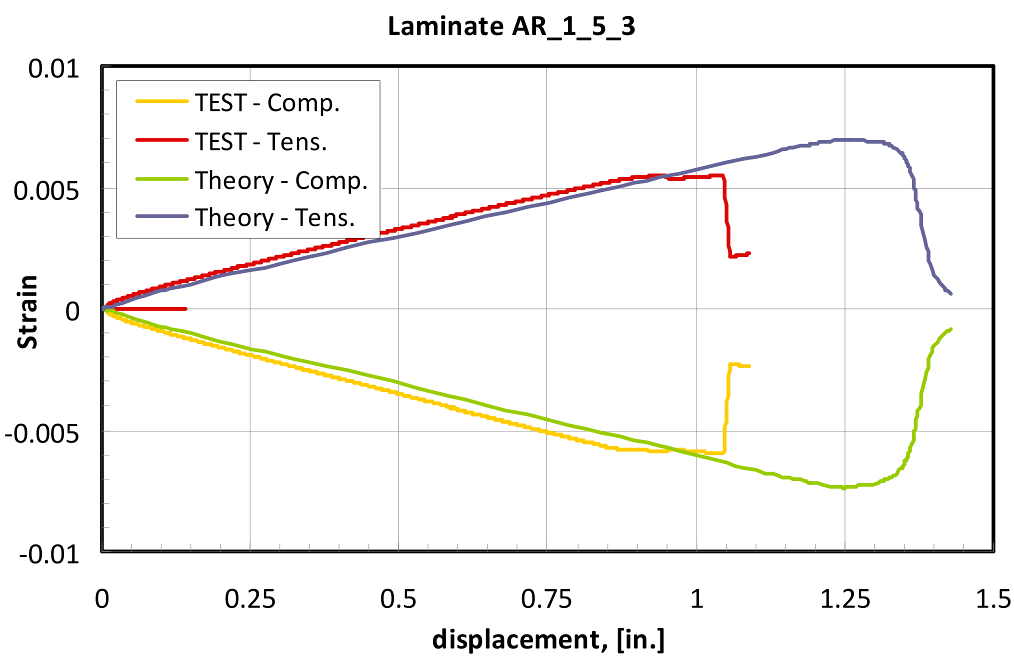

Figure A. 14 - Progressive Damage of Laminate AR_1_5_3

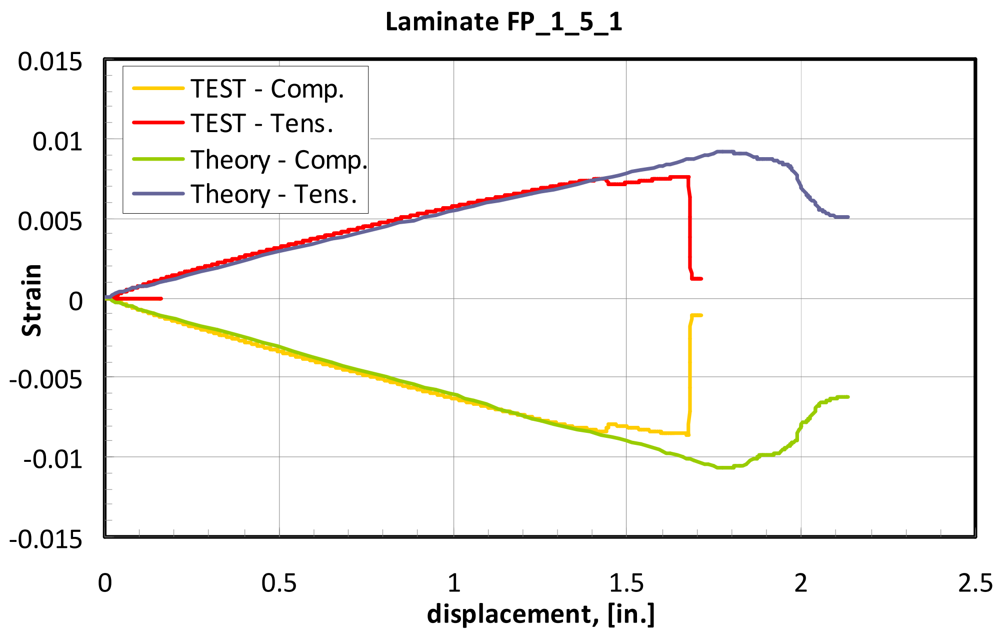

Figure A. 15 - Progressive Damage of Laminate FP_1_5_1

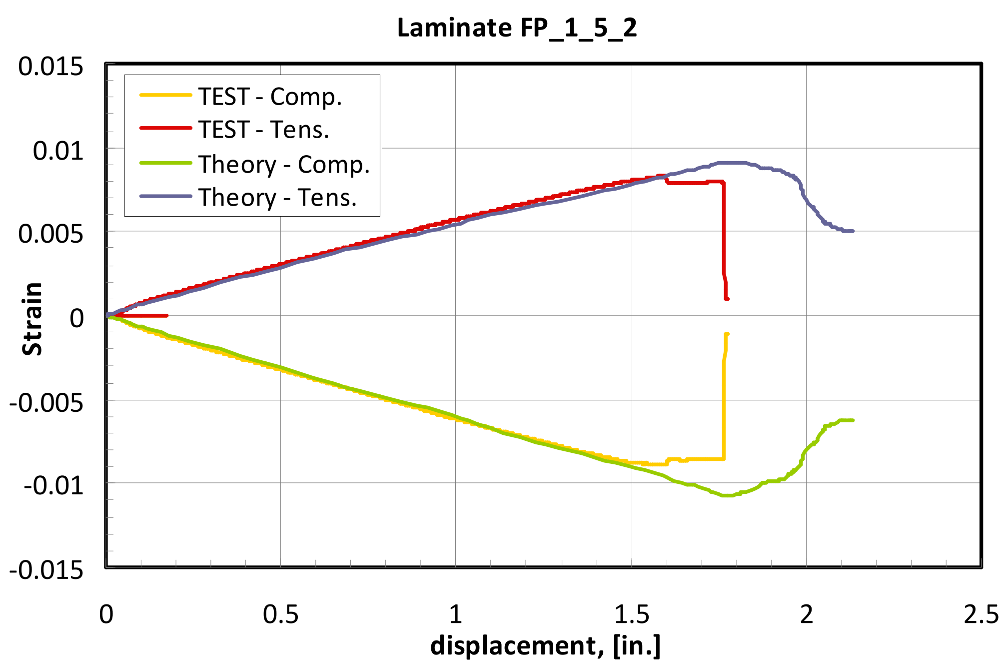

Figure A. 16 - Progressive Damage of Laminate FP_1_5_2

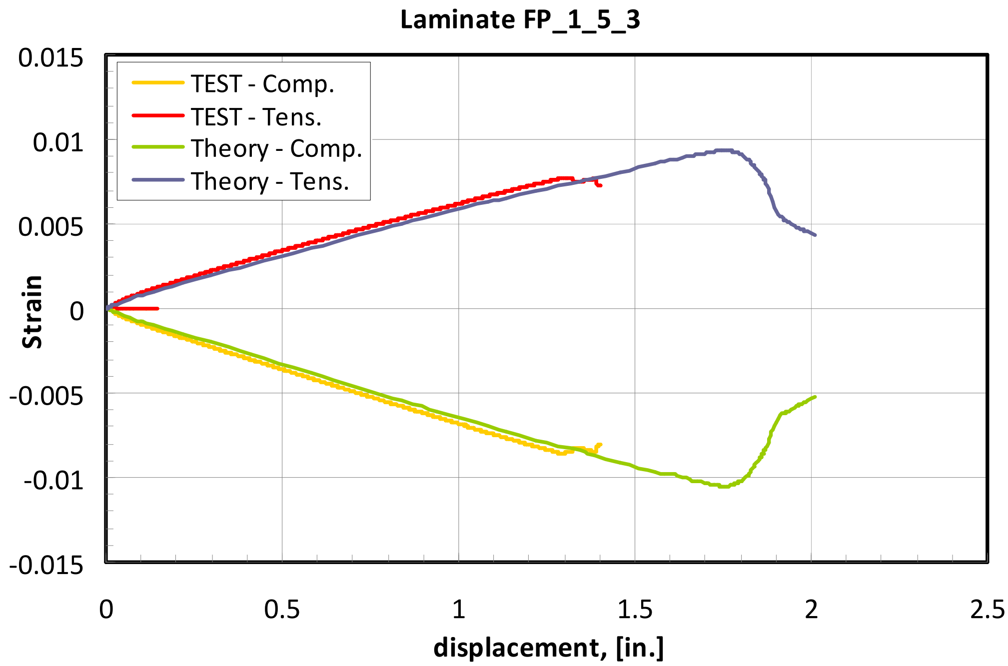

Figure A. 17 - Progressive Damage of Laminate FP_1_5_3

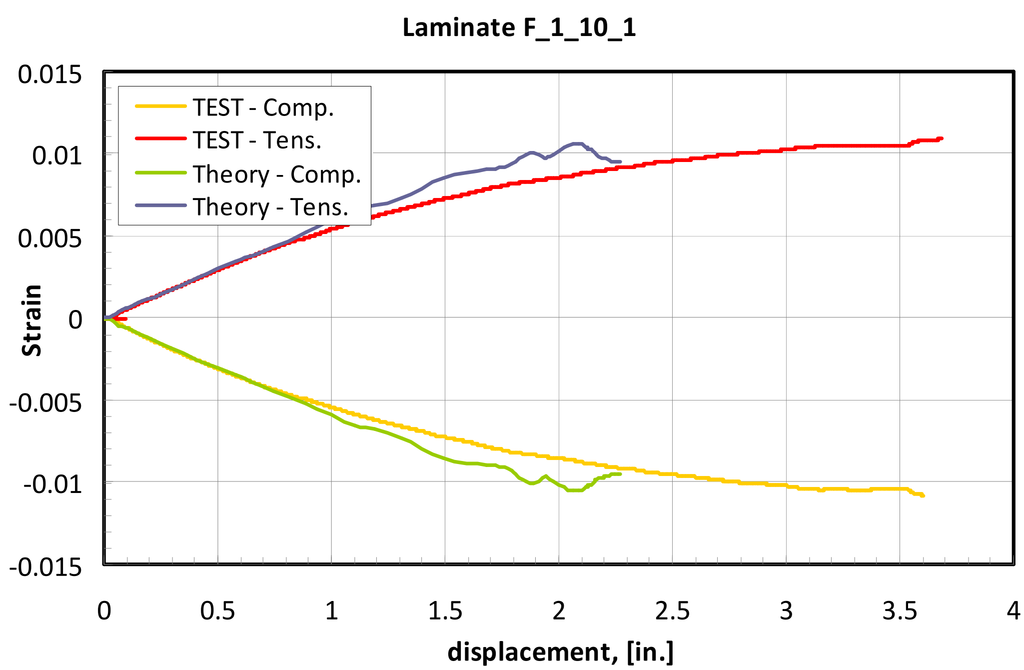

Figure A. 18 - Progressive Damage of Laminate F_1_10_1

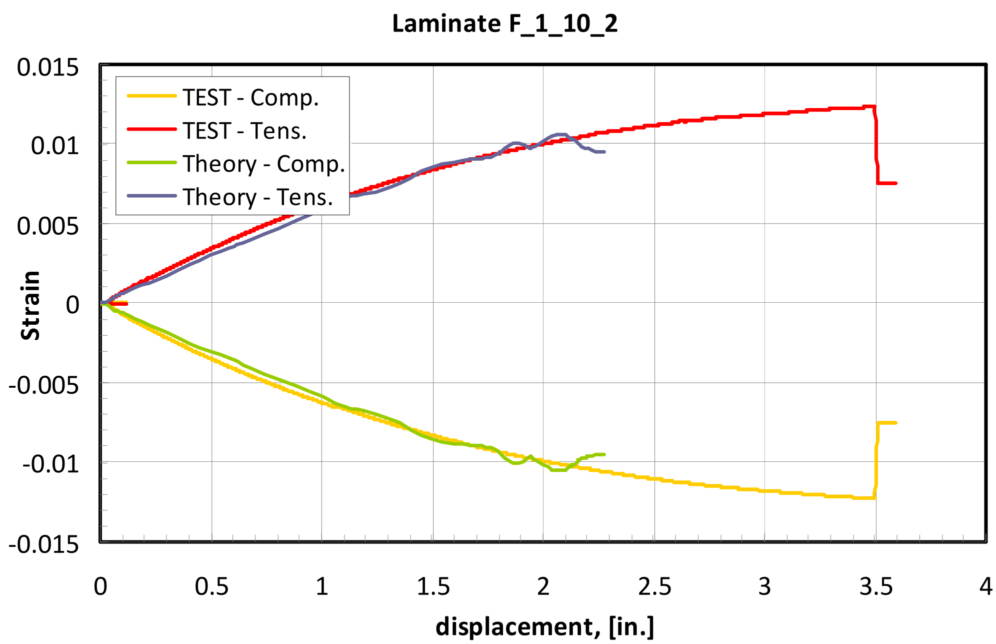

Figure A. 19 - Progressive Damage of Laminate F_1_10_2

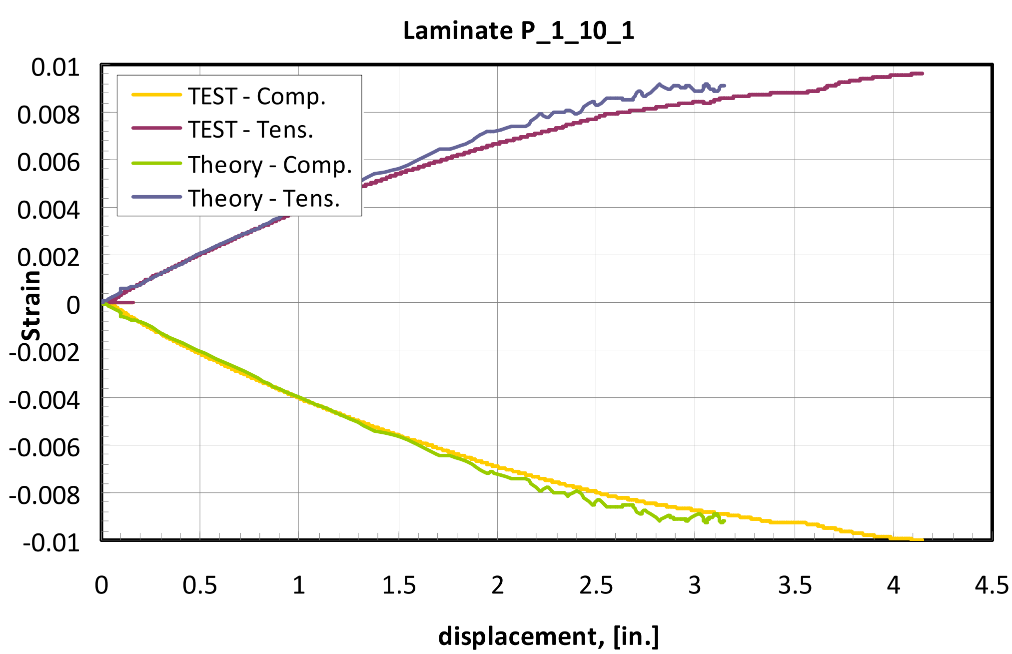

Figure A. 20 - Progressive Damage of Laminate P_1_10_1

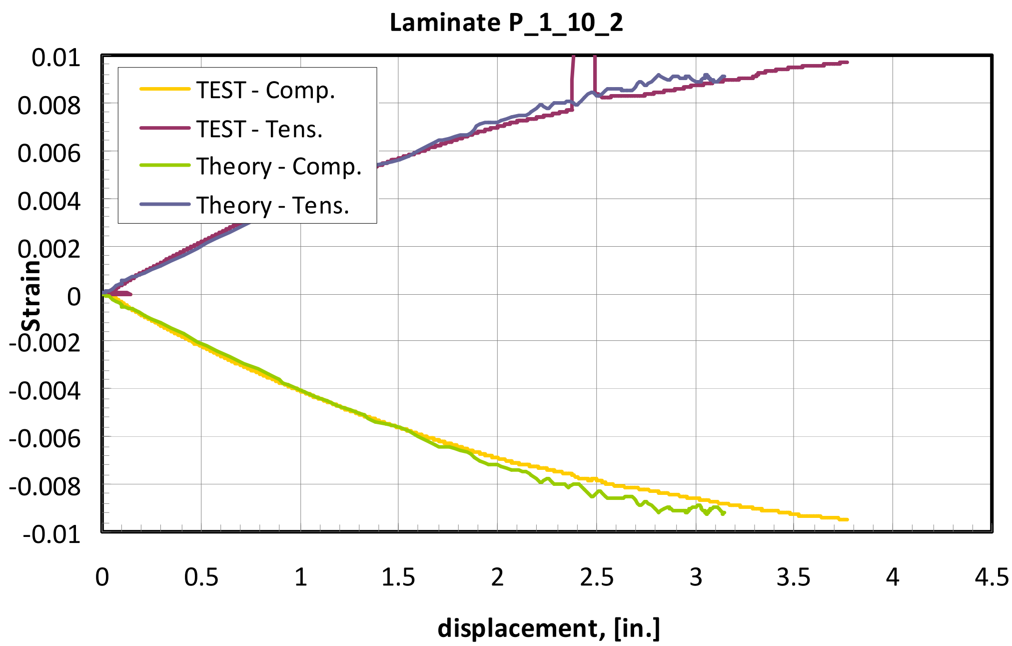

Figure A. 21 - Progressive Damage of Laminate P_1_10_2

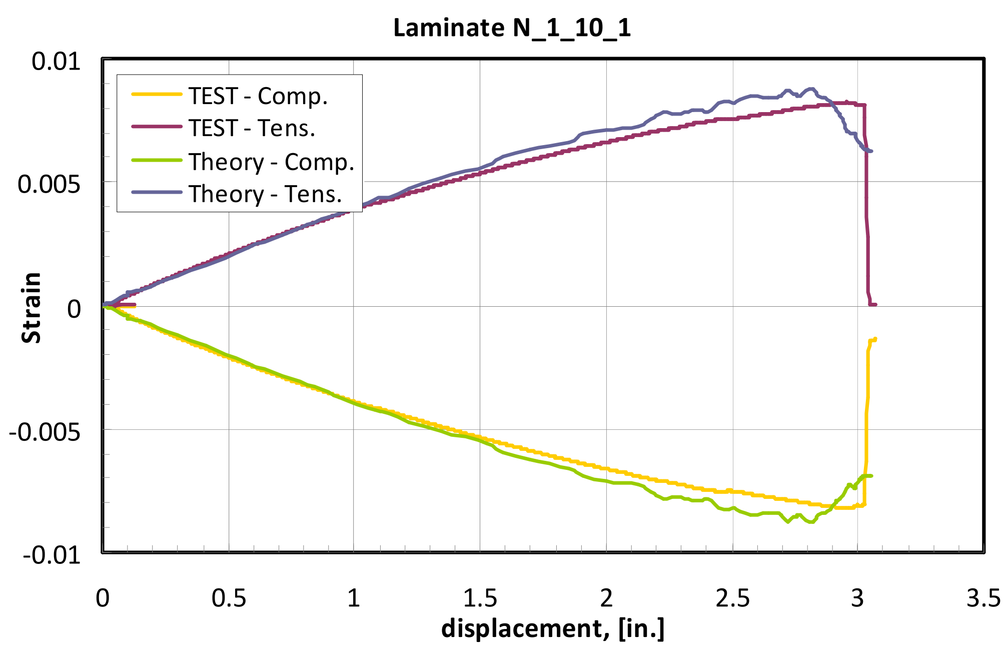

Figure A. 22 - Progressive Damage of Laminate N_1_10_1

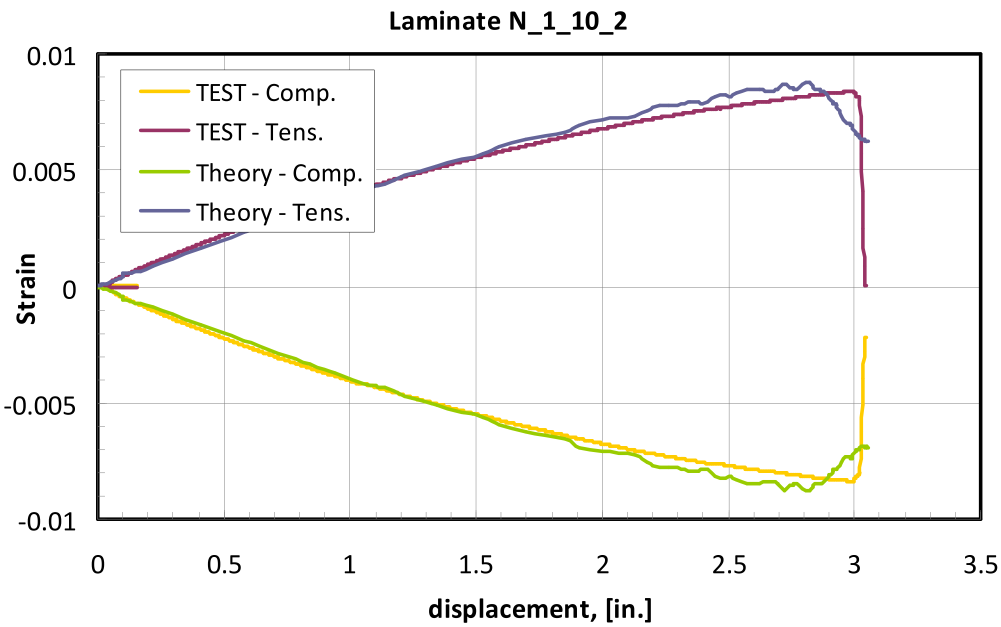

Figure A. 23 - Progressive Damage of Laminate N_1_10_2

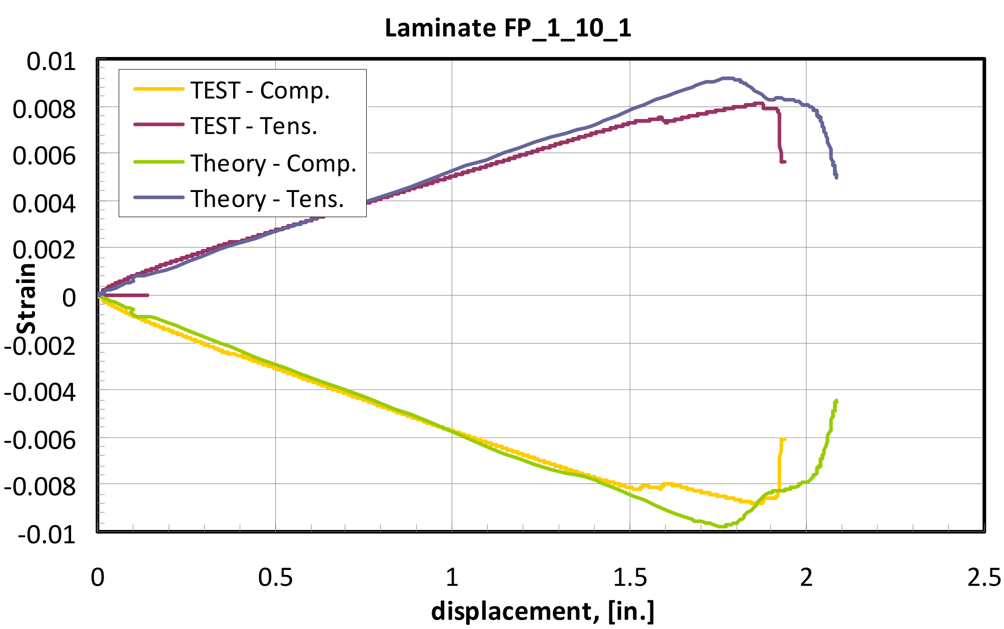

Figure A. 24 - Progressive Damage of Laminate FP_1_10_1

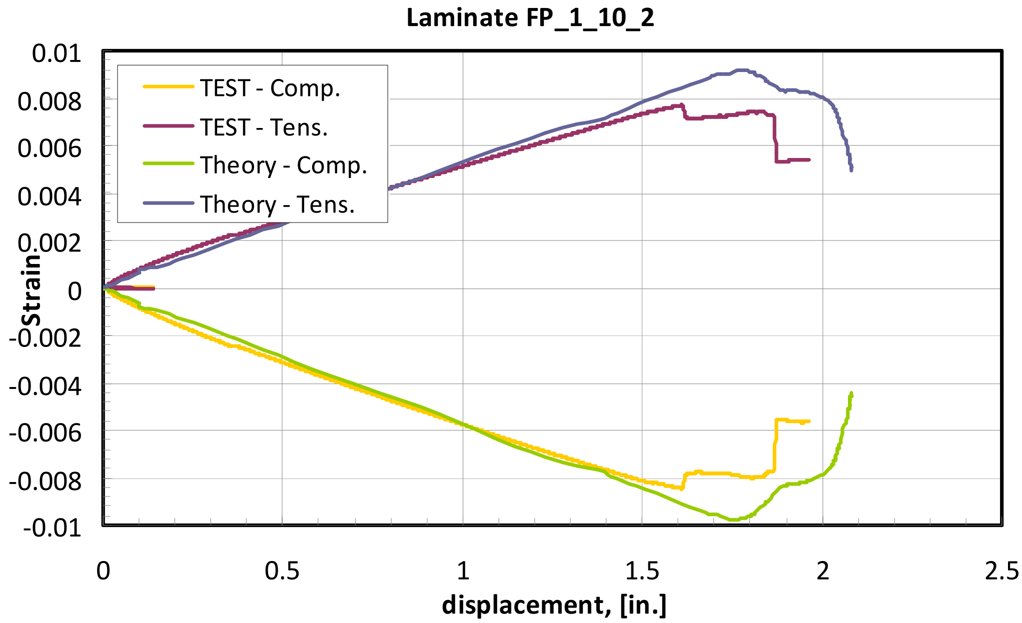

Figure A. 25 - Progressive Damage of Laminate FP_1_10_2

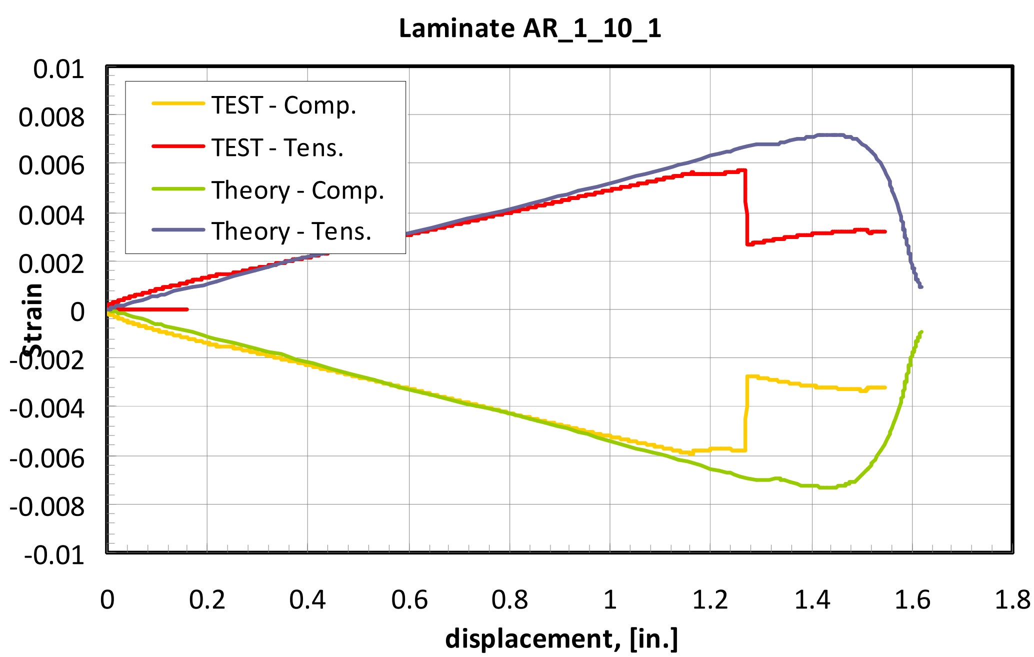

Figure A. 26 - Progressive Damage of Laminate AR_1_10_1

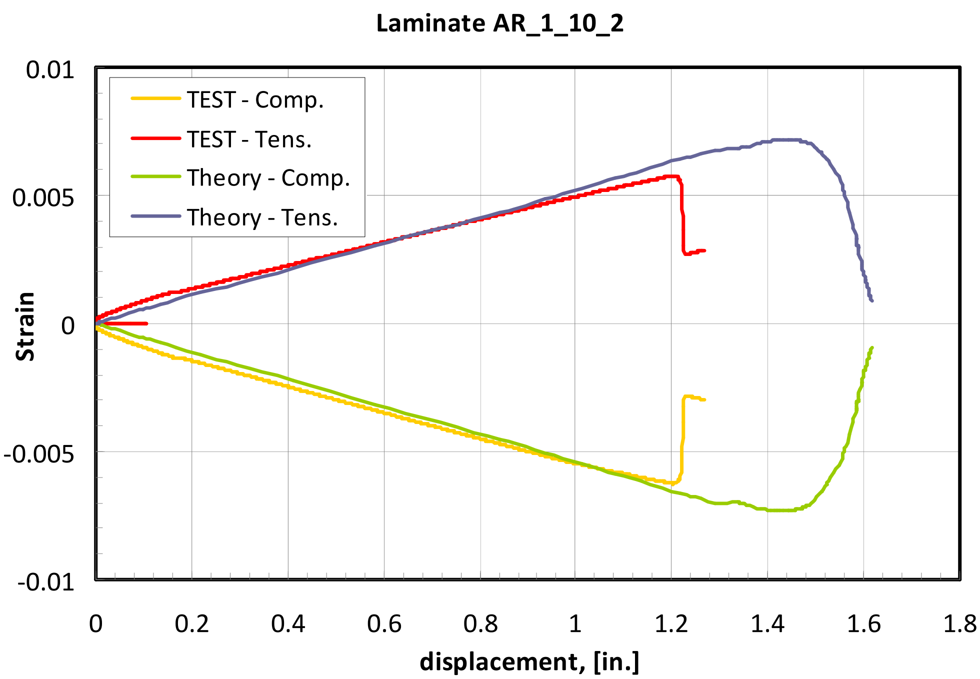

Figure A. 27 - Progressive Damage of Laminate AR_1_10_2

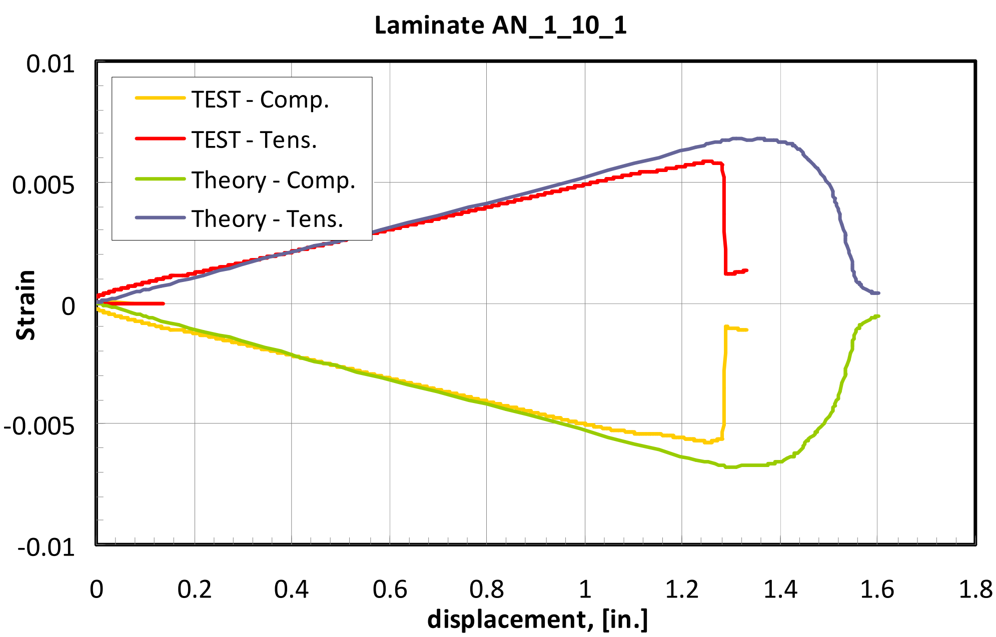

Figure A. 28 - Progressive Damage of Laminate AN_1_10_1

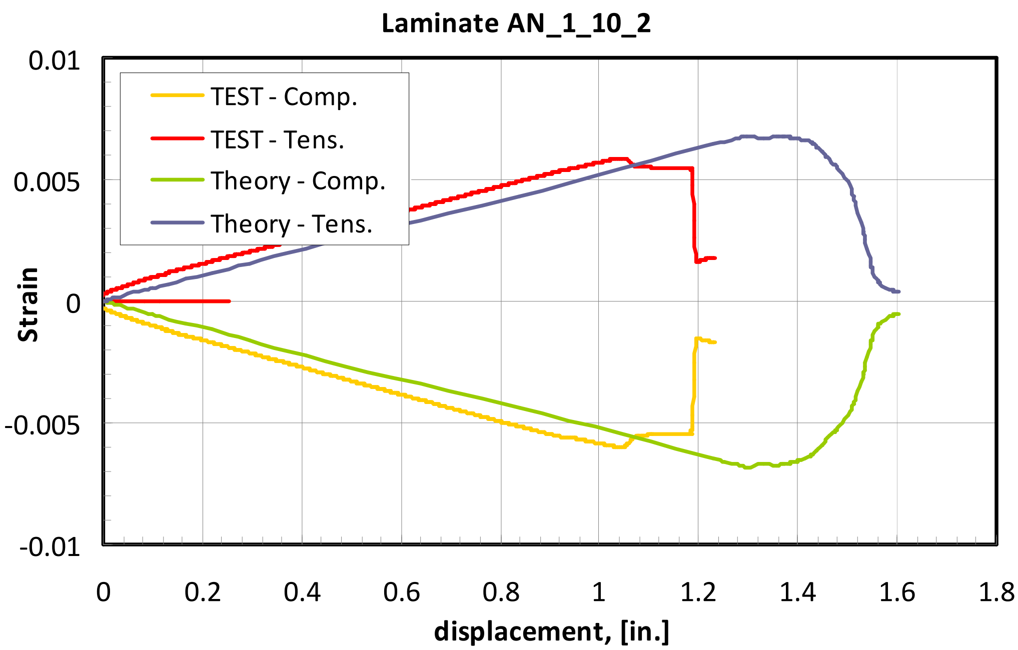

Figure A. 29 - Progressive Damage of Laminate AN_1_10_2

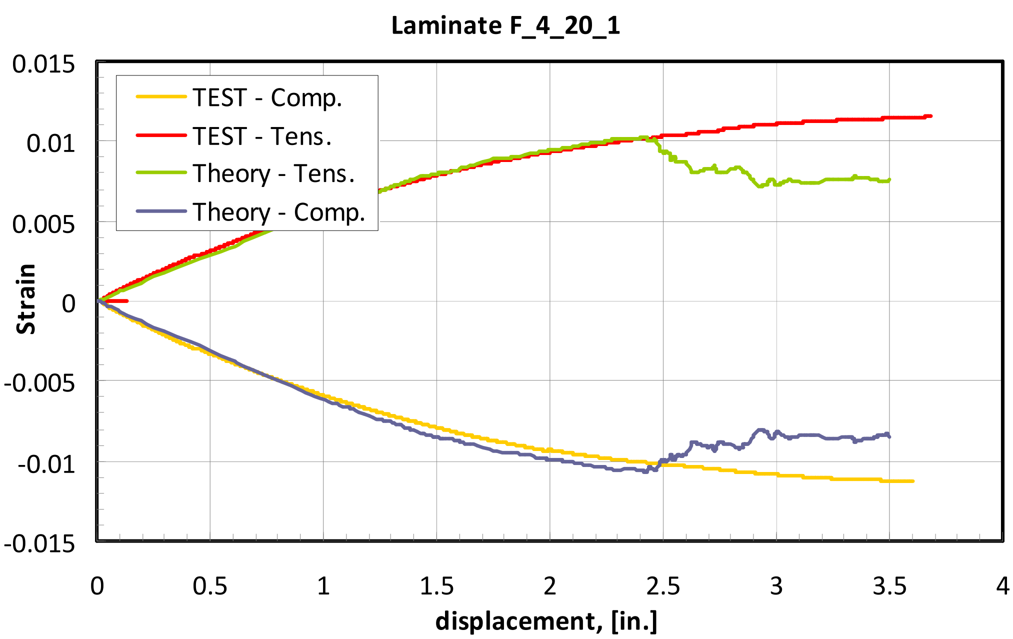

Figure A. 30 - Progressive Damage of Laminate F_4_20_1

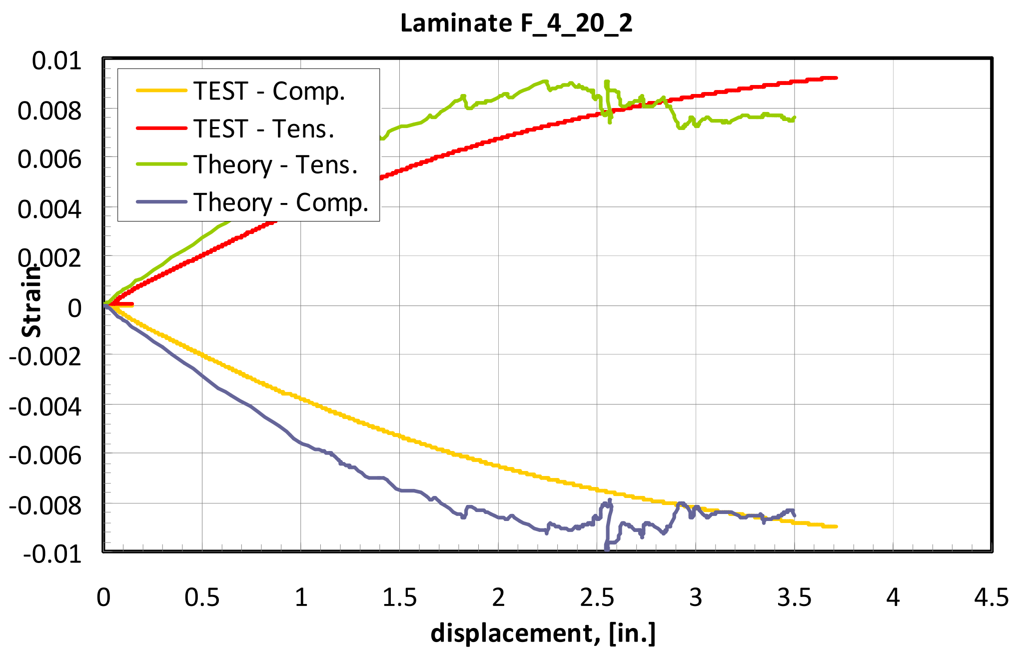

Figure A. 31 - Progressive Damage of Laminate F_4_20_2

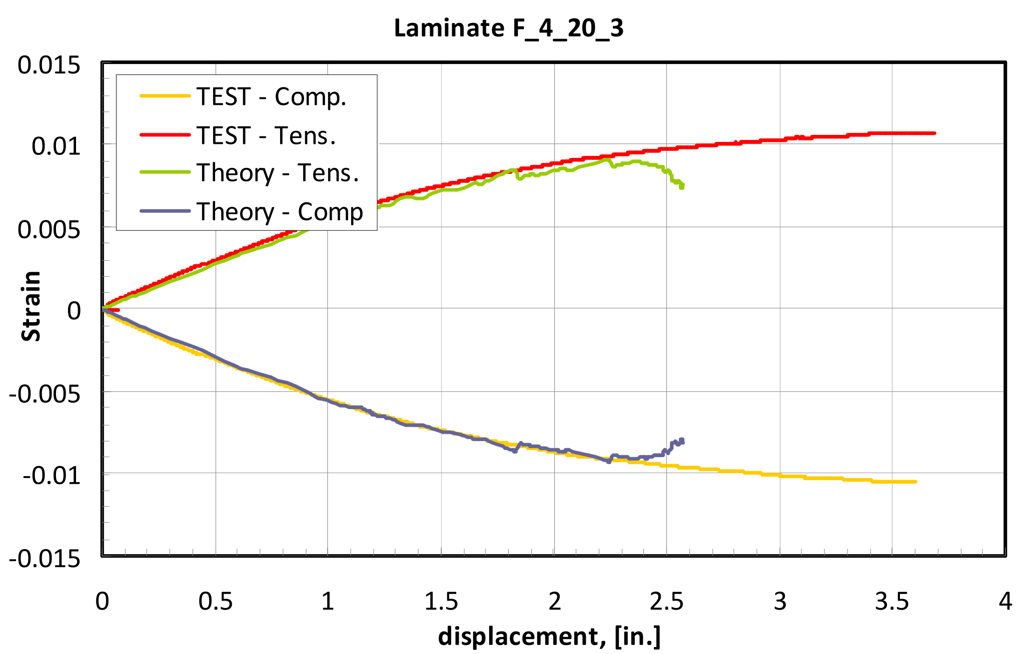

Figure A. 32 - Progressive Damage of Laminate F_4_20_3

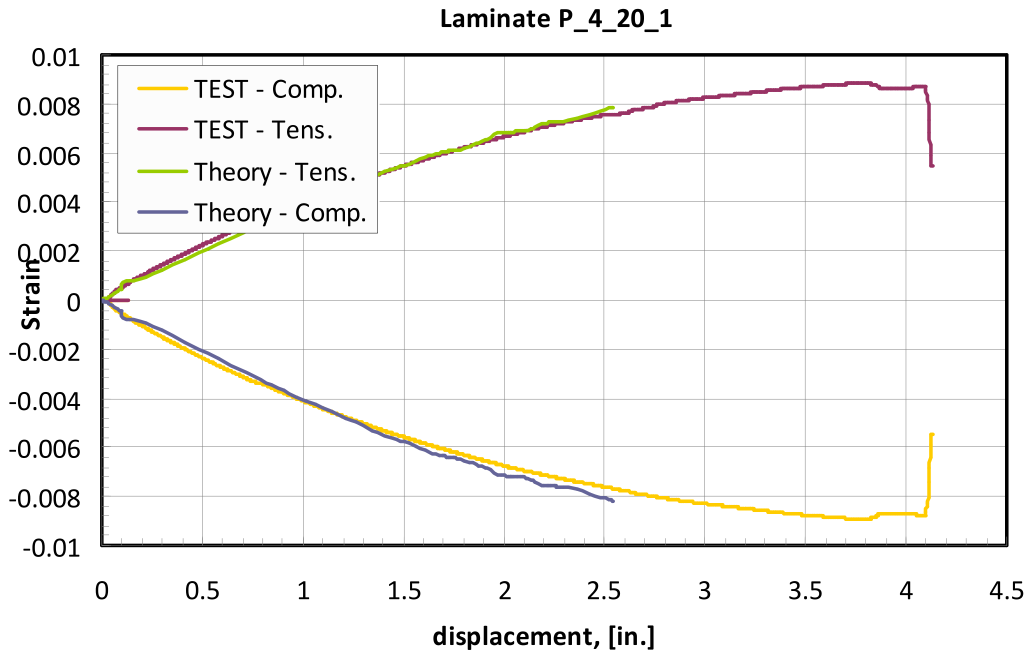

Figure A. 33 - Progressive Damage of Laminate P_4_20_1

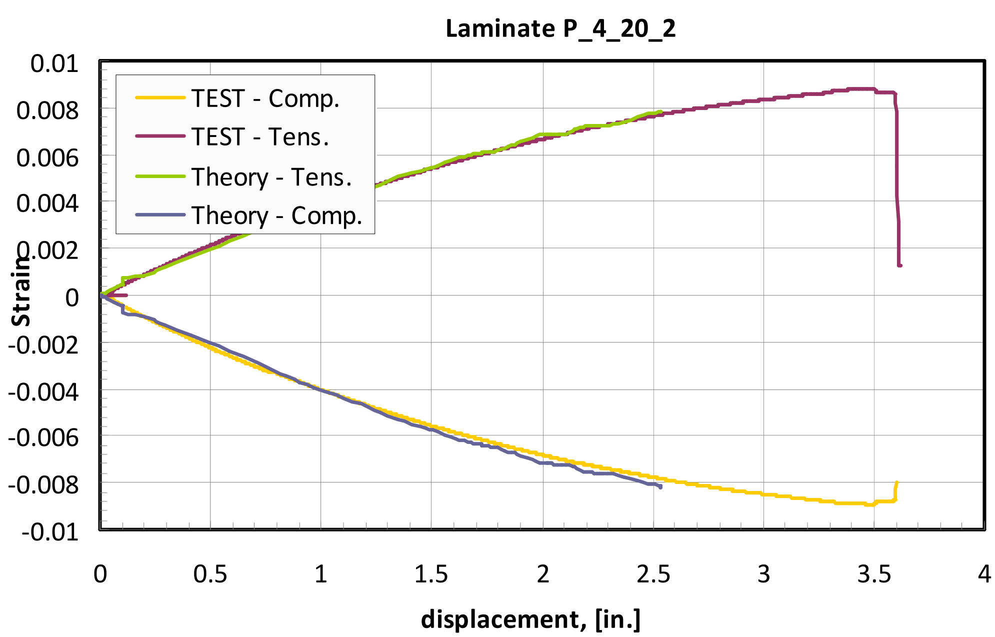

Figure A. 34 - Progressive Damage of Laminate P_4_20_2

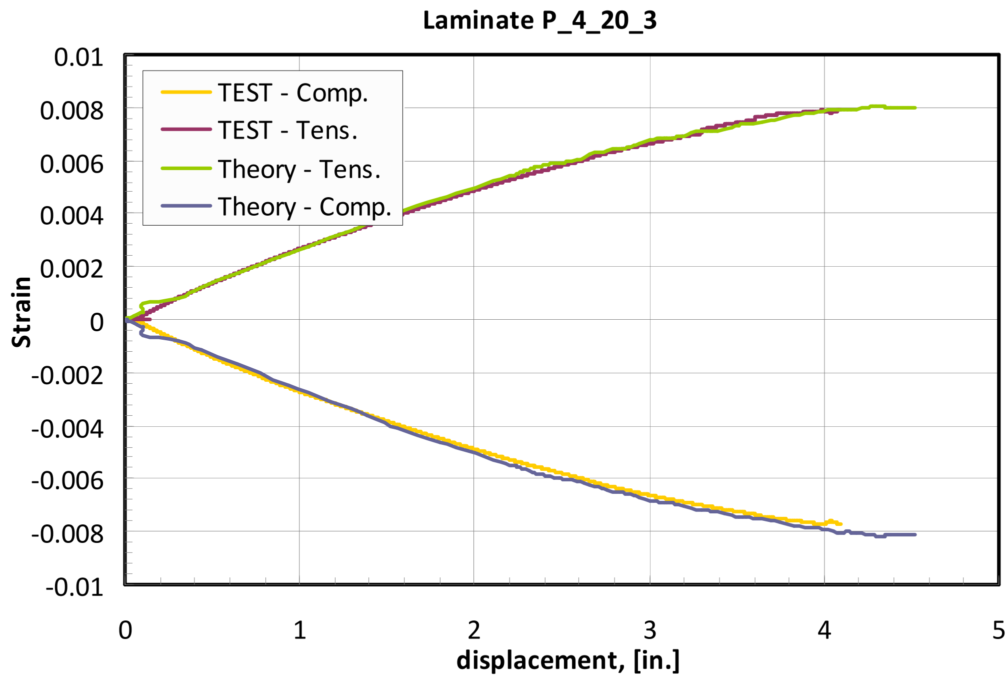

Figure A. 35 - Progressive Damage of Laminate P_4_20_3

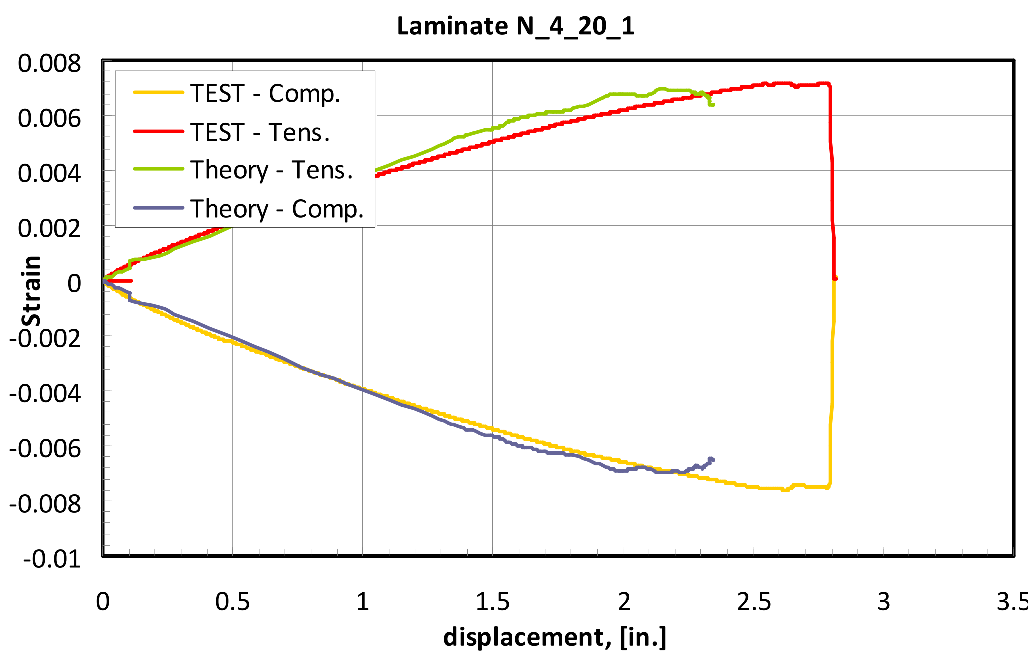

Figure A. 36 - Progressive Damage of Laminate N_4_20_1

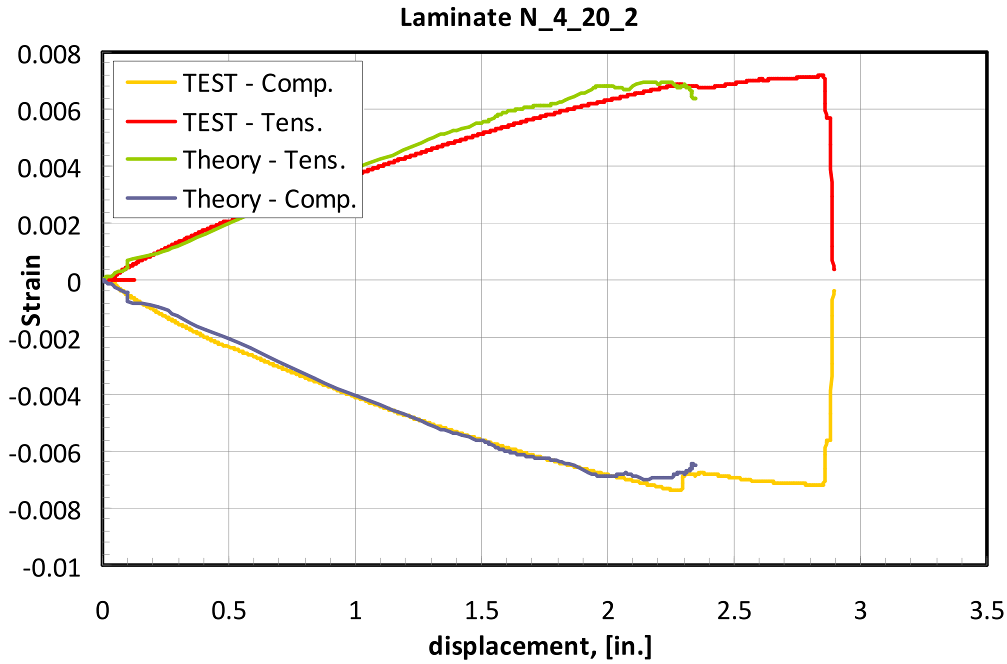

Figure A. 37 - Progressive Damage of Laminate N_4_20_2

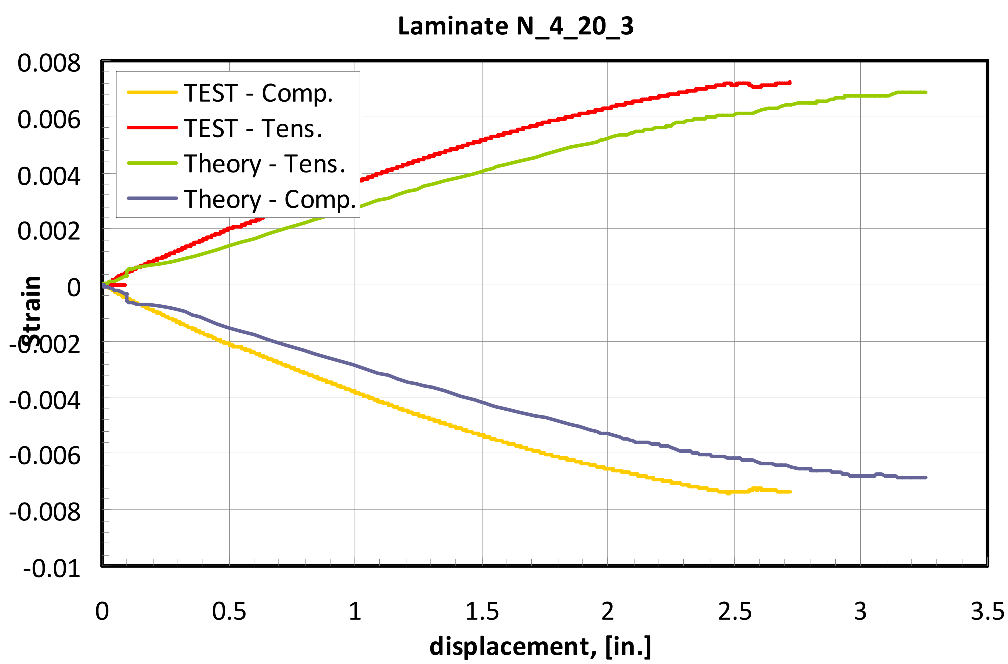

Figure A. 38 - Progressive Damage of Laminate N_4_20_3

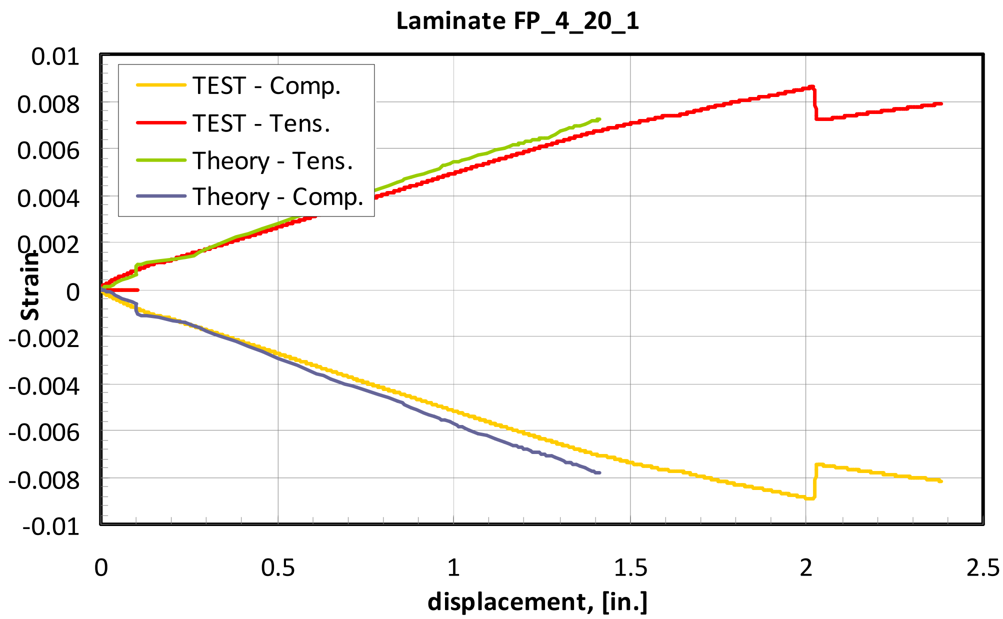

Figure A. 39 - Progressive Damage of Laminate FP_4_20_1

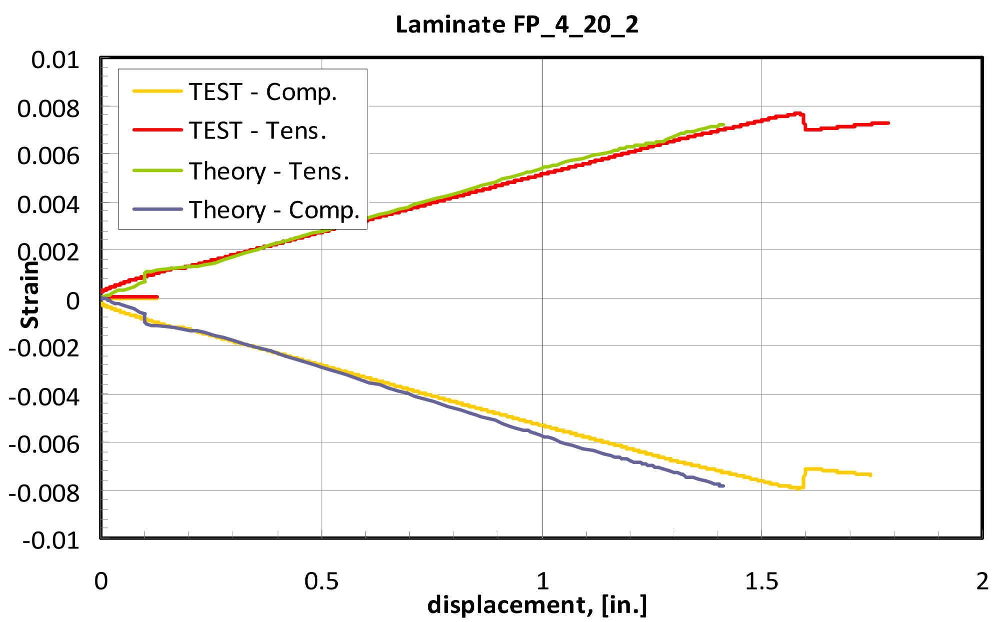

Figure A. 40 - Progressive Damage of Laminate FP_4_20_2

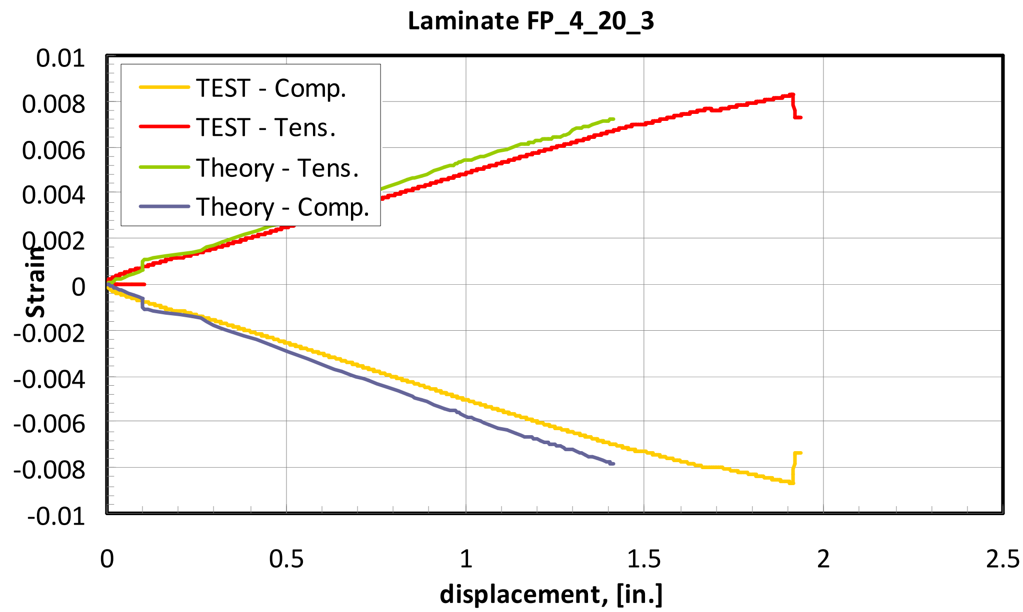

Figure A. 41 - Progressive Damage of Laminate FP_4_20_3

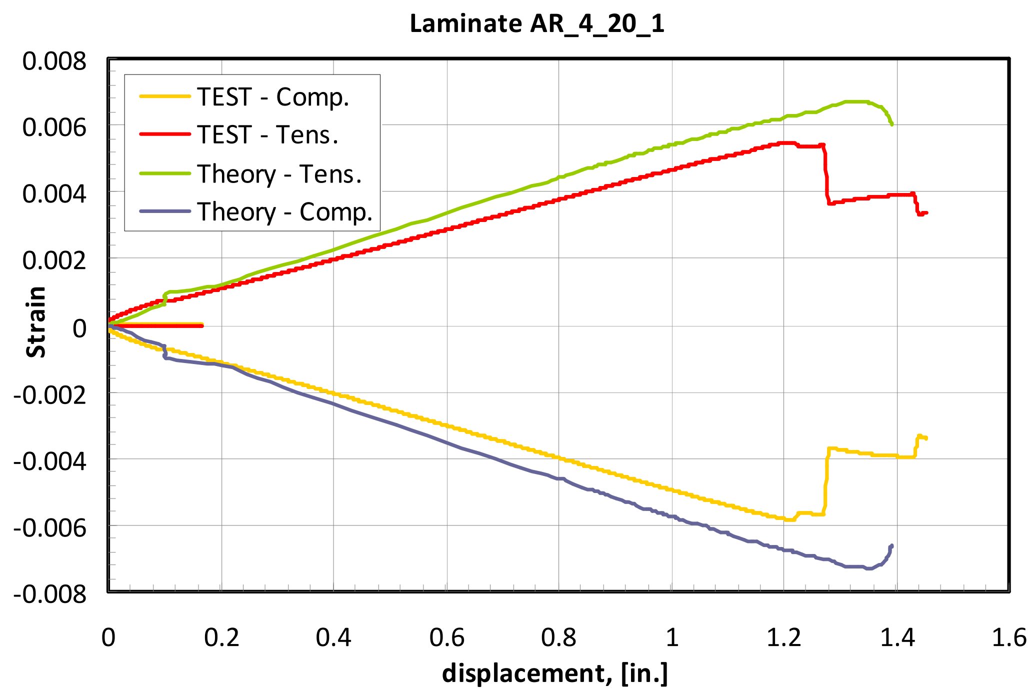

Figure A. 42 - Progressive Damage of Laminate AR_4_20_1

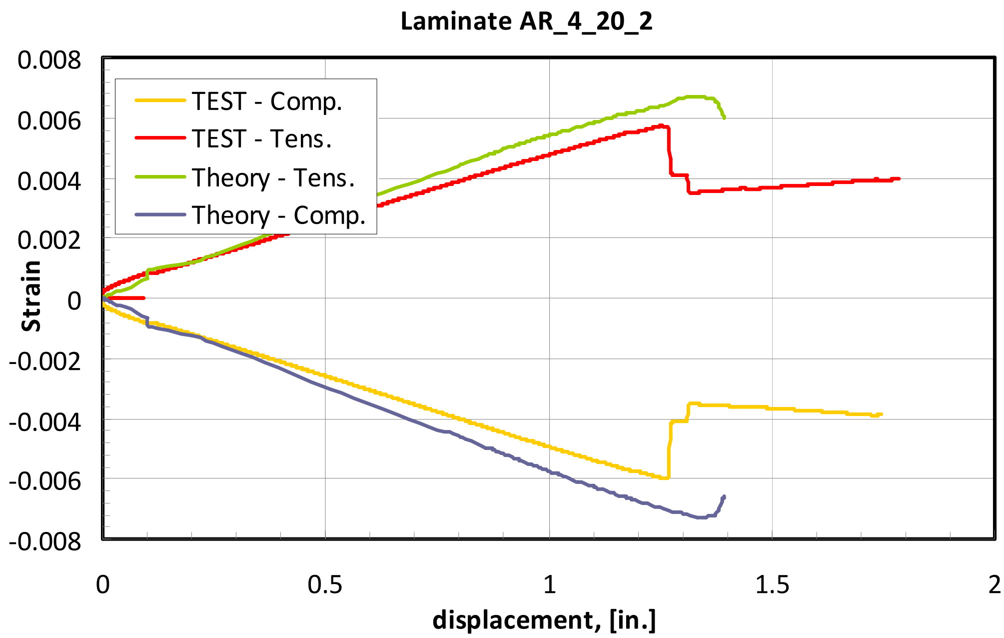

Figure A. 43 - Progressive Damage of Laminate AR_4_20_2

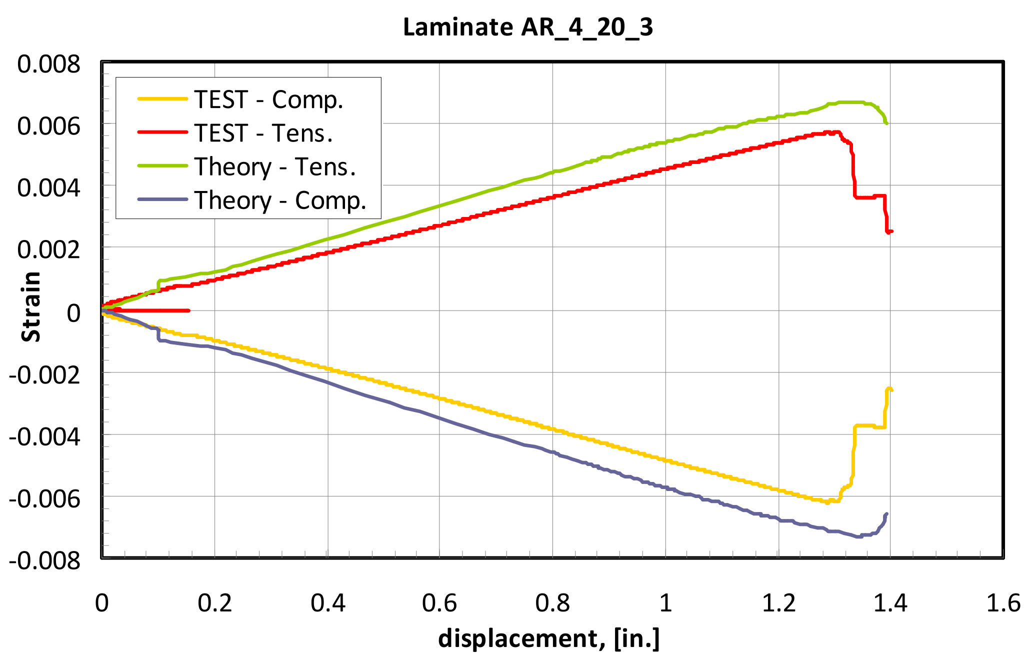

Figure A. 44 - Progressive Damage of Laminate AR_4_20_3

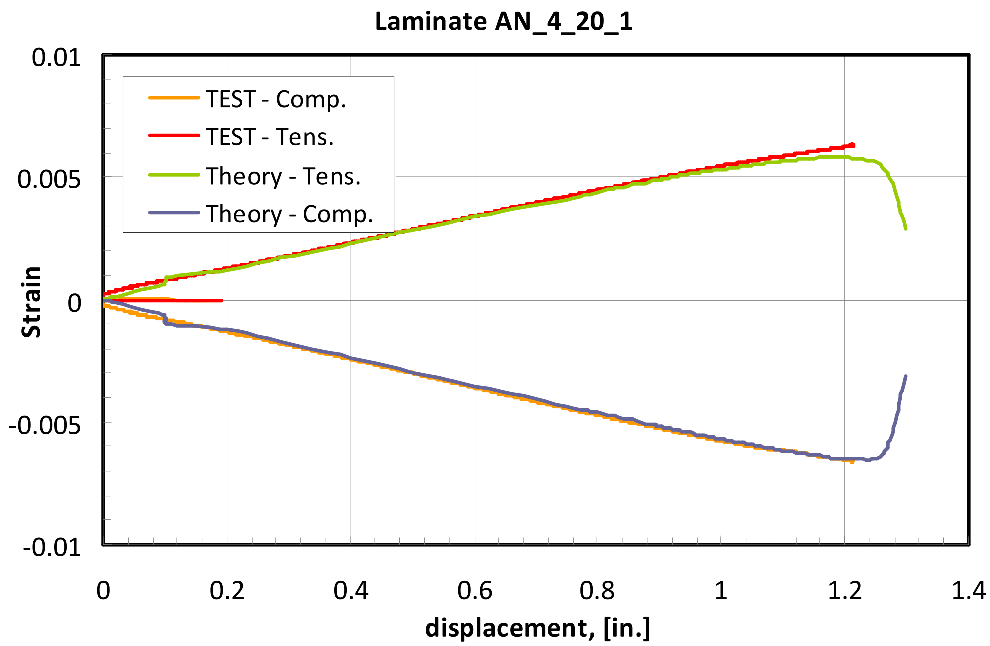

Figure A. 45 - Progressive Damage of Laminate AN_4_20_1

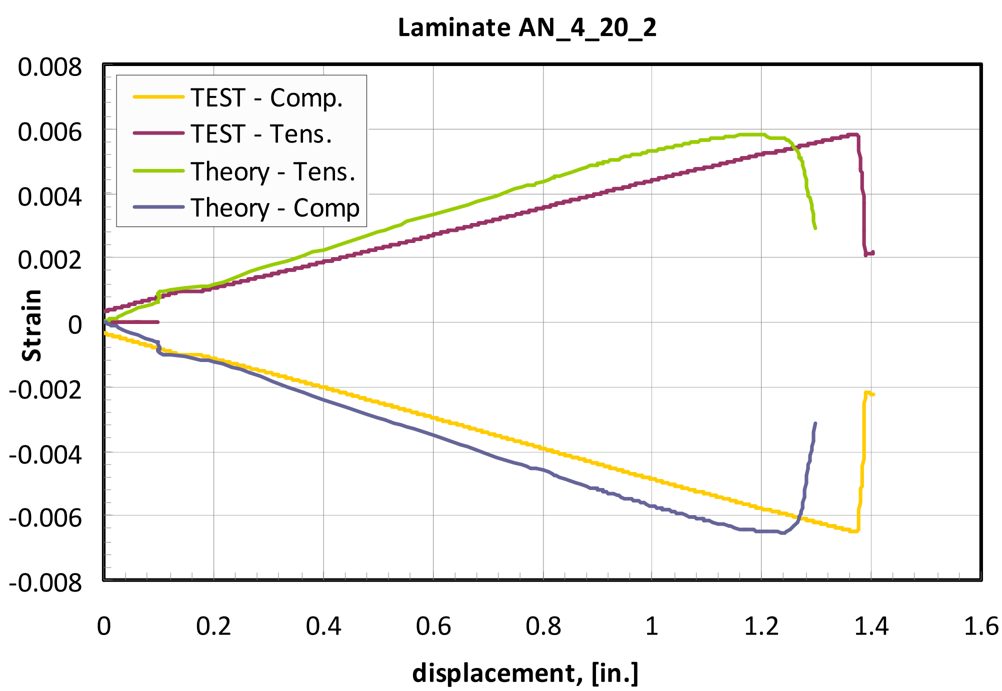

Figure A. 46 - Progressive Damage of Laminate AN_4_20_2

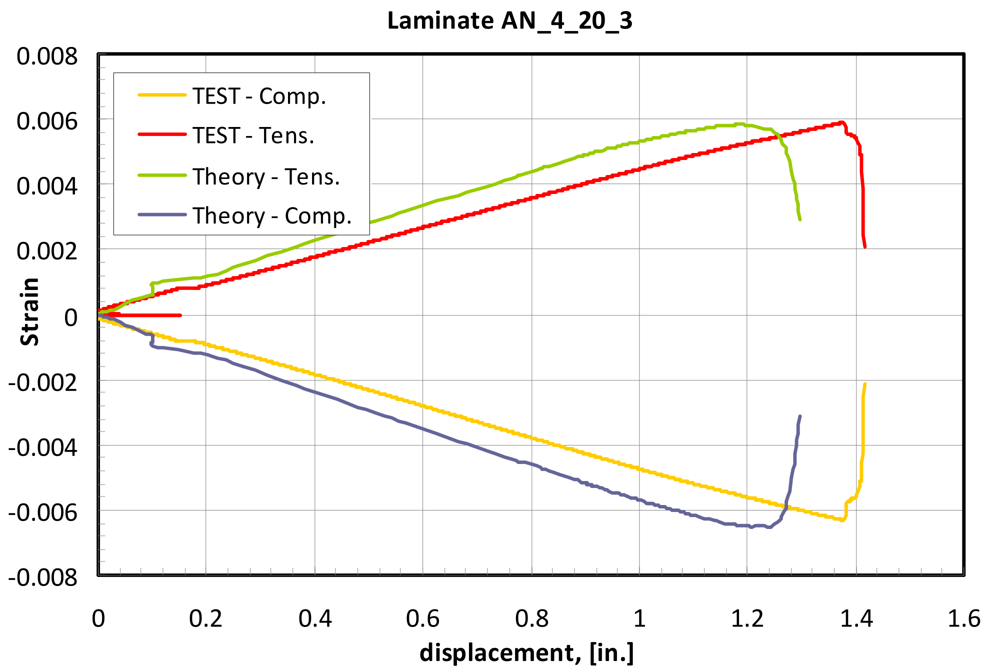

Figure A. 47 - Progressive Damage of Laminate AN_4_20_3

APPENDIX B – Photographic Images of the 20-ply Laminates after Failure

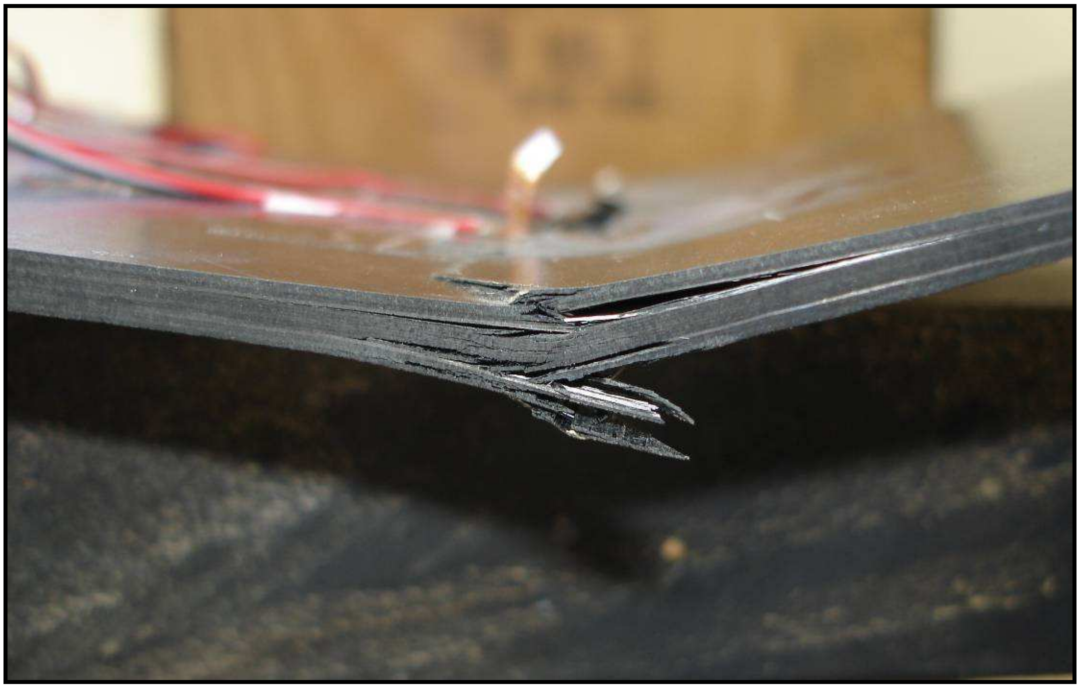

Figure B. 1 - Laminate F_1_5_1

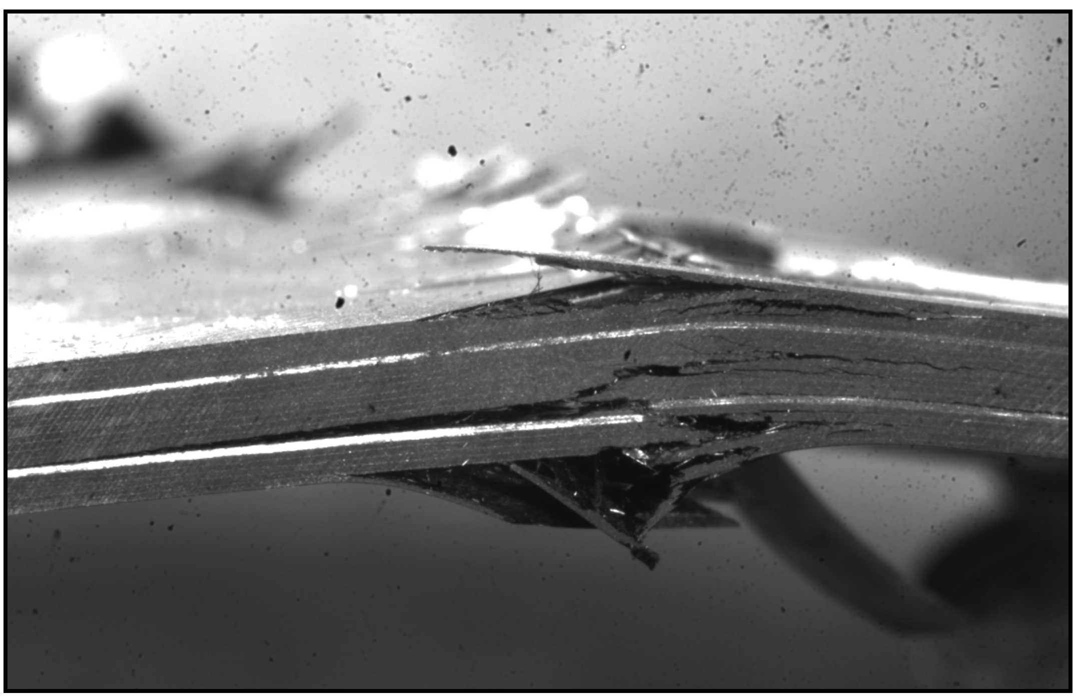

Figure B. 2 - Laminate F_1_5_2

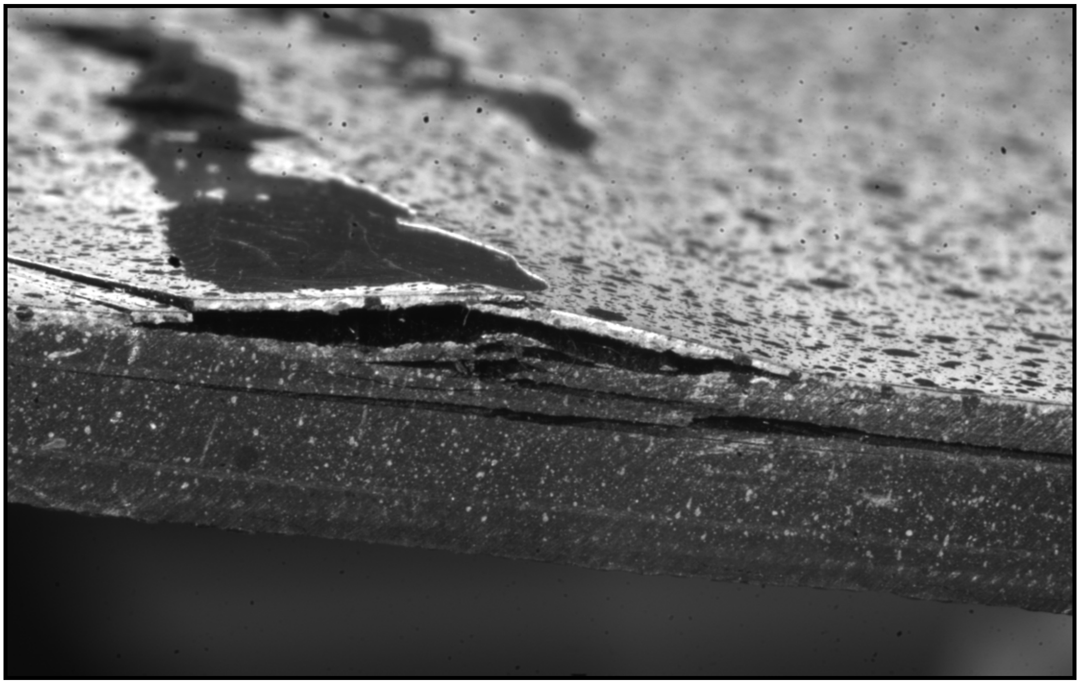

Figure B. 3 - Laminate F_1_5_3

Figure B. 4 - Laminate F_1_10_1

Figure B. 5 - Laminate F_1_10_2

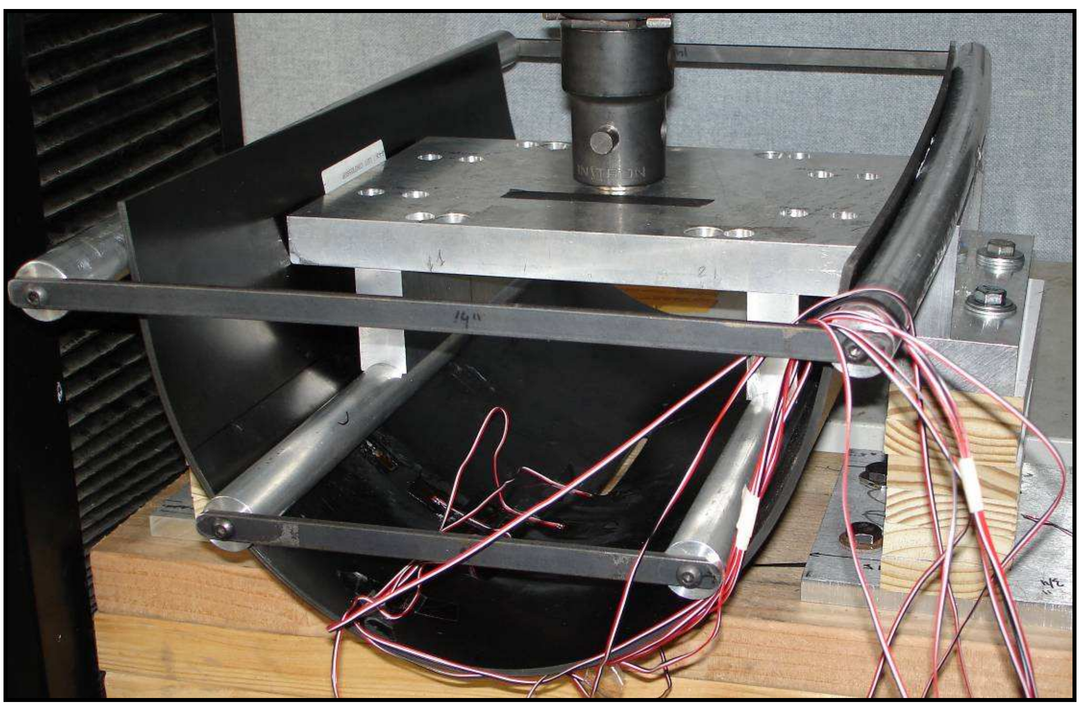

Figure B. 6 - Laminate F_4_20_1

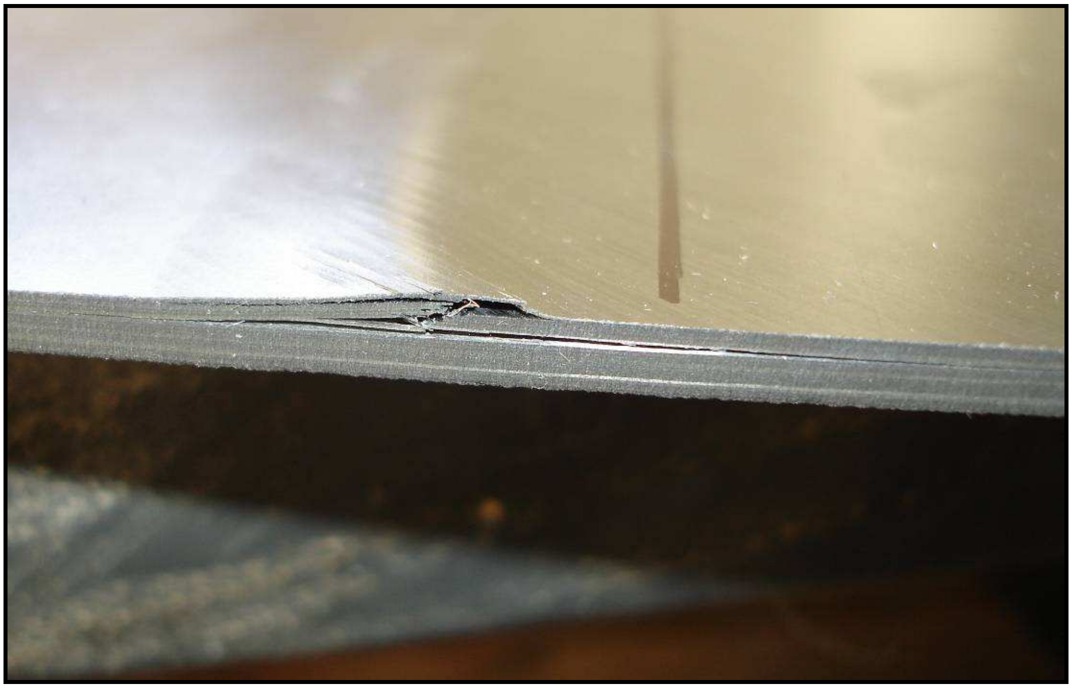

Figure B. 7 - Laminate F_4_20_2

Figure B. 8 - Laminate F_4_20_3

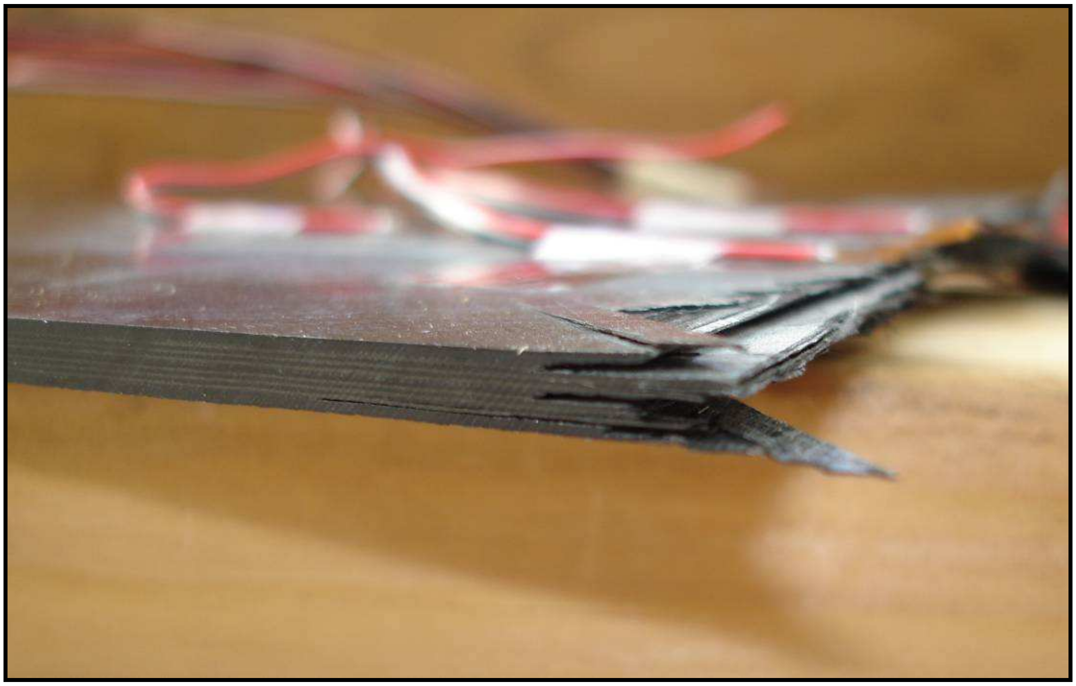

Figure B. 9 - Laminate P_1_5_1

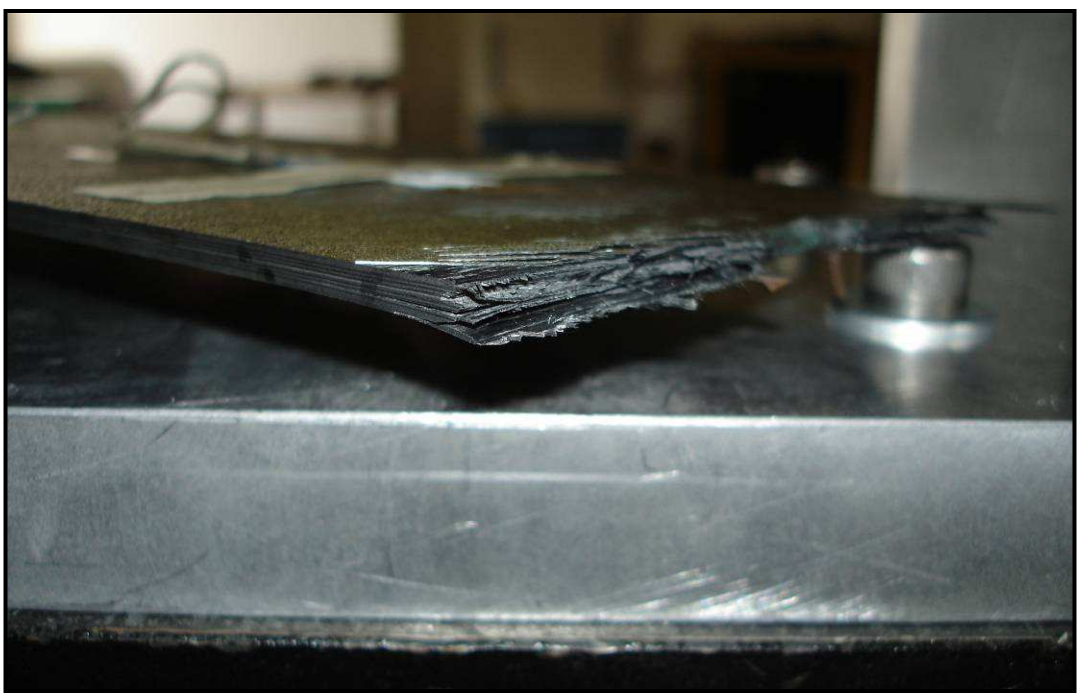

Figure B. 10 - Laminate P_1_5_2

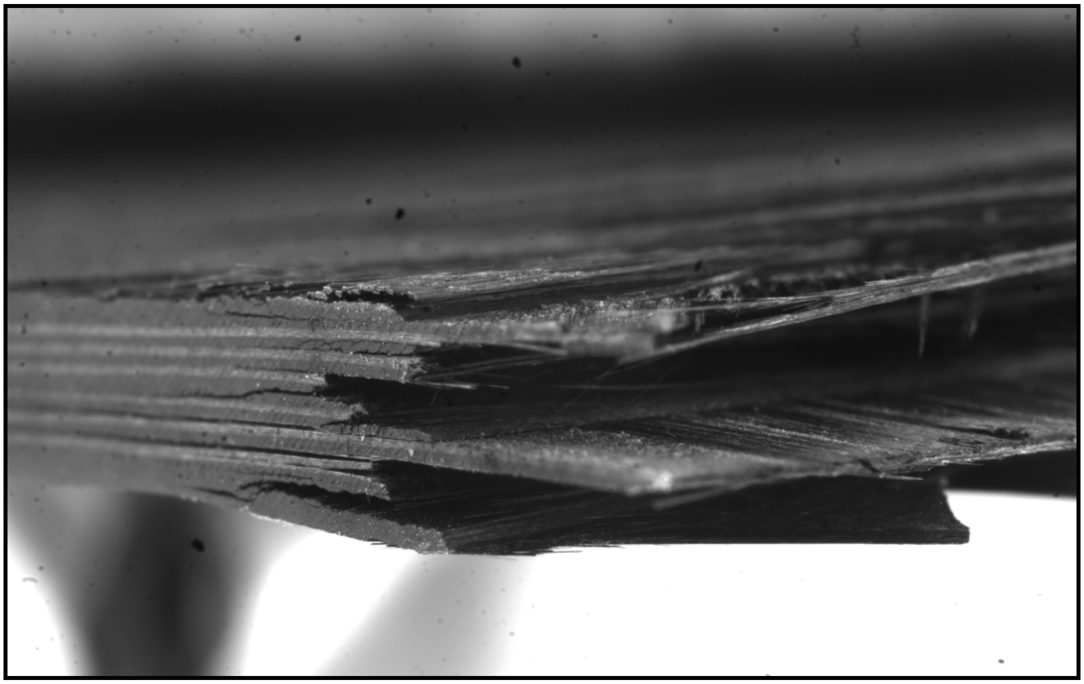

Figure B. 11 - Laminate P_1_5_3

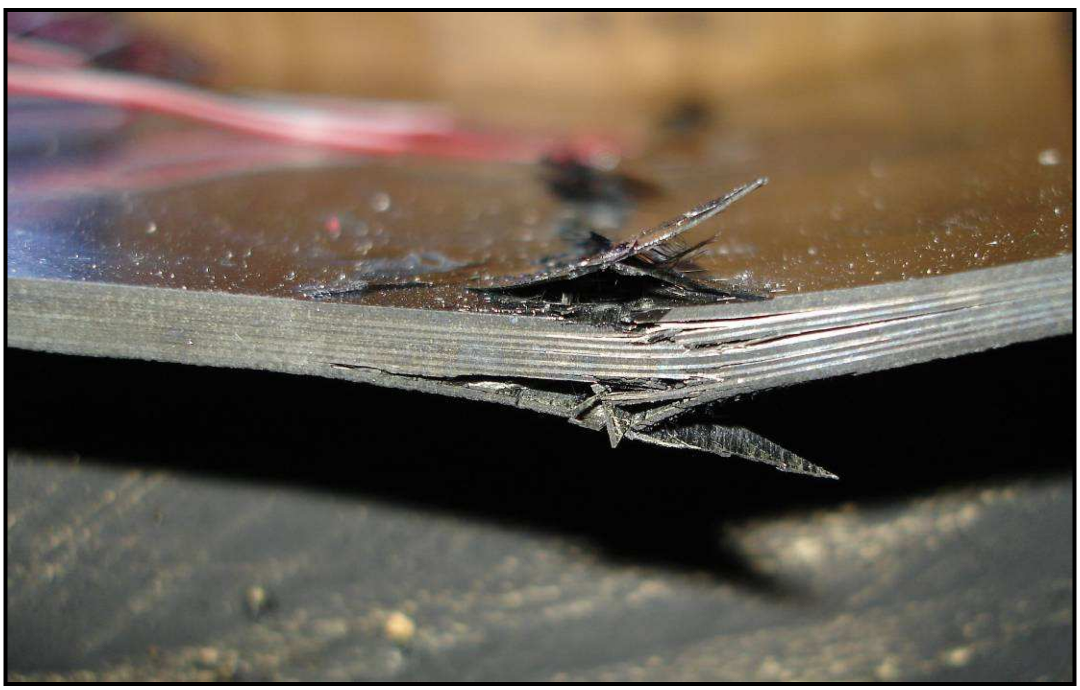

Figure B. 12 - Laminate P_1_10_1

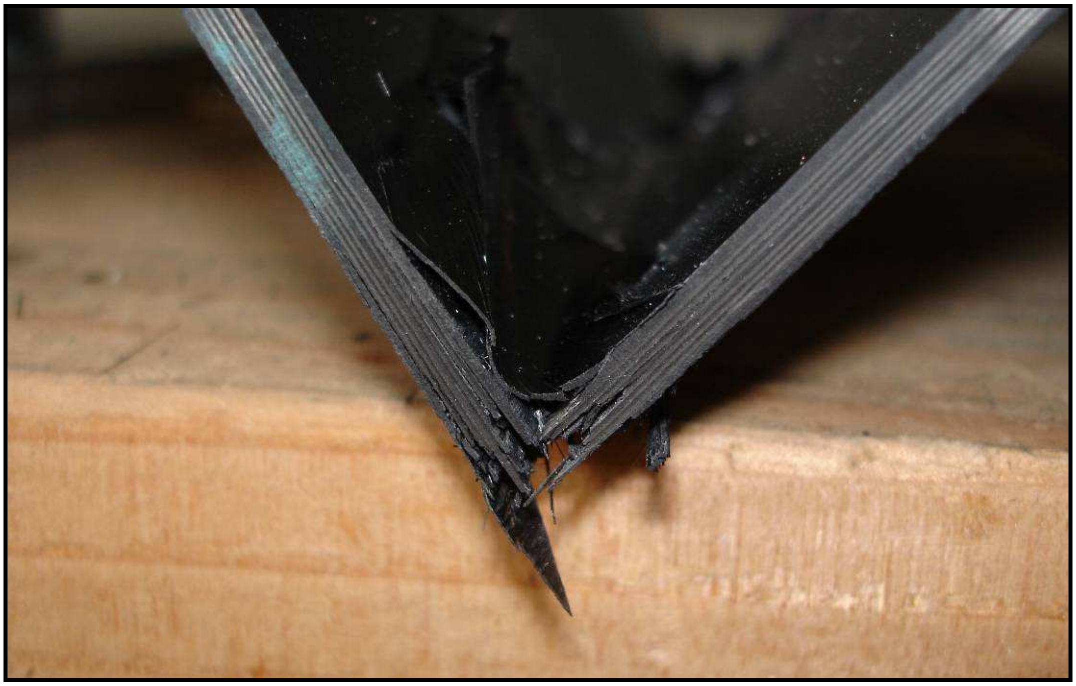

Figure B. 13 - Laminate P_1_10_2

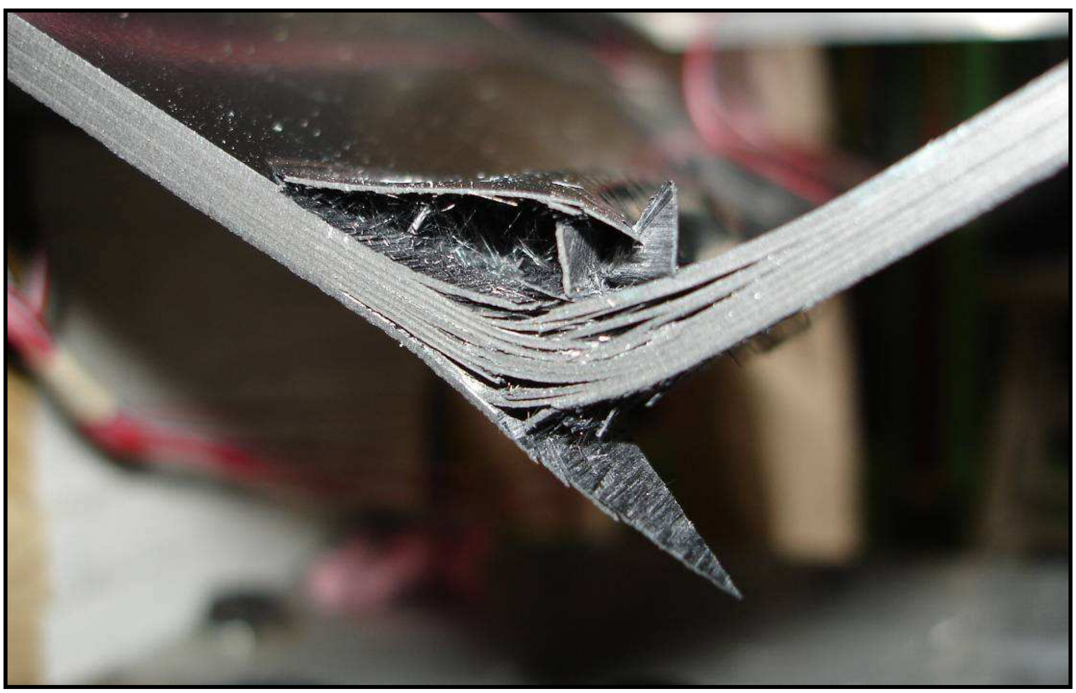

Figure B. 14 - Laminate P_4_20_1

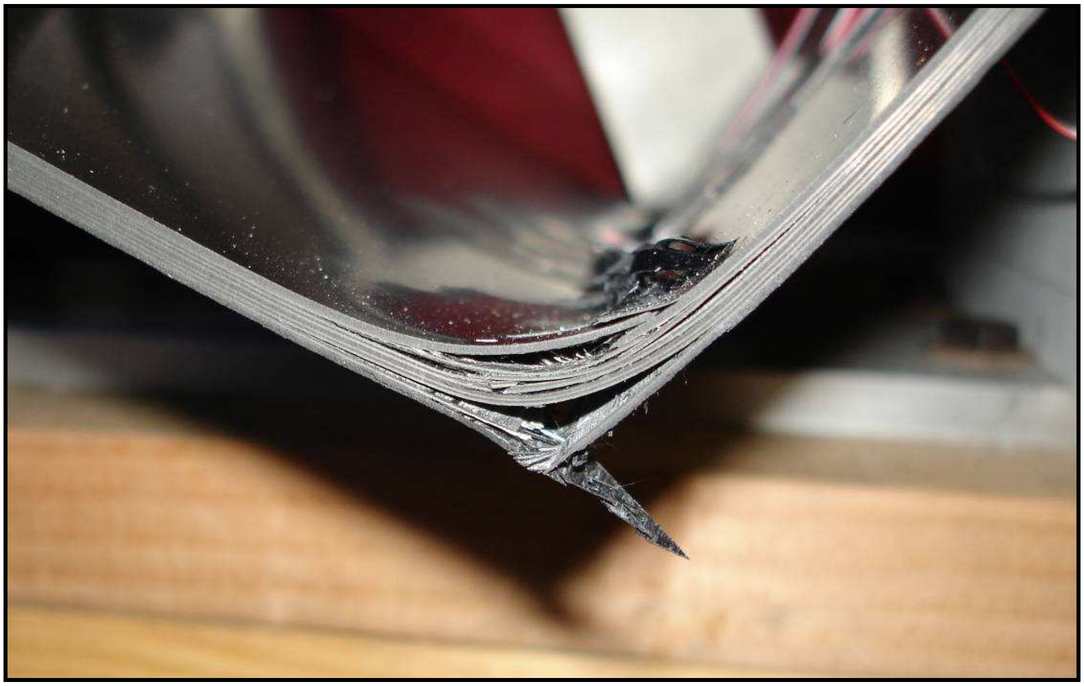

Figure B. 15 - Laminate P_4_20_2

Figure B. 16 - Laminate P_4_20_3

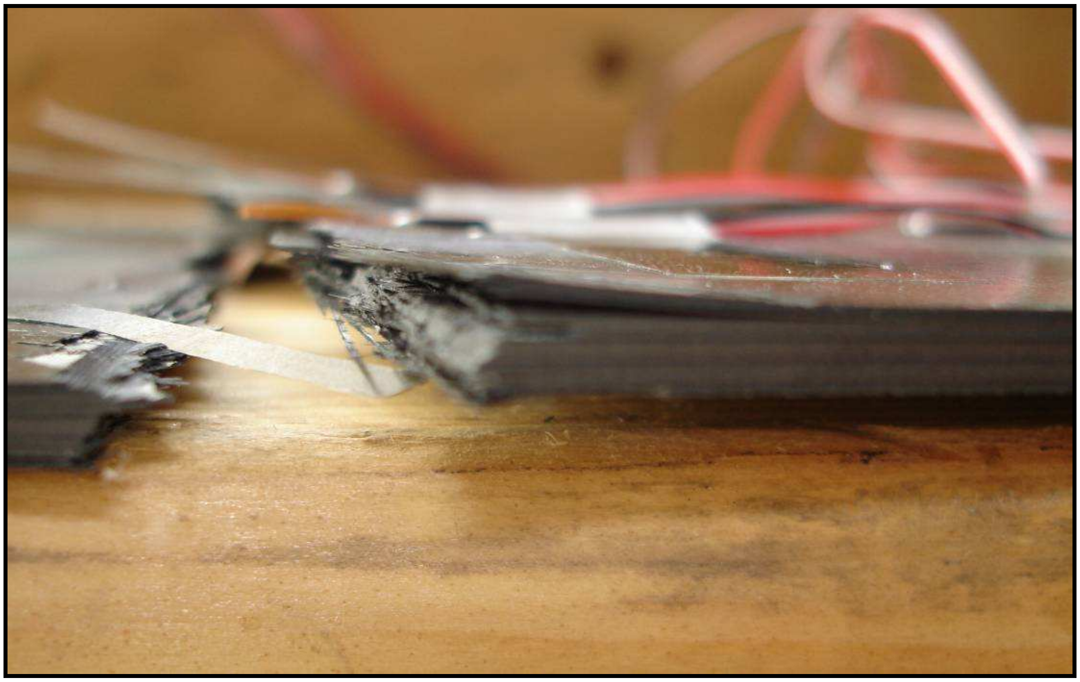

Figure B. 17 - Laminate N_1_5_1

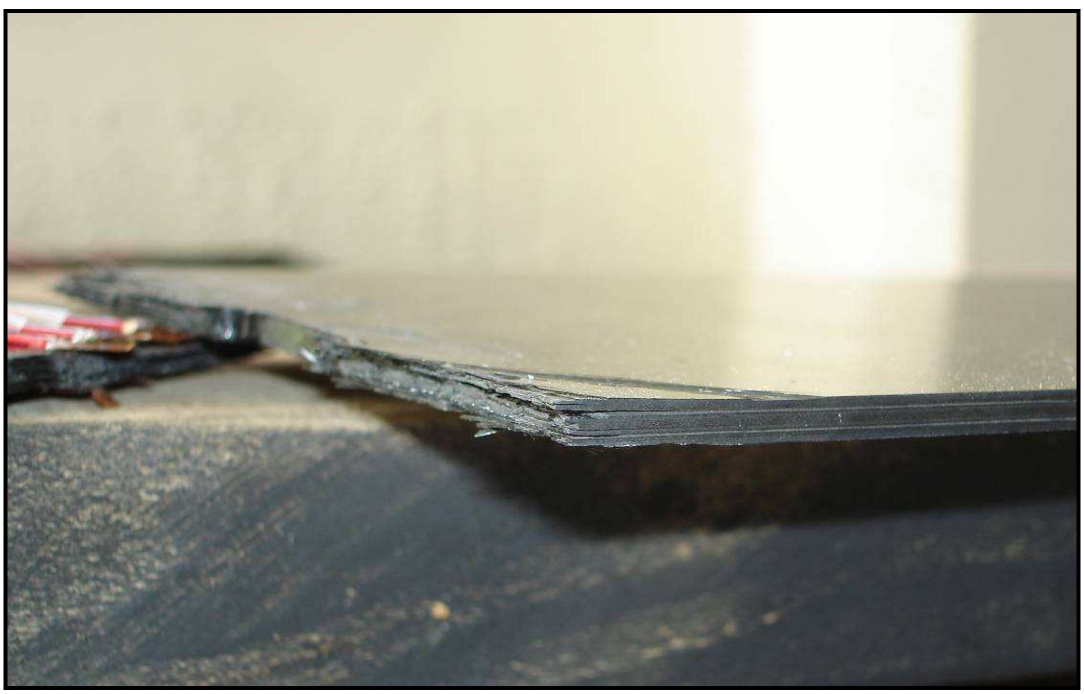

Figure B. 18 - Laminate N_1_5_2

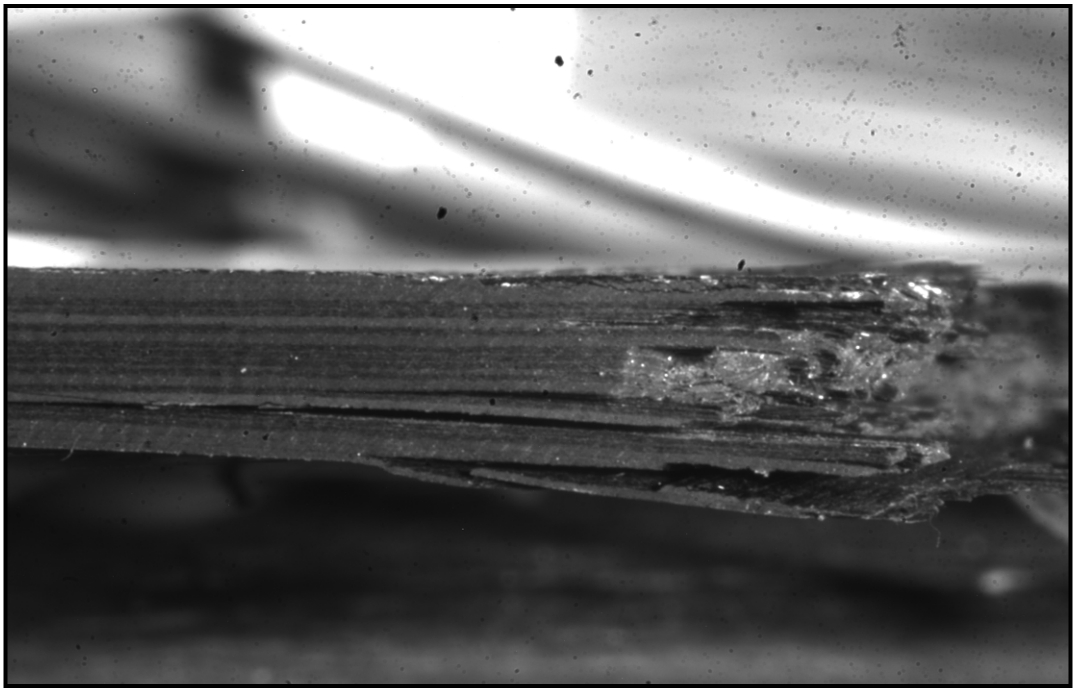

Figure B. 19 - Laminate N_1_5_3

Figure B. 20 - Laminate N_1_10_1

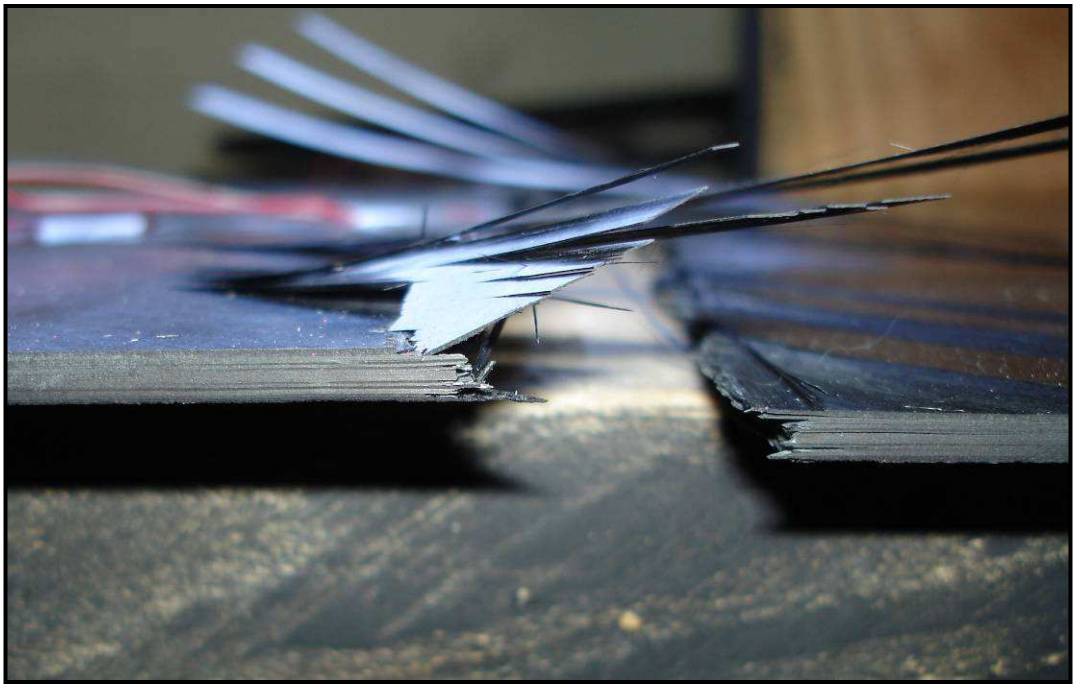

Figure B. 21 - Laminate N_1_10_2

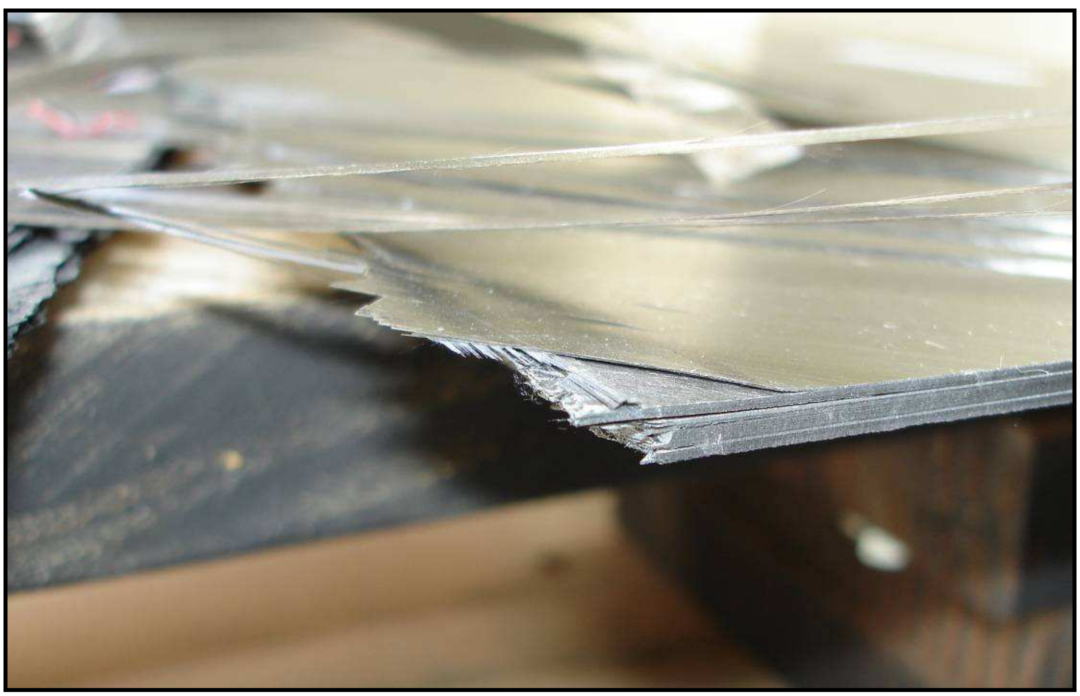

Figure B. 22 - Laminate N_4_20_1

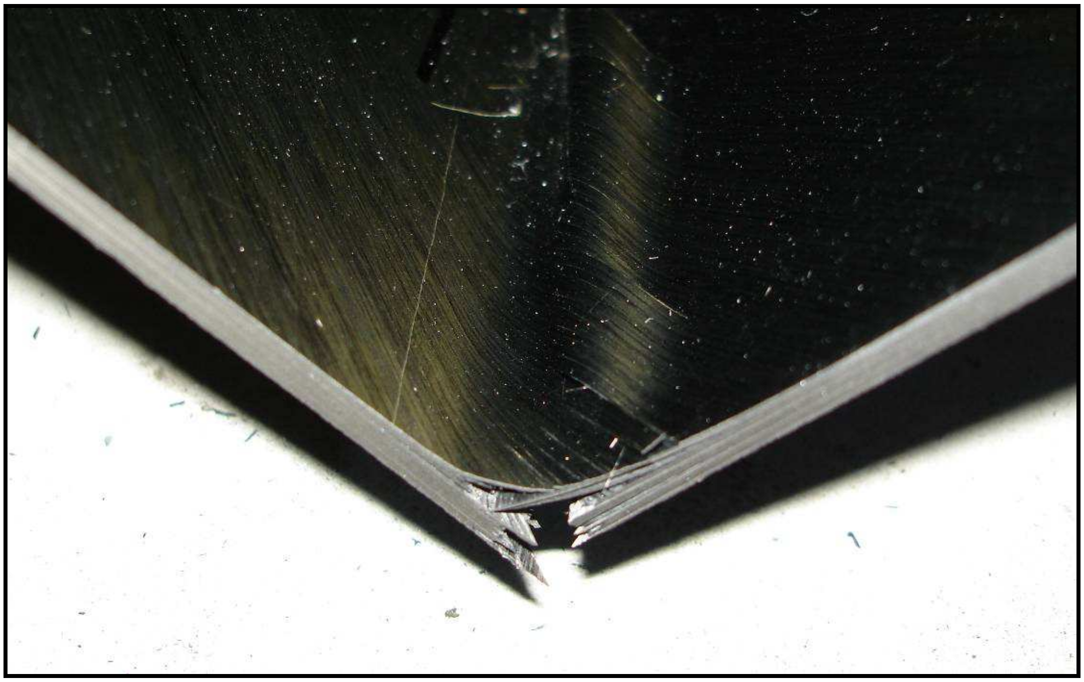

Figure B. 23 - Laminate N_4_20_2

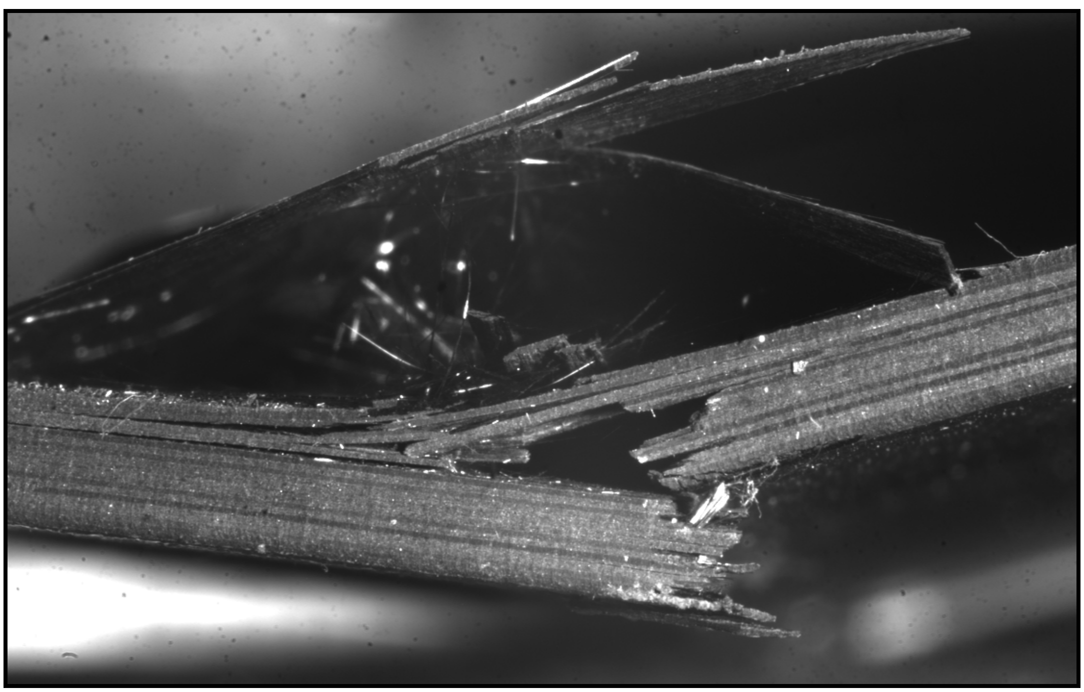

Figure B. 24 - Laminate N_4_20_3

APPENDIX C – Photographic Images of the 40-ply Laminates after Failure

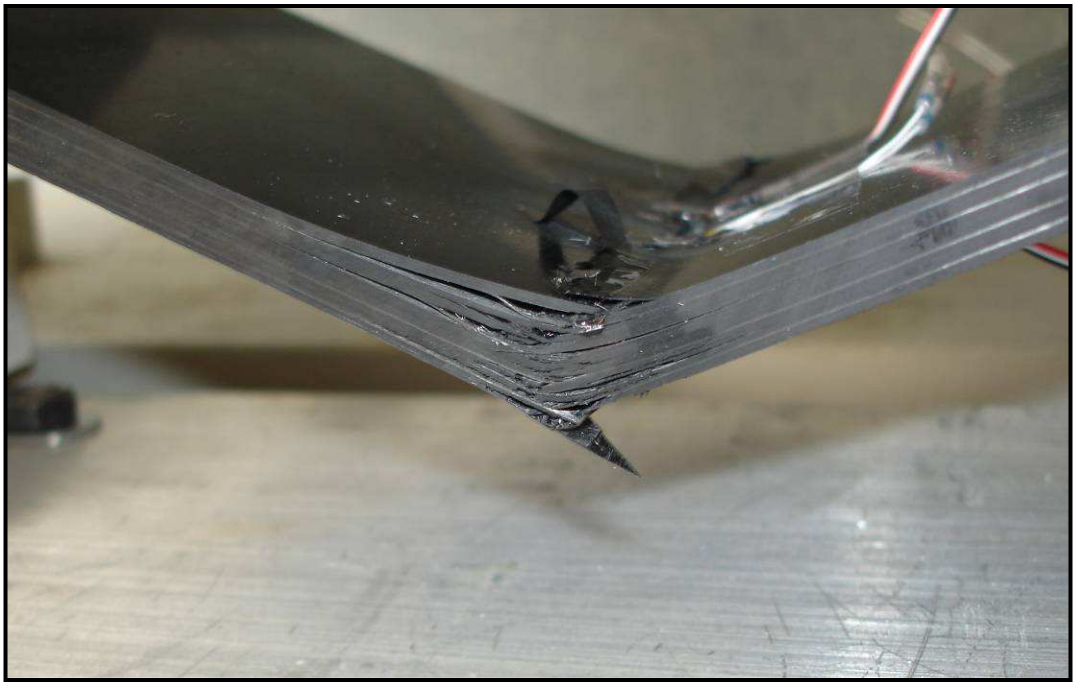

Figure C. 1 - Laminate FP_1_5_1

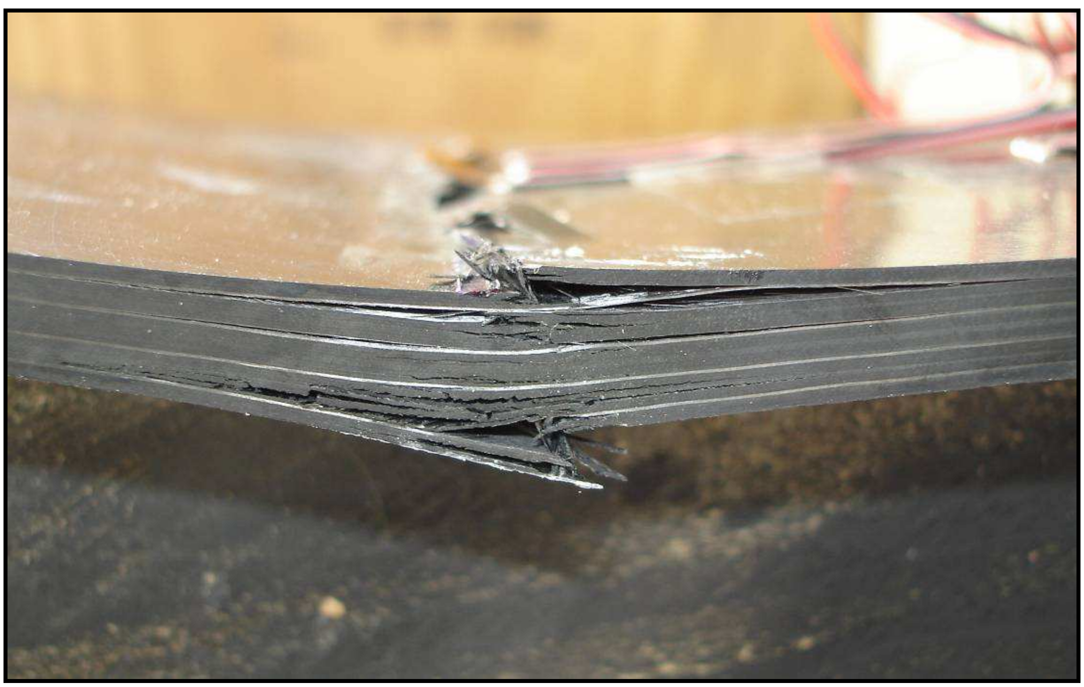

Figure C. 2 - Laminate FP_1_5_2

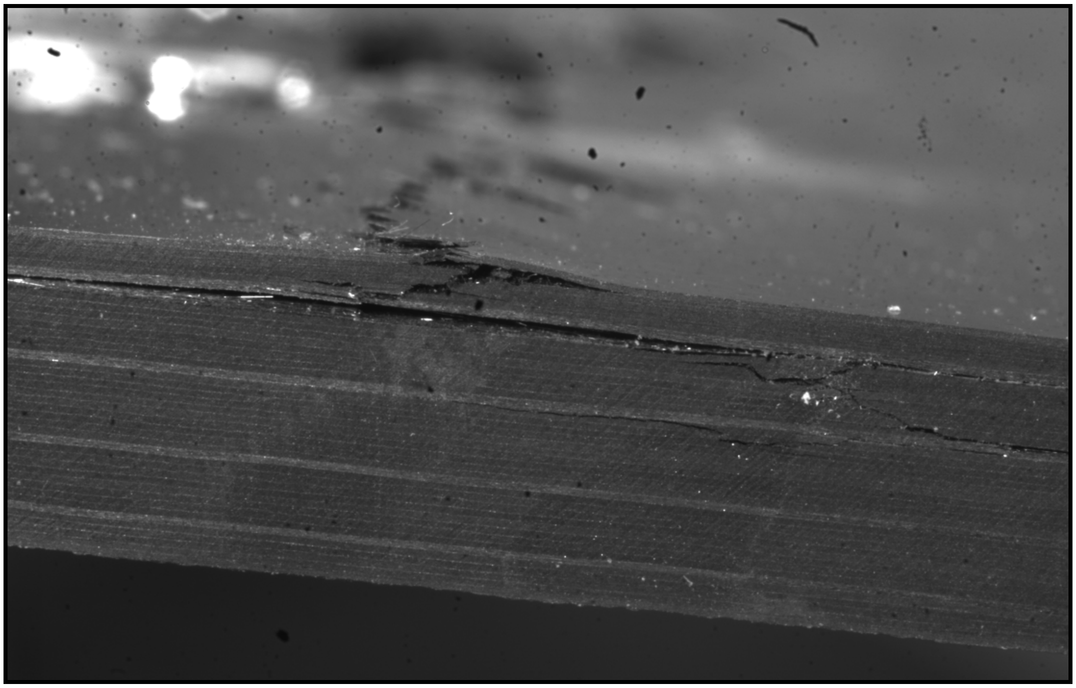

Figure C. 3 - Laminate FP_1_5_3

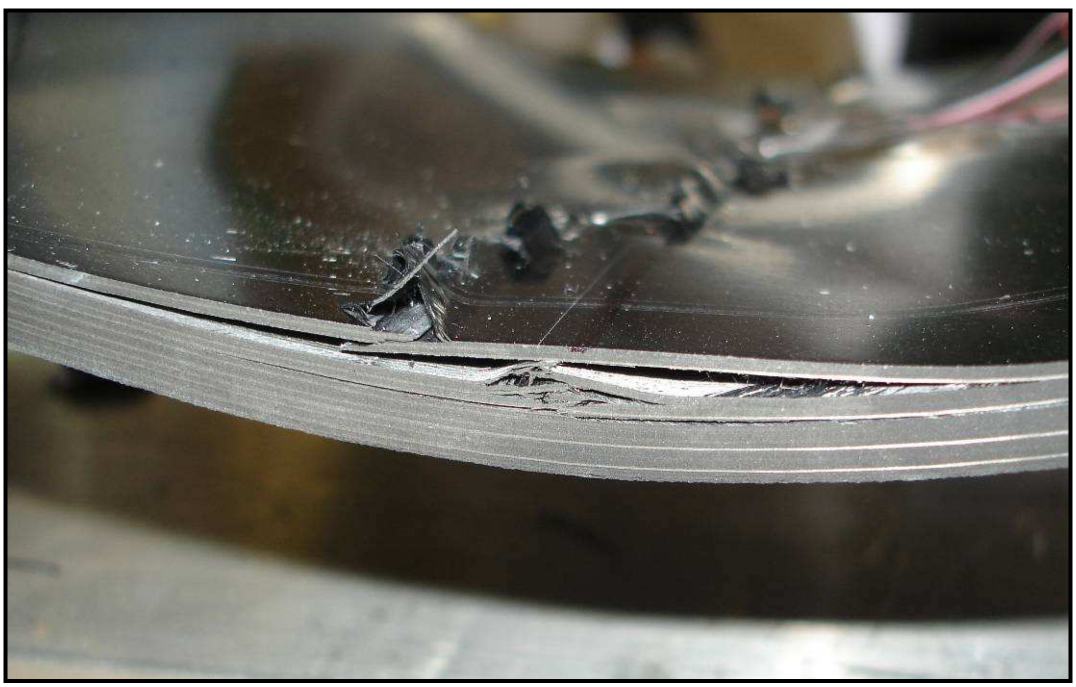

Figure C. 4 - Laminate FP_1_10_1

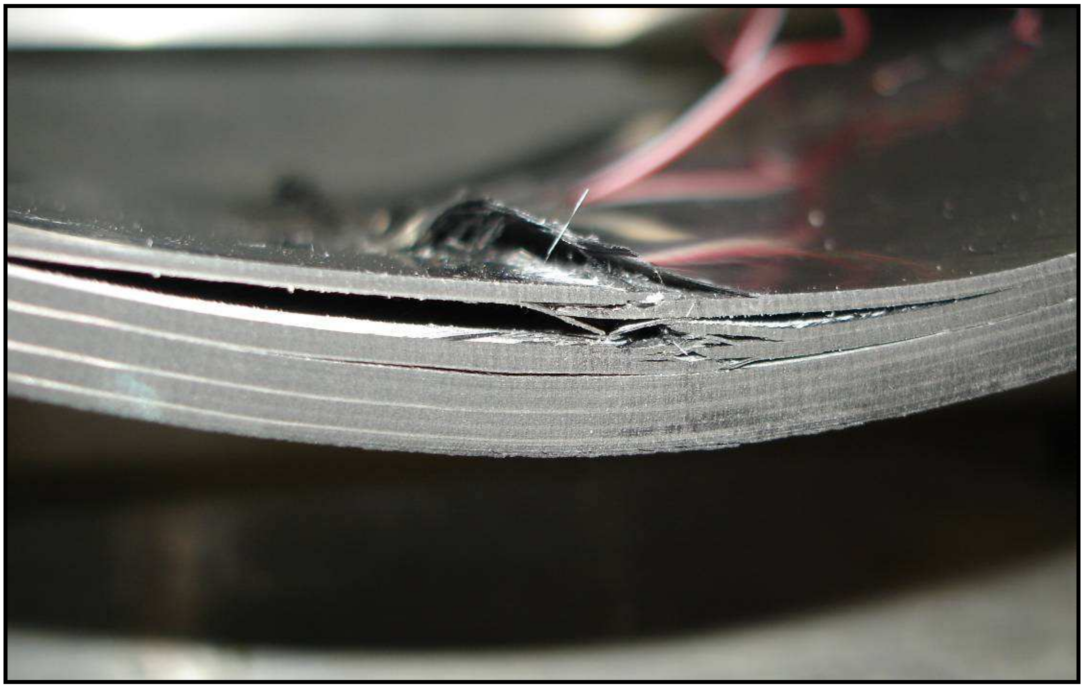

Figure C. 5 - Laminate FP_1_10_2

Figure C. 6 - Laminate FP_4_20_1

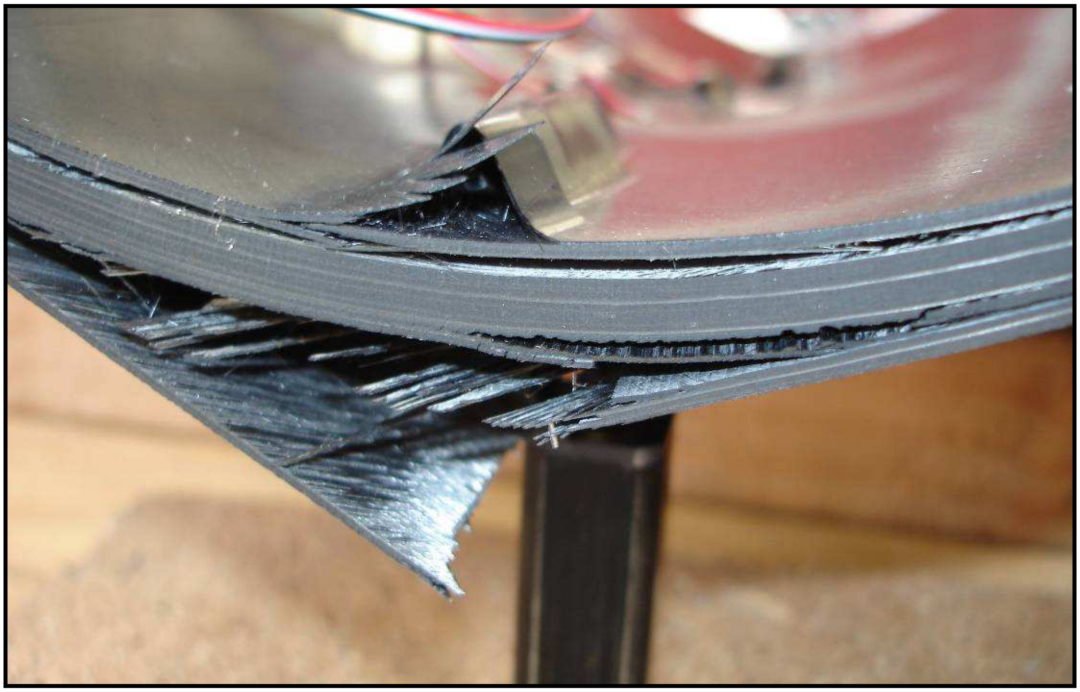

Figure C. 7 - Laminate FP_4_20_2

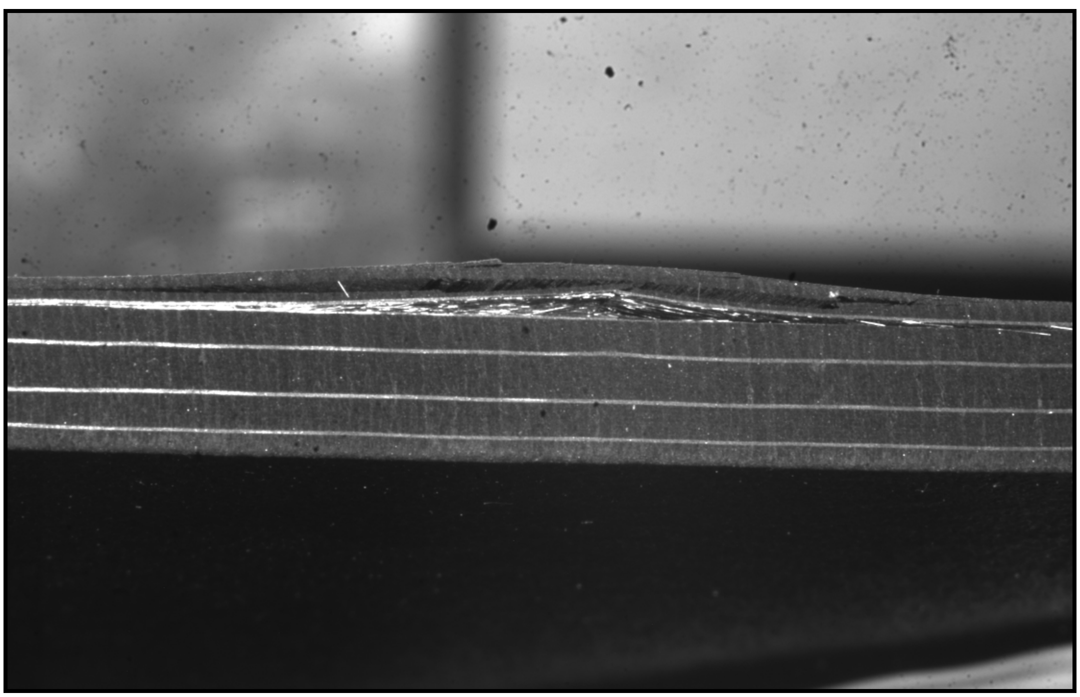

Figure C. 8 - Laminate FP_4_20_3

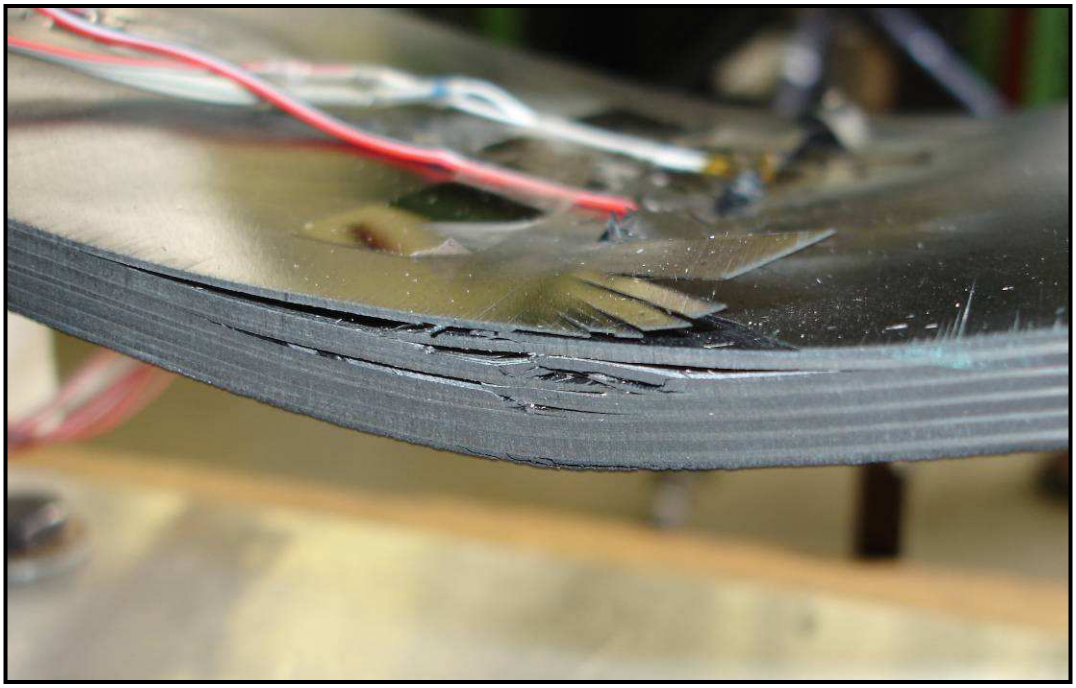

Figure C. 9 - Laminate AR_1_5_1

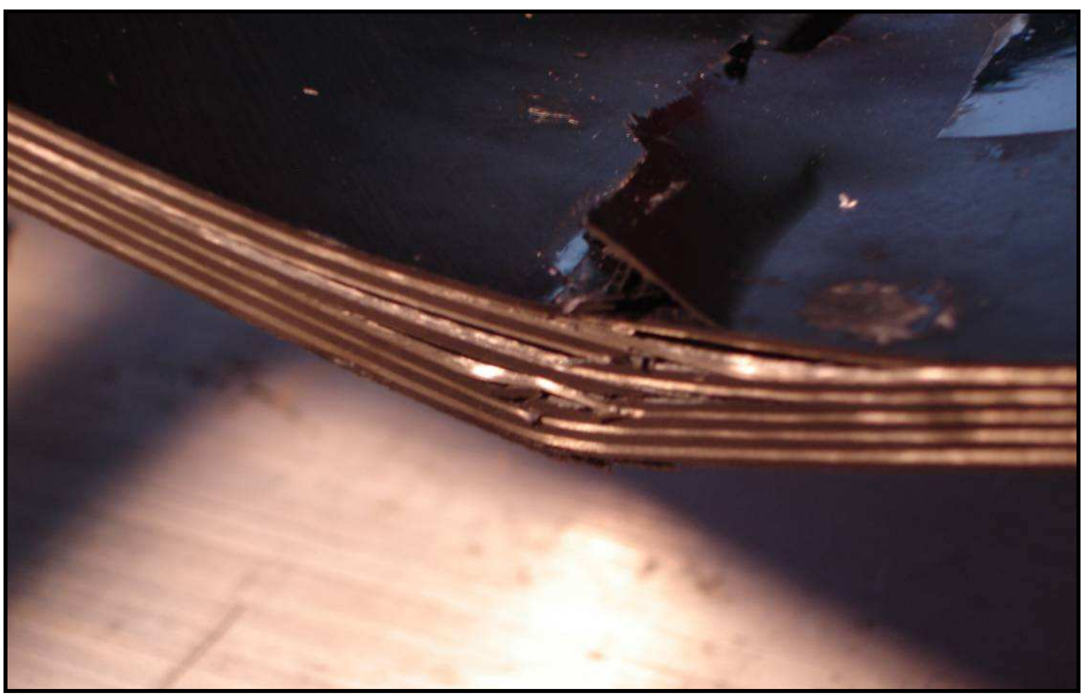

Figure C. 10 - Laminate AR_1_5_2

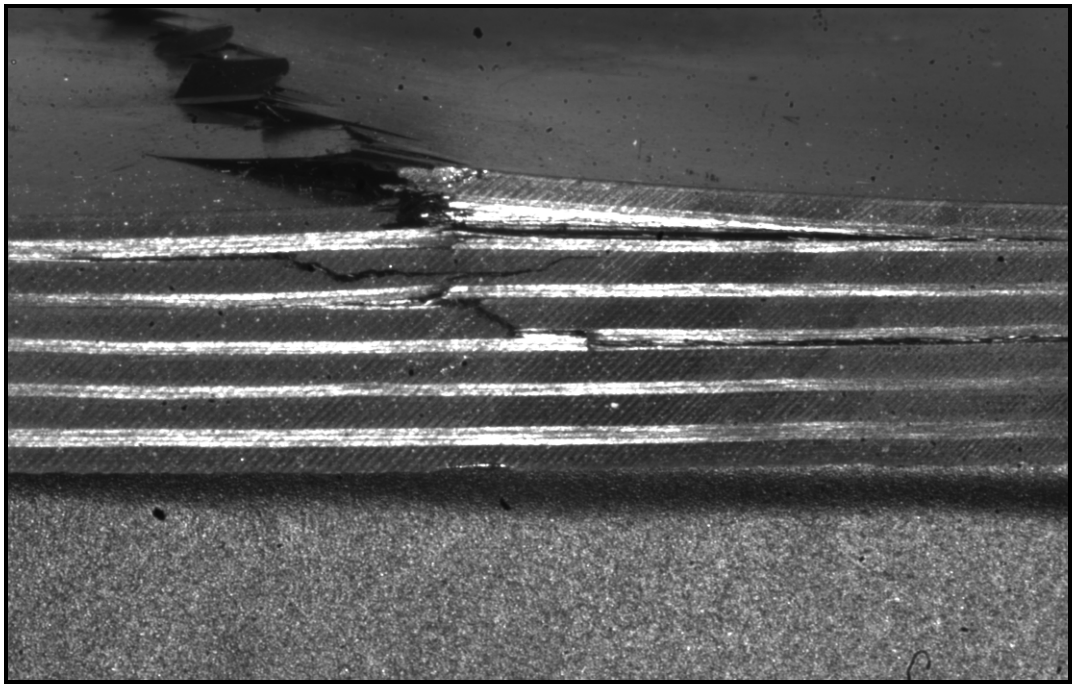

Figure C. 11 - Laminate AR_1_5_3

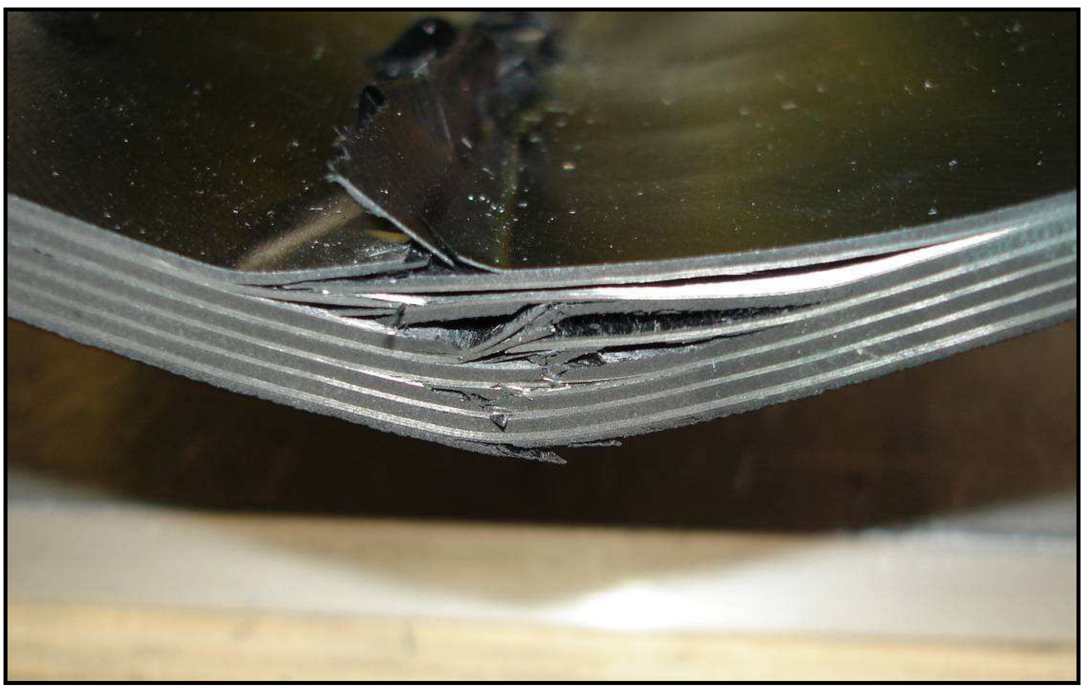

Figure C. 12 - Laminate AR_1_10_1

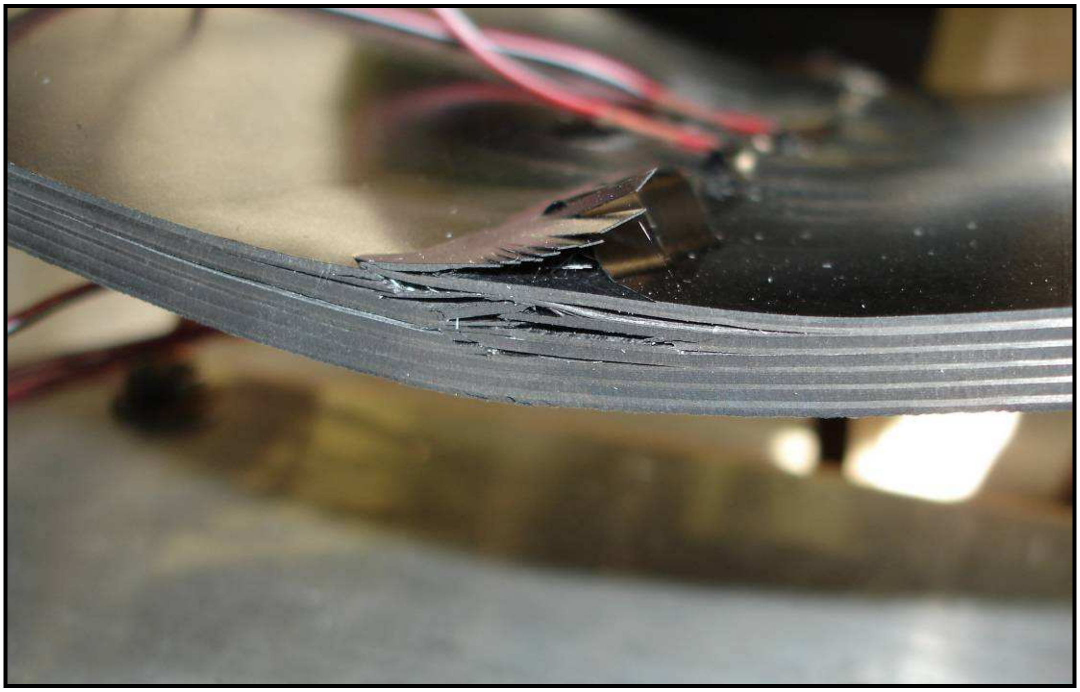

Figure C. 13 - Laminate AR_1_10_2

Figure C. 14 - Laminate AR_4_20_1

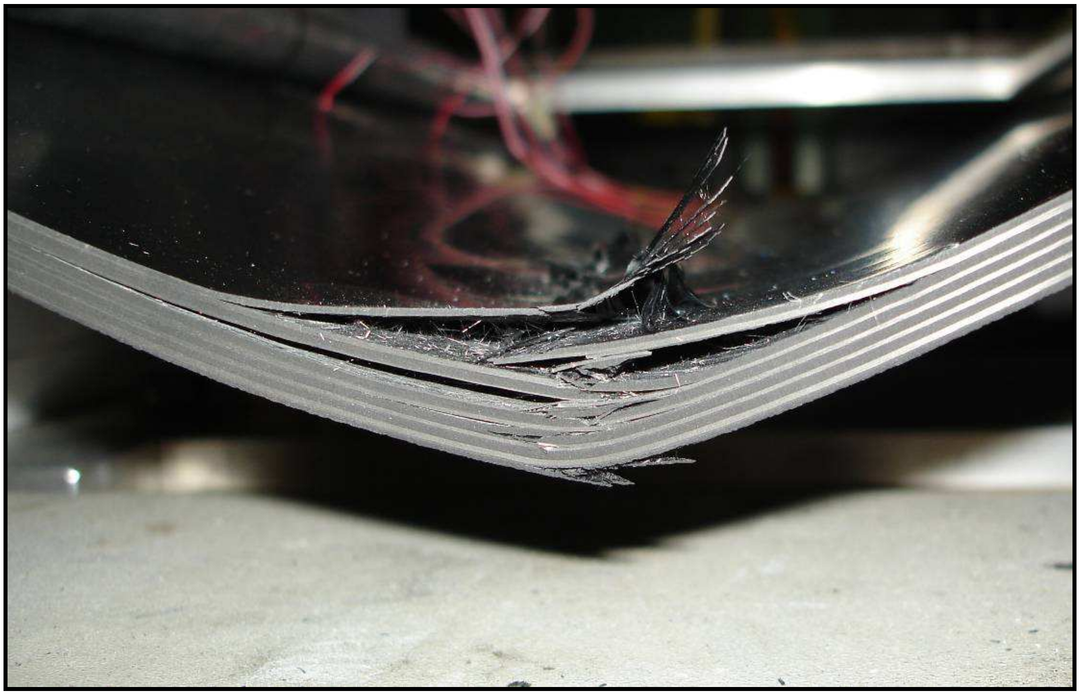

Figure C. 15 - Laminate AR_4_20_2

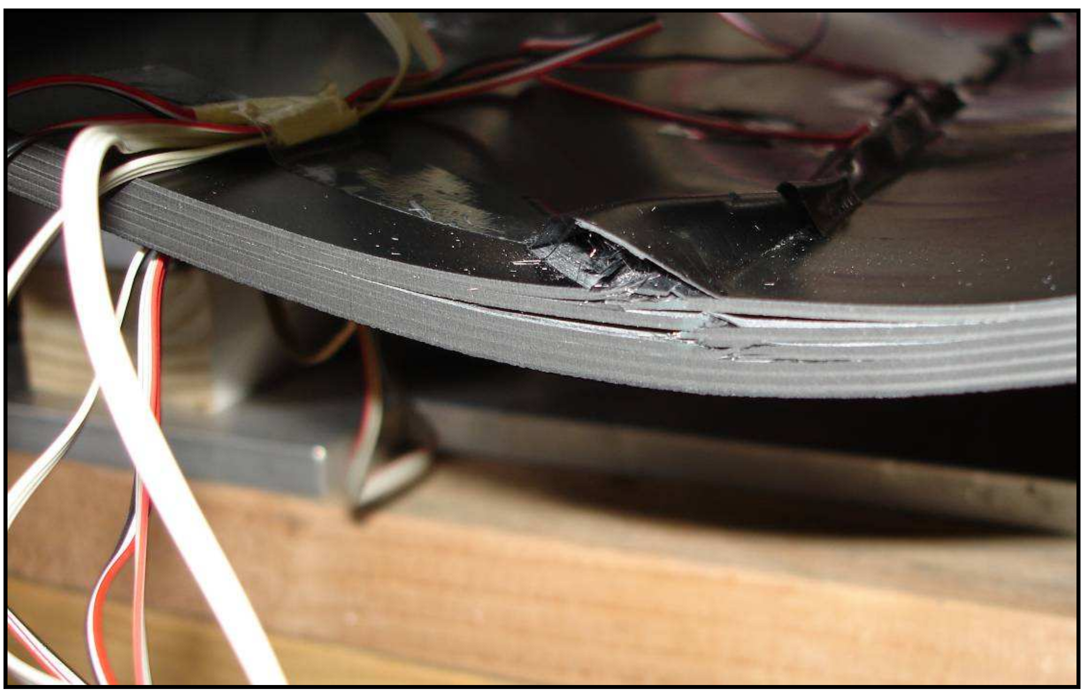

Figure C. 16 - Laminate AR_4_20_3

Figure C. 17 - Laminate AN_1_5_1

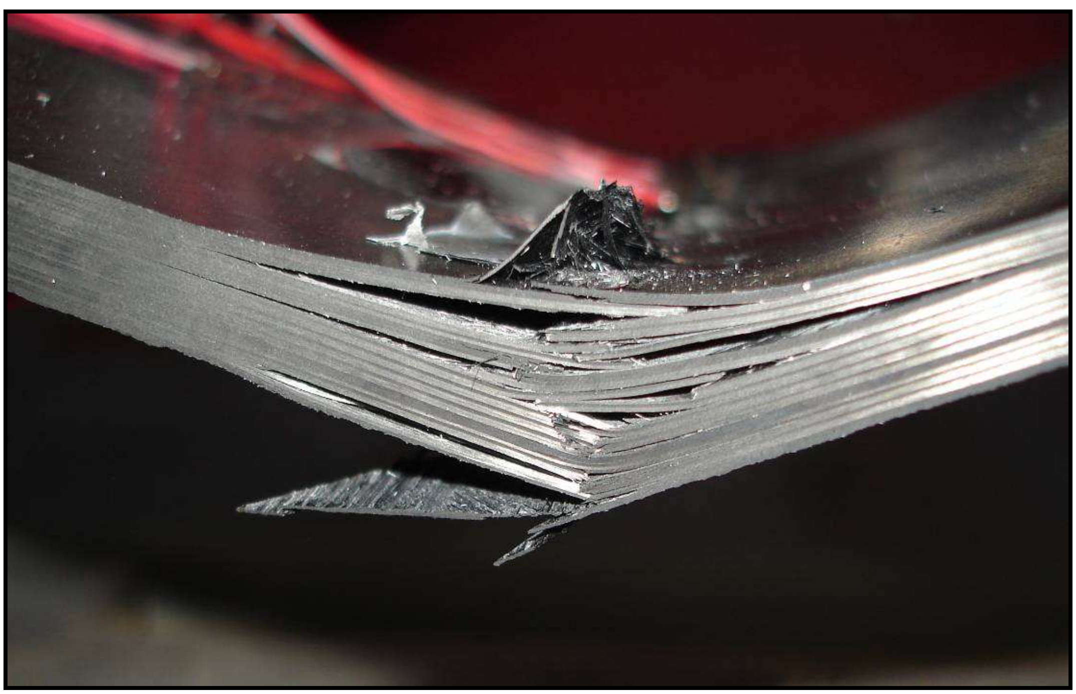

Figure C. 18 - Laminate AN_1_5_2

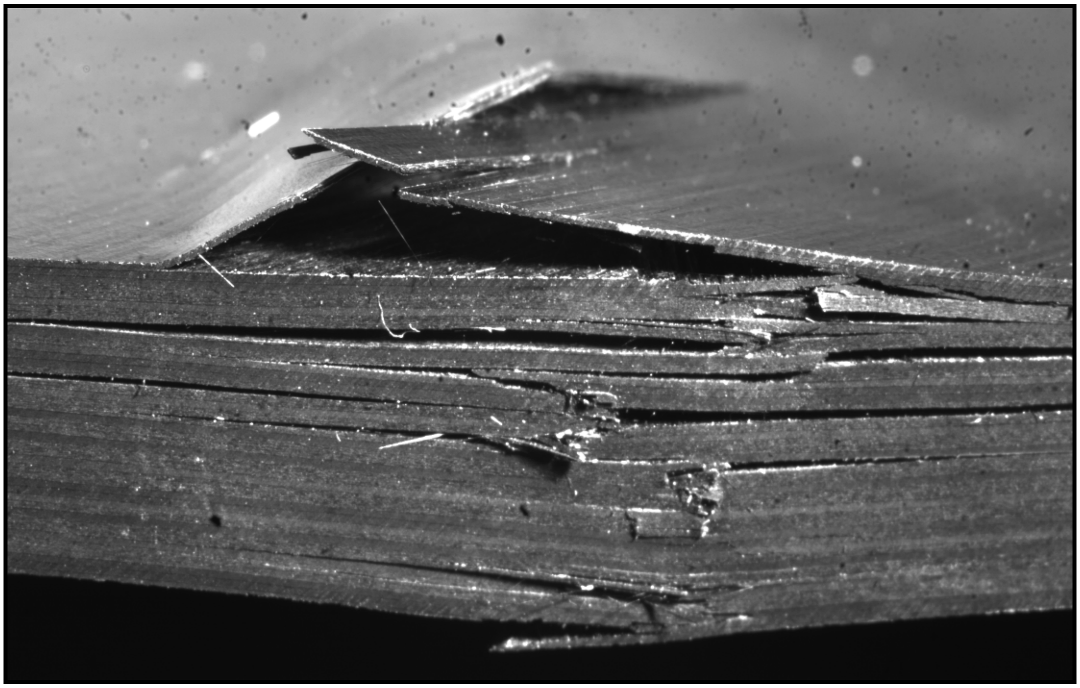

Figure C. 19 - Laminate AN_1_5_3

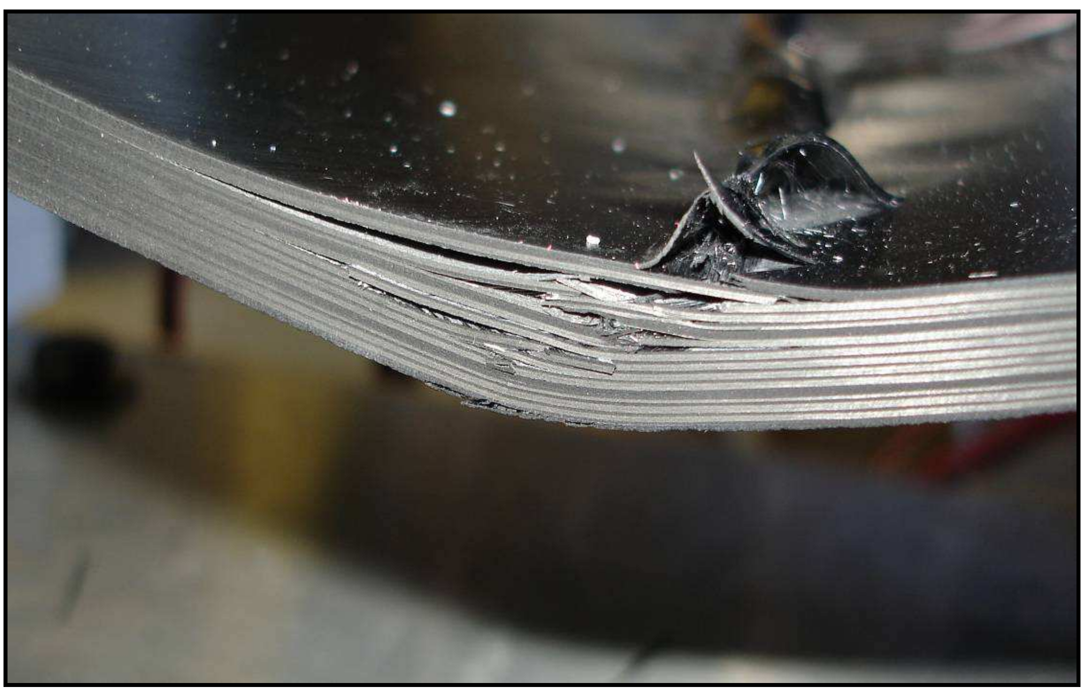

Figure C. 20 - Laminate AN_1_10_1

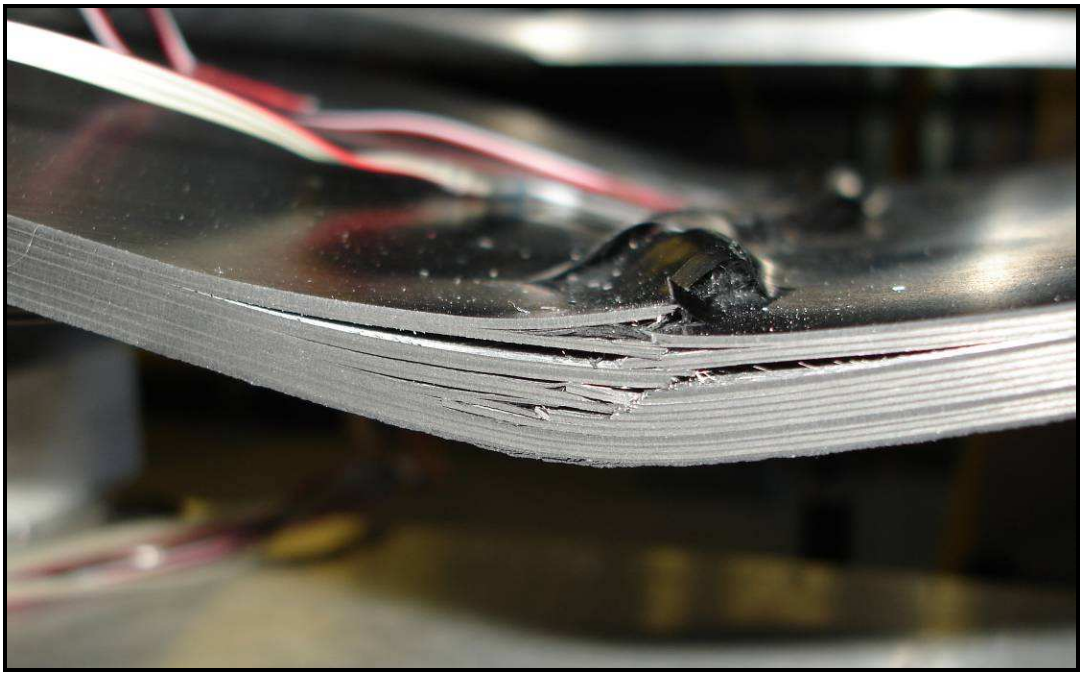

Figure C. 21 - Laminate AN_1_10_2

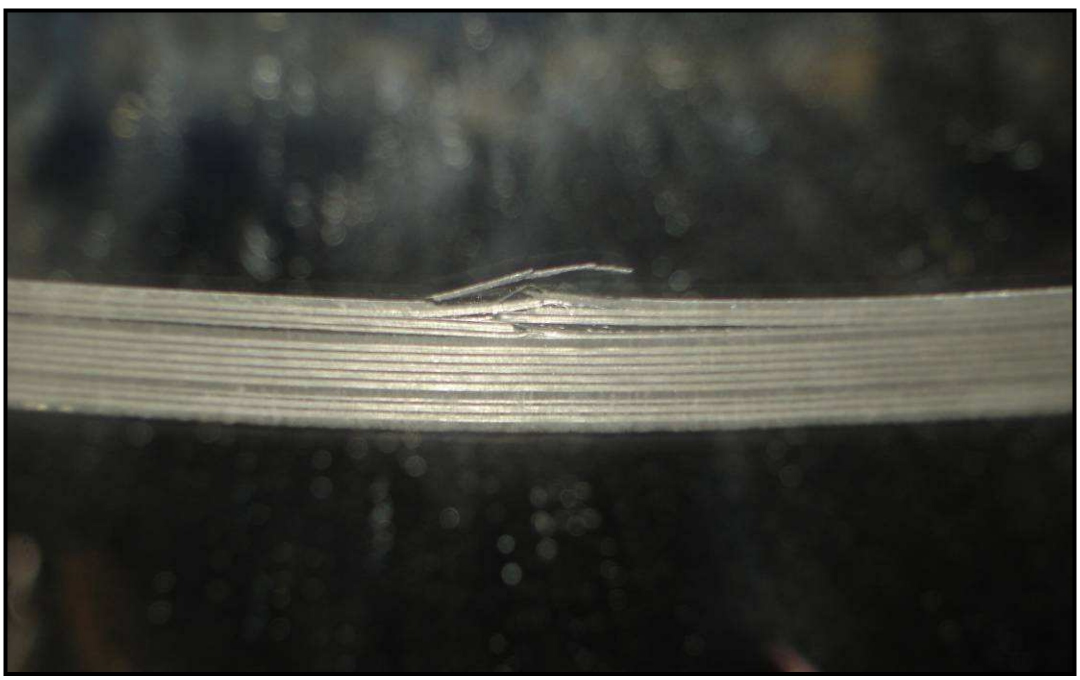

Figure C. 22 - Laminate AN_4_20_1

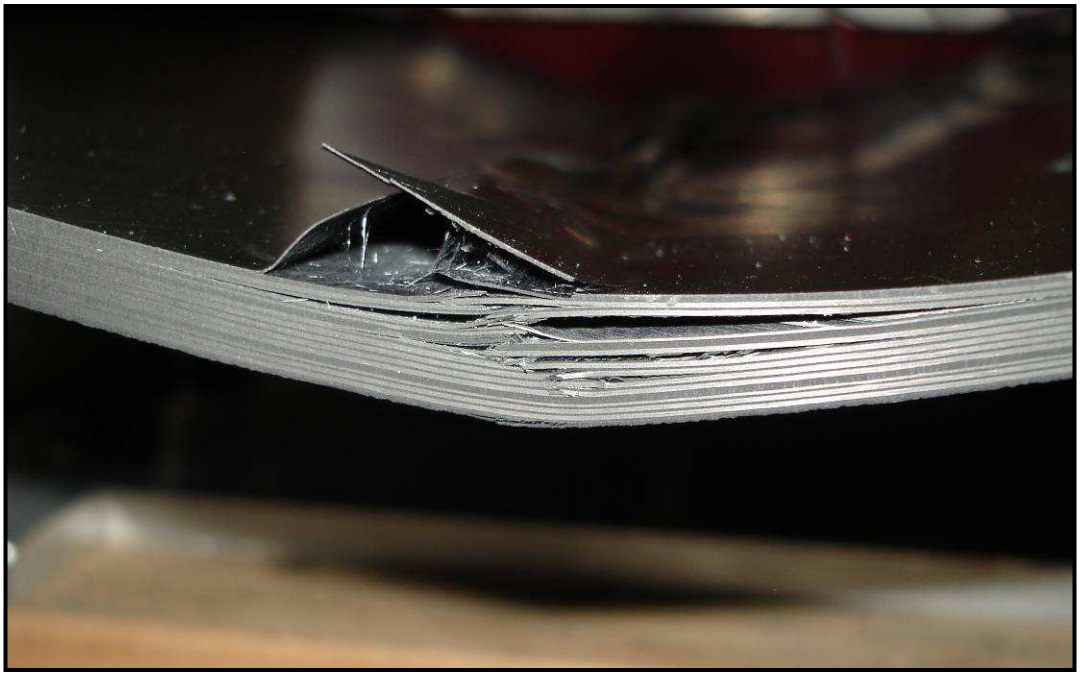

Figure C. 23 - Laminate AN_4_20_2

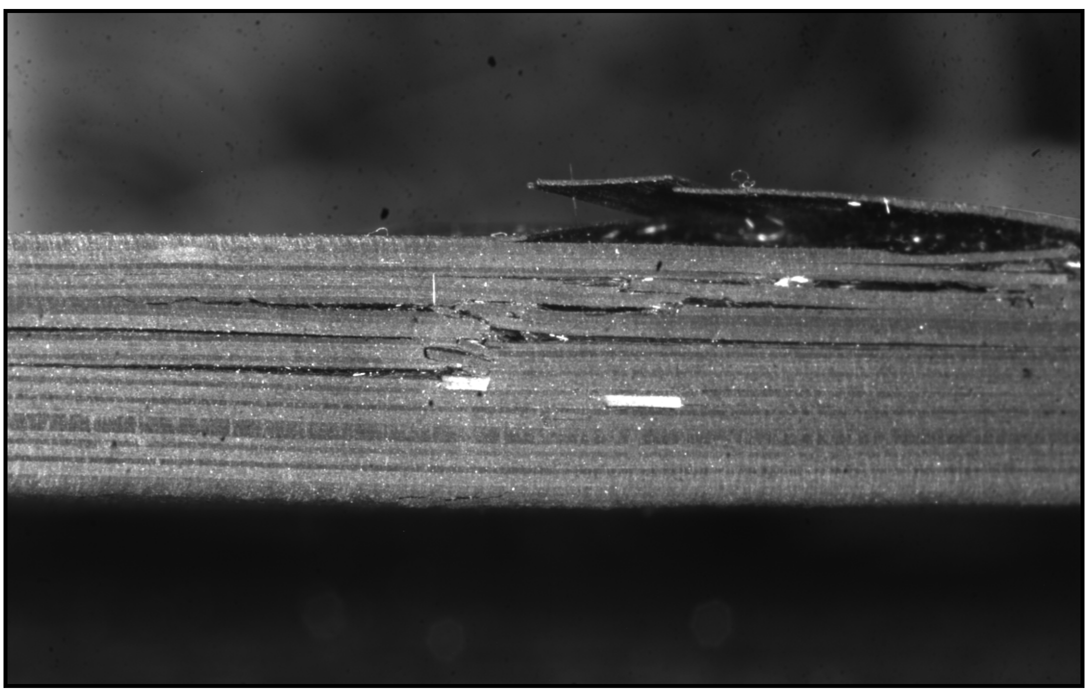

Figure C. 24 - Laminate AN_4_20_3

APPENDIX D – Labview Program

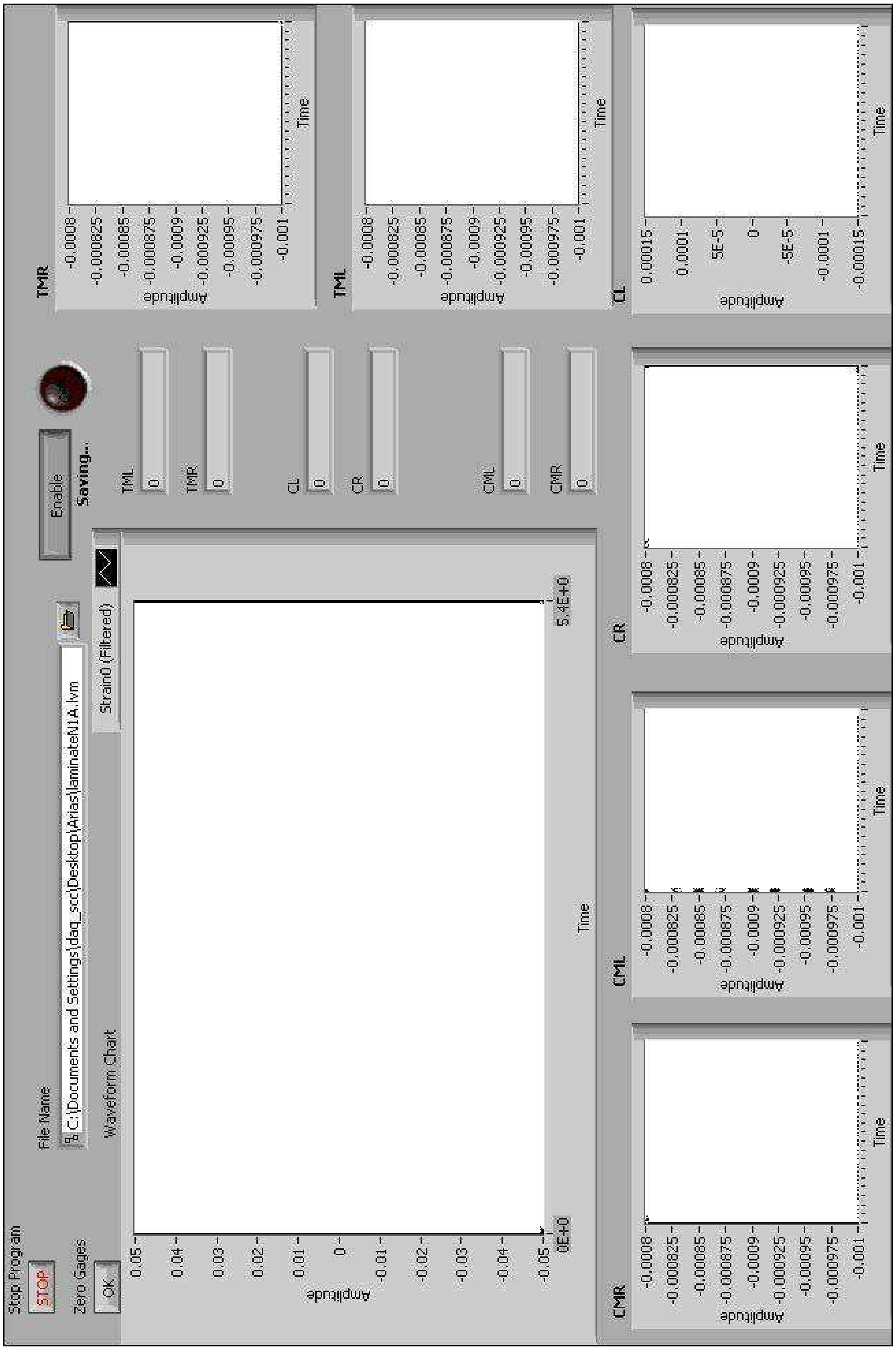

Figure D. 1 - Front panel of Labview program for a six gage output

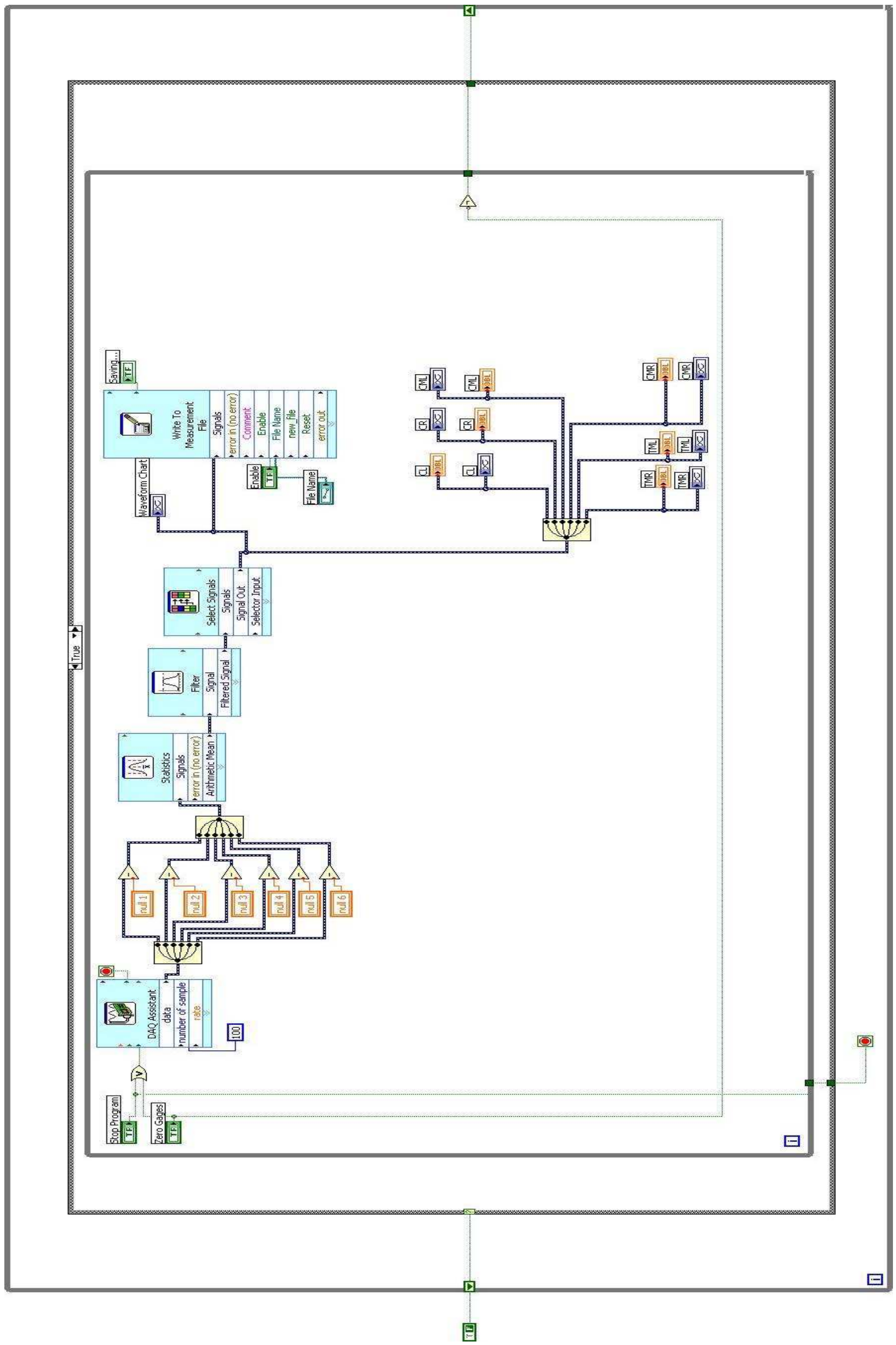

Figure D. 2 - Schematic of Loop1 of Labview progam

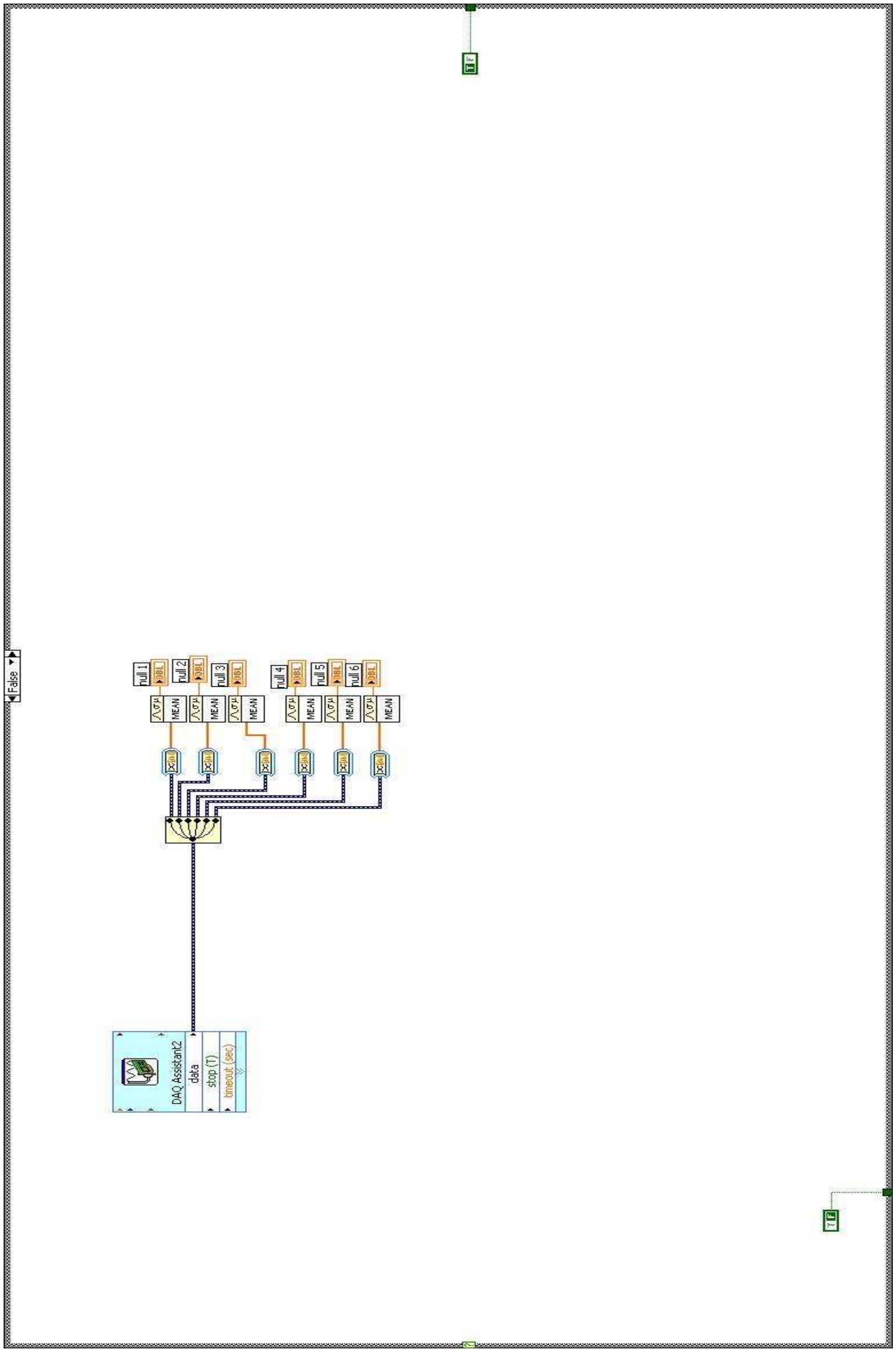

Figure D. 3 - Schematic of Loop2 of Labview program